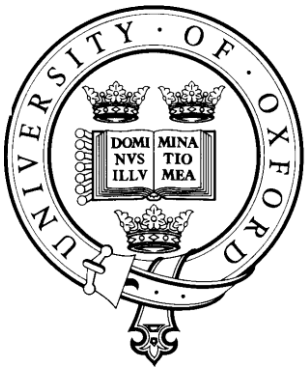



# Numerical modelling and experimental characterisation of mechanical performance of ceramic materials at multiple scales

DPhil Thesis

**Simone Falco**
*Exeter College*
*Solid Mechanics and Material Engineering Group*
*Department of Engineering Science*
*University of Oxford*

Supervised by: Prof Nik Petrinic & Prof Richard Todd
Trinity Term 2015

# Numerical modelling and experimental characterisation of mechanical performance of ceramic materials at multiple scales

Simone Falco, Exeter College, University of Oxford

For the degree of D.Phil. in Engineering Science, Trinity Term 2015

Among countless engineering applications of ceramic materials, the design of reliable ceramic armour remains one of the most challenging. The complexity of deformation and failure mechanisms amplified by the rate-dependent behaviour, observable in service and corresponding experiments, still hinders the development of novel materials capable of demonstrating a significantly improved performance.

The main aim of the research discussed in this thesis is to increase the understanding of the physical phenomena surrounding the response of ceramic materials to rapidly applied loading, such as that arising from explosion and collision, by combining experimental and numerical methodologies at different length scales.

Multiple experimental techniques have been adopted to characterise the materials considered. At the micro-scale, the mechanical properties of single grains, single grain boundaries, and polycrystalline structures have been measured with micro-cantilever beam tests, and the results. At me macro-scale, instead, the quasi-static characterisation tests have been combined with the outcome of high strain-rate tests (i.e. impact) to provide an overview of the macroscopic behaviour of the ceramic materials considered at multiple rates, thus increasing the understating of the rate dependent deformation and failure processes in ceramic materials.

The numerical approach also focused on two distinct scales, aiming to reproduce the geometrical features of the microstructures of polycrystalline ceramic materials, as well as the mechanical response at both the micro- and the macro-scales.

At the micro-scale an innovative method to model the grain structure of polycrystalline materials has been developed. Experimentally obtained results were used both in the generation of the models to guarantee their representativeness, as well as to validate the developed numerical simulation methodologies. This provided the required confidence in the algorithms developed to simulate the response of realistic, statistically representative micro-structures which would be extremely difficult to investigate experimentally. This offered the unique opportunities to explore the physical phenomena which would otherwise be very difficult to generate, let alone observe and measure in reality (i.e. in-situ dynamic crack propagation and branching within three-dimensional domains).

At the macro-scale a constitutive model for simulation of deformation and failure of ceramic materials has been developed, overtaking some limitations of the state-of-the-art material models. An analytical model of the crack growth has been implemented, based on the study of the behaviour of a single sharp crack randomly oriented within an elastic continuum medium, and embedded into an ad-hoc modified constitutive model to lay the fundaments for the future development of methodology for concurrent multi-scale modelling of ceramic materials subjected to impact loading.

# CONTENTS

**CONTENTS** ..... **III**

**NOTATION AND CONVENTIONS** ..... **VII**

**LIST OF TABLES** ..... **XI**

**LIST OF FIGURES** ..... **XIII**

**PREFACE** ..... **XX**

**1 INTRODUCTION** ..... **1**

1.1 Background and motivation ..... 1

1.2 Aim and objectives ..... 2

1.3 Research strategy ..... 3

1.4 Thesis Outline ..... 4

**2 STATE OF THE ART** ..... **6**

2.1 Ceramic materials ..... 6

*2.1.1 Definition and properties* ..... *7*

*2.1.2 Applications* ..... *9*

*2.1.3 Elastic properties of the single crystal* ..... *10*

*2.1.4 Strength and failure mechanisms* ..... *13*

2.2 Experimental techniques ..... 15

*2.2.1 Microscopic experiments* ..... *16*

*2.2.2 Macroscopic experiments* ..... *20*

2.3 Numerical methods ..... 27

*2.3.1 Generation of numerical models of polycrystalline microstructures* ..... *28*

*2.3.2 Continuum macroscopic constitutive models* ..... *35*

*2.3.3 Modelling discontinuities* ..... *42*

2.4 Conclusions ..... 45

**3 EXPERIMENTS ..... 47**

3.1 Micro-cantilever beam tests ..... 47

*3.1.1 Description of the test ..... 48*

*3.1.2 Calculation of deformation and failure properties ..... 51*

*3.1.3 Results and discussion ..... 56*

3.2 Macroscopic characterisation ..... 61

3.3 Dynamic indentation test ..... 62

*3.3.1 Experimental setup ..... 63*

*3.3.2 Preliminary tests ..... 72*

*3.3.3 Indentation tests at multiple strain-rates ..... 81*

*3.3.4 Impact tests on different grades of silicon carbide ..... 92*

3.4 Conclusions ..... 97

*3.4.1 Micro-scale ..... 98*

*3.4.2 Macro-scale ..... 98*

**4 MICROSTRUCTURAL MODELLING ..... 101**

4.1 Generation of virtual microstructures ..... 102

*4.1.1 Generation of arbitrarily shaped polycrystalline aggregates ..... 102*

*4.1.2 Definition of morphology and texture properties ..... 110*

4.2 Finite Elements model ..... 116

*4.2.1 Meshing procedure ..... 116*

*4.2.2 Bulk properties of the grains ..... 117*

*4.2.3 Definition of the grain boundaries and assembly of the structure ..... 119*

4.3 Simulation and validation of quasi-static deformation and failure ..... 122

*4.3.1 Evaluation of the Young's modulus of a polycrystalline aggregate ..... 122*

*4.3.2 Evaluation of the stress-intensity-factor at the tip of a notched plate ..... 127*

*4.3.3 Modelling and simulation of the micro-cantilever beam test ..... 132*

4.4 Simulation of dynamic failure ..... 139
*4.4.1 Propagation of cracks induced by a compressive pulse load ..... 139*
*4.4.2 Impact of a rigid sphere on a polycrystalline plate ..... 151*
4.5 Simulation of trans-granular crack propagation ..... 156
4.6 Conclusions ..... 161
*4.6.1 Generation of microstructural models ..... 161*
*4.6.2 Simulations of deformation and failure of the microstructure ..... 162*
*4.6.3 Summary of the outcomes ..... 163*
**5 MACROSCOPIC CONSTITUTIVE MODEL ..... 165**
5.1 "Modified Johnson-Holmquist" (JH2) constitutive model ..... 166
5.2 Implementation of the anisotropy ..... 172
*5.2.1 Single element verification ..... 174*
*5.2.2 Impact test validation ..... 179*
5.3 Introduction of a new "crack-based" damage evolution ..... 181
*5.3.1 Non-iterative rotation ..... 184*
*5.3.2 Minimization of the cumulative error ..... 185*
5.4 Conclusions ..... 188
**6 CONCLUSIONS ..... 190**
6.1 Micro-scale ..... 190
6.2 Macro-scale ..... 192
**7 FUTURE WORK ..... 194**
7.1 Experimental work ..... 194
*7.1.1 In-situ observation of 3D crack propagation ..... 194*
*7.1.2 Continuing the development of methodology for dynamic indentation ..... 194*
7.2 Numerical work ..... 195
*7.2.1 Trans-granular crack propagation ..... 195*

*7.2.2 Grain plasticity* ..... *196*

*7.2.3 Multi-scale model* ..... *196*

**APPENDIX** ..... **198**

A. Effect of the shear deformation on the micro-cantilever beam ..... 198

B. Stress intensity factor in the notched micro-cantilever beam ..... 199

C. Definition of the properties at the Hugoniot Elastic Limit ..... 200

**REFERENCES** ..... **201**

# NOTATION AND CONVENTIONS

*ABBREVIATIONS AND ACRONYMS*

| | |
|---|---|
| EOS: | Equation Of State |
| HEL: | Hugoniot Elastic Limit |
| LSE: | Local Stress-based Erosion |
| PDE: | Partial Differential Equation |
| RVE: | Representative Volume Element |

*NUMERICAL TECHNIQUES*

| | |
|---|---|
| BEM: | Boundary Element Method |
| CAD: | Computer Aided Design |
| FEM: | Finite Element Method |
| RKPM: | Reproducing Kernel Particle Method |
| XFEM: | Extended Finite Element Method |

*EXPERIMENTAL TECHNIQUES*

| | |
|---|---|
| DB FIB: | Dual Beam Focused Ion Beam |
| EBSD: | Electron Back-Scatter Diffraction |
| IET: | Impulse Excitation Technique |
| FIB: | Focused Ion Beam |
| SEM: | Scattering Electron Microscopy |
| SHB: | Split Hopkinson Bar |
| SHPB: | Split Hopkinson Pressure Bar |

*MATERIALS*

$Al_2O_3$: Alumina

$SiC$: Silicon Carbide

$TZP$: Tetragonal Zirconia Polycrystals

$WC$: Tungsten Carbide

$ZTA$: Zirconia Toughened Alumina

SYMBOLS

$A_b$: Cross sectional area of the gas gun barrel

$\tilde{a}_0$: Pidduck and Kent parameter

$\boldsymbol{B}$: Matrix of the shape functions derivatives

$\boldsymbol{C}$, : Stiffness and compliance matrices

$c$: Sound speed in the material

$D$: Macroscopic damage in the domain

$\overline{d_{gr}}$: Average grain size

$E$: Macroscopic Young's modulus

$F$: Load applied to the specimen

$G$: Shear modulus

$G_V$: Mass of the gas in the vessel

$H_1,\ H_2, H_3$: Extended Hardcore parameters

$h$: Height of the specimen

$I$: Moment of inertia of the cross section

$K_I$: Stress intensity factor in mode I

$K_1$: Bulk modulus

$L$: Length of the specimen

$L_{ind}$: Distance of the indenter from the constrained end of the micro-cantilever beam

$l_{max}^{el}$: Maximum element size

$l_b$: Length of the gas gun barrel

$m_p$: Mass of the projectile

$\boldsymbol{N}$: Matrix of the shape functions

$N$: Number of nuclei

$n_{gr}$: Number of grains

$n_{top}$: Number of topologies

$G$: Shear modulus

$P$: Pressure

$q$: Momentum of the load applied to the specimen

$R_{P_i}$: Set of points associated with the generic nucleus $P_i$

$S_N$, $S_T$: Normal and tangential strength of the grain boundaries

$S_{ij}$: Deviatoric stress

$u_U$, $u_D$: Displacement of the top and bottom crack tail nodes

$V$: Initial velocity of the impactor

$Vol$: Volume of the specimen

$G$: Shear modulus

$v_{ex}$: Velocity of the projectile at the end of the gas gun barrel

$\Delta t$: Duration of the load pulse

$\Delta\varepsilon_p$: Plastic strain increment

$\delta$: Displacement of the loading point of the micro-cantilever beam

$\delta_{kk}$: Kronecker delta

$\dot{\varepsilon}$: Strain rate

$\varepsilon_p^f$: Plastic strain to fracture under constant pressure

$\gamma$: Heat capacity ratio

$\kappa$: Kolosov constant

$\nu$: Poisson Ratio

$\Pi$: Pressure load applied to the specimen

$\rho$: Density of the material

$\rho_H$: Hardcore distance

$\rho_P$: Minimum edge length

$\sigma_C$: Strength of the grain

$\bar{\sigma}_F$: Failure load of the micro-cantilever beam

$\sigma_N$, $\sigma_T$: Normal and tangential traction on a grain boundary

$\sigma_Y$, $\sigma^*$: Material strength in the JH models

$\sigma_i$, $\varepsilon_j$: Stresses and strains expressed in the Voigt notation

$\vartheta_{m0}$: Unit bending moment

$\tau_1$: Time for the wave front to travel through the whole specimen

$\tau_2$: Time from the application of the load to the complete reflection of the wave

# LIST OF TABLES

Table 2.1: Symmetries of the compliance ($\boldsymbol{C}$) and stiffness ($\boldsymbol{S}$) matrices for the crystal classes ..... 12

Table 3.1: Stress intensity factor relative to the crack propagation along different basal planes ..... 57

Table 3.2: Young's modulus and failure strength of bi-crystal cantilever beams ..... 58

Table 3.3: Failure strength measure with uniaxial compression test ..... 62

Table 3.4: Summary of the projectile sets tested ..... 75

Table 3.5: Summary of the heat-treatment processes of the different projectiles sets ..... 78

Table 3.6: Summary of the outcome of the dynamic indentations using heat-treated steel indenters ..... 78

Table 3.7: Summary of the outcome of the dynamic indentations ..... 80

Table 3.8: Grain size distribution of the three materials tested ..... 82

Table 3.9: Summary of the impact tests ..... 84

Table 3.10: Summary of the diameter and depth of the indentation crater ..... 90

Table 3.11: Characterization of the two grades of silicon carbide ..... 94

Table 3.12: Summary of the impact tests on different grades of silicon-carbide ..... 95

Table 4.1: Non-zero terms of the stiffness ($\mathbf{C}$) and compliance ($\mathbf{S}$) matrices for $\alpha$-$Al2O3$ ... 119

Table 4.2: Dimensions of the three sets of topologies ..... 124

Table 4.3: Comparison of $KI$ evaluated numerically, with different mesh refinements, and analytically ..... 130

Table 4.4: Comparison of the maximum principal stress at the notch tip ($\sigma 11max$) and the crack opening displacement ($uU - uD$) for the isotropic and anisotropic models ..... 130

Table 4.5: Single grain properties for the anisotropic and the isotropic models ..... 134

Table 4.6: Single grain properties for the anisotropic and the isotropic models ..... 141

Table 4.7: Summary of the models ..... 142

Table 4.8: Summary of the set of models, with the varying parameters highlights with thick borders ..... 146

Table 4.9: Summary of the failure load of the structure and the mesh sensitivity ..... 159

# LIST OF FIGURES

Fig. 2.1: Ashby-style charts [4] reporting stiffness (top) and strength (bottom) against the density of several materials ..... 8

Fig. 2.2: Basal planes of alumina (hexagonal) crystal [17] ..... 15

Fig. 2.3: Typical shear band morphology in the micro-pillar [31] ..... 18

Fig. 2.4: Typical strain-rate values for several testing techniques ..... 20

Fig. 2.5: Side and front view of indenters ..... 22

Fig. 2.6: Hardcore condition for the nuclei ..... 32

Fig. 2.7: Examples of "classic" Voronoi (left) and Hardcore Voronoi (right) tessellations ..... 33

Fig. 2.8: Classification of constitutive models for ceramic materials ..... 35

Fig. 2.9: Strength definition in JH material models [90] ..... 38

Fig. 2.10: Pressure definition in JH1 and JHB (a) and JH2 (b) material models [90] ..... 38

Fig. 2.11: Normal (left) and shear (right) tractions across the cohesive surface [120, 121] ..... 44

Fig. 3.1: Cross section of the notched beam ..... 48

Fig. 3.2: Top view (left) and failure surface (right) of a bi-crystal micro-cantilever beam ..... 49

Fig. 3.3: Top and prospective view of a polycrystalline micro-cantilever beam [125] ..... 49

Fig. 3.4: Typical dimensions of the micro-cantilever beam and position of the loading point 50

Fig. 3.5: Micro-cantilever beam after the failure [125] ..... 50

Fig. 3.6: Load-displacement curve measured by the nano-indenter ..... 51

Fig. 3.7: Beams with small, medium, and large support cross section ..... 53

Fig. 3.8: Beams with support depths of $0.1 \cdot Lind$ (left) and $0.5 \cdot Lind$(right) ..... 53

Fig. 3.9: Effect of the cross section size and the depth on the deformation of the beam ..... 54

Fig. 3.10: Variation of the compliance error with the aspect ratio in linear and logarithmic scales ..... 55

Fig. 3.11: Failure surfaces along the *m-plane* (left), *c-plane* (middle), and *a-plane* (right) [38] ..... 57

Fig. 3.12: Young's modulus with (solid) and without (dashed) the correction suggested in Eq. (20) ..... 59

Fig. 3.13: Strength of the micro-cantilever beams ..... 59

Fig. 3.14: Failure modes of the last set of micro-cantilever beams ..... 60

Fig. 3.15: CAD design (left) and final realisation (right) of the gas gun ..... 63

Fig. 3.16: Schematic diagram of the gas gun (not to scale) ..... 64

Fig. 3.17: Prediction of the exit velocity with the energy based Eq. (26) and Pidduck & Kent Eq. (24) relations ..... 66

Fig. 3.18: Cylindrical projectile mounted on the sabot ..... 66

Fig. 3.19: Strippers with different internal diameters ..... 67

Fig. 3.20: FE model of the impact test ..... 69

Fig. 3.21: Strain history in the cross sections of backing bar ..... 69

Fig. 3.22: Envelope of the maximum values of the strain for all the cross sections ..... 70

Fig. 3.23: Positioning and connections of the strain gauges on the backing bar ..... 70

Fig. 3.24: Typical voltage vs. time profile of the impact test on alumina target ..... 71

Fig. 3.25: Comparison of the velocity predicted by Eq. (24) (green) and Eq. (26) (blue) against experimental measurements ..... 73

Fig. 3.26: Projectile (circled) flying, from right to left,towards the target and ruled bar in the background ..... 74

Fig. 3.27: Comparison of projectile velocities measured by the light gauges and the high speed camera ..... 74

Fig. 3.28: Real bullet (left) and projectile (right) machined from the bullet core ..... 76

Fig. 3.29: Impact of the tungsten-carbide projectile ..... 76

Fig. 3.30: Impact of the WC sphere on the target ..... 77

Fig. 3.31: Impact of a stainless steel projectile on the ceramic target at $\sim 100\ m/s$ (left) and $\sim 300\ m/s$ (right) ..... 77

Fig. 3.32: Blunted (left) and broken (right) heat-treated steel indenter ..... 79

Fig. 3.33: Typical video footage of a dynamic indentation test ..... 83

Fig. 3.34: Comparison of the momentums measured with the light gages and with the backing bar ..... 85

Fig. 3.35: Primary compression peak for alumina dynamic indentation tests ..... 86

Fig. 3.36: Primary compression peak for ZTA dynamic indentation test ..... 86

Fig. 3.37: Primary compression peaks for TZP dynamic indentation test ..... 86

Fig. 3.38: Video footage of the flash observed in TZP ..... 87

Fig. 3.39: Comparison of quasi-static and dynamic load applied during the indentation tests 88

Fig. 3.40: Visual reconstruction of the indenter after a dynamic (left) and quasi-static (right) indentation test ..... 89

Fig. 3.41: Optical microscopy of the dynamic (top) and quasi-static (bottom) indentation sites respectively on Alumina (a), ZTA (b) and TZP (c) ..... 89

Fig. 3.42: Depth profile of quasi-static (top) and dynamic (bottom) indentations of alumina. 91

Fig. 3.43: Ring crack appereance of quasi-static (left) and dynamic (right) indented ZTA ... 92

Fig. 3.44: SEM micrographs of the fracture surfaces of SiC-D (top) and SiC-E (bottom) ..... 94

Fig. 3.45: Backing bar measurements for the impact tests on SiC D targets ..... 96

Fig. 3.46: Backing bar measurements for the impact tests on SiC E targets ..... 96

Fig. 3.47: Camera footage of the impact on SiC-E1 specimen ..... 97

Fig. 4.1: Distributions of the number of faces (left) and normalised grain radius (right) of different tessellations and real polycrystalline structures ..... 103

Fig. 4.2: Random distribution of nuclei in a cubic seeding volume, and additional nuclei on the vertices ..... 104

Fig. 4.3: Procedure to cut the grain ..... 106

Fig. 4.4: Examples of solid shapes: cube (a), pyramid (b), triangular prism (c), and half-cylinder (d) ..... 106
Fig. 4.5: Cutting of a concave domain..... 107
Fig. 4.6: Cutting of a concave domain with three (left) and four (right) faces..... 109
Fig. 4.7: Examples of concave shapes: cube with rectangular notch (a), plate with semi-circular slot (b), triangular prism with triangular notch (c)..... 109
Fig. 4.8: Comparison of the "isotropic" (left) and the “extended” (right) Hardcore assumptions ..... 111
Fig. 4.9: Comparison of 1000 grains structures with "isotropic" (left) and extended (right) Hardcore assumptions ..... 112
Fig. 4.10: Variation of the aspect ratio (AR) distribution with both $H1$ and $\rho$ ..... 112
Fig. 4.11: Stretching of the tessellation (left) by 50%, 100%, and 200% (left to right) in the horizontal direction..... 114
Fig. 4.12: Pole figures representing the grain orientation of three sets of specimens ..... 115
With this approach the grains are defined as separate domains with individual material properties, to allow for the reproduction of the multiple crystallographic orientations of the type presented in Fig. 4.13. The interface elements on the grain boundaries permit to simulate the initiation and propagation of inter-granular cracks. ..... 116
Fig. 4.14: FE model (left) and element faces on the grain boundaries (right)..... 120
Fig. 4.15: Examples of topologies consisting of 25, 50, and 100 grains..... 124
Fig. 4.16: Young's moduli of the single simulations (triangles), the single topology (asterisks), and measured experimentally (lines)..... 125
Fig. 4.17: Distribution of Young's modulus values for models with 25 (a), 50 (b), and 100 (c) grains ..... 126
Fig. 4.18: Single edge crack plate with finite width (b) subject to pure tension load ..... 127
Fig. 4.19: Polycrystalline notched plate ..... 128

Fig. 4.20: Models of the notched plate with different mesh sizes: 0. 4$\mu m$ (a), 0.3$\mu m$ (b), and 0.2$\mu m$ (c) ..... 129

Fig. 4.21: Contour of the maximum principal stress ($\sigma 11 maxGPa$) in the isotropic (a) and anisotropic (b-f) plates ..... 131

Fig. 4.22: Dimensions of the model of the micro-cantilever beam and position of the loading point ..... 132

Fig. 4.23: Virtual micro-cantilever beams ..... 133

Fig. 4.24: Visual comparison of a virtual and an experimental beam ..... 133

Fig. 4.25: Apparent Young's modulus of the micro-cantilever beams ..... 135

Fig. 4.26: Comparison of the numerical and experimental values for the Young's modulus. 136

Fig. 4.27: Visual comparison of the experimental and numerical fractured surfaces ..... 137

Fig. 4.28: Failure strength of the micro-cantilever beams ..... 138

Fig. 4.29: Dimensions of the compression specimen ..... 140

Fig. 4.30: FE model (a) and contact segments on the grain boundaries (b) ..... 140

Fig. 4.31: Square pulse load applied to the specimen ..... 141

Fig. 4.32: Percentage of interfaces failed for different topologies with isotropic grains ..... 142

Fig. 4.33: Crack propagation in the structure CP1 ..... 144

Fig. 4.34: Percentage of interfaces failed for the same topology with different crystal orientations ..... 147

Fig. 4.35: Percentage of interfaces failed for different load magnitude, with constant momentum ..... 148

Fig. 4.36: Interfaces failed when the wave front reflects, for the models CP1-iso-B1, CP1-iso-A1, CP1-iso-C1 ..... 148

Fig. 4.37: Percentage of interfaces failing for different load durations with constant magnitude ..... 149

Fig. 4.38: Grains and interfaces of the FE model of the target ..... 151

Fig. 4.39: Model of the test and table of the impact velocities.....152

Fig. 4.40: Percentage of interfaces failed for different impact velocities.....152

Fig. 4.41: Crack pattern at different times (columns) after the impact for the analysed velocities (rows) .....154

Fig. 4.42: Maximum principal stress in the target after $1.2 \cdot 10 - 3\ \mu s$ from the impact .....155

Fig. 4.43: Topologies of the notched plate .....157

Fig. 4.44: Models of the notched plate with different mesh sizes: $0.4\mu m$ (a), $0.3\mu m$ (b), and $0.2\mu m$ (c) .....157

Fig. 4.45: Propagation of the trans-granular crack from the notch tip to the closest grain boundary .....158

Fig. 4.46: Failure of the structure due to the combination of trans- and inter-granular crack propagation .....158

Fig. 4.47: Propagation of the trans-granular crack (left) and complete failure of the structure (right) .....160

Fig. 5.1: Definition of the material strength in JH2 model.....167

Fig. 5.2: JH2 test cases [89].....169

Fig. 5.3: Comparison of test case results using user defined material and LS-Dyna JH2.....170

Fig. 5.4: Comparison of stresses between the isotropic and anisotropic models subject to uniaxial load .....175

Fig. 5.5: Comparison of stresses between the isotropic and anisotropic models subject to asymmetric biaxial load.....176

Fig. 5.6: Comparison of stresses between the isotropic and anisotropic models subject to symmetric biaxial load.....177

Fig. 5.7: FE model of the impact test .....179

Fig. 5.8: Backing bar measurement for impact test on alumina targets .....180

Fig. 5.9: Damage distribution on the target using the isotropic (left) and anisotropic (right) JH2 material model.....180
Fig. 5.10: Pattern of isolated inclined cracks and sample volume with a single inclined penny-shaped crack .....182
Fig. 5.11: Stress state on the crack (a), opening force created by the stress state (b) and crack growing direction induced by the opening force (c).....183
Fig. 5.12: Propagation of micro-cracks under horizontal compression load [156] .....183
Fig. 5.13: Chart of the rotation method proposed.....186
Fig. B.1: Normalised compliance vs. normalised notch depth for different positions of the notch .....199

# ACKNOWLEDGMENTS

I wish to thank Prof Nik Petrinic and Prof Richard Todd for having given me the opportunity to take a DPhil at Oxford, and for their supervision and support over the years, and Prof Peter Brown for his guidance, his particularly direct managing approach made working with him extremely stimulating.

I would also like to thank all my colleagues in the IEL team, past, present, and newcomers. Making Begbroke a fun and friendly environment was not a trivial task but we managed to have a really great time.

Coming to Oxford gave me the opportunity to cross path with so many people that really made the whole experience unique and unforgettable. Most of you left (or at least tried to leave) this city, and even if we are not as much in contact as I am very grateful of the time spent together. Special mention to Emanuele, Paolo, and the rest of the "Fonderia Oxford" (what an adventure it has been!), and to Alessandro that during the several years of cohabitation has become the closest thing to a family I had in Oxford.

However, moving to another country can be a bit scary at start, and I have to deeply thank my friends for having always made me feel their presence. We never let the geographical distance affect our friendship, and even if we are scattered across Europe we never let life drift us apart. I think this is amazing, and I feel very grateful for it. A special thought for that goes to Guido and Dario with whom time and distance don't really seem to matter. As for the others, I do not dare listing you all to avoid making just a sequence of names, but be assured you are all in my thoughts.

Finally, the most important thanks go to my parents and my brother Claudio, it is much easier to face forward knowing that somebody always has your back. All of this could not have happened without you.

It was a fun ride, bumpy at times, but thanks to you totally worth it!

# PREFACE

This thesis accounts for the work carried out by the author in the Department of Engineering Science, University of Oxford, under the supervision of Prof Nik Petrinic (Department of Engineering Science) and Prof Richard Todd (Department of Materials).

The research work presented is part of a collaborative project involving the Materials departments of the University of Oxford and the University of Loughborough, the Engineering department of the University of Oxford, and Morgan Advanced Materials, and has been jointly funded by the Defence Science and Technology Laboratory (DSTL) and the Engineering and Physical Sciences Research Council (EPSRC), grant code: EP/G042748/1.

No part of this work has been previously submitted for a degree at this or other university. The work of others has been freely drawn upon and is duly acknowledged and referenced in the relevant points in the text.

Parts of the work described in the thesis are reported in published and submitted publications, and have been presented at international conferences.

*List of publications*

- **S. Falco**, C.E.J. Dancer, R.I. Todd, & N. Petrinic: "*A new anisotropic constitutive model for ceramic materials failure*". Developments in Strategic Materials and Computational Design III, (2012) 93-103.
- **S. Falco**, N.A. Yahya, R.I. Todd, & N. Petrinic: "*Explicit Modeling of Crack Initiation and Propagation in the Microstructure of a Ceramic Material Generated with Voronoi Tessellation*". Developments in Strategic Materials and Computational Design IV, (2013) 185-196.
- **S. Falco**, P. Siegkas, E. Barbieri, & N. Petrinic: "*A new method for the generation of arbitrarily shaped 3D random polycrystalline domains*". Computational Mechanics, 54 (2014) 1447-1460.

- A.D. Norton, **S. Falco**, N. Young, J. Severs, & R.I. Todd: "*Microcantilever investigation of fracture toughness and subcritical crack growth on the scale of the microstructure in $Al_2O_3$*". Journal of the European Ceramic Society, 35 (2015) 4521-4533.

- **S. Falco**, F. De Cola, & N. Petrinic. "*A method for generation and geometrical packing of statistically representative 3D polyhedral grains*". Computer Methods in Applied Mechanics and Engineering (Submitted).

- **S. Falco**, & E. Barbieri. "*A computational method for three-dimensional trans- and inter-granular crack propagation in polycrystalline media*". Computer Methods in Applied Mechanics and Engineering (Submitted).

*List of oral presentations at international conferences*

- "*High strain rate modelling of ceramics"* (2011). Defense Ceramics Network seminar (DCERN7). Dstl, Porton Down, UK.

- "*A new anisotropic constitutive model for ceramic materials failure*" (2012). International Conference on Advanced Ceramics and Composites (ICACC). Daytona Beach, US.

- "*Numerical simulation of failure in 3D polycrystalline aggregates*" (2012). Centre of Excellence for Design in Light Metals Annual Conference (ARC). Monash University, Melbourne, AU.

- "*Explicit modelling of crack propagation in ceramic microstructure*" (2013). International Conference on Advanced Ceramics and Composites (ICACC). Daytona Beach US.

- "*Modelling of crack initiation and propagation in polycrystalline microstructures*" (2014). International Conference on Impact Loading of Lightweight Structures (ICILLS). Cape Town, SA.

- "*Modelling of crack propagation in three-dimensional ceramic microstructures*" (2015). MACH Conference. Annapolis, US.

# 1 INTRODUCTION

## 1.1 Background and motivation

Despite the research of armour materials possibly being as old as the invention of weapons, there are still huge margins of improvements for such devices, especially for the protection of personnel. Currently ceramic materials are the most widely used for both personnel and vehicle protection since they can be very effective at stopping ballistic projectiles by breaking and/or eroding them, often in combination with other materials (e.g. Kevlar, steel) to create "armour systems".

However those systems, and in particular the ceramic component, can be extremely heavy (up to $10 kg/m^2$), hence limiting the mobility and speed of soldiers and policemen in critical situations. Moreover, ceramic armour lacks multi-hit capability, mainly because of its excessive fragmentation during the impact, again endangering the life of the people exposed to threats.

The limited understanding of the physical mechanisms involved in the failure of ceramics – especially at high strain rates – prevents the determination of their ideal properties for armour applications, thus hindering the development of new ceramics for armour. There are several challenges – which are strongly interwoven – in improving armour efficiency, related to both the difficulties of experimental characterization of short-lived impact events involving severe fragmentation, and the numerical difficulties of simulating the actual behaviour of the material considering all the relevant scales.

On the experimental side, a range of mechanical testing techniques have been developed over the decades to characterise the behaviour of ceramic materials at different

scales (from single grains to macroscopic devices) and strain rates (from quasi-static to ballistic), as extensively described in the literature review presented in Section 2.2.

The challenges and the costs related to the experiments have raised the necessity of developing numerical methods to model the behaviour of ceramic materials at high strain-rates. Numerous attempts have been made to simulate armour ceramics, however none of the available literature has presented a methodology to predict the deformation and the fracture of ceramic materials based on the actual composition and properties of the microstructure, as diffusely illustrated in the literature review in Section 2.3.

## 1.2 Aim and objectives

The ultimate aim of the research presented in this thesis is to increase the understanding of the behaviour of ceramic materials, as it is recognised that a deeper comprehension of the phenomena governing the deformation and failure mechanisms of ceramics is crucial to determine a systematic process of improvement of the performance of such materials.

In particular, in the present thesis this aim comprises of the following objectives: to develop a methodology that combines experimental tests and numerical modelling to generate statistically representative models of polycrystalline ceramic microstructures, to simulate the deformation and failure of the material at different strain rates at the grain scale, and to introduce a macroscopic material model to overcome some of the limitations exhibited by the "state-of-the-art" constitutive model for ceramic materials (i.e. Johnson-Holmquist, JH2).

This lays the foundations for the development of a multi-scale modelling approach that bridges the micro- and the macro-scales, thus allowing to take into account the effect of

the microstructural morphology on the deformation and failure mechanisms of macroscopic devices.

The above aim and corresponding objectives follow from the capability gap analysis resulting from the comprehensive literature review presented in Chapter 2.

## 1.3 Research strategy

To increase the understanding of the behaviour of ceramic materials the research work presented combines experimental and numerical approaches both at the micro- and the macro-scales.

At the micro-scale a new method for the generation of statistically representative models of the microstructure of ceramic materials has been created. The proposed innovative approach consists of shaping the final domain from an unconfined aggregate mimicking the actual machining procedure. Experimental characterization techniques have been adopted both to directly measure the properties of single crystals and grain boundaries (to produce representative models of real ceramic microstructures), and to provide validation for the numerical simulations of more complex structures.

The micromechanical models are based exclusively on directly measured material properties, and provide crucial information about the behaviour of the microstructure of the material, permitting the simulation of conditions that can hardly be reproduced experimentally. However, the currently available computational power limits the use of the micro-mechanical approach to the simulation of very small volumes. Nevertheless the simulations at the grain scale provide important pieces of information, which can be used as input for macroscopic modelling of ceramics.

At the macro-scale, a set of experimental techniques have been designed to increase the understanding of the actual behaviour of ceramic materials under impact loading conditions, to highlight the effects of the strain rate. On the numerical side, improvements to the "state-of-the-art" constitutive model are presented. The definition of a fully anisotropic damage variable and the implementation of a new damage evolution law are the main enhancements introduced, thus setting the basis for the implementation of a multi-scale approach that integrates the micro-mechanic into macroscopic models of ceramic materials.

## 1.4 Thesis Outline

The present thesis – structured in 5 chapters – first presents (in Chapter 2) a literature review on both modelling methods and experimental testing techniques for ceramic materials at different scales, focusing on the specific objectives presented in Section 1.2.

Chapter 3, then, describes the experimental work carried out at the two scales analysed in this thesis. First the micro-cantilever tests performed at the grain scale are reported in Section 3.1, to characterise the elastic and failure properties of single grain boundary and polycrystalline microstructure of alumina $\alpha$-$Al_2O_3$. Then, at the macro-scale, both the quasi-static characterisation (Section 3.2) and the dynamic indentation test (Section 3.3) of different materials (including alumina) are presented.

Chapter 4 illustrates an innovative method to generate (concave or convex) polycrystalline domains, which are proven to be statistically representative of real ceramic microstructures. Each grain of the microstructure is discretised separately into tetrahedral elements, and then the structure is assembled by adding – if required – interface entities on the grain boundaries, thus building a Finite Elements (FE) model of the polycrystalline material that have the capability to simulate the initiation and propagation of inter-granular cracks.

Several simulations of deformation and failure of polycrystalline ceramic microstructures are reported, validating the simulations against both analytical calculations and experimental evidence, therefore showing the ability of the microstructures to accurately simulate the deformation and failure of ceramic materials.

Finally, Chapter 5 reports the modifications of the JH2 material model, introducing important novelties, such as the definition of a fully anisotropic damage matrix (in place of the single isotropic value of the JH2 model), and the implementation of a novel damage evolution law that is linked to the micro-mechanics of crack propagation. The model developed sets the base for the implementation of a multi-scale model for ceramic materials which takes into account the microstructural features of the material.

# 2 STATE OF THE ART

In this section the state of the art of the technologies and techniques utilised in the thesis are briefly introduced, to present the basis for the research activities illustrated in subsequent chapters.

Firstly the nature of ceramic materials is explored, describing the general properties of this broad class of materials (Section 2.1.1), their applications (Section 2.1.2), the elastic properties of the single crystals (Section 2.1.3), and the failure mechanisms (Section 2.1.4).

Then the experimental techniques utilised in the work described in the thesis are briefly introduced, both at the micro- (Section 2.2.1) and macro- (Section 2.2.2) scales.

Finally the numerical methods adopted at the micro and macro-scales are described. Section 2.3.1 focuses on the generation of statistically representative models of real polycrystalline ceramic microstructures, Section 2.3.2 on the constitutive (macroscopic) models for ceramic materials, and finally Section 2.3.3 provides a brief overview of the numerical modelling of discontinuities.

## 2.1 Ceramic materials

Among the three broad categories of engineering materials (i.e. metals, ceramics, and composites) ceramics were the first man-made materials ever realised. Archaeological evidence shows that ceramic devices (e.g. pots, crockery, bricks) were produced by shaping and firing mixtures of clay and inorganic substances considerably earlier than the bronze and the iron ages. The word ceramic comes from the ancient Greek word “Keramos”, which some believe to mean “burned earth”, reflecting the initial manufacturing process of such materials [1, 2].

### *2.1.1 Definition and properties*

From a chemical point of view, ceramics are inorganic materials usually produced from a compound of metals (e.g. Al, Mg) or semi-metals (e.g. Si, B) and non-metals (e.g O, C, N). The heating (i.e. sintering) of the compound generates primary ionic and/or covalent bonds between the elements forming the material. The pressure during the sintering process plays an extremely important role, influencing noticeably both the mechanical properties and the microstructure of the final material.

The chemical composition of such materials can vary widely, from single-element materials (e.g. $Si$, $C$), two-element compounds (e.g. $Al_2O_3$, $SiC$, $BN$, $B_4C$) to mixtures of complex phases bonded together. The properties of the materials also vary noticeably because of the differences in the bonds.

Given the light weight of the atoms composing the cited elements and the nature of the atomic bonds, ceramic materials have relatively low densities and high melting points, and often solid ceramics sublime instead of liquefying. Some properties (e.g. chemical inertness, thermal expansion, electrical conductivity) are strongly influenced by the percentage of covalent (i.e. between atoms with similar electronegativity) and ionic (i.e. between atoms at the extremes of the periodic table) bonds in the compound.

Nevertheless, most ceramic materials have mechanical properties in common such as high hardness and stiffness, low ductility, and brittleness. Moreover ceramic materials have a very high compressive strength, but are quite weak in tension, with a tensile value that can be even 5-10 times smaller than the compressive one. Finally, ceramic materials exhibit an extremely limited amount of plastic deformation, before brittle failure. The importance of plasticity is suspected to increase at higher strain rates as well as in the area around an indentation, but this topic is still being debated [3].

The comparison of stiffness, strength, and density for different classes of materials is reported in Fig. 2.1.

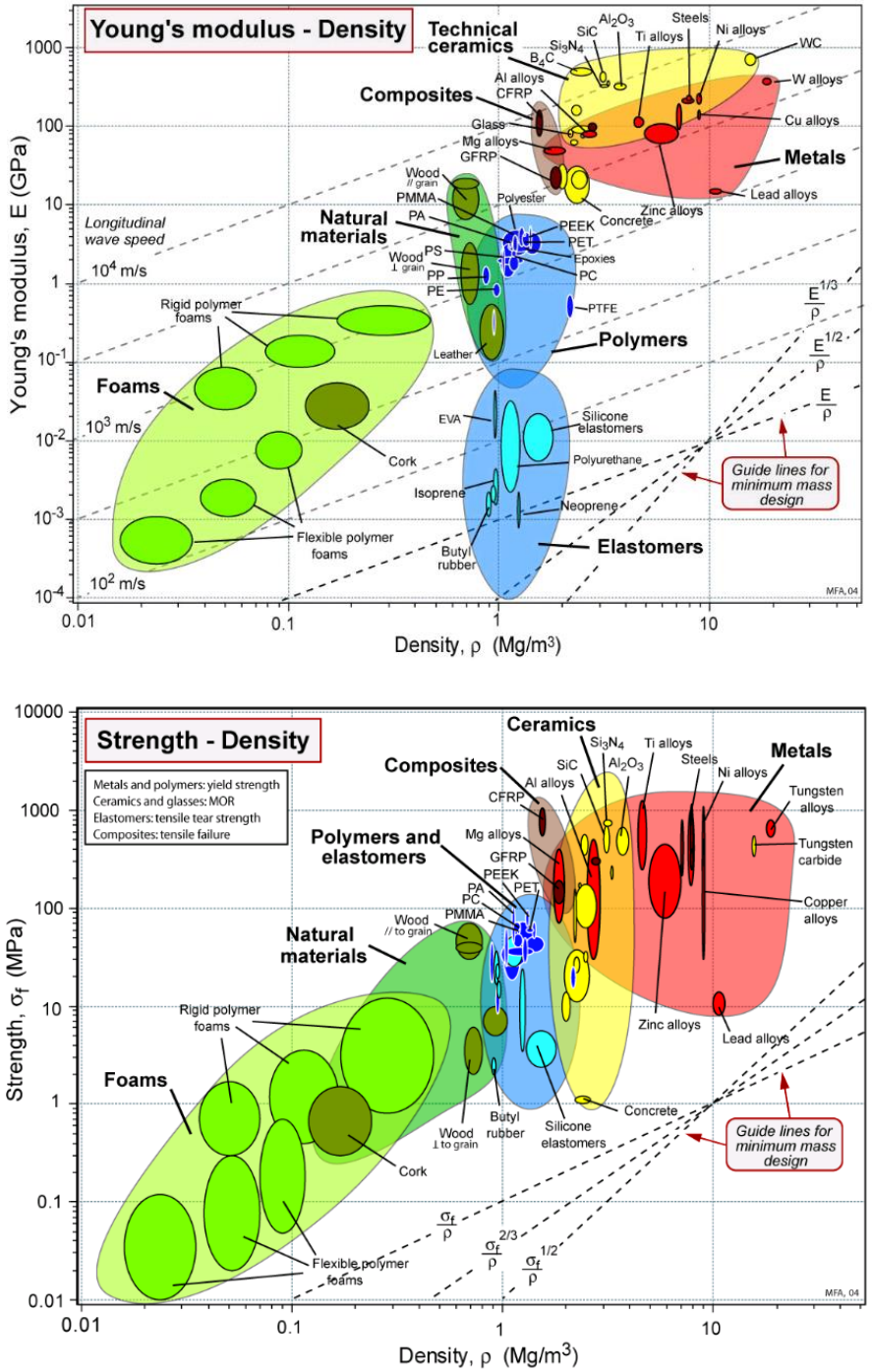



**Fig. 2.1:** Ashby-style charts [4] reporting stiffness (top) and strength (bottom) against the density of several materials

The logarithmic charts reported in Fig. 2.1 were developed by Ashby [4] and report respectively the stiffness (i.e. Young's modulus) and the strength (compressive strength for the ceramics and glasses) against the density of a large number of materials, divided into classes. Ceramics sit at the top of both charts, showing their extremely high stiffness and strength compared to any other material. As mentioned before, the density of ceramic materials is relatively low compared with metals and engineering alloys.

### *2.1.2 Applications*

The peculiar properties of ceramic materials and the abundance and relative inexpensiveness of most of the base elements contribute to the enormous diffusion of such materials with numerous disparate applications.

Beside the devices for everyday use (e.g. pottery, pipes, brick, tiles), ceramic materials have important applications in various areas: electrical/electronic (e.g. insulators, resistors, capacitors, optical fibres), biotechnological (e.g. bone and tooth reconstruction), aerospace (e.g. thermal barriers, engines components), defence (e.g. vehicle and personnel armours) to cite only a part of the immense range of utilization.

The most critical application in terms of mechanical loading is, arguably, the protection from high-velocity impacts. Such impacts can be caused, for example, by debris hitting the ceramic components on aerospace devices (e.g. turbine components, heat-protection tiles) or by bullets colliding on armour.

Ceramic materials seem an unconvincing choice for the use in impact protection being the archetypal brittle material, but their properties make them very effective in defending against high-velocity impacts [5, 6]. The high hardness of the ceramics is their main advantage in defeating projectiles, since it causes the deformation and possibly fracture of the impacting object, lowering its penetration ability. The brittleness also plays an important role,

as the brittle failure mechanisms contribute in reducing the velocity of the projectile, absorbing very effectively the kinetic energy of the impacting object to propagate cracks within the armour material. Finally, the ceramic material around the impact point is highly comminuted and interlocked, and the powder erodes the projectile as it penetrates into the armour, further reducing its kinetic energy [7].

### *2.1.3 Elastic properties of the single crystal*

The properties of the single crystal are strongly related to its geometrical configuration, and in particular with its possible symmetries. Among all the possible symmetry operations, the symmetry elements that can be identified in the geometry of a crystal reduce to four:

- Centre of symmetry,
- Mirror plane,
- 1-, 2-, 3-, 4-, or 6-fold rotation axes,
- 1-, 2-, 3-, 4-, or 6-fold inversion axes,

The possible combinations of symmetry elements are generally referred to as *point groups* [8]. Johann F. C. Hessel in 1830 identified 32 possible different point groups, that define 32 *crystal classes* according to the point group symmetry the crystal possesses [9]. Numerous notations have been developed to identify the classes, but arguably the most widely adopted is the short form of the "Hermann-Mauguin" notation (also defined as "international" by some authors) [10]. This notation assigns a symbol to each class that identifies it unambiguously, summarising its essential symmetry elements. The notation may not include all the symmetry elements of a class, but the presence of the ones indicated by the notation necessarily implies the presence of all the others. For example the $4/mmm$ crystal (that in full notation is: $4/m\ 2/m\ 2/m$) states the presence of 4-fold rotation axes perpendicular to a

mirror plane $(4/m)$, together with a mirror plane containing the axis $(2/m)$ and another mirror plane containing the axis at $45°$ to the latter plane $(2/m)$. The omission of the two "$2/$" in the short form is due to the redundancy of such information, since the mirror planes can be unambiguously obtained from the combination of the symmetry elements in the short symbol.

The 32 classes of crystals can be grouped into 7 *crystal systems*, defined according to their isometries, namely: triclinic, monoclinic, orthorhombic, tetragonal, cubic, trigonal, and hexagonal [8, 11].

The properties of the crystal systems depend on the symmetry elements, and therefore on the crystal classes, and whilst some properties may vary substantially across the classes (e.g. a piezoelectric matrix has 24 different configurations, depending on the class of the crystal), elastic deformations are mainly related to the crystal system.

The description of the elastic properties of the material with the generalised form of Hooke's law (i.e. 21 independent elements) can be reduced by accounting for the fact that symmetry elements of the crystal system represent its elastic behaviour. In particular, the reduction of the number of independent components of the perfectly general (triclinic) stiffness tensor for the different crystal classes is reported in Table 2.1.

The ceramic materials reported in this thesis exhibit different crystal structures: alumina (trigonal), silicon carbide (cubic, hexagonal), tungsten carbide (hexagonal), and zirconia (monoclinic, subject to transitions to tetragonal and cubic).

| | | |
|---|---|---|
| ○ | Zero component | |
| • | Non-zero component | |
| •—• | Equal components | |
| •—□ | Equal and opposite components | |
| ◊ | Twice the value of the heavy dot component to which it is linked | For $S$ |
| | Equal to the heavy dot component to which it is linked | For $C$ |
| **X** | $2(S_{11} - S_{12})$ | For $S$ |
| | $0.5(C_{11} - C_{12})$ | For $C$ |

| | |
|---|---|
| TRICLINIC (Both classes) | TETRAGONAL $4, \bar{4}, 4/m$ $4mm, \bar{4}2m, 422, 4/mmm$ |
| MONOCLINIC (All classes) | TRIGONAL $3, \bar{3}$ $32, \bar{3}m, 3m$ |
| ORTHOROMBIC (All classes) | HEXAGONAL (All classes) |
| CUBIC (All classes) | ISOTROPIC |

**Table 2.1:** Symmetries of the compliance ($\boldsymbol{C}$) and stiffness ($\boldsymbol{S}$) matrices for the crystal classes

The ability of the zirconia to transform from tetragonal to monoclinic is suspected to induce the peculiar reduction of the peak force transmitted by "zirconia-alumina composites" studied in Section 3.3.3

The numerical work presented in this thesis focuses on the simulation of the behaviour of polycrystalline $\alpha$-Alumina, $Al_2O_3$ (hereinafter referred to as Alumina), which is composed of crystals that exhibit a trigonal structure of class $\bar{3}m$. The definition of the stiffness matrix of the single crystal of alumina and its application to the construction of the FE model of polycrystalline aggregates are reported in Chapter 4.

### *2.1.4 Strength and failure mechanisms*

The work presented in this thesis focuses on the structural behaviour of ceramic materials, and in particular on the deformation and failure of such materials under loads at different strain rates. The mechanisms involved in the failure of ceramic materials, in particular on the initiation and propagation of cracks under different loading conditions, have been largely studied in the past century.

The theoretical strength of ceramic materials can be estimated from the force required to break the atomic bonds. During the separation of two atoms the attractive force increases to a maximum (i.e. theoretical strength) to then decrease tending asymptotically to zero. The maximum stress $\sigma_{max}$ can be related to the surface energy $\gamma$, as:

$$\sigma_{max} = \sqrt{\frac{\gamma E}{4x_0}} \tag{1}$$

$E$ is the Young's modulus of the material and $x_0$ is the equilibrium distance between atoms. Values of strength approaching the theoretical limit presented in Eq. (1) have been measured on whiskers (i.e. single crystal fibres). However the strength measured with bulk specimens considerably reduces [12].. In particular, ceramic materials show a relatively high (but still less than the theoretical value) compressive strength with a remarkable low tensile strength (several times smaller than the theoretical value). This behaviour is due to the

presence of imperfections in the bulk material, such as pores, large grains, or even scratches on the surface that lead to stress concentration and possibly to crack initiation.

The dependence of the tensile strength on the presence of flaws in the material reflects in the great influence of the size and shape of the specimen – in addition to the surface finishing and the distribution of the flaws in the bulk material – on the maximum tensile stress in the sample (i.e. the so called "size effect" [13]). In compression, instead, the imperfections play a different – and less important – role in the failure of ceramic materials, since the stress state tends to close the flaws. The failure occurs by growth and coalescence of such defects, hence it depends on the total flaw population rather than on the most severe (i.e. largest and sharpest) crack-like imperfection [1].

Within polycrystalline ceramics – which encompasses the vast majority of ceramics – two distinct failure modes have been observed, depending on the path followed by the crack front with respect to the grains. Depending on the strength of the grain boundaries and the grain itself the crack can propagate either inter-granularly (i.e. along the grain boundaries) or trans-granularly (i.e. through the grains). The fracture modes of many ceramic materials have been experimentally measured showing a reduced influence of the grain size and the manufacturing process [14], indicating that the type of crack propagation depends mainly on the chemical composition of the material.

In particular, alumina exhibits mainly inter-granular fracture due to noticeable difference in strength between the grain boundaries and the crystals [15]. The experimental tests presented in Section 3.1 estimate that the grain boundaries are about 2.5 times weaker than the single crystal.

Finally, the strength of the single grain is affected by the anisotropy of the hexagonal structure of the crystal [16].

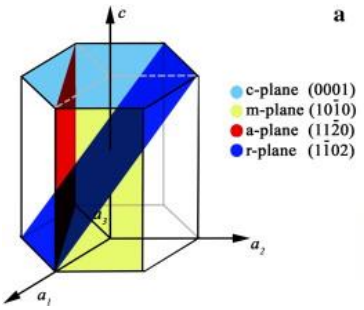



**Fig. 2.2:** Basal planes of alumina (hexagonal) crystal [17]

In Section 3.1 the values of the stress intensity factor along the different basal planes are evaluated, showing that, beside the elastic anisotropy represented by the stiffness matrix introduced in Table 2.1, alumina crystals exhibit direction-dependent behaviour also for the trans-granular crack propagation mechanisms.

## 2.2 Experimental techniques

Since the definition of scientific method by Galileo, countless techniques have been developed to determine the dependence of the behaviour of a material over different parameters (e.g. loading conditions, specimen shape, etc…).

In the following sections a brief overview of the most common experimental techniques to characterise the microscopic (Section 2.2.1) and macroscopic (Section 2.2.2) properties of solid materials is given. Within this general framework, the techniques adopted in the work presented in this thesis are further described to provide a more detailed picture of the experimental work performed.

In particular, the definition of the topological features of the grain structure (i.e. morphology and texture) and the characterisation of the microstructural properties (i.e. elastic moduli and failure strength) are described in Section 2.2.1. At the macro-scale, instead, the quasi-static and dynamic indentation testing techniques are described, setting the scene for the

introduction of the direct comparison performed in Section 3.3, to explore the effect of the strain-rate on the failure of ceramic material.

### *2.2.1 Microscopic experiments*

The high number of mechanisms competing in the deformation and damage of polycrystalline materials hinders the understanding of the effect of single phenomena from the results of classic mechanical tests. With the increasing of the mechanical precision several microscopic techniques have been developed to observe and measure the topological features (e.g. morphology, texture) of polycrystalline microstructures, thus permitting the development of tests able to isolate and study elastic and inelastic fundamental behaviours at the grain scale.

*Experimental determination of the topology of polycrystalline microstructure*

Several experimental techniques have been developed to measure the topology of polycrystalline materials, providing crucial information (e.g. the distribution of grain size and the number of crystal faces). However, generally, those techniques are fairly complex, expensive and extremely time consuming. They can be divided in non-destructive and destructive.

Within the non-destructive measurement approaches, the techniques based on ultrasonic excitation or its variants (e.g. acoustic microscopy, laser ultrasonics [18-20]) rely on the reflection of high-frequency acoustic waves and have limited application for grain imaging in metals. X-ray (micro-) tomography, instead, can be used to produce a representation of the morphology of a wider range of materials, including ceramics. However, it does not provide any information about the orientation of the grains and must be complemented by other techniques (e.g. electron backscatter diffraction EBSD [21]) to

identify the crystallographic orientation, thus allowing for the differentiation of the grains within the scanned volume/domain.

In the family of destructive methods, new techniques for the assessment of the microstructure have been introduced more recently, based on statistical interpolation of 2D images to construct the 3D topology of polycrystalline material. The 2D images are produced by sectioning the material at given intervals. One of the most promising serial sectioning methods is the "dual-beam focused ion beam-scanning electron microscopy" (DB FIB-SEM). This technique is not able to provide any information about the orientation of the crystals, therefore a complete description of the polycrystalline morphology requires the support of an EBSD system [22-25].

All the experimental techniques presented are fairly expensive and produce a huge amount of data, which requires complex and time consuming post-processing. Moreover the procedure can lead to non-unique topologies, due to the possibility of apparent overlapping of grains in the reconstructed structure.

*Measurement of the single crystal elastic properties*

The understanding of the elastic behaviour of polycrystalline ceramics relies ultimately on the evaluation of the elastic properties of the single crystal, which can be measured either with resonant ultrasound spectroscopy (RUS) [26, 27] or with x-ray stress measurements [28].

Multiple assumptions can be made to calculate the elastic properties of the single crystal from x-ray measurements, among which the most well-known and simplest are the Voigt [29] and the Reuss [30]. The first assumes that all the crystals experience equal strain, whilst the second method assumes that all the crystals are under equal stress and that the strain varies based on the compliance in the direction used for the x-ray measurement.

The single crystal properties used in the numerical work presented in this thesis are based on the measurements performed by Hovis et al. [28] with the Voigt method.

*Grain-scale mechanical tests*

Mechanical testing at the grain-scale is extremely useful to determine the properties of all the microscopic features (i.e. grains, grain boundaries, flaws, and defects). Arguably the most promising techniques for the micro-mechanical testing of ceramic materials are the micro-pillars and micro-cantilever experiments.

The micro-pillar testing consists of performing a compression test on a cylindrical structure machined (with FIB) on the surface of the specimen, as presented in Fig. 2.3 [31]:

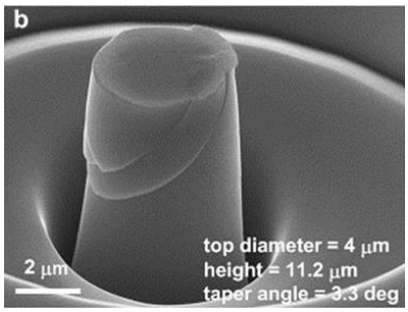



**Fig. 2.3:** Typical shear band morphology in the micro-pillar [31]

The results of such tests, however, have to be carefully analysed since a multitude of geometrical effects may lead to an erroneous prediction of the mechanical properties of the material.

The micro-cantilever beam test, also, has been extensively used for the study of the micro-mechanical behaviour of several materials. The original technique to produce micro-cantilever beams is based on the use of etchants such as potassium hydroxide (KOH) [32]. However the etching techniques do not provide enough control on the thickness of the beam and are often not applicable for ceramic materials. Hence, the FIB machining is, in this context, more appropriate to generate beams. The flexibility of this technique allows for

different shapes of the beam cross-section to be machined, such as pentagonal [33], rectangular [34], and triangular [35].

The test itself consists of imposing a displacement (or a force) to the free end of the cantilever beam measuring the reacting force (or the displacement) until the complete failure of the specimen. Several mechanical properties can be evaluated from these tests, the most important of which are the elastic modulus, the fracture strength, and the toughness.

The Young's modulus of the beam can be calculated with classical beam theory as a function of the applied force ($F$), the beam deflection ($\delta$), the distance of the loading point from the fixed end ($L_{ind}$), and the moment of inertia of the cross section ($I$).

$$E = \frac{F}{\delta}\frac{L_{ind}^3}{3I} \tag{2}$$

The strength, instead, can be determined from the failure load ($F_f$), the distance of the loading point from the failure surface ($L_f$), and the section modulus ($Z$):

$$\sigma_f = \frac{F_f L_f}{Z} \tag{3}$$

There are many advantages in measuring the strength at such a small scale. In particular it allows to both explore the effect of the flaw size, and study materials and phenomena that cannot be linked to the results of macroscopic tests (e.g. anisotropy of dentin-enamel junction in teeth [36], stress corrosion cracking [37]).

Finally, the toughness of the material can be estimated by machining notches on the surface of the beams, thus evaluating the critical stress intensity factor ($K_{Ic}$) as a function of the fracture stress ($\sigma_f$), the notch depth ($\alpha$), and a dimensionless shape factor dependent on the sample geometry ($\Phi_g$):

$$K_{Ic} = \Phi_g \sigma_f \sqrt{\alpha\pi} \tag{4}$$

Examples of such calculations for ceramic materials can be found in the work by Norton et al. [38], as well as for other materials (e.g. coating [33], metal alloys [39]).

The relations (2), (3), and (4) are expressed in their general form, and apply for straight beams with any cross-sectional shape. In this work, however, they will be used in the form related to triangular cross-sections, since – among the three most common beam cross-sections (i.e. pentagonal, rectangular, and triangular) – it has the advantage to provide more control over the geometry during the FIB machining, thus minimising the error in the prediction of the mechanical properties. Also the limitations of the classic beam theory for relatively short beams are explored, and a correction is proposed in Section 3.1.2.

### *2.2.2 Macroscopic experiments*

The experimental techniques developed to determine the macroscopic properties of solid materials can be classified according to the strain-rate ($\dot{\varepsilon}$) imposed on the specimen. A partial list of techniques, with the relative approximate range of strain-rates achievable [40-42], is presented in Fig. 2.4.

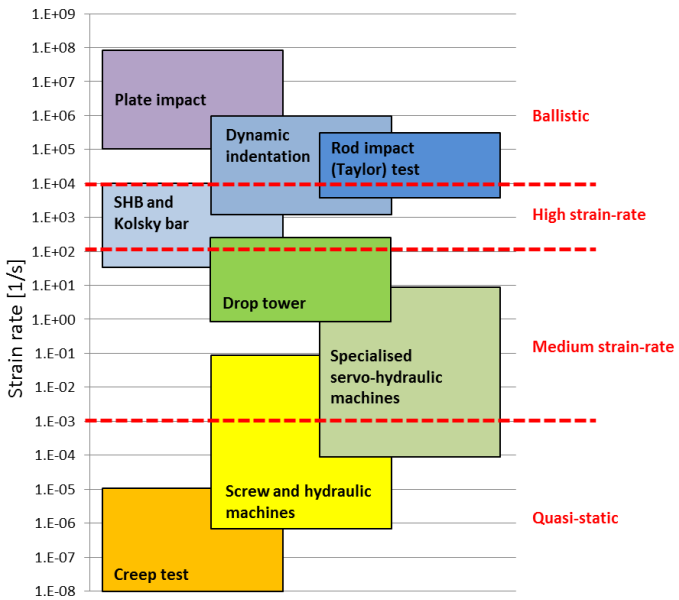



**Fig. 2.4:** Typical strain-rate values for several testing techniques

In the graph is also suggested a possible division of the testing methodologies into four regions: "quasi-static" (i.e. $\dot{\varepsilon} = ]0 - 10^{-3}]$), "medium strain-rate" (i.e. $\dot{\varepsilon} = [10^{-3} - 10^{2}]$), "high strain-rate" (i.e. $\dot{\varepsilon} = [10^{2} - 10^{4}]$), and "ballistic" ($\dot{\varepsilon} > 10^{4}$).

At the low end of the *quasi-static* domain sit the creep tests, which are particularly important to study the long term behaviour of materials in extreme (e.g. high temperature) environment. With screw and hydraulic machines, instead, is possible to perform countless tests with different combinations of loading conditions and specimen shape to explore the mechanical behaviour of a material (e.g. axial tension and compression, indentation, bending, shear, torsion). In particular several types of strength can be defined according to loading conditions: such as for example ultimate, yield, buckling (only in compression). If the realisation of the compression test is too difficult, costly, or time consuming, indentation testing can provide a good estimate of the mechanical strength of the material, alongside other characteristics of the material (e.g. hardness).

In contrast to the quasi-static regime, the study of the medium strain-rate domain is very challenging, due to the importance of the wave propagation mechanisms that are extremely difficult to account for [41]. The only techniques able to carry out tests in this regime are some specialised servo-hydraulic machines and drop towers [43].

In the high strain-rate regime, instead, the most used apparatus is probably the so called Split Hopkinson Pressure Bar (SHPB). The original design developed by Bertram Hopkinson was modified by Davies [44] and Kolsky [45] introducing the configuration with the specimen sandwiched between two metallic bars and subjected to a compressive load [40]. Over the decades further improvement have been proposed to design highly accurate devices that can provide high strain-rate loads in tension [46], torsion [47], and simultaneous torsion and compression [48]. Hopkinson bar tests can achieve a maximum strain-rate of about $10^{4}s^{-1}$ (limit that can be slightly increased for particular materials and geometries).

To generate higher strain rates the use of compressed gas or explosives driven guns is required to accelerate the projectile to impact velocities not reachable by the SHPB. Examples of such tests are the rod impact Taylor test (both symmetric [49] and asymmetric [50]), the flying plate impact test, and the dynamic indentation. Whilst the Taylor and flying plate impact tests provide information about the stress-strain flow curve for the material undergoing high strain rate compressive and shear loads [40], the dynamic indentation test provides insights into the influence of the strain-rate over the inelastic properties of the material.

In the next sections a more detailed description of the two experimental techniques (i.e. quasi-static and dynamic indentation tests) used for the work presented in this thesis is presented.

*Quasi-static indentation tests*

A wide range of information about the properties of materials can be obtained using indentation tests. Depending on the type of material tested and on the geometry of the indenter, several different behaviours can be observed (e.g. brittle fracture, plastic deformation), although the most common application of the indentation test is the measurement of the hardness of materials [51].

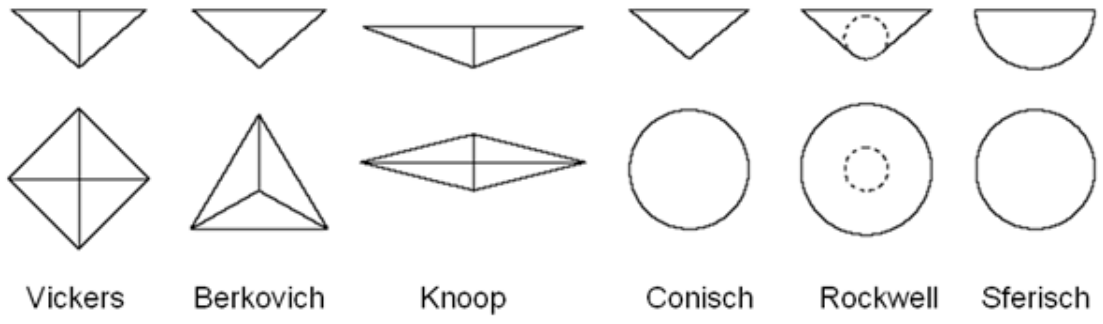



**Fig. 2.5:** Side and front view of indenters

The most common shapes of the indenters are, generally, spherical, pyramidal, conical, or tetrahedral, which can be used to determine different measures of the material

hardness, such as for example Vickers (HV), Brinell (BHN), Rockwell (HRA to HRG). Examples of possible indenters are reported in Fig. 2.5

The indenter is usually made of a material significantly stiffer and stronger than the specimen, in order to avoid any inelastic deformation of the indenter and minimise its elastic deformation.

The test consists of pushing the indenter against the material – with a prescribed displacement rate – to impress a permanent deformation into the specimen surface. The dimensions of the mark can be related – according with the indenters and the techniques adopted – to different properties of the material.

In this work the Vickers indentation has been used to quantify the hardness (proportional to the length of the diagonal of the indentation mark) of the projectiles for the impact tests presented in Section 3.3, whilst Berkovich indenters have been used to impose the displacement on the micro-cantilever beams presented in Section 3.1.

Finally, for ceramic materials, the radius of the radial crack induced by a spherical indenter (i.e. Hertzian) is commonly used as a measure of the maximum tensile strength.

*Dynamic indentation and functioning of the gas gun*

Dynamic indentation consists of impacting a specimen with an indenter to impress a permanent deformation into the target. For relatively low strain-rates the indenter can be installed at the end of a SHPB, whilst to achieve higher impact velocities (i.e. strain-rates) a gas gun is normally used.

The gas gun is a device that accelerates an object (projectile) converting pressure differential into kinetic energy. The pressure differential can be created either decreasing the pressure in front of the projectile or increasing the pressure at its back. The first solution can impose a maximum differential of $1\,atm$ (i.e. pressure difference between the room

conditions and the vacuum), and therefore is often used only as a complement to the pressurised gas pushing the projectile to achieve higher velocities.

Therefore the generic design of a gas gun consists of a vessel that contains pressurised gas, connected to the barrel with a release system. Possibly at the end of the barrel the chamber containing the target can be vacuumed to increase the pressure differential. There are several systems that can be adopted to release the gas, among which the most common are: bursting diaphragms, clamping devices and valves.

The first technique consists of inserting a calibrated diaphragm between the vessel and the projectile, which bursts at a pre-determined pressure, applying the load uniformly on the back of the projectile. Clearly, adopting this technique, the control of the release pressure is limited and the production of calibrated diaphragms creates additional workload per test.

The clamping devices, instead, hold the projectile (or its support) in place whilst the pressure differential is applied. When the desired pressure is reached the projectile is released. This technique provides uniform load on the back of the projectile coupled with complete control over the release pressure. However those advantages come at a price of an additional system that imposes a new maximum possible pressure differential (linked with the maximum clamping force applicable) and further work is required to shape the projectile (or the support) in order to accommodate the clamps.

Finally, the valves consist of a moving part that releases the gas from the vessel into the barrel. These devices do not require any additional manufacturing, but, for particularly high pressures, might not provide uniform and constant pressure on the back of the projectile during the valve opening time.

Indubitably one of the most important factors in the operation of the gas gun is the dependence of the velocity of the projectile on its mass, the pressure differential, and the structural parameters of the device (e.g. barrel inner diameter, length, vessel volume). The

exit velocity of a projectile from a gas gun – providing a constant pressure differential – can be analytically estimated under the assumption that the entire work done by the pressure at the base of the projectile ($W_P$) is converted into the kinetic energy of the projectile ($K_p$). The work done by the force generated from the pressure ($P_V$) is proportional to the area of the projectile base ($A_b$) and distance travelled down the barrel ($x_b$).

$$W_p = P_V A_b x_b \tag{5}$$

The kinetic energy of the projectile, on the other hand, is proportional to its mass ($m_p$) and velocity ($v_p$).

$$K_p = \frac{1}{2} m_p v_p^2 \tag{6}$$

Imposing the equality of those two quantities when the projectile has travelled the whole length of the barrel ($l_b$), the exit velocity ($v_{ex}$) can be extrapolated.

$$K_p = W_p \quad \Rightarrow \quad \frac{1}{2} m_p v_{ex}^2 = P_V A_b l_b \quad \Rightarrow \quad v_{ex} = \sqrt{\frac{2 P_V A_b l_b}{m_p}} \tag{7}$$

This approach is reported in many early works on the functioning of gas guns (e.g. [52]). However, it was soon evident that the simplistic assumption of considering that the pressure at the base of the projectile remains constant for the whole duration of the test may lead to a significant error in the prediction of the gun performance.

There are two main mechanisms that influence the pressure at the base of the projectile. The first is the drop of the pressure due to the increasing of the volume of the system (i.e. vessel and barrel) during the test, and can be minimised using a vessel large enough to make the increase of volume negligible. The second mechanism that influences the exit velocity is related to the effect of the shedding and reflection of release waves from the rear of the projectile. As it accelerates down the barrel the projectile leaves a low pressure volume that propagates upstream until it reaches the breech. The change in cross-sectional

area in the connection between the vessel and the barrel partially reflects the pressure wave as a compressive pulse. The wave travels upstream hitting the base of the projectile, imposing an additional acceleration. Since the speed of sound in compressed gas is several times bigger than its ambient value, this effect is not negligible [53].

A possible approach to take into account the effect of the rear waves is proposed by Pidduck and Kent, and reported in [54]. They assumed that the effect of the wave in the barrel can be approximated with the asymptote of the oscillatory function that describes the wave arrivals on the rear of the projectile.

Adopting this approach the velocity becomes also dependent upon: the speed of sound in the compressed gas ($c_0$), the ratio of specific heats of the gas ($\gamma$), the mass of gas in the vessel ($G_V$), and a parameter $\tilde{a}_0$.

$$v_{ex} = \frac{2c_0\sqrt{\tilde{a}_0}}{\gamma - 1}\sqrt{1 - \left(1 + \frac{\gamma P_V A_b l_b}{c_0^2 G_V}\right)^{(1-\gamma)}} \tag{8}$$

The parameter $\tilde{a}_0$ is a function fitted from the numerical integration of Eq. (9):

$$\frac{G_V}{m} = \frac{2\gamma}{\gamma - 1}\tilde{a}_0(1 - \tilde{a}_0)^{-\frac{\gamma}{\gamma-1}}\int_0^1 (1 - \tilde{a}_0\mu^2)^{\frac{1}{\gamma-1}}d\mu \tag{9}$$

Under the hypothesis of ideal gases, the heat capacity ratio ($\gamma$) is function only of the degrees of freedom of the molecule ($f$) by the relation:

$$\gamma = 1 + \frac{2}{f} \tag{10}$$

Therefore for the monoatomic gases (i.e. the noble gases such as helium or argon), that have only 3 degree of freedom, $\gamma = 5/3 \cong 1.67$, whilst for the diatomic gases (e.g. nitrogen, oxygen), that have 5 degrees of freedom, $\gamma = 7/5 = 1.4$. These values are highly consistent for relatively low temperature, for example dry air exhibits a deviation of just 0.2% in the range from 0 to 200 °C.

Assuming an ideal behaviour of the gas, $G_V$ can be expressed in terms of the volume of the vessel ($V_V$), molecular mass ($M_g$), temperature ($T_V$) and pressure of the gas ($P_V$):

$$G_V = \frac{P_V V_V M_g}{R T_V} \tag{11}$$

The ideal gas constant ($R$) is fixed, the molecular mass ($M_g$) is given by the choice of the gas, and the vessel volume ($V_V$) comes from design constraints. Assuming the change in temperature ($T_V$) negligible (i.e. the gas is constantly at room temperature $\sim 300°K$), $G_V$ is linearly proportional to the gas pressure.

The function presented in Eq. (9) can be solved numerically for a given value of $G_V/m$ and the resultant value of $\tilde{a}_0$ substituted in Eq. (8), to calculate the exit velocity of the projectile.

Additional corrections can be made to take into account, for example, the change of section from the vessel to the barrel, or the effect of the gas-wall friction. However these effects are considered to be of secondary importance and are therefore not accounted for in this work.

These considerations, as well as the verification of the absence of inelastic deformation of the gas gun structure, are used for the actual design of the gas gun used to perform the dynamic indentation tests (as presented in Section 3.3).

## 2.3 Numerical methods

With the continuous increase of the available computational power, the capabilities of the numerical methods are constantly improving, making them a fundamental complement to the experimental work in order to increase the understanding of the behaviour of materials.

In this thesis numerical methods developed both to generate statistically representative models of polycrystalline (ceramic) microstructures, and to simulate the behaviour of the material under different loading conditions are presented.

In Section 2.3.1 an excursus of the methods adopted in literature to generate models of polycrystalline microstructures is given, with a particular focus on the implementation of the Voronoi tessellation technique.

In Section 2.3.2 brief introduction of the macroscopic constitutive models developed to simulate the behaviour of ceramic materials is provided, highlighting advantages and limitations of both *isotropic* and *anisotropic* material models.

Finally, in Section 2.3.3, several possible approaches to simulate discontinuities (i.e. cracks) within the Finite Element Approach are presented.

### *2.3.1 Generation of numerical models of polycrystalline microstructures*

The understanding of the mechanisms governing deformation and failure of polycrystalline ceramic materials at the grain level is crucial to increase the comprehension of the macroscopic behaviour of these materials. Many important phenomena occurring in polycrystalline materials depend on the characteristics of the microstructure, such as the single grain properties, the orientation of the crystals, and the topology of the structure (i.e. shape and distribution of the grains). In particular the first two characteristics mainly control the global behaviour of the material (e.g. macroscopic elastic properties), whilst the additional modelling of realistic morphologies is necessary to predict localised phenomena (e.g. stress concentration, crack initiation).

In the recent decades several techniques have been developed to generate models of the topology of polycrystalline aggregates, either based on experimental measurements (introduced in Section 2.2.1) or virtually generated.

As presented in Section 2.2.1, the main limitations of the experimental techniques to reproduce real microstructures are the cost and the complexity of the post-processing required to analyse the huge amount of data produced. Moreover the procedure may lead to non-unique topologies, due to the possibility of apparent overlapping of grains in the reconstructed structure.

The introduction of numerical methods to generate models of the microstructure of polycrystalline materials overcomes the difficulties encountered in the experimental determination of the material morphology. The first attempts to numerically investigate the micro-mechanics of polycrystalline materials were mainly based on the generation of 2D microstructures. Baczmansky et al. [55] used several thousand square grains to predict the residual stresses in plastically deformed steel, whilst Ortiz and Suresh [56] found that accurate estimate of residual stresses requires at least two hundred regular hexagonal grains. However, the approaches based on regular grain geometries do not provide statistically representative models, hence alternative methods are needed to simulate the variability in size and shape of the grains. Despite the existence of several methods to discretise the two-dimensional space (e.g. Potts models for grain growth [57]), Voronoi tessellations have dominated the modelling of metallurgic and ceramic 2D microstructures in the recent decades [58-62]

In the last few years – with the increasing of computational power – an increasing number of researchers have developed algorithms to generate 3D polycrystalline models. As for the 2D models, many authors have proposed the simulation of 3D polycrystalline microstructures using regular morphologies (e.g. cubes [63], regular dodecahedra [64], truncated octahedra [65]). The regular morphologies have the advantage of being extremely easy to generate and to mesh, but are not representative of the variability in the grain shape and size observed in real polycrystalline materials, which makes them unable to simulate localised phenomena. Several authors have proposed analytical and numerical methods to

generate random polycrystalline morphologies (e.g. Montecarlo Potts modes [66], phase-field models [67] surface evolver approach [68]), but – like for the generation of 2D microstructures – Voronoi tessellation approaches are generally preferred.

Voronoi tessellation methods are sometimes considered to provide coarse modelling of microstructures [69], because they underestimate the variability in size and overestimate the number of faces of the grains. However, among randomly generated morphologies, Voronoi tessellations have the advantage of reproducing an ample range of variability of both size and shape of the grains, of being defined analytically, and of consisting of grains with straight edges and planar faces [70]. In particular, Laguerre-Voronoi, Poisson-Voronoi, and Hardcore-Voronoi tessellation algorithms are widely accepted to generate statistically representative models of microstructures of metallic and ceramic materials [59, 60, 71-74].

*Voronoi tessellation*

Besides the modelling of polycrystalline microstructures, Voronoi tessellations have numerous applications in the most diverse fields such as astronomy [75], biology [76, 77], and engineering. Also within the field of engineering the Voronoi tessellations have disparate usage, as for example data compression in image processing [78], coverage of wireless communications [79].

Voronoi tessellations decompose the entire space into convex polyhedral domains (i.e. *cells*) from an arbitrarily assigned set of points (i.e. *nuclei*). A single cell is generated from each nucleus, consisting of all the points closer to the correspondent nucleus than to any other nucleus. All thus generated cells are convex polyhedral – i.e. bounded by planar surfaces (i.e. *faces*) with polygonal perimeter (i.e. *edges*).

Mathematically the *i-th* cell generated from the Voronoi tessellation of the three-dimensional space seeded with $N$ nuclei can be expressed as:

$$\{R_P\} = \{\boldsymbol{x} \in R^3 | d(\boldsymbol{P}_i, \boldsymbol{x}) \leq d(\boldsymbol{P}_k, \boldsymbol{x}), k = 1,2, \dots, N : k \neq i\} \quad (12)$$

$\boldsymbol{P}_k$ is the position of the *k*-th nucleus, $R_P$ is the set of points associated with the nucleus $\boldsymbol{P}_i$ (i.e. points composing the Voronoi cell) and $\boldsymbol{x}$ is any point in the three-dimensional space.

From this definition several variants of tessellations have been proposed in the past few decades, most used of which are the "Laguerre-Voronoi", the "Poisson-Voronoi", and the "Hardcore-Voronoi" tessellations. The first introduces an extended definition of the distance within the nuclei, whilst the other two tessellations impose additional constraints to the distribution of nuclei [80].

The "Laguerre Voronoi" introduces a different definition of the distance, defining the power distance as alternative to the Euclidian norm imposed by the "classic" Voronoi tessellation method, hence modifying Eq. (12) to:

$$\{R_P\} = \left\{\boldsymbol{x} \in R^3 | pow\big(\boldsymbol{x}, (\boldsymbol{P}_i, w_i)\big) \leq pow\big(x, (\boldsymbol{P}_k, w_k)\big), k = 1,2, \dots, N : k \neq i\right\} \quad (13)$$

The power distance assigns a weight ($w_i$) to each nucleus ($\boldsymbol{P}_i$), and is mathematically defined as:

$$pow\big(\boldsymbol{x}, (\boldsymbol{P}_i, w_i)\big) = \|\boldsymbol{x} - \boldsymbol{P}_i\|^2 - w_i \quad (14)$$

If the weight $w_i$ is positive this expression represents the power of the point $\boldsymbol{x}$ with respect to a sphere centred in $\boldsymbol{P}_i$ with radius $r_i = \sqrt{w_i}$, hence the name "*power distance*". This distance can be considered as an extension of the Euclidian norm, to which it reduces if all the nuclei have the same weight (i.e. $w_i = w_k \; \forall i, k = 1,2, \dots, N$).

A generic Laguerre-Voronoi cell can be either convex or concave and does not necessarily contain its nucleus. Moreover, under certain conditions, a nucleus may not generate a cell [81].

The "Poisson-Voronoi" tessellation, instead, imposes that the nuclei are positioned following the special Poisson point process. The nuclei are stochastically independent and the

probability of the number of points in region $A$ being equal to a generic value $k$ is given by the Poisson distribution:

$$P(N(A) = k) = \frac{\left(\lambda V(A)\right)^k}{k!} e^{-\lambda V(A)} \tag{15}$$

The only degree of freedom of the distribution is the density of the Poisson point field $\lambda$ (i.e. the mean number of points per unit volume) [82, 83] .The two Voronoi-based tessellations presented so far can also be combined to generate the so-called "Poisson-Laguerre-Voronoi" tessellation.

Finally, the "Hardcore-Voronoi" tessellation imposes a minimum distance between the nuclei:

$$\left|\boldsymbol{P}_i - \boldsymbol{P}_j\right| > \rho_H \; \forall i, j = 1,2, \dots, N : i \neq j \tag{16}$$

If a nucleus falls closer than $\rho_H$ to another nucleus it is moved to another position within the seeding domain, as illustrated in Fig. 2.6:

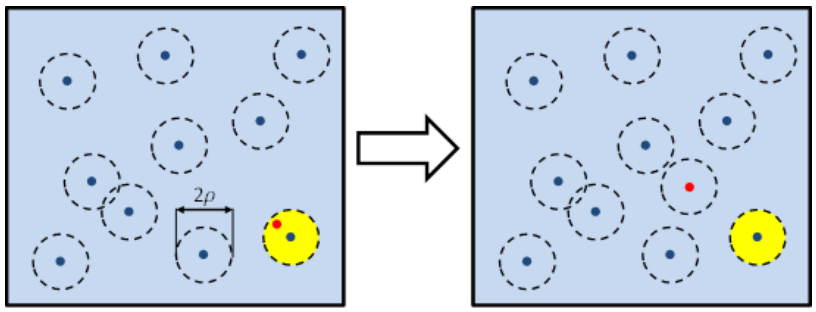



**Fig. 2.6:** Hardcore condition for the nuclei

This technique allows for the avoidance of the generation of highly distorted or excessively irregular cells, for which spatial finite element discretisation would require either a highly refined mesh or distorted elements, both of which would seriously affect the numerical analysis.

Within the different techniques generally used to generate tessellations with cells with a more regular shape, the Hardcore Voronoi represents a balanced choice between

effectiveness and simplicity. It produces more regular cells, drastically reducing the number of small entities [74]. The effect of the adoption of the Hardcore assumption in 2D is represented in Fig. 2.7:

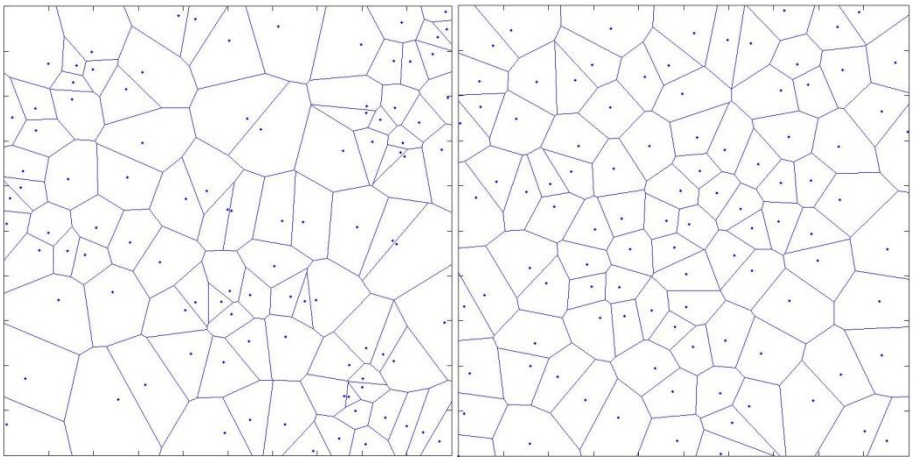


**Fig. 2.7:** Examples of "classic" Voronoi (left) and Hardcore Voronoi (right) tessellations

In the work presented in this thesis the Hardcore assumption is adopted to generate models of three-dimensional microstructures of polycrystalline ceramics. In particular the Hardcore Voronoi tessellations can be interpreted in terms of the homogeneous growth process of metallurgical or ceramic grains under the following assumptions [84].

- All the nuclei have the same weight, appear simultaneously, and remain fixed at their initial location during the entire growth process.
- The nuclei have an initial finite size represented by a sphere of radius $\rho_H$
- The growth is uniform and isotropic with a constant rate.
- Each grain grows in a direction until it contacts the boundary of another grain.
- The entire space is tessellated, without voids in between the grains.
- The grains do not overlap.

Finally, in Section 4.1.2 an extension of the Hardcore assumption is proposed that eliminates the simplistic hypothesis of uniform growth of the grains, thus allowing for the

modelling of the anisotropic growth of the grains (observed in ceramic and metallurgic materials subjected to particular manufacturing processes).

Despite the extensions proposed there are still some limitations of Voronoi cells for the modelling of real polycrystalline microstructures, such as the presence in the models of sharp vertices and of edges shared by multiple (i.e. more than 3) grains, which are absent in real microstructures because of the minimization of the energy during the grain growth process. The limited appearance of these features, however, ensures the representativeness of the models generated.

For other properties of the Voronoi tessellation, the comprehensive review given by Aurenhammer [70] is suggested.

*Algorithm implementation*

Numerous approaches have been implemented to generate models of microstructures of polycrystalline metals or ceramics (e.g. Voro++ [85], Neper [86]) based on different techniques. However such approaches are based on the definition a-priori of the final shape of the domain, which limits the possibility of generating concave domains and leads to non-uniform grain properties in the domain due to the effect of the boundaries.

The presence of a concavity in a domain defined a-priori shadows the nuclei during the generation of the Voronoi cells, thus hindering them from propagating over the concave edges. Additionally the absence of nuclei outside the a-priori defined domain makes the cells on the boundaries theoretically unbounded, therefore possibly topologically different from the bounded cells inside the domain.

Possible ways of circumvent such limitations presented in literature are, respectively, to impose the radius of curvature of the concavities several times larger than the grain size and to define periodic distributions of the grains to simulate the presence of nodes external to

the domain. However the first approach still leaves unsolved the issue of the generation of domains with narrow concavity, as for example structures with notches of sizes comparable to the grain size. The second, instead, implies the addition of a huge number of nuclei (e.g. 27 times more in the method proposed by Fritzen et al. [74]), and the constraint of using extremely regular geometries for the domain.

The method presented in this work, and described in detail in Section 4.1, elegantly overtakes both issues introducing a more physical approach to the generation of models of polycrystalline microstructures, also providing great control over the statistical properties of the grain distribution. It consists of seeding the nuclei in a domain larger than the desired structure to then producing the final shape by cutting the unconfined grains along planar surfaces. This allows for the generation of any desired (both convex and concave) virtual polycrystalline structure.

### *2.3.2 Continuum macroscopic constitutive models*

At the macroscopic scale several constitutive models have been developed to simulate the behaviour of ceramic materials. The continuum models found in the open literature can be graphically classified as presented in Fig. 2.8:

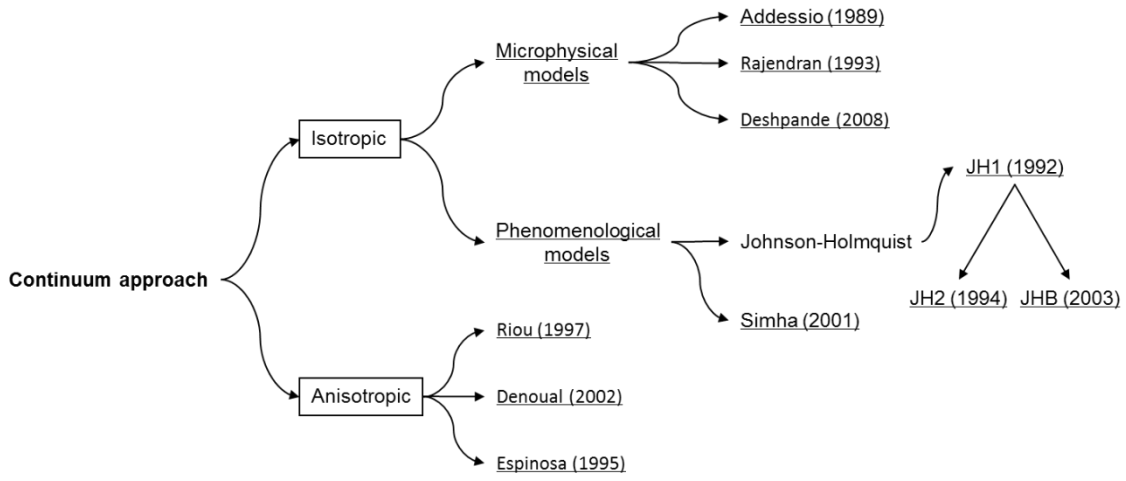



**Fig. 2.8:** Classification of constitutive models for ceramic materials

The constitutive models based on the continuum approach consider the ceramic materials as continuum, homogeneous solids. The effect of the crack initiation, growth and coalescence are embedded in a damage variable that governs the decreasing of the material strength with the propagation of the cracks.

The material models presented in this section have three common features:

- Strength model, that defines the limit of the elastic region and the condition for the increasing of the damage
- Equation of state (EOS)
- Damage law, which governs the damage evolution.

Within such common ground, two main categories of constitutive models can be defined: the models assuming an isotropic evolution of the damage, and the models that take into account the intrinsic anisotropic nature of the cracking mechanisms by evaluating the damage propagation along different directions.

The assumption of isotropic evolution of the damage is usually justified assuming that – for fine spatial discretisation – the error is acceptable compared to the simplification (i.e. reduction of computational cost and number of parameters). Moreover, in highly dynamic deformations that rapidly deform the material to a comminuted state, the effect of the anisotropy has been proven to be negligible [87]. However, in the context of developing a physically based approach to the modelling of ceramic materials, the anisotropic nature of the failure mechanisms is considered to be of significative importance.

*Isotropic models*

Isotropic constitutive models assume that the damage evolves equally in all directions in the material (i.e. the damage is defined as a scalar value). Thus the only effect of the crack growth is the degradation of the strength of the whole domain.

The hypotheses of the isotropic constitutive models are:

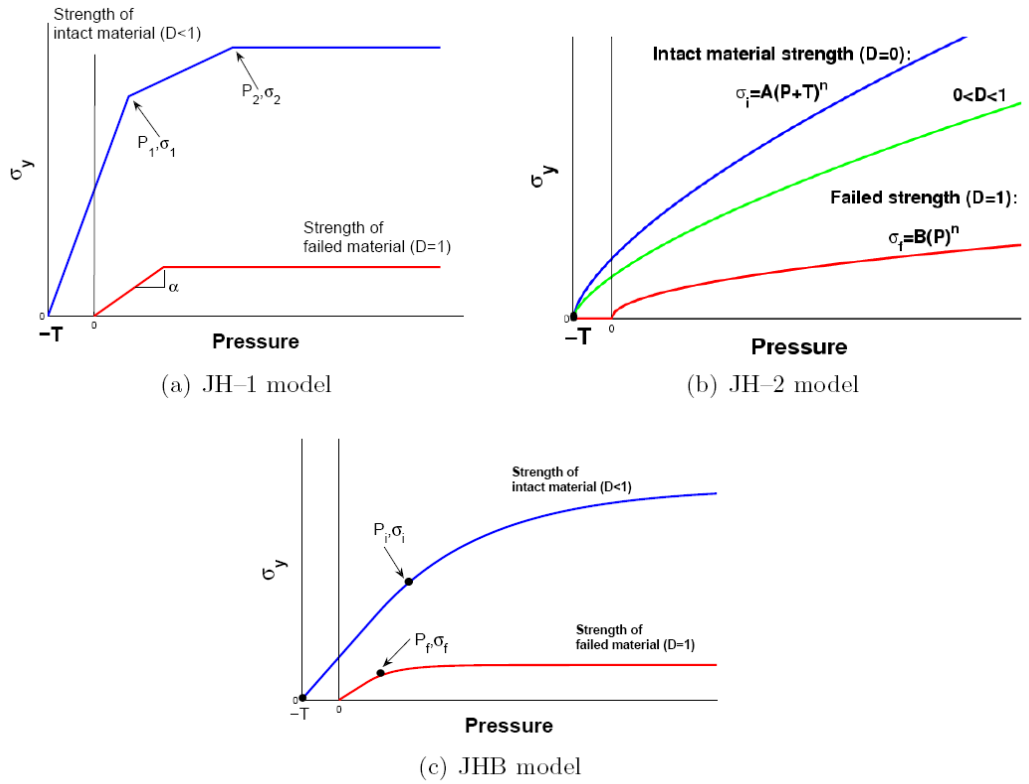
- the material is isotropic and initially elastic;
- the damage is homogeneously distributed over the RVE;
- the material is initially populated with a large number of randomly oriented micro-cracks;
- the interaction within cracks is limited to their coalescence, which defines the material failure.

The material models developed by Johnson and Holmquist, commonly known as JH1 [88], JH2 [89], and JHB [90] in chronological order, are arguably the most widely used models to simulate the behaviour of ceramic materials. In particular, the JH2 model is implemented in several commercial software packages (e.g. Autodyn, Epic, LS-Dyna [91]), being – in some cases – the only constitutive model for ceramics implemented.

These models – that are widely used in armour design and simulation [92, 93] – are based on the definition of a scalar damage variable $D$, whose increment is proportional to the plastic strain rate:

$$D = \sum \frac{\Delta \varepsilon_p}{\varepsilon_p^f} \tag{17}$$

In particular, the damage increment is given by the ratio of the increment of plastic strain ($\Delta \varepsilon_p$) over the 'plastic strain to fracture under constant pressure' ($\varepsilon_p^f$) which is a function of the pressure within the RVE. The damage ranges from 0 (i.e. intact material) to 1 (i.e. completely failed material), and affects the strength $\sigma_Y$ (Fig. 2.9) and the pressure $P$ (Fig. 2.10) in the element.




(a) JH–1 model (b) JH–2 model

(c) JHB model

**Fig. 2.9:** Strength definition in JH material models [90]

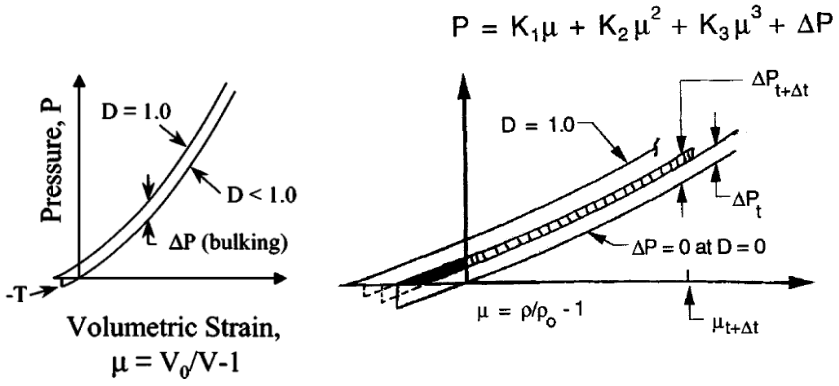



**Fig. 2.10:** Pressure definition in JH1 and JHB (a) and JH2 (b) material models [90]

The JH2 model is the only one of the JH models to take into account the gradual decrease of material strength due to the increase in damage, whilst in the JH1 and JHB models the damage switches suddenly from the intact to the completely failed value.

In all the JH models the material properties are defined through a number of empirical parameters (up to 20 in the JH2 model) most of which have to be inferred statistically with a polynomial fit from different types of tests.

The JH2 model will be described more in detail in Section 5.1, given its importance in fully appreciating the development and characteristics of the constitutive model presented in this thesis (Section 5).

Another important phenomenological constitutive model for ceramic materials has been developed by Simha [94]. This model defines the damage as a function either of the shear stress (in compression) or of the principal stresses (in tension). The damage gradually affects the strength of the material until its complete failure. As for the JH models, the model proposed by Simha needs to combine several types of testing to obtain the necessary calibration parameters.

Other isotropic constitutive models developed in the past few decades are based on physical considerations concerning the evolution of the cracks rather than on the phenomenological determination of calibration parameters that fit measurements obtained from different experimental tests.

Addesio and Johnson [87] determine the instability criteria by considering the energy balance on an isolated penny shaped crack. They define two "damage surfaces" – for tension and compression – that represent all the combinations of stress, pressure, and crack size at which the damage starts increasing (i.e. the work of the external forces is equal to the internal energy of the system). In particular, when the elastic predictor exceeds either damage surface, the cracks grow proportionally to the inelastic strain generated in the process – which is in turn proportional to the stress return to the damage surface – until the "stress-pressure-crack size" combination lies on the damage surface. The crack propagation velocity is assumed to depend on the difference between the stress state and the damage surface.

The model developed by Rajendran [95, 96] is, instead, based on the Griffith criterion for the crack growth [97]. The damage increases (and the stress relaxes) when the strain energy release rate under mode I, or under modes II and III of an isolated penny shaped crack exceeds a critical value. A threshold micro-crack density is defined to induce the complete failure of the material (i.e. comminuted state), at which the element loses the capability of carrying tensile stress and its compression strength follows a Mohr-Coulomb law.

More recently Deshpande and Evans [98] extended the approach introduced by Ashby and Sammis [99] developing a 3D constitutive model for ceramic materials. From the analysis of the behaviour of a single isolated crack, it is demonstrated that the flaws grow along the direction of the maximum principal stress. From this consideration the possible crack configurations are divided in three regimes: first the absence of relative sliding of the flaw faces, then the frictional sliding and finally the loss of contact between the faces (i.e. crack opening). The damage induces a softening in the material, expressed as the increase of the strain energy density (in turn related to the mode I stress intensity factor at the tip of each crack).

*Anisotropic models*

Given the intrinsic anisotropic nature of the crack growth mechanisms in ceramic materials, various authors have developed continuum models that assume a non-uniform distribution of cracks and allow for the separate propagation of the damage in different directions.

The model presented by Denoual and Hild [100] evaluates the damage along three orthogonal directions (not necessarily the principal ones), thus generating an orthotropic evolution of the damage. The stress state around each crack is simplified in a Boolean function that represents the relaxed area that surrounds the crack. Complex crack patterns are

therefore modelled as overlapping relaxed areas in which the initiation of new cracks is prevented.

Espinosa [101], instead, developed a model that takes into account the damage propagation along an indefinite number of arbitrary directions (e.g. in [102] 13 separate directions are defined, but there is no theoretical limit to their number) to define an almost fully anisotropic damage propagation. The micro-crack growth along each direction depends on the average energy release rate for modes I, II, and III.

Finally, the model developed by Riou [103] introduces a truly anisotropic definition of the damage, by evaluating it along the three principal directions of the stress field at each time step. The damage is then rotated in the local coordinate system, thus allowing for the evaluation of the maximum damage direction. The model, however, does not provide a definition for the velocity of the crack propagation, which is therefore defined as an initial constant parameter.

As already stated, the introduction of anisotropic crack propagation comes at the price of additional computational cost and of a higher complexity of the model (both in terms of formulation and of extrapolation of the parameters). However, in the framework of linking the constitutive model to the physical properties of the material (both micro and macroscopic), the simulation of the anisotropic evolution of the damage is considered crucial.

Therefore, in Section 5 an approach is proposed that combines the simplicity of the JH2 formulation, physical considerations about the evolution of the crack (following the classic approach of Ashby [99]), and an anisotropic definition of the damage. The formulation of the anisotropic damage proposed, in particular, aims to minimise the error and the computational cost that such an approach usually implies.

### *2.3.3 Modelling discontinuities*

Both the methods for the generation of polycrystalline domains and the constitutive models presented in the previous sections can be complemented by the introduction of discontinuities within the solid, to explicitly simulate the cracks.

Several techniques have been developed to simulate the initiation and propagation of cracks in two- and three-dimensional domains. Among the most successful, the boundary elements method (BEM) has been extensively applied to three dimensional linear elastic fracture problems [104], including the propagation of inter-granular cracks within polycrystalline microstructures [105]. Other recent classes of methods include extended finite element methods (XFEM) [106, 107], and meshfree methods (discontinuous Galerkin [108], reproducing kernel particle method RKPM [109]), that have been extensively used to simulate fracture problems in disparate fields. These approaches, although providing extremely interesting results, are still fairly new and require further development to be established as real alternatives to the finite element method (FEM).

Finite element analysis (FEA) was first developed in 1943 by Courant, who obtained approximate solutions of vibration systems utilising the Ritz method of numerical analysis and minimization of variational calculus [110] Then, in 1956, Turner et al. published a work focusing on the "stiffness and deflection of complex structures" that established a broader definition of numerical analysis [111]. For those early years the numerical analyses were limited to a few expensive computers, mainly owned by defence, automotive, aeronautic, and nuclear industries. The 70's, with the development of more powerful computers and the simultaneous decrease of their cost, saw a boost in the development of FEA – thanks to the work of numerous researchers – soon becoming the most widely utilised numerical method to simulate the behaviour of complex structures. In the present day FEA is an extremely

powerful technique that is able to simulate the behaviour of complex structures with remarkable precision, and is utilised in a vast range of applications.

Within the classic finite elements method (FEM), the most diffuse approaches to deal with crack propagation are element erosion and element de-bonding methods.

The element erosion technique consists of the deletion of the element that fulfils a certain criterion (e.g. reaches a threshold value of stress). Clearly, the crude removal of the elements leads to a non-physical loss of mass in the model that results in a gap along the fracture surfaces and in the blunting of the crack tip. In the past few years several implementations of the element removal approach have been proposed to account for the correct energy dissipation, (e.g. nulling the stress in the "deleted" element, replacing the removed element with rigid masses, etc). However, as showed by Song et al. [112], the element erosion algorithms are extremely mesh sensitive, especially in dynamic fracture problems. Nevertheless, due to their simplicity, they are often incorporated into commercial software packages, and several researchers are still working to improve this technique. For example Pandolfi and Ortiz [113] have recently presented an "eigenerosion" approach for brittle fractures – derived from the eigenfracture approach developed by Smidth et al. [114] – that, contrary to many other element erosion approaches, converges to Griffith fracture in the limit of vanishingly small mesh sizes.

The element de-bonding approach, instead, correctly calculates the energy dissipation without the need of any adjustment, and predicts the crack speed with accuracy comparable to the XFEM approach [112]. Unless it is possible to determine the crack path a-priori (e.g. polycrystalline materials with weak grain boundaries, composite material with weak matrix-fibre interface), the de-bonding approach tends to inaccurately simulate the crack path as it is forced to follow the element boundaries. More accurate crack paths can be reproduced with finer meshes, thus increasing the computational cost of the analysis.

Nevertheless, given the a-priori knowledge of the possible crack paths in polycrystalline materials with weak grain boundaries, the de-bonding approaches have been used to simulate the propagation of inter-granular cracks within 2D [115-117] and 3D [118, 119] microstructures.

Several authors have presented different versions of cohesive entities, which can be classified under two main categories: *intrinsic* and *extrinsic*.

The intrinsic elements, which generally follow the formulation of Xu and Needleman [120, 121], are inserted a priori between the bulk elements, and their cohesive law is characterised by a finite initial stiffness, as the ones presented in Fig. 2.11. The presence of cohesive elements with a finite stiffness in a FE model, however, introduces an *artificial compliance* that alters the elastic behaviour of the intact material [108].

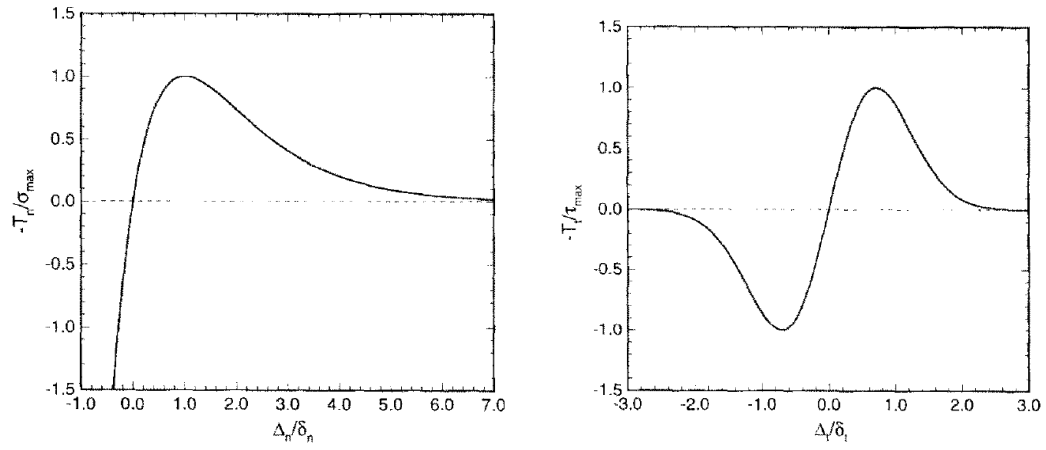



**Fig. 2.11:** Normal (left) and shear (right) tractions across the cohesive surface [120, 121]

To overtake this limitation several authors have introduced extrinsic cohesive elements, also known as *initially rigid elements*. Camacho and Ortiz [122] defined an adaptive method to insert cohesive elements in a 2D model only when a certain criterion is met in the bulk elements or the element edges are contiguous to a crack tip. The cohesive law describing these newly inserted elements is monotonically decreasing. This approach has, lately, been extended to 3D structures by Ortiz and Pandolfi [123].

For a more in-depth description of the computational methods for fracture in brittle materials the comprehensive review given by Rabczuk is suggested [124].

In the present work, since the modelled material (i.e. polycrystalline alumina) fails principally at the grain boundaries, it is possible to adopt the de-bonding technique to simulate the inter-granular crack propagation (Section 4.3.3, 4.4.1, and 4.4.2). Moreover the element erosion approach is used in Section 4.5 to model trans-granular cracks, reproducing qualitatively the trans-granular failure of a polycrystalline material. However the simulations presented highlight the limits of such a technique in providing quantitatively accurate results.

## 2.4 Conclusions

In this chapter, the definition, properties, and applications of ceramic materials are first illustrated in Section 2.1.

Then, the experimental characterisation techniques and numerical simulation methods, both at the microstructural scale and at the macro-scale, are presented, respectively in Sections 2.2 and 2.3.

In Section 2.2.1, experimental techniques to characterise the microstructural features of polycrystalline ceramics are described, focusing on the problems addressed in the work presented in this thesis: determination of the topology of polycrystalline microstructures, measurement of the single crystal elastic properties, and the mechanical testing of microscopic specimens with micro-cantilever beams.

In Section 2.2.2, an overview of macroscopic characterisation techniques at different strain rates is presented, with a more detailed description of the quasi-static and dynamic indentation tests, which have been used for the work presented in this thesis.

On the numerical side, particular attention has been paid to the techniques to generate models of polycrystalline microstructures (Section 2.3.1), as well as to the existing constitutive models for ceramic materials (Section 2.3.2).

Finally, Section 2.3.3 is dedicated to the possible methods for the modelling of discontinuities to simulate crack initiation and propagation both at micro- and macro-scale.

The review of the literature highlighted the limitations of the available methods for the generation of numerical models of polycrystalline microstructures, especially in the definition of concave domains, as well as in modelling discontinuities, such as inter- and trans-granular cracks. Also the simplistic hypotheses adopted by the macroscopic constitutive models for ceramic materials are presented. As a result, the aim and objectives proposed in the introductory chapter are justifiable.

The following chapters will present the results of the experimental and numerical work carried out at both the micro- and macro-scale.

Chapter 3 reports the results of the experimental tests performed. At the micro-scale, the stiffness and failure strength of polycrystalline alumina are measured with micro-cantilever beam tests. At the macro-scale, the comparison of dynamic and quasi-static indentation tests for different materials (i.e. alumina, zirconia, and alumina-zirconia composite) is presented.

Chapter 4 illustrates the development of an algorithm to generate statistically representative models of ceramic (polycrystalline) microstructures, and presents the results of simulations of elastic deformation and failure of alumina microstructures at different rates. The numerical results are validated against the quasi-static tests presented in Chapter 3, whilst a qualitative justification is provided for the dynamic tests.

Chapter 5, finally, describes the implementation of a novel macroscopic constitutive model for ceramic materials, developed as a progressive improvement of the state-of-the-art model (i.e. JH2) presented in Section 2.3.2.

# 3 EXPERIMENTS

This chapter presents the experimental work performed to explore the behaviour of ceramic materials, both at the micro- and macro-scales, thus providing motivations for the development of the numerical methodologies presented in the next chapter.

At the grain scale, the micro-mechanics of alumina is explored by measuring the deformation and failure of polycrystalline micro-cantilever beams. The test is described in Section 3.1.1, and the results are reported and discussed in Section 3.1.3.

At the macro-scale the work presented focuses on measuring the macroscopic elastic properties and on the design of a dynamic (impact) test comparable with a quasi-static indentation test, which allows for the exploration, as directly as possible, of the effect of the strain rate on the failure mechanisms of ceramic materials.

Both the elastic properties and the failure strength of alumina are measured by coupling uniaxial compression test with acoustic techniques, as presented in Section 3.2.

Finally, the dynamic indentation test is presented in Section 3.3, first describing the experimental setup (Section 3.3.1), then reporting and discussing the results of: preliminary calibration tests (Section 3.3.2), tests on alumina (Section 3.3.3) and silicon carbide (Section 3.3.4) targets.

## 3.1 Micro-cantilever beam tests

The tests presented in this section aim to measure directly the properties of the microstructural features of polycrystalline alumina by gradually deforming micro-cantilever beams until their complete failure.

The combination of in-situ measurements of the reacting force of the beam and of post-mortem analysis of the failure surfaces provides crucial pieces of information on the mechanical behaviour of both grains and grain boundaries.

### *3.1.1 Description of the test*

The experimental test consists of machining a cantilever beam with triangular cross section from the surface of alumina samples.

Three types of materials were tested: single crystal alumina, diffusion bonded sapphire (Fig. 3.2), and polycrystalline alumina (Fig. 3.3).

For the study of the mechanical strength of the single crystal, three types of single crystal alumina specimens were manufactured, with the cross section of the beam parallel to the *m*, *c*, and *a* plane of the crystal. Additionally a notch is made on the top surface of the beam to induce the failure and observe the differences in the propagation mechanisms on the three basal planes Fig. 3.1.

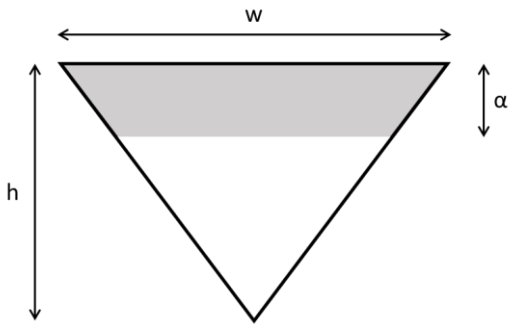



**Fig. 3.1:** Cross section of the notched beam

The bi-crystal beams were milled from the surface of diffusion-bonded sapphire, with the beam oriented parallel to the c-axis. The single boundary between the two crystals is perpendicular to the beam length and uniform across the whole cross section (Fig. 3.2).

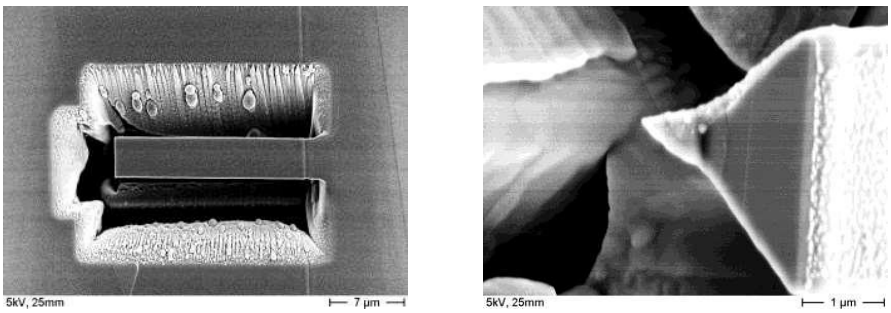



**Fig. 3.2:** Top view (left) and failure surface (right) of a bi-crystal micro-cantilever beam

The polycrystalline beams, instead, provide measures of deformation and failure of the overall material, thus providing precious elements for the validation of the numerical approach adopted.

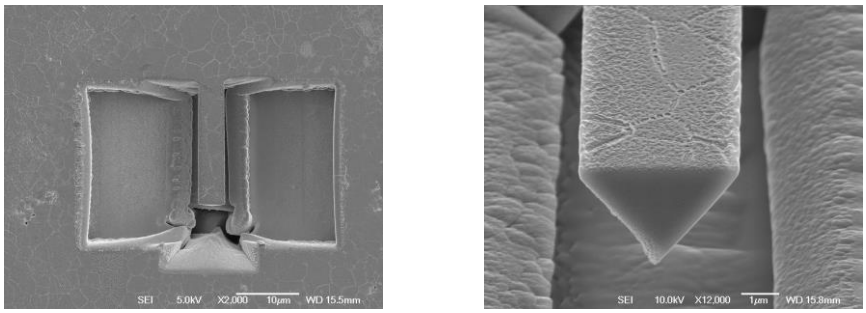
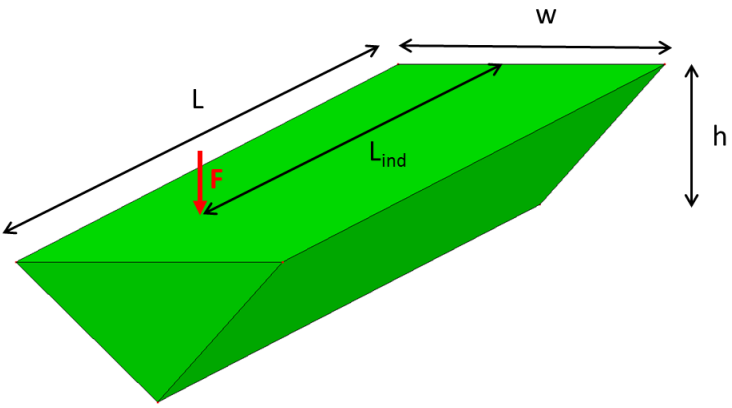


**Fig. 3.3:** Top and prospective view of a polycrystalline micro-cantilever beam [125]

The production of the alumina and the manufacturing of the beams was performed by Andrew Norton (Materials Department, University of Oxford) [126]. The material was produced using TM-DAR alumina powder (>99.99% purity, mean particle size $150\,nm$, Taimei Chemicals Co., Ltd, Tokyo, Japan). The discs obtained after uniaxial and isostatical cold pressing and vacuum sintering were flat bed ground and cut into smaller pieces. The faces were polished to a $1\,\mu m$ finishing and the micro-cantilever beams were milled using FIB (FEI FIB200, $30\,kV$). The choice of the triangular cross section is motivated by the simplicity of manufacturing in the presence of beam drift from specimen charging, which is almost inevitable in a non-conducting ceramic such as alumina. However, to minimise the extent of the drift a thin ($10\,nm$) layer of platinum was deposited on the surface prior to milling.

The beam dimensions were measured using SEM images, and the typical beam dimensions are reported in Fig. 3.6.




| | |
|---|---|
| $L\ [\mu m]$ | 20 |
| $w\ [\mu m]$ | 4.2 |
| $h\ [\mu m]$ | 2.47 |
| $L_{ind}\ [\mu m]$ | 17.23 |

**Fig. 3.4:** Typical dimensions of the micro-cantilever beam and position of the loading point

The testing method mimics what is described by Armstrong et al. [35]: the structure is loaded as indicated by the red arrow in Fig. 3.4 imposing a linearly increasing displacement with a Berkovich nano-indenter until the complete failure of the beam (Fig. 3.5).

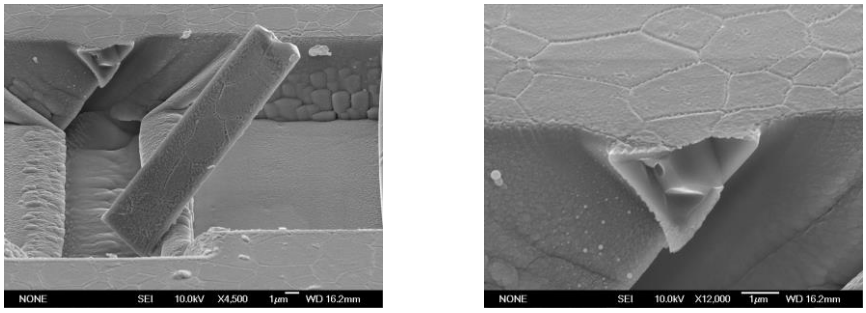



**Fig. 3.5:** Micro-cantilever beam after the failure [125]

A typical measurement of the nano-indenter is reported as the solid line in Fig. 3.6. The first segment of the graph represents the elastic deformation of the beam until the sudden initiation and propagation of the crack through the thickness of the specimen. After the failure of the beam the nano-indenter continues applying the displacement reading fictitious values of the load (i.e. second segment) and finally the vertical segment represents the end of the measurements.

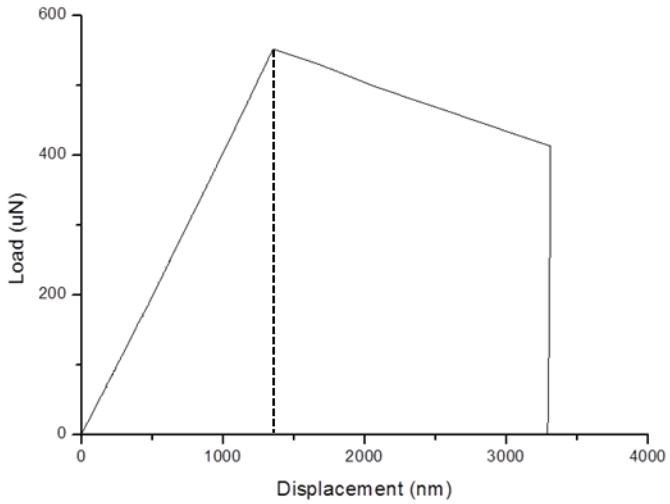



**Fig. 3.6:** Load-displacement curve measured by the nano-indenter

The real behaviour of the beam, instead, consists of a linear elastic deformation, followed by a sudden brittle fracture, as represented by the dashed line in Fig. 3.6. A more detailed description can be found in the work by Norton [126].

In the next sections the stiffness and the strength of the material are evaluated in terms of Young's modulus ($E$) and failure strength ($\sigma_f$), from the results of the micro-cantilever tests performed by Noor A. Yahya and Andrew Norton (Materials Department, University of Oxford) [126]. The tests are all consistent in terms of geometrical shapes, but they exhibit some differences both in the dimension of the beams and in the average grain size. Whilst the effect of the beam dimensions is taken into account in the definition of $E$ and $\sigma_f$, the influence of the grain size (for polycrystalline beams) appears in the results. Specifically, the beams tested by N.A. Yahya have an average grain size of $\sim 1\mu m$, whilst the ones tested by A. Norton have $\overline{d_{gr}} \cong 2.5\mu m$.

### *3.1.2 Calculation of deformation and failure properties*

From the measures of the displacement of the indenter tip and the force applied to the beam the Young's modulus ($E$), failure strength ($\sigma_f$), and the critical stress intensity factor at the notch tip ($K_{Ic}$) of the material can be calculated. These parameters provide information on

the elastic deformation and the failure of the material independently from the geometry of the specimens, hence allowing for the direct comparison of the experimental results despite the slight differences in the size of the specimens due to the limitations in manufacturing precision.

*Calculation of the Young's modulus*

The calculation of the elastic behaviour of the entire beam is performed using the Euler-Bernoulli theory (also known as classical beam theory) for the deflection of thin beams [127], which expresses the Young's modulus as:

$$E = \frac{F}{\delta}\frac{L_{ind}^3}{3I} \tag{18}$$

$F$ is the load applied, $\delta$ is the displacement of the loading point, $L_{ind}$ is the distance of the loading point from the fixed end of the beam, and $I$ the moment of inertia of the cross section. For a triangular shape of height $h$ and width $w$, the moment of inertia is defined as:

$$I = \frac{wh^3}{36} \tag{19}$$

This simplistic expression of the elastic behaviour of the beam defines a "global" elastic modulus of the whole specimen that allows the comparison of experiments and numerical simulations of beams with different topologies.

The Euler-Bernoulli theory, however, applies correctly only for long thin beams, with aspect ratio ($AR$) – defined as the ratio of the length with the width of the beam – of the order of 20 or more. For beams with lower aspect ratio, other mechanisms have to be taken into account. The work by Armstrong et al. [35] suggests that for beam with $AR < 20$ the parameter that mainly affects Eq. (18) is the deformation of the fixed end, that can be expressed in terms of slope at the fixed end due to unit bending moment ($\vartheta_{m0}$). Moreover the effect of the shear deformation in short beams can be taken into account using Timoshenko beam theory [128].

Adding the terms accounting for the effect of the inclination of the supported end and the shear deformation – respectively second and third in Eq. (20) – to the Euler-Bernoulli formulation, the Young's modulus can be expressed as:

$$E = \frac{F}{\delta}\frac{L_{ind}^3}{3I} + \vartheta_{m0}L_{ind}^2 + \frac{2(1+\nu)F}{\kappa^2\delta A}L_{ind} \tag{20}$$

The effect of the shear (i.e. third term) over the prediction of the Young's modulus is proven to be negligible ($\approx 1\%$). See Appendix A for the detailed calculation.

The effect of the bending of the support, instead, is not negligible, and the magnitude of the correction of the Young's modulus is explored numerically. Firstly several FE models that include part of the bulk material behind the beam have been generated to explore the effect of both the size of the cross section and the depth of the support over the predicted deflection of the beam. Then the most effective geometry is chosen to explore the changing of Young's modulus with the aspect ratio.



**Fig. 3.7:** Beams with small, medium, and large support cross section

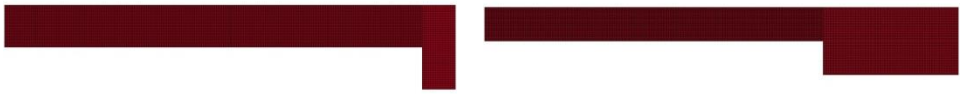


**Fig. 3.8:** Beams with support depths of $\mathbf{0.1 \cdot} \boldsymbol{L_{ind}}$ (left) and $\mathbf{0.5 \cdot} \boldsymbol{L_{ind}}$(right)

To define the optimum support size, three different cross sections (Fig. 3.7): small ($6.2x3.5\ \mu m$), medium ($8.4x4.9\ \mu m$), and large ($14.2x7.4\ \mu m$) have been combined with five depths: 0.1, 0.2, 0.3, 0.4, and 0.5 times $L_{ind}$ (Fig. 3.8), for a total of 15 FE models.

All but the top face of the support are fully constrained, therefore assuming the effect of the not-included part of the support as a perfect encastre.

The effect of the cross section size and depth of the support on the deflection of the beam is summarised in Fig. 3.9. In the graph the percentage error between the compliance of the beam without and with support is plotted against the depth of the support. The convergence of the results ensures that the bigger models fully capture the effect of the backing support on the compliance.

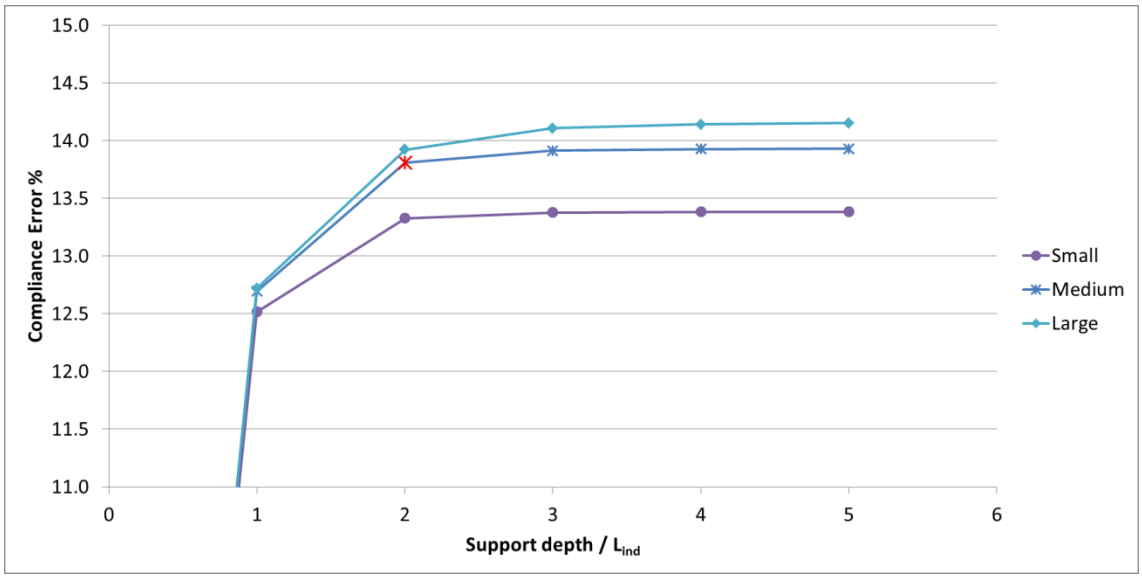



**Fig. 3.9:** Effect of the cross section size and the depth on the deformation of the beam

The combination of medium cross section with a depth of $0.2 \cdot L_{ind}$ (red asterisk in Fig. 3.9) has been considered to provide an adequate prediction of the behaviour of the beam, since any further increase of the dimensions of the support does not provide an advantage that justifies the additional computational cost required.

Once the optimal geometry for the model has been selected, the effect of the aspect ratio ($AR = L_{ind}/w$) is explored, moving the loading point along the length of the beam, for a range of $AR = [2 - 7]$. The results are illustrated in Fig. 3.10:

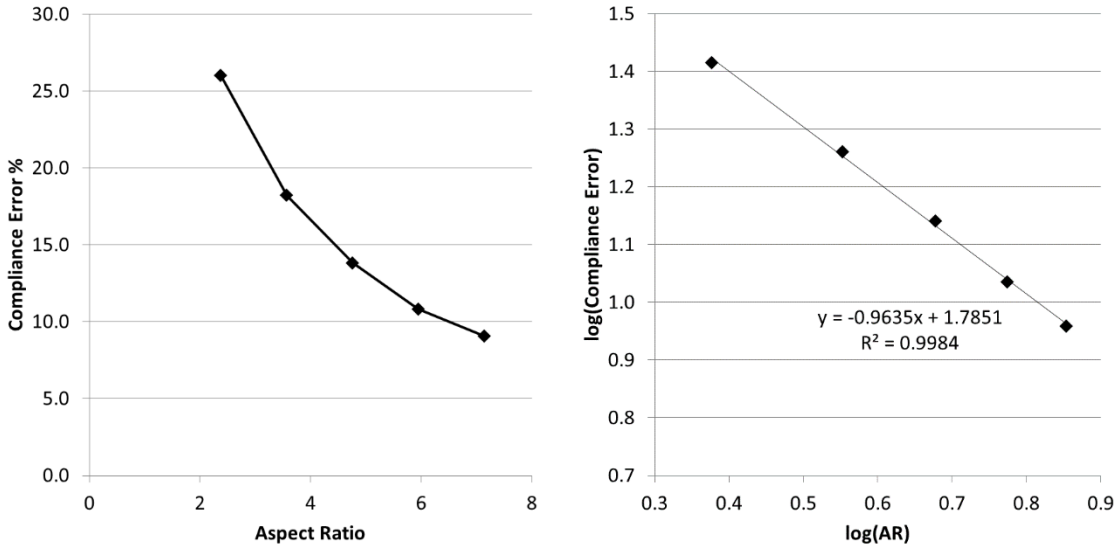



**Fig. 3.10:** Variation of the compliance error with the aspect ratio in linear and logarithmic scales

For short beams the effect of the support is noticeable. In particular Eq. (18) underestimates the compliance of the beam of about 10% for the cantilever beams considered in this work. The linearity of the logarithmic values confirms that the results of the simulations are described by the first two terms of Eq. (20), because the ratio between the first and the second term is proportional to $L_{ind}$.

*Calculation of the failure strength*

The failure strength ($\sigma_f$) is defined to directly compare the inelastic behaviour of the different – numerical and experimental – micro-cantilever-beams [129]. For triangular cross-sectional beams, the relation to evaluate $\sigma_f$ for a generic straight beam is:

$$\sigma_f = \frac{12F_f L_f}{wh^2} \tag{21}$$

The strength corrects the failure load ($F_f$) with respect to the distance between the indenter tip and the broken point ($L_f$), and the dimensions of the cross section, hence it is not affected by the geometry of the beam and the position of the failure surface.

*Calculation of the stress intensity factor*

The critical stress intensity factor ($K_{Ic}$) at the notch tip defines the condition for the crack to propagate within the material, and the determination of this value along different planes (i.e. *m*-, *c*-, and *a-planes*) provides crucial insights on the crack propagation mechanisms within the single crystals of alumina.

The reproduction of "classical" stress concentration at the notch tip due to mode I opening of the crack (which have an analytical description, as reported in Section 4.3.2) at microscopic scale present relevant difficulties related to the imposition of the displacement (e.g. gripping). For this reason calculation of $K_{Ic}$ presented in this work is performed on notched micro-cantilever beams.

A notch is made on the top surface of the beam, perpendicularly to the length direction, and then a linearly increasing displacement is applied to the free end of the specimen until its complete failure. To derive the correlation of $K_{Ic}$ with the failure load ($L_f$) and the notch depth ($\alpha$), a FEA compliance study was performed, providing the following semi-empirical relationship:

$$K_{Ic} = \frac{12F_f L_f}{wh^2} 1.12\sqrt{\pi\alpha}\left[1 + 0.123\frac{\alpha}{h} + 5.456\left(\frac{\alpha}{h}\right)^2 + 0.073\left(\frac{\alpha}{h}\right)^3 - 0.023\left(\frac{\alpha}{h}\right)^4\right] \qquad (22)$$

The detailed derivation of Eq. (22) is reported in Appendix B.

### *3.1.3 Results and discussion*

The methodology presented in the previous section is used to calculate the elastic modulus and the failure strength of single crystal (along three different planes), bi-crystal and polycrystalline specimens.

*Single crystal*

Examples of the failure of the single crystal of alumina along *m*-, *c*-, and *a-planes* can be observed in Fig. 3.11. The fracture surfaces along the *m*- and *a-planes* are smooth, in

contrast with the one along the *c-plane*, which is heavily faceted. In particular the orientation of the facets suggests that they might be on the *r-plane*, which is consistent with microscopic studies showing that the toughness of the *c-plane* is extremely higher than the one of the *r-plane* [16].

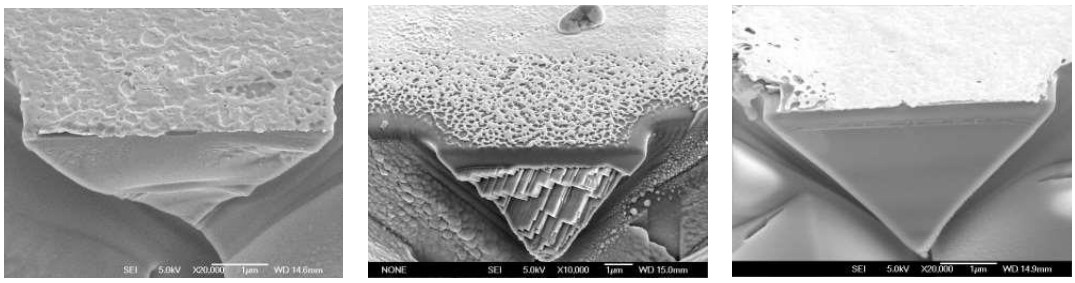


**Fig. 3.11:** Failure surfaces along the *m-plane* (left), *c-plane* (middle), and *a-plane* (right) [38]

Table 3.1 reports the evaluation of $K_{Ic}$ along the three basal planes analysed and the values measured for inter-granular cracks, both for single grain boundaries (i.e. bi-crystal) and polycrystalline structures.

| **Fracture location** | **Specimen** | $\boldsymbol{K_{Ic}}$ $[\boldsymbol{MPa\sqrt{m}}]$ |
|---|---|---|
| m-plane | Single crystal | 1.5 |
| c-plane | Single crystal | 1.6 |
| a-plane | Single crystal | 1.4 |
| Grain boundary | Bi-crystal | 0.7 |
| Grain boundary | Poly-crystal | 0.7 |

**Table 3.1:** Stress intensity factor relative to the crack propagation along different basal planes

The value reported for the *c-plane* is lower than the actual strength along the specific basal plane because of the evolution of the crack on the, notoriously weaker, *r-plane*.

These measure, besides providing an indication on the dependence of the preferred directions for the propagation of trans-granular cracks, also provide additional confirmation of the tendency of alumina to fail along the grain boundaries.

*Single grain boundary*

Three bi-crystal micro-cantilever beams produced on the surface of diffusion bonded sapphire were tested. The mechanical properties measured from the tests are reported in

| **Test** | $\boldsymbol{E}$ $[\boldsymbol{GPa}]$ | $\boldsymbol{\sigma_f}$ $[\boldsymbol{GPa}]$ |
|---|---|---|
| Beam 1 | 433 | 5.4 |
| Beam 2 | 457 | 5.0 |
| Beam 3 | 493 | 5.0 |

**Table 3.2:** Young's modulus and failure strength of bi-crystal cantilever beams

The Young's modulus ($E$) and the failure strength ($\sigma_f$) are evaluated respectively with using Eq. (20) and Eq. (21). The measured values are quite consistent, with $E$ equal to $(465 \pm 25)\ GPa$ and the $\sigma_f$ equal to $5.2 \pm 0.2\ GPa$.

The fracture surfaces were smooth, indicating that the crack initiated at the thermal groove and propagated along the grain boundary.

The strength of the single grain boundary measured with the tests is used as input of the FE models of polycrystalline domains presented in this work, thus providing experimentally based values for the numerical simulations performed.

*Polycrystalline beams*

For the polycrystalline beams, 5 sets of tests have been performed. The first four by Noor A. Yahya and the last one by Andrew Norton (Materials Department, University of Oxford) [126].

The graph in Fig. 3.12 reports the values of the Young's moduli for the 5 sets of micro-cantilever beams, evaluated both with the classic beam theory Eq. (18) (striped bars) and considering the bending of the support (solid bars).

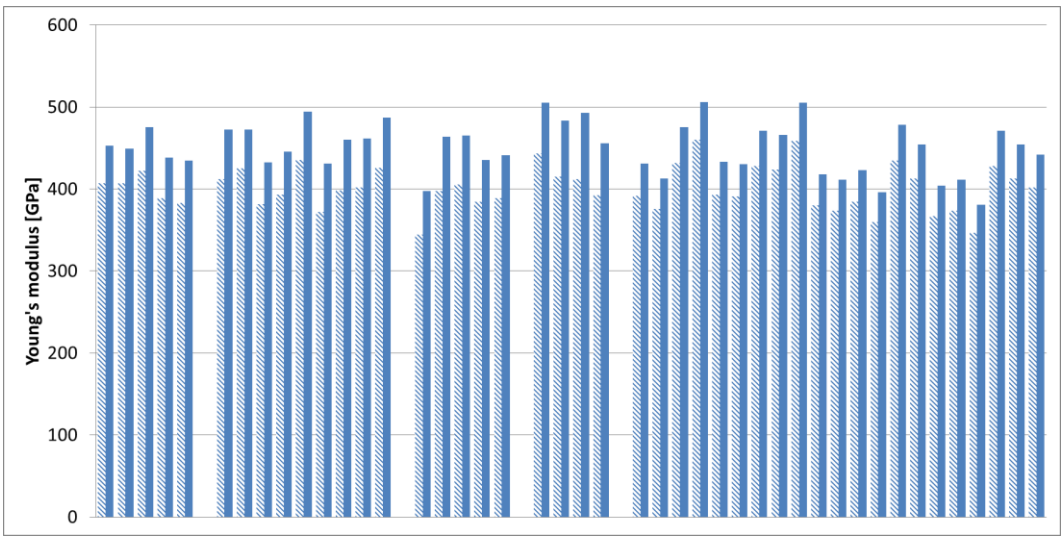



**Fig. 3.12:** Young's modulus with (solid) and without (dashed) the correction suggested in Eq. **(20)**

In particular from the experiments performed by N.Y. Yahya the Young's modulus measured was $459 \pm 48\ GPa$, whilst the one measured by A. Norton was $442 \pm 51\ GPa$. These values are used in Section 4.3.3, to validate the results of the numerical simulations performed.

Fig. 3.13, instead, reports the values of the strength measured for the five sets of micro-cantilever beams analysed.

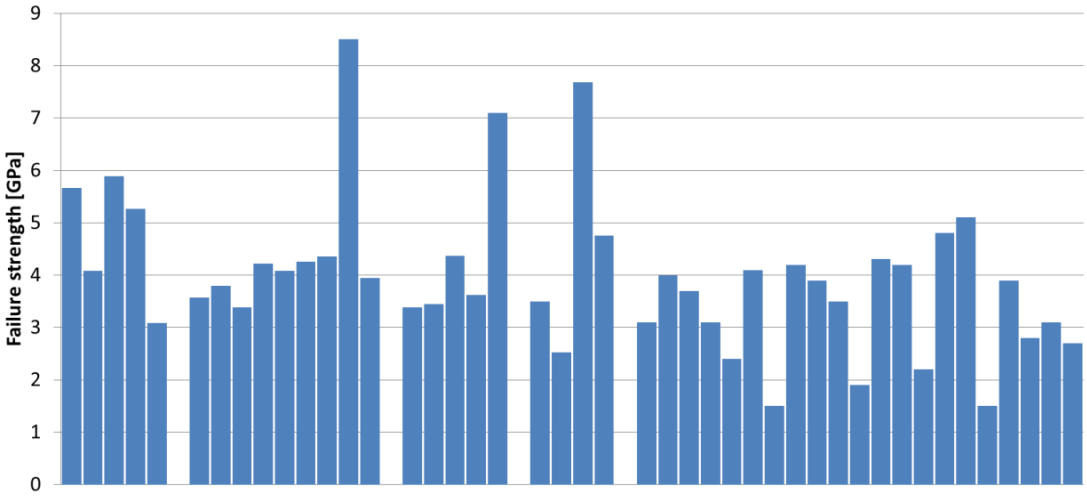



**Fig. 3.13:** Strength of the micro-cantilever beams

Whilst most of the beams exhibit values of the strength in the range $3 - 5\ GPa$, there are some outlying values that can suggest the presence of different failure mechanisms, other

than the expected inter-granular propagation of cracks starting at the grain boundaries. For example excessively large values of the strength can be related to the presence of large grains at the root of the beam failing trans-granularly, whilst the particularly low values can be related to the presence of flaws in the beam inducing the initiation of the crack at lower stresses.

The possible types of failure can be divided in four categories, given by the combination of the two possible initiation features (i.e. flaw or grain boundary) and the two possible propagation mechanisms (i.e. inter- or trans-granular).

To verify the initiation and propagation mechanisms of the cracks, post-mortem analysis have been performed on the last set of specimens, revealing that the vast majority (more than 70%) of the failures started from a grain boundary and propagated inter-granularly, as reported in Fig. 3.14.

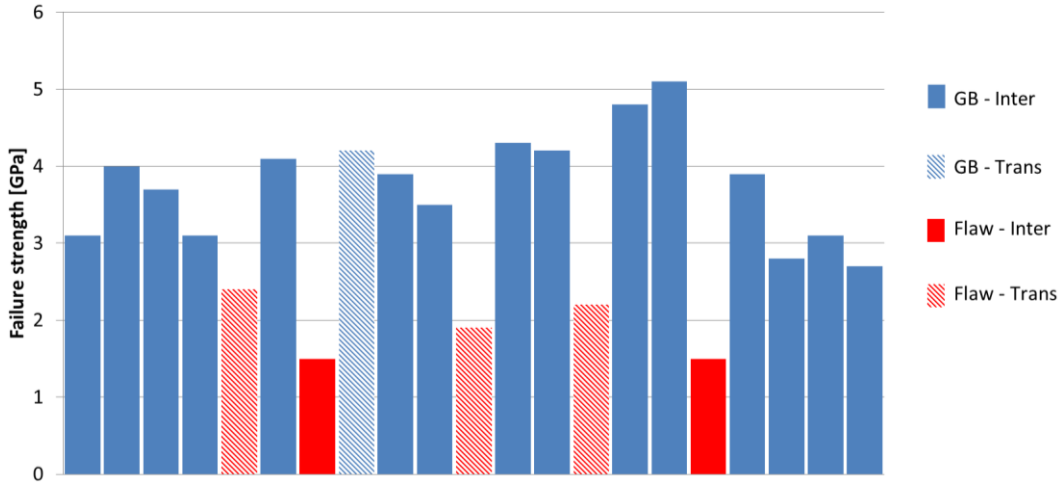



**Fig. 3.14:** Failure modes of the last set of micro-cantilever beams

*Uncertainty in the measures*

The calculations of both the Young's modulus and the failure strength are affected by the uncertainty in the measurement of the dimensions of the beam. Several causes can be identified, the most influent of which are suspected to be the not perfect straightness of the beam and the presence of re-deposited material on the surface of the beam.

The straightness of the beam is affected by the beam drift, which is almost inevitable in a non-conductive material such as alumina. To minimise the extent of the drift a thin layer (10 $nm$) of platinum was deposited on the surface before milling.

The re-deposited layer of milled material on the beam during the machining process, instead, increases the apparent dimension of the beam without adding a significant mechanical effect. Precautions have been adopted to minimise such phenomena (i.e. milling thin layers of material each time) in order to have more control over the final dimension of the beam and to reduce the amount of powder that can deposit on the structure.

In Section 4.3.3 the numerical models generated to simulate the micro-cantilever beam tests are described and the predictions of the Young's modulus and of the strength are compared against the experimental measurements presented.

## 3.2 Macroscopic characterisation

At the macroscopic scale, measurements of the density and the speed of sound of the material were performed, respectively with Archimedes' method and acoustic technique, used for a non-mechanical estimation of the elastic modulus of the material, thus avoiding any possible damage to the material. Samples with three different values of grain size (i.e. 1.7 $\mu m$, 3.2 $\mu m$, and 5.6 $\mu m$) were analysed. The measured Young's were respectively equal to $414 \pm 9\ GPa$, $413 \pm 8\ GPa$, and $392 \pm 10\ GPa$. The uniaxial pressure applied to alumina powder during the sintering process is suspected to have induced a texture alignment in the samples with a small grain size, thus increasing the apparent value of the Young's modulus.

Additionally, the failure strength of alumina was measured with uniaxial compressive test coupled with acoustic emission recorder to identify the failure of the specimen. The results of the tests on 12 samples are reported in Table 3.3.

| Sample | $\sigma_f$ [$GPa$] | Sample | $\sigma_f$ [$GPa$] | Sample | $\sigma_f$ [$GPa$] |
|---|---|---|---|---|---|
| 1 | 3.88 | 5 | 2.68 | 9 | 1.41 |
| 2 | 5.14 | 6 | 3.17 | 10 | 2.98 |
| 3 | 3.71 | 7 | 2.90 | 11 | 2.80 |
| 4 | 3.88 | 8 | 2.97 | 12 | 3.06 |

**Table 3.3:** Failure strength measure with uniaxial compression test

Even excluding sample 9 – which is suspected to have exhibited such a low value of failure strength because of the presence of pre-existing defect in the specimen – the results show a considerable spread, further motivating the necessity of exploring the micro-mechanic of the failure, to increase the understanding on the fundamental mechanisms contributing to the inelastic behaviour of ceramic material.

## 3.3 Dynamic indentation test

Finally a methodology to explore the influence of the strain-rate on the behaviour of the material is presented. It consists of performing indentation tests at different rates in the attempt of isolating the dynamic effects.

One of the main issues in comparing dynamic and quasi-static indentations is the variation of the behaviour of the indenter with the strain-rate. In particular, the classic quasi-static indentation techniques are based on the absence of permanent deformations of the indenter that is considered elastic, or even rigid. Unfortunately, the combination of high hardness of the target ceramics and dynamic effects makes this hypothesis not valid at high strain-rates. Hence a series of preliminary tests have been performed to explore the behaviour of projectiles of various shape and size, to determine the indenter that best responds to the test requirements (Section 3.3.2).

Having assessed the behaviour of different projectiles, two groups of tests have been performed. First the comparison of the deformation generated by quasi-static and dynamic indentations is performed to identify the effect of the high-rate loading conditions on the

damage evolution of three different ceramic materials (Section 3.3.3). Then the response of different grades of the same material (i.e. silicon carbide) under impact is analysed, in the attempt of correlating the macroscopic damage mechanisms with the microstructural properties (Section 3.3.4).

### *3.3.1 Experimental setup*

The dynamic indentation tests are conducted firing the indenter perpendicularly to the ceramic target at controlled velocities. To perform the tests presented in this chapter, a single stage gas gun has been designed and manufactured. The assembled model of the gun realised with the computer-aided-design (CAD) software SolidWorks, and the final realisation are reported in Fig. 3.15:

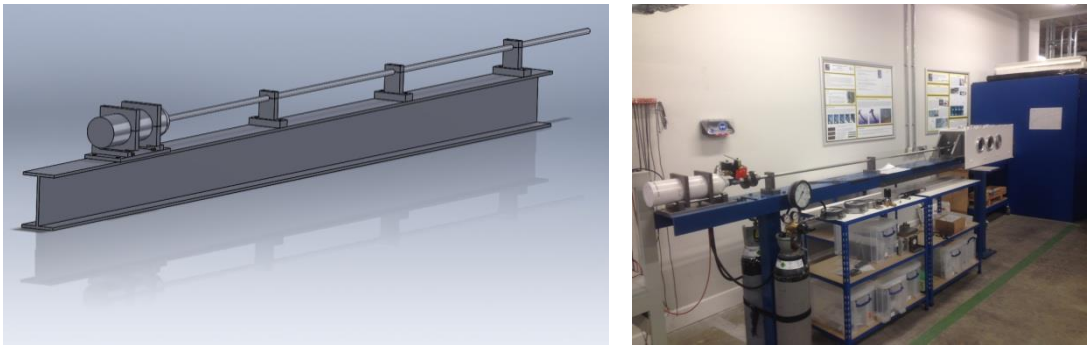


**Fig. 3.15:** CAD design (left) and final realisation (right) of the gas gun

The gas gun accelerates the projectile, mounted on a sabot, through the barrel using the thrust provided by high pressure gas contained in the vessel, as schematically sketched in Fig. 3.16.

More detailed description of the design and the operation of the single stage gas gun are given in Section 2.2.2.

The behaviour of target and indenter are investigated with both live measurements and post-mortem analyses.

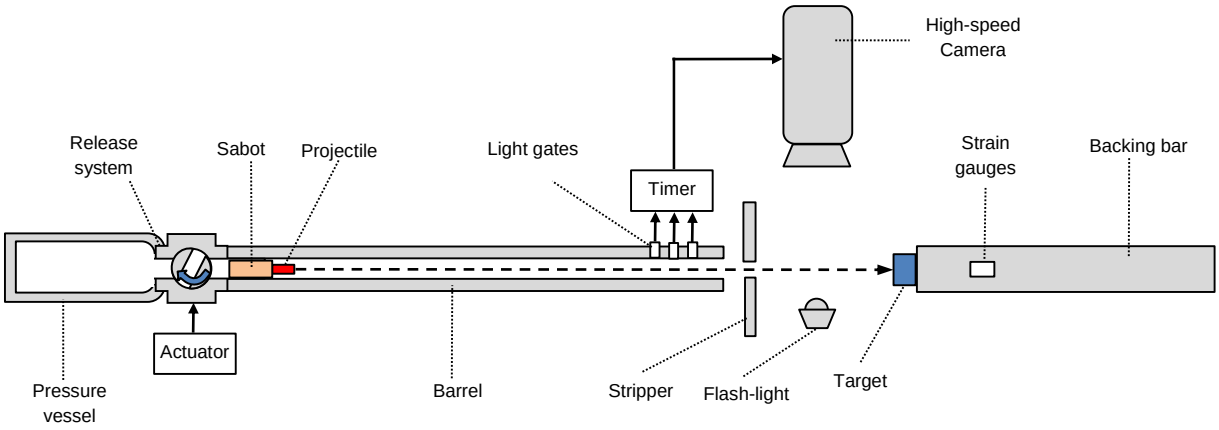



**Fig. 3.16:** Schematic diagram of the gas gun (not to scale)

The in situ measurements consist of both observing the impact with the use of high-speed cameras, and measuring the profile of the force that the target transmits to the backing support (both devices are reported in Fig. 3.16).

The "post-mortem" analyses, instead, are defined as the ensemble of all the measurements performed on the target after the test. The list of possible characterizations include: optical microscopy and profilometry, scanning-electron microscopy (SEM) fractography, and $Cr^{3+}$ fluorescence spectroscopy.

The design of the single stage gas gun, as well as the functioning and the performance of the high-speed cameras and of the gauged support are described in this section.

*Design of the single stage gas gun*

A generic gas gun consists of a pressure vessel connected to a barrel with a gas-release system. When the high pressure gas is released from the vessel, the pressure differential accelerates the projectile down the barrel.

The possible gas-release systems generally used in similar devices and their advantages and weaknesses are discussed in Section 2.2.2. In particular, the gas gun designed for the set of tests presented in this section is equipped with a spherical valve to connect the pressure vessel and the barrel.

The pressure vessel is a steel bottle with a capacity of 3 litres (i.e. $3 \cdot 10^6\ mm^3$), and a maximum bearable pressure of $8\ MPa$, whilst the barrel is a steel tube, which dimensions are designed to best suit the desired experimental conditions.

The inner diameter of the barrel is defined by the maximum possible dimension of the projectiles ($12mm$), whilst the length ($2400mm$) is imposed to keep the ratio between the inner volume of the barrel and the capacity of the vessel negligible (i.e. less than 10%), so that the acceleration of the projectile can be considered at constant pressure.

The external radius of the barrel ($r_e$), instead, is equal to $10mm$. Such value guarantees a safety factor ($\Omega$) – defined as the ratio between the maximum hoop stress ($\sigma_{\theta\theta}$) for the most severe operating conditions (i.e. $P = 8MPa$) and the yield stress of the material ($\sigma_Y \cong 240\ MPa$) – of about 14, as reported in Eq. (23):

$$\Omega = \frac{\sigma_Y}{\sigma_{\theta\theta}} = \frac{\sigma_Y}{P}\frac{r_e^2 - r_i^2}{r_e^2 + r_i^2} \cong 14.1 \tag{23}$$

The last step in the design of the gas gun is to verify if a device with such dimensions is able to provide the range of velocities desired with the prescribed projectiles. The evaluation of the velocity of the projectile is performed using the expressions introduced in Section 2.2.2:

$$v_{ex} = \frac{2c_0\sqrt{\tilde{a}_0}}{\gamma - 1}\sqrt{1 - \left(1 + \frac{\gamma P_V A_b l_b}{c_0^2 G_V}\right)^{(1-\gamma)}} \tag{24}$$

$$\frac{G_V}{m} = \frac{2\gamma}{\gamma - 1}\tilde{a}_0(1 - \tilde{a}_0)^{-\frac{\gamma}{\gamma-1}}\int_0^1 (1 - \tilde{a}_0\mu^2)^{\frac{1}{\gamma-1}}d\mu \tag{25}$$

The parameter $\tilde{a}_0$ is calculated by solving numerically Eq. (25) for $G_V/m$ equivalent to the range of pressure from 0 to $1\ MPa$, for the average projectile mass (i.e. $\sim 4.1g$) – and then substituted in Eq. (24).

The resultant theoretical curves for nitrogen and helium are plotted in Fig. 3.17, together with the simplistic expression of the exit velocity based on energy considerations (also introduced in Section 2.2.2):

$$v_{ex} = \sqrt{\frac{2P_V A_b l_b}{m_p}} \tag{26}$$

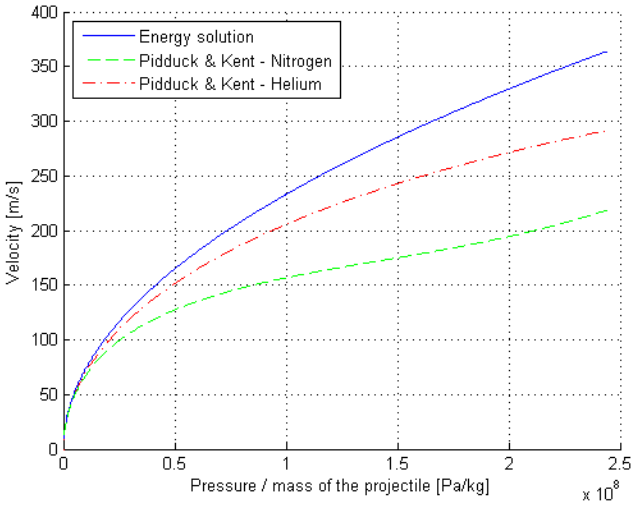



**Fig. 3.17:** Prediction of the exit velocity with the energy based Eq. **(26)** and Pidduck & Kent Eq. **(24)** relations

The adoption of the correction for the nature of the gas reduces noticeably the predicted velocity with respect to the "energy-based" solution and is able to capture the extra velocity provided by the use of a lighter gas to accelerate the projectile.

To allow for efficient and controllable transfer of energy from the pressure differential to the kinetic energy of the projectile, a nylon cylinder (called sabot) is utilised to hold the indenter, as shown in Fig. 3.18.



**Fig. 3.18:** Cylindrical projectile mounted on the sabot

The sabot – that has a diameter of $11.3\,mm$ – comfortably fits into the barrel to maximise the efficiency of the high-pressure gas, minimising the gas leak around the projectile. In addition, the adoption of this device allows for the use of indenters of multiple shapes and dimensions with the same gun design (i.e. with the same barrel).

The barrel is also equipped, at its exit end, with three light gages to measure the projectile speed, as the ratio between the (fixed) distance between the gates and the time the projectile spends to travel from one gage to the consecutive (measured with a high precision timer).

Finally, a stripper is positioned between the exit of the barrel and the target, to separate the sabot from the indenter before the impact. It consists of a hollow cylinder which internal diameter dimension is devised such as the indenter goes through undisturbed, whilst the sabot is stopped from reaching the target. Two strippers for projectiles of different sizes are shown in Fig. 3.19.



**Fig. 3.19:** Strippers with different internal diameters

*High speed image recording*

The last instants of the free fly of the indenter and its impact with the target were recorded with a "Phantom 7.1 High Speed Video Camera" (Vision Research, USA). The frame rate was pushed to the best performance achievable by the device, capturing 66,667 frames-per-second, with $2\,\mu s$ exposure time and $13\,\mu s$ inter-frame time gap. The spatial resolution varies within the tests according with the desired phenomena to observe, remaining of the order of 5000 pixels.

Natural sunlight or the usual artificial internal illumination does not provide enough illumination for the camera to capture any visible image in such a short exposure time, therefore an external source of light is required. The additional illumination of the test is provided by a Cordin light (Cordin, USA).

*Data acquisition system*

Given the inability of performing any direct measurement by placing any sensors directly on the target during the test, the information on the response of the material is gathered indirectly from the deformation of the backing bar that supports the target. The load cell consists of a strain gauged bar – on low friction supports – designed to measure the force that the target applies to the bar. The evolution of this force can then be linked to the deformation and the propagation of the damage within the target.

The target is positioned on the base of the bar, facing the end of the barrel perpendicularly to the direction of fire. This configuration allows considering the stress (and strain) propagation in the bar generated from the impact of the projectile unidirectional (i.e. the bar does not undergo any bending deformation).

The design of the backing bar is based on a numerical parametrical study, considering that the diameter of the bar is constrained to the size of the target, and is therefore imposed to be equal to $25.4\,mm$ to fully support the biggest specimen to test (i.e. alumina disc with a diameter of $25\,mm$) avoiding any possible bending of the non-backed parts.

The ideal behaviour of the load cell consists of a purely elastic deformation with relatively high strains for all the loading conditions (i.e. impact velocities). The only constraint on the length of the bar, instead, is that the reflection of the stress wave generated by the impact with the projectile does not interfere with the measurements of the stress wave itself.

An example of the FE models of the impact test, consisting of the projectile (red) hitting a disc target (blue) backed by a long cylindrical bar (green), is presented in Fig. 3.20.

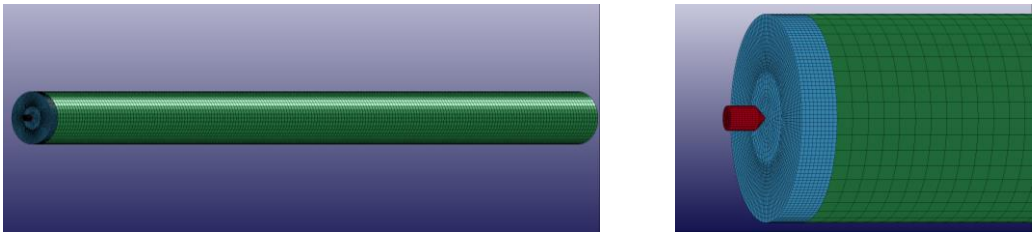


**Fig. 3.20:** FE model of the impact test

The material and the dimensions of the projectile are chosen as the ones imposing the most severe loading conditions the system would undergo (within the set of planned tests). A purely elastic constitutive model is adopted, therefore adding an extra strength to the projectile for not accounting for its possible permanent deformation and/or failure.

The target, instead, is modelled with the JH2 material model (introduced in Section 2.3.2), using the properties of pure alumina – the weakest material to be tested.

Finally, the bar is modelled with a purely elastic material model using the properties of aluminium 6061.

Due to design constraints the minimum length of the bar is $400mm$, that has been demonstrated to be sufficient to fulfil the "non-overlapping" of the incident and the reflected waves for aluminium 6061, as illustrated in Fig. 3.21 and Fig. 3.22.

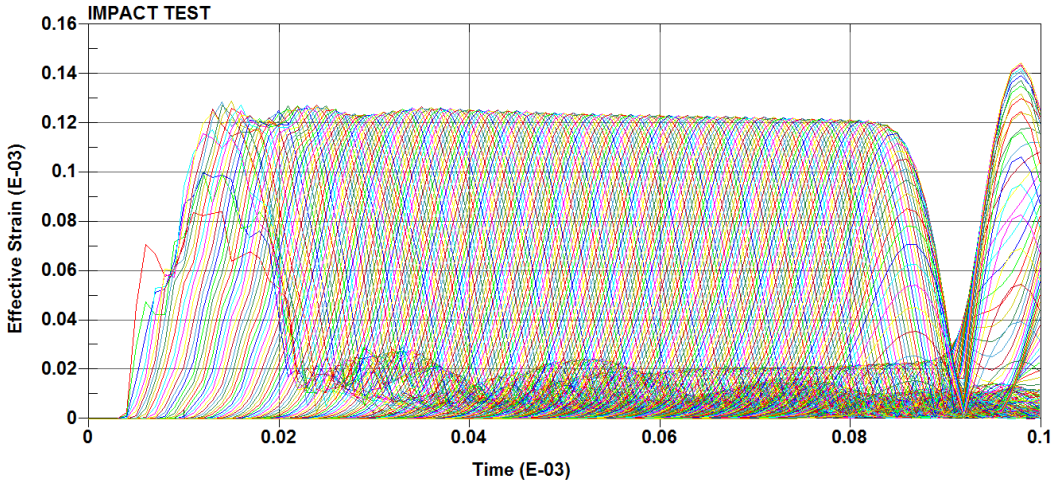



**Fig. 3.21:** Strain history in the cross sections of backing bar

The graph presented in Fig. 3.21 reports the history of the effective strain in 200 cross sections, equally spaced along the backing bar for the most severe testing conditions (i.e. maximum impact velocity of the longest and heaviest of the projectiles). The interpolation of the maximum values at each time instant (Fig. 3.22) presents three regimes.

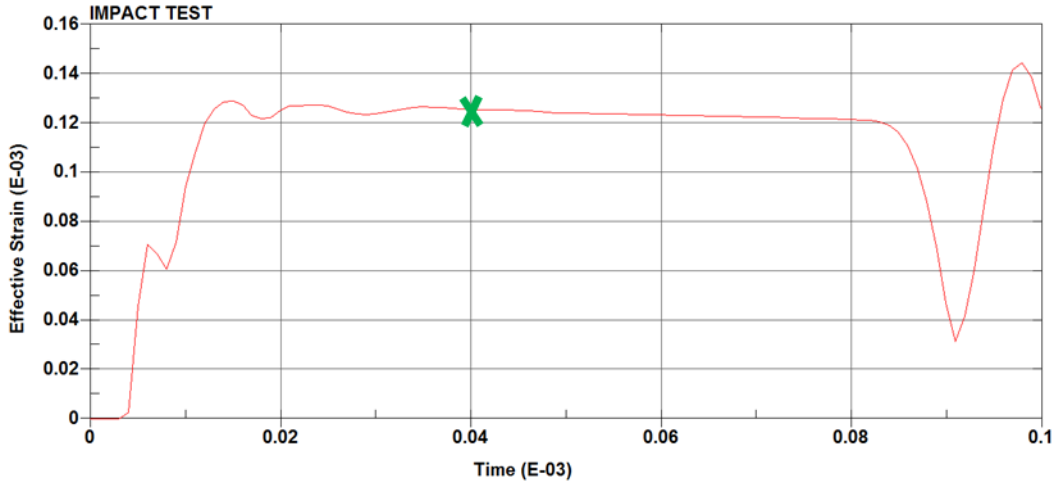



**Fig. 3.22:** Envelope of the maximum values of the strain for all the cross sections

First the curve shows an oscillatory behaviour, to then stabilise until the drop due to the reflection of the stress wave at the end of the bar. To avoid the oscillations in the strain measurement observed in the numerical simulation in the cross sections at the front of the bar, the strain gauges are positioned at 138 $mm$ from the front of the bar.

Finally, the predicted stress in the bar is always lower than the yield stress of aluminium 6061, thus fulfilling the hypothesis of perfectly elastic behaviour of the unit cell.

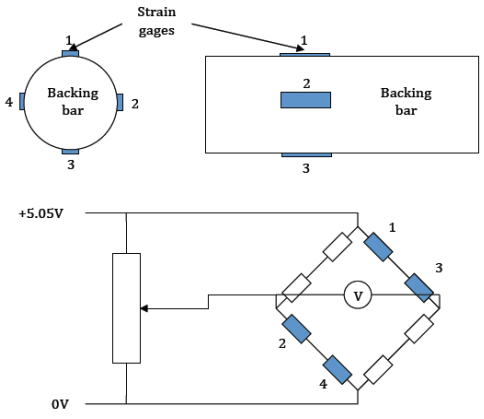



**Fig. 3.23:** Positioning and connections of the strain gauges on the backing bar

A set of four *fla-2-23 gages* (2mm long, 2.16 gauge constant, 120Ω) are spaced of 90° on the same cross section, and mounted on a half bridge circuit, as described in Fig. 3.23.

The position of the gauges is such that any contribution of the possible bending of the bar is erased, averaging the measurements of the opposite gauges that are positioned in series.

The typical signal recorded by the backing bar during an impact test is reported in the voltage-VS-time graph in Fig. 3.24.

The first compressive (i.e. negative) peak corresponds to the impact, whilst the rest of the peaks are measures of the stress wave travelling back and forth in the beam after the first reflection. It is worth to notice that the sign of the peak changes after each reflection because both the ends of the bar are free boundaries.

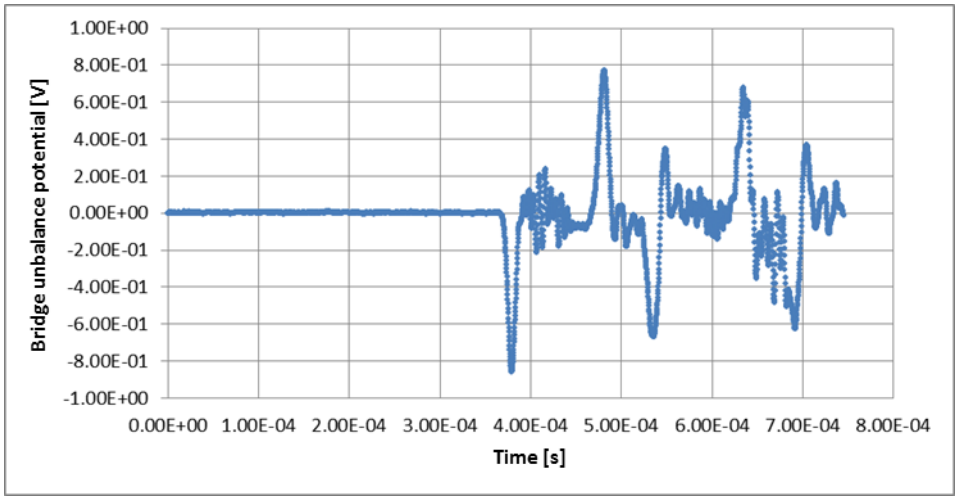



**Fig. 3.24:** Typical voltage vs. time profile of the impact test on alumina target

The axial strain ($\varepsilon$) is measured from the output voltage ($V_{out}$) of the half-bridge circuit as:

$$\varepsilon = \left(\frac{V_{out}}{G}\right)\frac{2}{GF \cdot V_{in}} \tag{27}$$

The input voltage ($V_{in}$) and the gain ($G$) are constant of the system, whilst the gauge factor ($GF$) is a property of the strain gauge, as listed previously.

The force ($F_{bb}$) transmitted from the target to the unit cell is linked to the strain, under the assumption of elastic deformation of the bar, through the Young's modulus ($E$) and the cross section ($A_{bb}$) of the backing bar.

$$F_{bb} = \varepsilon E A_{bb} \tag{28}$$

Finally the impulse transmitted to the bar ($I_{bb}$) can be calculated as the integral of the forces applied in the duration of the compression pulse ($T$), or approximated with a discrete sum:

$$I = \int_0^T F\, dt \approx \sum_0^T F\Delta t \tag{29}$$

### *3.3.2 Preliminary tests*

Before performing any material characterisation of the newly built gas gun several preliminary tests have been performed, to verify both the performance of the gun itself and the behaviour of different types of projectiles impacting ceramic targets.

The first set of preliminary tests verifies the validity of the calculation made during the design process illustrated in Section 3.3.1, whilst the second set provides fundamental pieces of information to better design the experiments to characterise ceramic materials at high strain-rates.

*Verification of the velocity prediction*

The performances of the gun predicted during the design process – reported in Section 3.3.1 – are compared with experimental measurements. The 167 tests reported in Fig. 3.25 are performed accelerating projectiles of various shapes and dimensions with pressurised nitrogen.

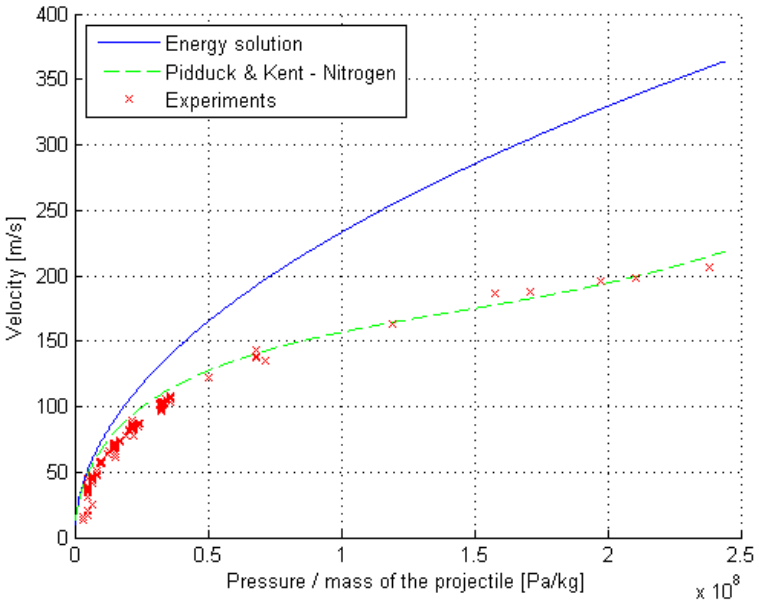



**Fig. 3.25:** Comparison of the velocity predicted by Eq. (24) (green) and Eq. (26) (blue) against experimental measurements

On the horizontal axis is reported the ratio between the pressure of the compressed gas and the mass of the projectile ($P_V/m$), to compare the results of experiments performed using projectiles with different masses.

The correction implemented following Pidduck and Kent solution reproduces extremely well the experimental results, slightly over-predicting the velocity of the projectiles at low pressure-mass ratios. The increase of the volume of the gas during the acceleration of the projectile, and the consequent drop of pressure, are considered to be the main cause of such behaviour. However, the reduced volume of the barrel ($\sim$10% of the volume of the vessel) limits such effect, thus it is considered negligible for the gas gun considered.

Finally the validity of the velocity measured with the light gauges is verified, showing the scarce influence of the stripping (i.e. separation of the projectile from the sabot) on the projectile velocity. The verification is performed evaluating the velocity from the camera footage (i.e. after the stripping), with the help of a ruled bar positioned behind the projectile

(Fig. 3.26), and comparing such velocity with the one measured by the light gauges (i.e. before the stripping).

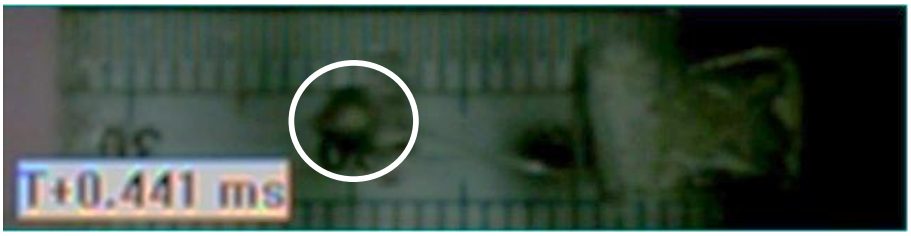



**Fig. 3.26:** Projectile (circled) flying, from right to left,towards the target and ruled bar in the background

The comparison is presented in the following chart (Fig. 3.27), which reports the velocity measured by the light gages on the horizontal axis and the one calculated from the camera footage on the vertical axis.

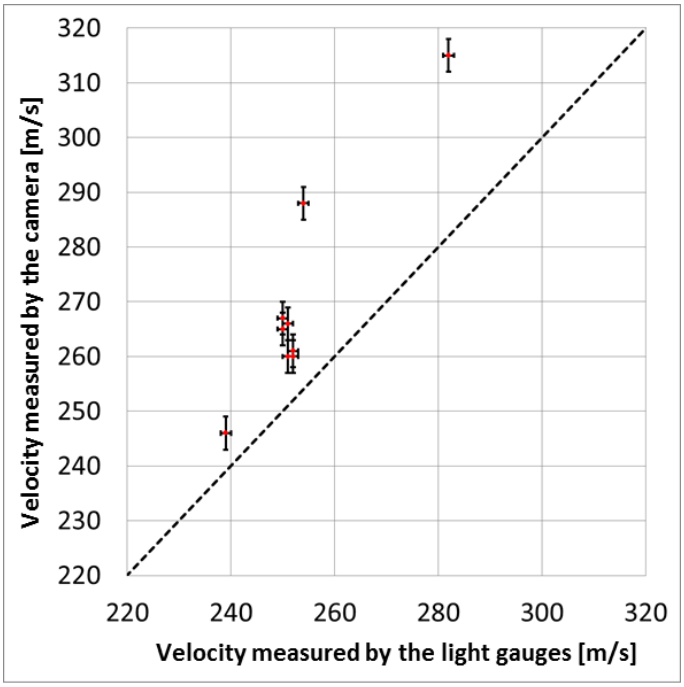



**Fig. 3.27:** Comparison of projectile velocities measured by the light gauges and the high speed camera

The velocity measured analysing the camera footage is consistently higher than the one predicted by the light gauges within a range of $[3.1\% - 11.8\%]$ for the tests performed.

Since the presence of the stripper can only reduce the velocity of the projectile, the observed discrepancy between the two velocities might be due to an error in the camera measurements, possibly linked to the distance between the projectile and the ruled bar.

However the comparison shows that the stripper has a scarce influence on the final velocity of the projectile.

*Choice of the indenter*

In this work the behaviours of four different sets of projectiles are compared, to gather information about the influence of material and shape of the projectile on its behaviour at the impact with a ceramic target. To guarantee the consistency of the results all the tests are performed using alumina targets.

The material, the shape and the range of impact velocities of the four sets of projectiles are summarised in Table 3.4.

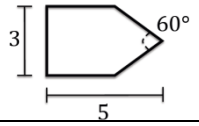
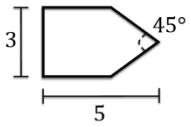
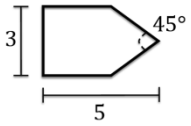
| Shape | Material | Dimensions $[cm]$ | Velocity $[m/s]$ |
|---|---|---|---|
| Cylinder with 60° conical tip | Tungsten-carbide (WC) |   | $67 - 96$ |
| Sphere | Tungsten-carbide (WC) |   | $100 - 300$ |
| Cylinder with 45° conical tip | Stainless steel (SS) |   | $100 - 300$ |
| Cylinder with 45° conical tip | Heat-treated tool steel (TS) |   | $127 - 195$ |

**Table 3.4:** Summary of the projectile sets tested

Firstly a set of tungsten-carbide (WC) cylindrical projectiles with a conical tip (60° tip angle) are machined from the core of real bullets, as shown in Fig. 3.28.

The projectiles were tested for a quite narrow range of velocities (i.e. from 67 to $96\,m/s$). All of them indented the alumina target, shattered in several pieces at the impact, hence exhibiting an extremely brittle behaviour.




**Fig. 3.28:** Real bullet (left) and projectile (right) machined from the bullet core

Fig. 3.29 shows the impact of one of the projectile and its failure (the opaque substance on the base of the projectile is a residual of the adhesive used to glue the projectile to the sabot and does not have any effect on the test).

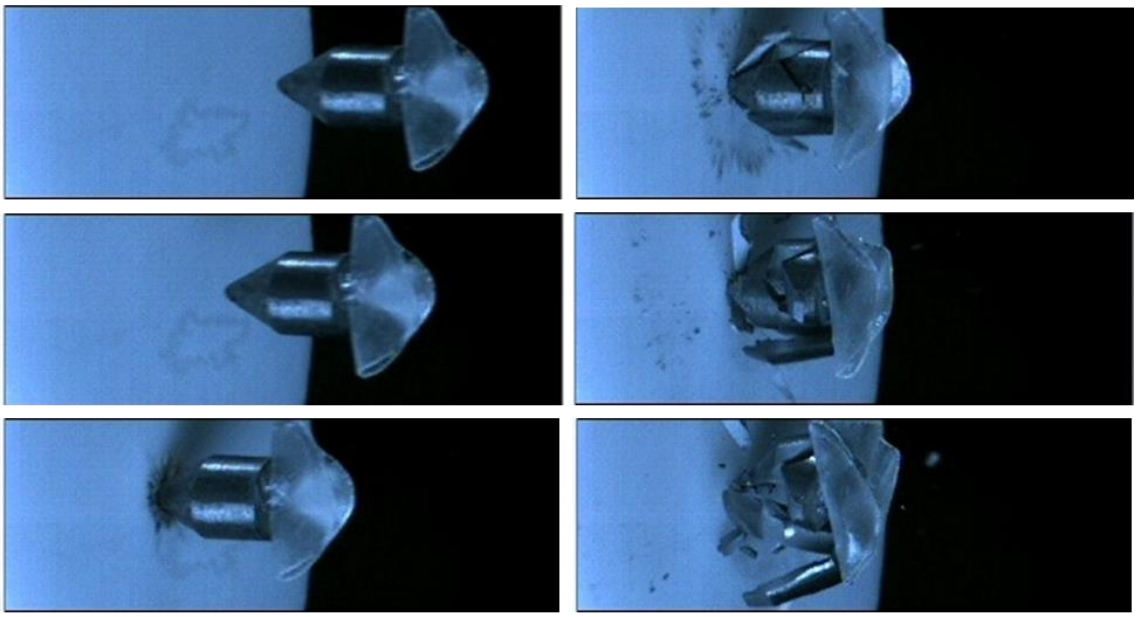


**Fig. 3.29:** Impact of the tungsten-carbide projectile

To verify that the type of failure exhibited by the projectile at the impact is not related to its shape and/or to the size (i.e. bigger projectiles are more likely to contain defects), relatively small WC spherical indenters (diameter of $0.3mm$) are tested in a wider range of impact velocities (i.e. $100$ to $300\,m/s$).

The result of the dynamic test, however, did not change. The spheres indented the target breaking in several pieces at the impact, as reported in Fig. 3.30.

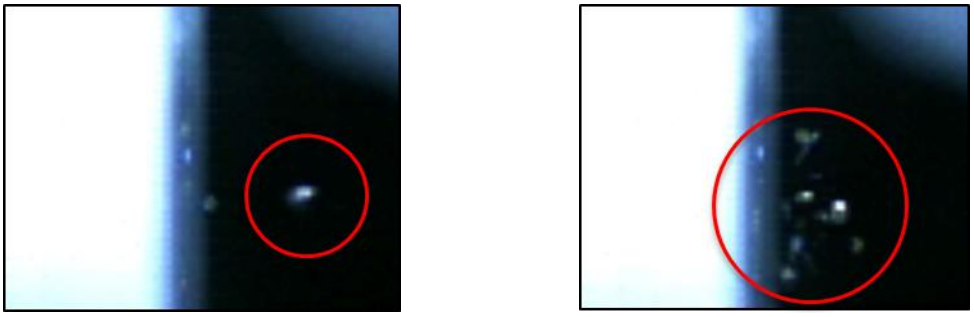


**Fig. 3.30:** Impact of the WC sphere on the target

Confirmed that the tungsten carbide shatters at the impact with the target, a new set of stainless steel (SS) cylinders with conical tips is produced (45° tip angle).

Several shots with velocities varying from 100 to 300$m/s$ are performed, showing consistently a severe plastic deformation of the projectiles at the impact. The targets, instead, remained intact for low impact velocities (i.e. $\sim 100 m/s$) and broke in few pieces for higher ones (Fig. 3.31). However none of the targets showed any measurable indentation during the post-mortem analyses.

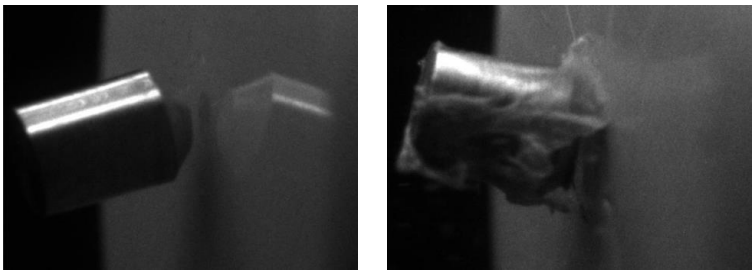


**Fig. 3.31:** Impact of a stainless steel projectile on the ceramic target at $\sim \mathbf{100}\ \boldsymbol{m/s}$ (left) and $\sim \mathbf{300}\ \boldsymbol{m/s}$ (right)

Finally, in the attempt of combining the plastic behaviour of the steel projectiles with the ability of indenting the target, a set of tool steel (TS) projectiles are manufactured and then heat-treated with different processes. The summary of the quenching and tempering procedures adopted for the different sets of projectiles is reported in Table 3.5:

| Projectile set | Heating temperature $[°C]$ | Quenching liquid | Temper temperature $[°C]$ | Hardness (HV) $[GPa]$ |
|---|---|---|---|---|
| A | 810˚ | Oil | 250˚ | 5.2 |
| B | | | 200˚ | 8.0 |
| C | | | 150˚ | 8.9 |
| D | | | No reheating˚ | 8.8 |
| E | 760˚ | Water | 250˚ | 7.1 |
| F | | | 200˚ | 7.2 |
| G | | | 150˚ | 8.5 |
| H | | | No reheating | 9.1 |

**Table 3.5:** Summary of the heat-treatment processes of the different projectiles sets

| Projectile set[1] | Velocity $[m/s]$ | Target status | Projectile status |
|---|---|---|---|
| A | 153 | Intact | Blunted |
| B | 175 | Intact | Blunted |
| C | 196 | Indented | Broken |
| D | 175 | Intact | Broken |
| E | 175 | Indented | Blunted |
| | 195 | Indented | Blunted |
| F | 152 | Intact | Blunted |
| | 172 | Indented | Blunted |
| G | 147 | Indented | Blunted |
| | 165 | Indented | Broken |
| H | 127 | Intact | Blunted |
| | 153 | Intact | Broken |
| | 166 | Indented | Blunted |
| | 175 | Indented | Blunted |

**Table 3.6:** Summary of the outcome of the dynamic indentations using heat-treated steel indenters

[1] Projectile sets refer to Table 3.5.

The so-produced projectiles are characterised by measuring the surface hardness – as reported in Table 3.5 and then tested against alumina targets at different impact velocities. The results are summarised in Table 3.6.

This round of testing rendered several useful pieces of information. The heat-treated steel behaves somewhere in between tungsten carbide and stainless steel, as the hardness measurements suggest.

The quenching in oil provides projectiles that are generally unable to generate any damage to the target, and the hardest projectiles shattered at the impact.

On the other hand, the quenching in water produces projectiles able to indent the target surface for impact velocities above $\sim 150\, m/s$. Moreover, most of the tests carried out ($\sim 80\%$) resulted in the blunt deformation of the tip of the projectile tip. Finally, in the tests in which the projectile broke, the average number of pieces is in between 2 and 3 (e.g. Fig. 3.32), rather than the 30 or more observed in tungsten carbide for similar impact velocities.



**Fig. 3.32:** Blunted (left) and broken (right) heat-treated steel indenter

The outcome of all the tests presented in this section is summarised in Table 3.7.

The examination of the targets under optical microscope shows that the depth of the indentation caused by the heat-treated steel projectiles is lower than the one caused by tungsten-carbide indenters for similar velocities. This result can be linked to a combination of lower hardness and density of the steel. The first induces a greater deformation in the indenter, whilst the latter reflects in a lower momentum of the projectile at the impact.

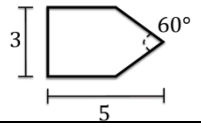
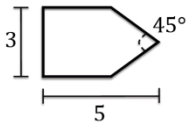
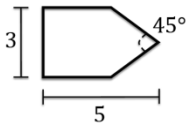
| Material | Shape and dimensions $[cm]$ | Velocity $[^{m}/_{s}]$ | Target status | Projectile status |
|---|---|---|---|---|
| Tungsten-carbide (WC) |   | $67 - 96$ | Indented | Shattered |
| Tungsten-carbide (WC) |   | $100 - 108$ | Intact | Shattered |
| | | $199 - 291$ | Indented | |
| Stainless steel (SS) |   | $96 - 102$ | Intact | Blunted |
| | | $199 - 267$ | Broken | |
| Heat-treated tool steel (TS) |   | $127 - 195$ | See Table 3.6 | |

**Table 3.7:** Summary of the outcome of the dynamic indentations

To conclude, the investigation of the different projectiles presented shows the undoubted superiority of the tungsten-carbide for the indentation of ceramic materials, in terms of damage inflicted to the target and depth of the indentation caused. However, the hardened steel causes – albeit shallower – indentation in ceramic materials, without exhibiting the brittle failure characteristic of the tungsten-carbide. Finally, the stainless steel is not to be further considered since its inability to induce any damage in the target.

The ductile behaviour of the hardened steel projectiles allows for a direct comparison of dynamic and quasi-static indentation presented in Section 3.3.3, whilst the superior ability of the tungsten carbide projectiles to damage the target is exploited in the tests illustrated in Section 3.3.4.

### *3.3.3 Indentation tests at multiple strain-rates*

The main purpose of designing a dynamic test comparable to a quasi-static indentation is to, therefore, isolate and highlight the rate dependencies in the mechanisms governing the failure of ceramic materials.

Numerous works performed in the past decades – perhaps confirmed by the numerical simulations performed in Section 4.4 – indicate that the main difference in the failure mechanisms at different strain rates is linked with the evolution of the crack growth. In particular the quasi-static indentation load induces the initiation of few micro-cracks that propagate inside the material preventing other crack to be initiated, whilst a dynamic load initiates multiple micro-cracks, creating a more complex crack pattern.

The tests presented in this section compare the level of damage caused by dynamic indentation – with similar momentum exchange – on target of three different materials. The momentum measured by the backing bar is then used to define the load path in quasi-static indentation tests, to finally explore the effect of the strain rate on the damage evolution in the three ceramic materials analysed.

Firstly the two test typologies are described, and then the results of the dynamic and quasi-static indentation tests are illustrated and compared.

*Description of the test*

In this section is proposed a methodology to perform directly comparable dynamic and quasi-static indentation tests to highlight the influence of the strain rate on the failure mechanisms of the material.

The dynamic test presented in this thesis consists of impacting perpendicularly the surface of the ceramic specimen with a projectile accelerated in the gas gun, as described in Section 3.3.1. The force transmitted to the support is measured with the backing bar, and the load path measured is used as input to the quasi-static indentation test.

The first issue to face in performing such a comparison is linked with the behaviour of the indenter. The classic tests for the quasi-static evaluation of the material hardness assume the absence of any permanent deformation of the indenter, given the considerable higher stiffness of the indenter in respect with the specimen. However, the dynamic effects, combined with the high hardness of the ceramic materials tested, prevent the projectile from behaving rigidly, or even elastically.

To privilege the "comparability" of the quasi-static and the dynamic conditions, the indenters are made of heat-treated steel. In particular the tool steel projectiles are heated at $780°C$ and quenched in water without reheating, obtaining measured Vickers hardness (HV) of $9.3GPa$. Such projectiles deform plastically at the impact with the ceramic target at all the strain-rates tested (as proven in Section 3.3.2), and only rarely (i.e. less than the 20% of the cases) they break in few pieces at high impact velocities.

Three types of commercial lab prepared ceramic materials were provided by Morgan Technical Ceramics:

- Alumina with glassy phase due to multiple oxide additions (95% alumina);
- Zirconia-alumina composite (90% alumina, 10% zirconia), henceforth called "ZTA";
- Tetragonal zirconia polycrystals (94% zirconia, 5.4% yttrium), henceforth called "TZP".

The microstructural topology (i.e. grain size distribution) and the Vickers hardness of the materials are reported in Table 3.8.

| **Material** | **Grain size** $[\mu m]$ | **Standard deviation** $[\mu m]$ | **Hardness (HV)** $[GPa]$ |
|---|---|---|---|
| **TZP** | $0.58 \pm 0.11$ | 0.065 | $12.8 \pm 0.15$ |
| **Alumina** | $5.8 \pm 1.3$ | 0.860 | $12.5 \pm 0.25$ |
| **ZTA** | $1.9 \pm 0.32$ | 0.267 | $18.3 \pm 0.5$ |

**Table 3.8:** Grain size distribution of the three materials tested

The specimens are discs of $25mm$ diameter (i.e. almost the dimension of the cross section of the backing bar) and $5mm$ thickness, and are held in place by a thin layer of silicon grease.

*Dynamic indentation tests*

Three dynamic indentations per each material are carried out. In Fig. 3.33 are presented selected images from a typical video footage, showing the blunt deformation of the projectile after the impact with the target.

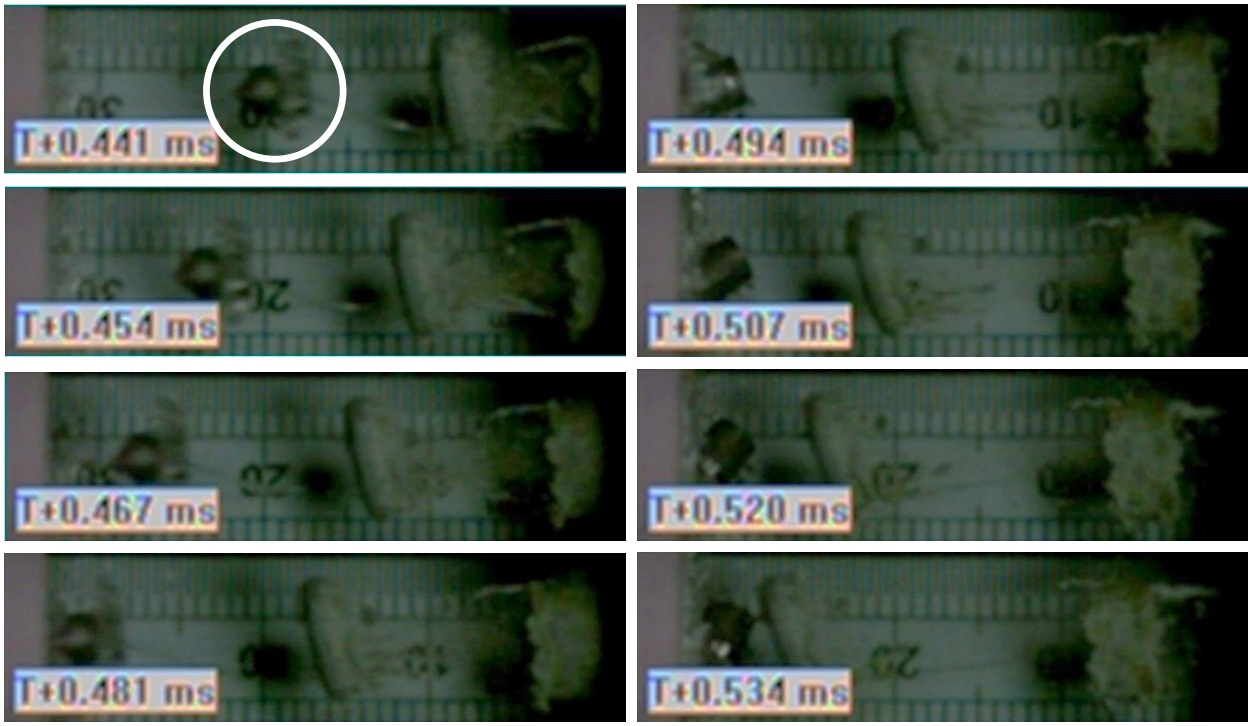



**Fig. 3.33:** Typical video footage of a dynamic indentation test

The results of the tests are summarised in Table 3.9 The values reported provide several interesting pieces of information, such as: the slight discrepancy of the momentum calculated from the projectile velocity and the measurements of the backing bar, the modest increase of peak force measured in ZTA with respect to the alumina, and the significantly lower peak force measured in the tests involving TZP targets.

| **Target material** | **Mass** $\pm 0.0001$ $[g]$ | **Velocity (Light gauges)** $\left[\frac{m}{s}\right]$ | **Momentum (Light gauges)** $\left[kg\frac{m}{s}\right]$ | **Momentum (Backing bar)** $\left[kg\frac{m}{s}\right]$ | **Peak Force** $[N]$ |
|---|---|---|---|---|---|
| **TZP** | 0.1818 | 239.2 | 0.0435 | 0.0539 | 3388 |
| | 0.1972 | 250 | 0.0493 | 0.0518 | 3389 |
| | 0.1962 | 253.8 | 0.0498 | 0.0536 | 3601 |
| **Alumina**[2] | 0.1875 | 250.5 | 0.0470 | 0.0521 | 5311 |
| | 0.185 | 250.5 | 0.0463 | 0.0577 | 5568 |
| | 0.187 | 250 | 0.0468 | - | - |
| | 0.1766 | 250 | 0.0440 | 0.0616 | 5508 |
| **ZTA** | 0.2077 | 282 | 0.0586 | 0.0621 | 5840 |
| | 0.2068 | 252 | 0.0521 | 0.0556 | 6113 |
| | 0.2059 | 252 | 0.0519 | 0.0572 | 5341 |

**Table 3.9:** Summary of the impact tests

The first consideration is further analysed generating the graph presented in Fig. 3.34. The horizontal axis reports the values of the momentum calculated from the projectile velocity, whilst the vertical axis report the measurements of the backing bar. Finally the bisector line represents equality between the two values.

Even considering the error of the measurement techniques adopted, the backing bar measures a momentum consistently higher than the one predicted from the impact velocity. A possible explanation of this behaviour may be in the incorrect assumption of perfectly inelastic impact in the calculation of the momentum from the light gauges measurement, implying that the rebound of the projectile provides additional momentum to the target-and-

[2] An additional impact was performed on alumina due to equipment (i.e. baking bar) failure

bar system. This comparison highlights the importance of using the backing bar as loading cell to measure the momentum and provide insights on the behaviour of the ceramic material at the impact.

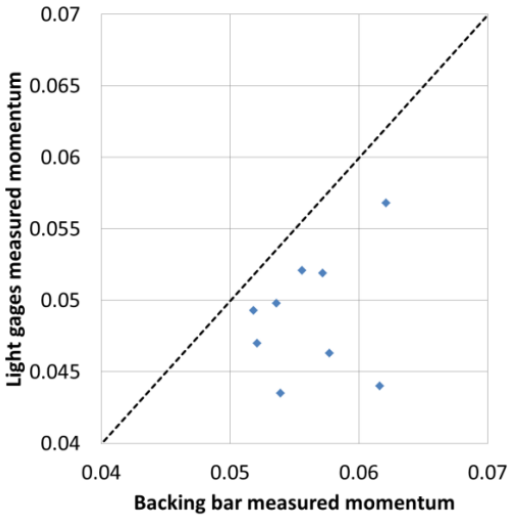



**Fig. 3.34:** Comparison of the momentums measured with the light gages and with the backing bar

The investigation of the meaning of the differences in the measured peak forces for the three materials is performed analysing the force-time curve trends obtained from the backing bar measurements. Such curves are reported – respectively for alumina, ZTA, and TZP – in Fig. 3.35, Fig. 3.36, and Fig. 3.37.

The first two materials (i.e. alumina and ZTA) show a very similar behaviour, with a slightly higher peak force measured with the ZTA samples. The difference, however, is too small to allow for any speculation on the effect of the addition of zirconia to the alumina.

The TZP, instead, exhibits a massively different behaviour at the impact, with a second compression peak that reduces of more than 40% the compressive peak with respect to alumina and ZTA, for comparable total momentum. The video footage reported in Fig. 3.38 offers additional evidence, showing a flash appearing just after the impact has occurred on the TZP target.

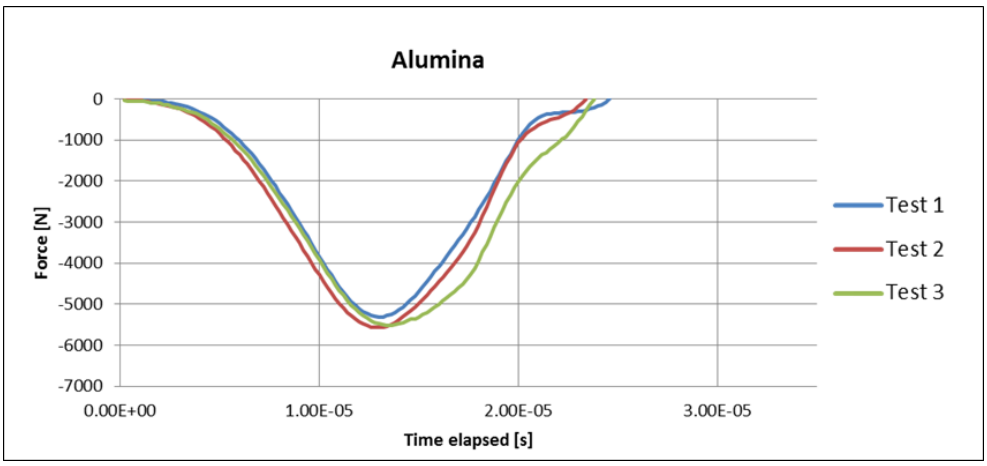



**Fig. 3.35:** Primary compression peak for alumina dynamic indentation tests

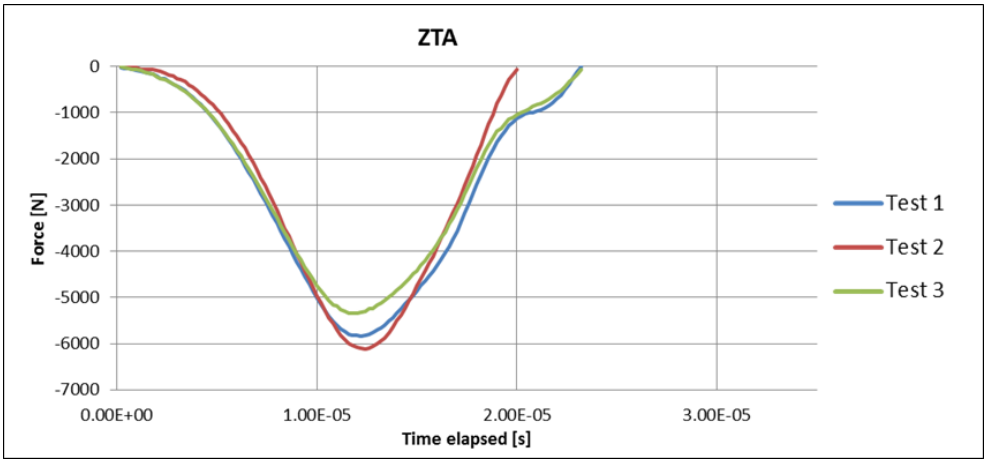



**Fig. 3.36:** Primary compression peak for ZTA dynamic indentation test

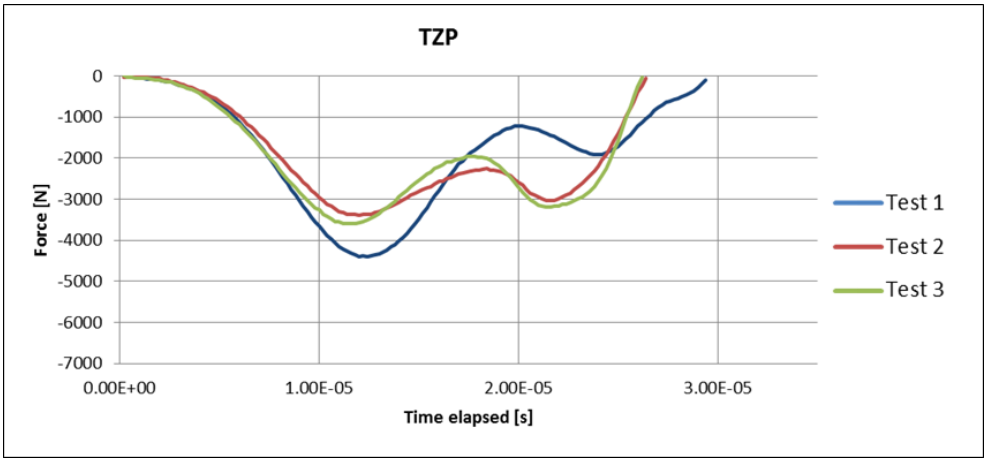



**Fig. 3.37:** Primary compression peaks for TZP dynamic indentation test

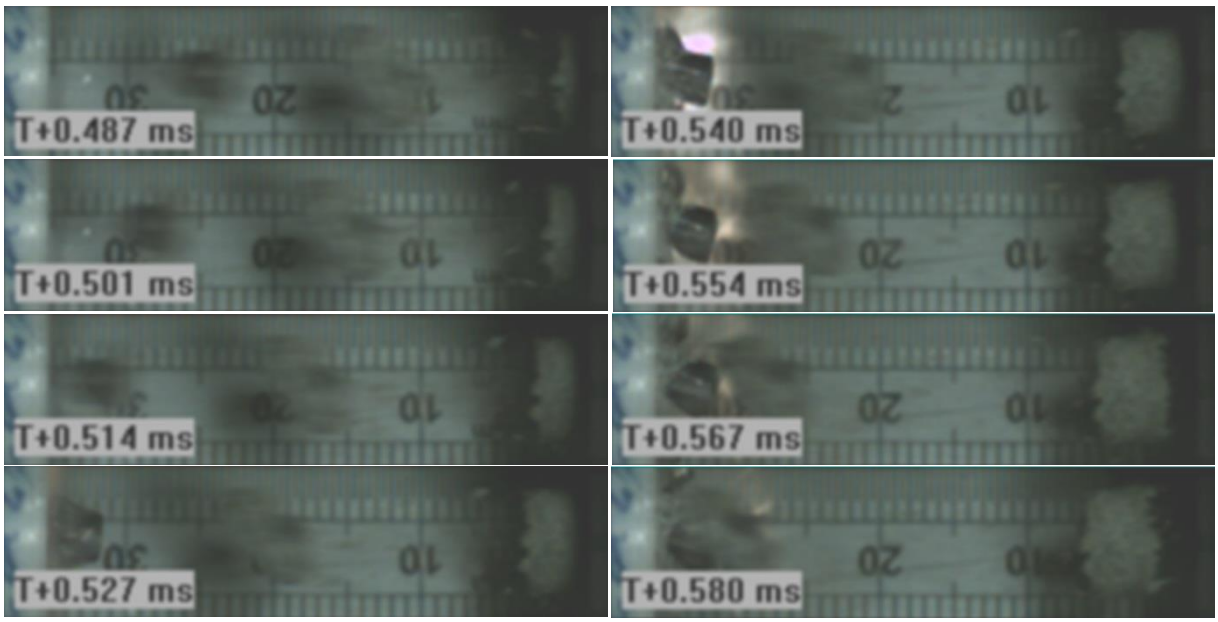



**Fig. 3.38:** Video footage of the flash observed in TZP

Similar behaviour is not observed in any other material, and the origin is unknown. It is possible that the effect is related to the transformation of the crystal structure from tetragonal to monoclinic, which is known to occur in zirconia based materials [130]. The transformation is accompanied by a volume increase, which would justify the second peak observed in Fig. 3.37. Unfortunately the transformation is not reversible, so the post-mortem analyses could not provide further insight on the phenomenon.

*Comparison with quasi-static indentation tests*

The outcome of the dynamic indentations is used to design a comparable quasi-static indentation test, in the attempt of isolating the rate dependency of the deformation and damage evolution in the materials tested.

In particular the quasi-static indentation is performed adopting as indenters the projectiles utilised for the dynamic tests, whilst the load path is imposed to follow the force trend measured dynamically. The graph in Fig. 3.39 reports the quasi-static and the dynamic load-time curves for alumina specimens

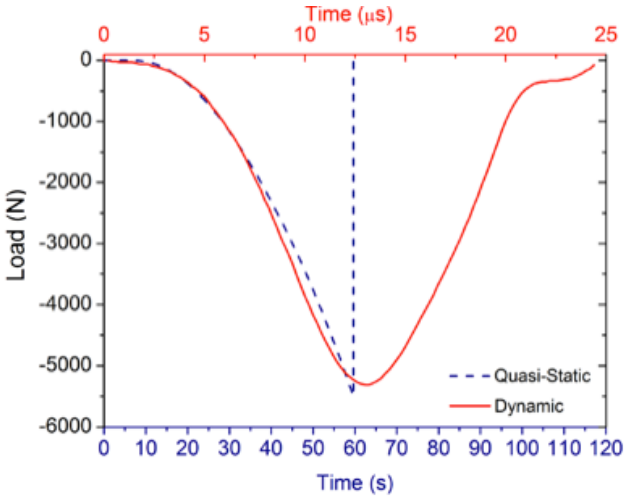



**Fig. 3.39:** Comparison of quasi-static and dynamic load applied during the indentation tests

The quasi-static load path experiences a sudden drop of the load when the displacement rate is reversed, whilst the dynamic curve slowly decreases as the projectile rebounds.

Finally given the not reproducible shape of the dynamic response of TZP, the quasi-static indentation of such material is performed using the load path determined for alumina.

The results of the two sets of tests present numerous differences, both in the behaviour of the indenter and of the specimens.

Firstly the dynamic indentation results in a blunter tip of the indenter after the test, as shown in Fig. 3.40. The cross section area reported in Fig. 3.40 is identical for the both cases, hence indicating the noticeably larger deformation occurring in the indenters during the dynamic tests. This difference is suspected to be due to the rise in temperature, deriving from the adiabatic heating that the projectile experiences during the impact, which enhances the plastic deformation of the metal.

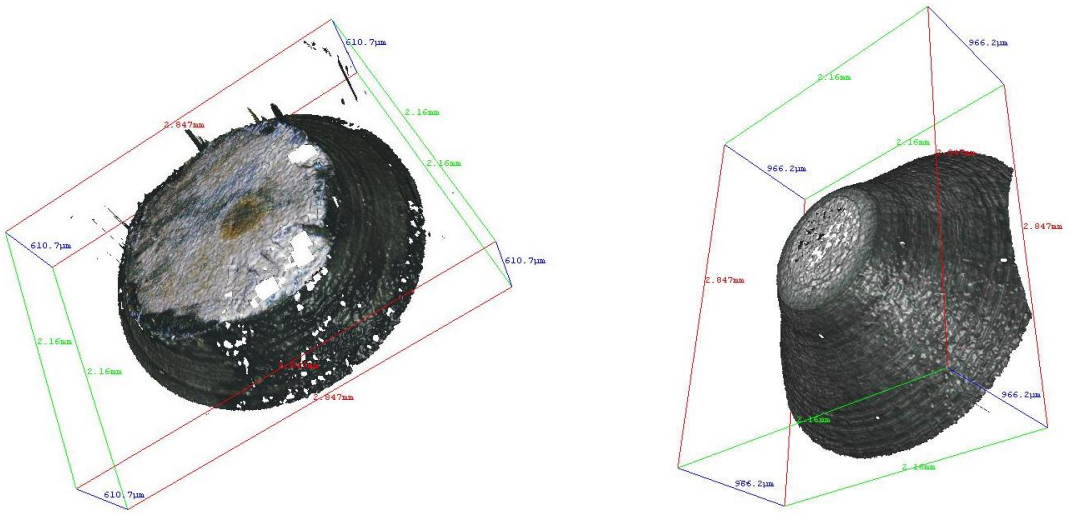


**Fig. 3.40:** Visual reconstruction of the indenter after a dynamic (left) and quasi-static (right) indentation test

On the other hand, the ceramic specimens show prominent differences too, as it is evident from the optical microscopy of the indented areas reported in Fig. 3.41.

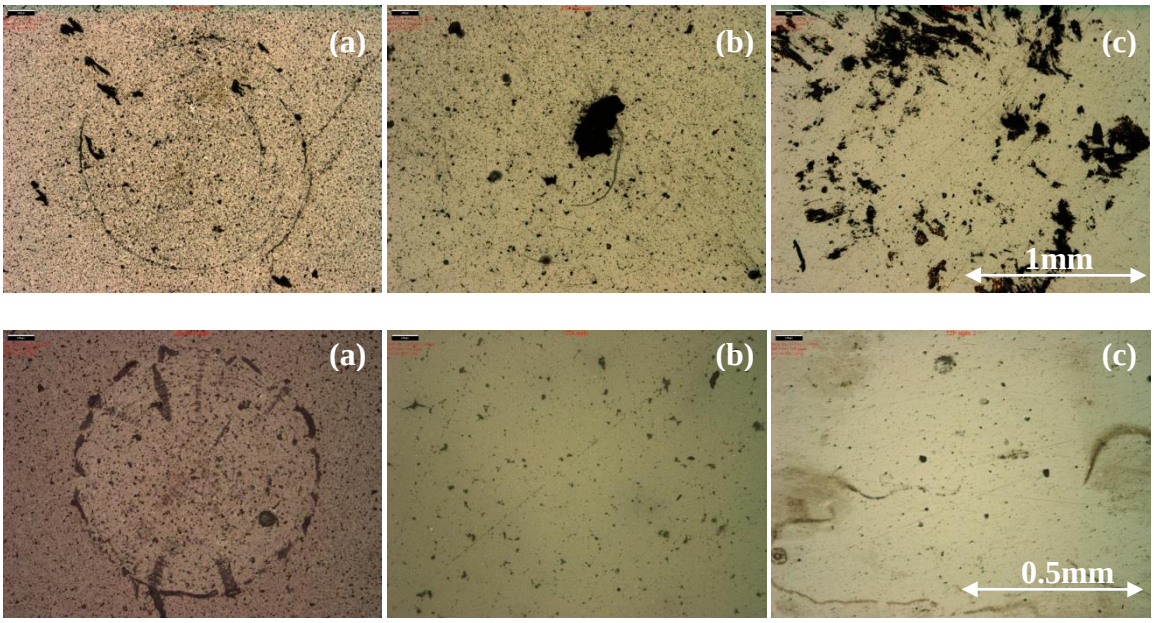



**Fig. 3.41:** Optical microscopy of the dynamic (top) and quasi-static (bottom) indentation sites respectively on Alumina (a), ZTA (b) and TZP (c)

The optical micrographs show clearly visible cracks for both dynamic and quasi-static alumina indentation (although with differences in size and depth). The indentation is less noticeable in ZTA and practically non-existent in TZP. Finally, the dark regions in the dynamic indentations are residual steel contamination on the target surface.

The difference between the quasi-static and dynamic indentations is quantified comparing the average diameter and depth of the crater, as reported in Table 3.10.

| **Material** | **Indentation type** | **Diameter** [$\boldsymbol{mm}$] | **Maximum depth** [$\boldsymbol{\mu m}$] |
|---|---|---|---|
| **Alumina** | Quasi-static | 0.9 | 4 |
| | Dynamic | 1.4 | 0.7 |
| **ZTA** | Quasi-static | 0.8 | 0.1 |
| | Dynamic | Not visible | Not visible |
| **TZP** | Quasi-static | 0.9 | 0.6 |
| | Dynamic | Not visible | Not visible |

**Table 3.10:** Summary of the diameter and depth of the indentation crater

For alumina the dynamic indentation produces a much shallower indentation than the quasi-static one, but with a wider diameter of the crater. On ZTA and TZP targets, instead, the dynamic indentation does not leave any optically measurable crater, whilst the quasi-static indentation leaves a barely measurable dent. This shows the changes in the alumina behaviour induced by the addition of zirconia in the ZTA (i.e. 90% alumina, 10% zirconia).

The profilometry of quasi-static and dynamic alumina are reported in Fig. 3.42, to visually show the difference in the crater left by the indenter.

The apparent peak at the limit of the crater in the dynamic indentation is due to the presence of steel debris on the surface of the ceramic.

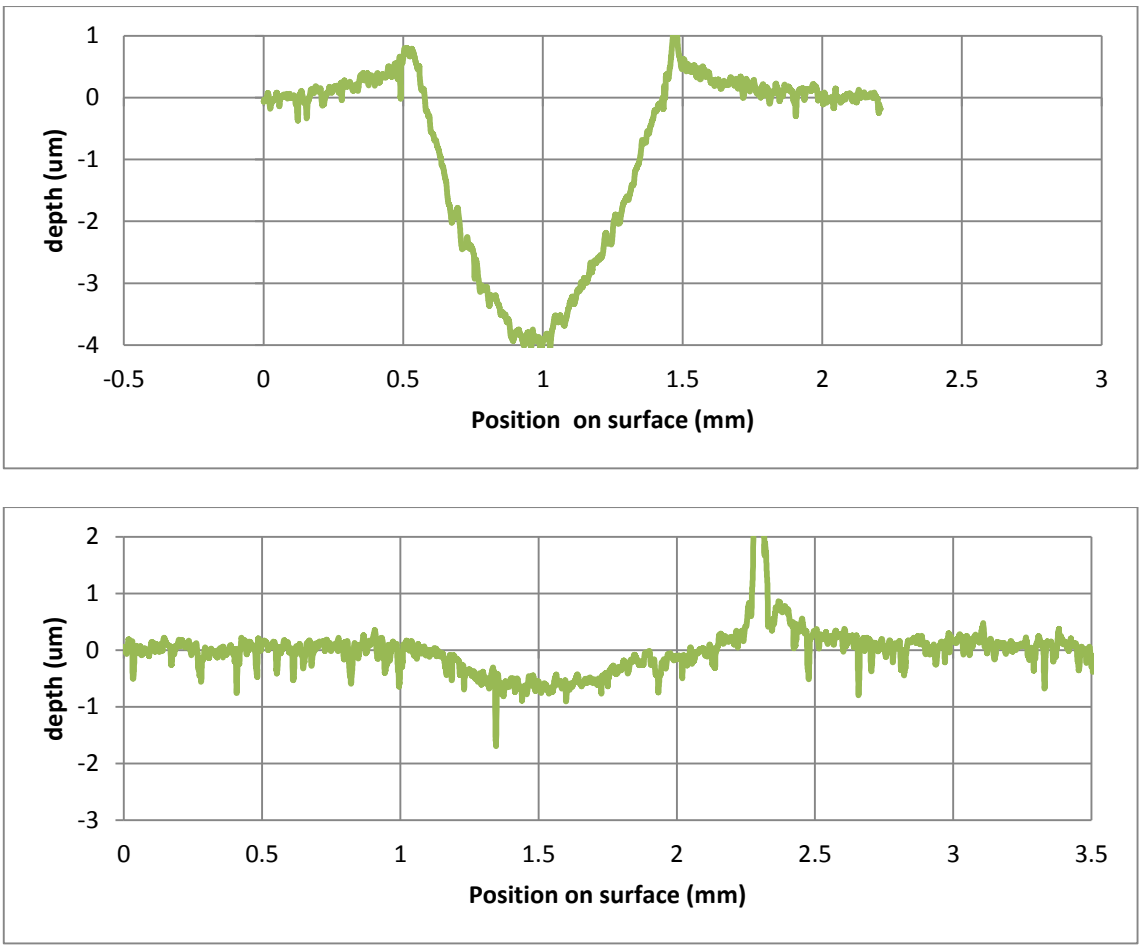



**Fig. 3.42:** Depth profile of quasi-static (top) and dynamic (bottom) indentations of alumina

Finally the SEM spectroscopy on the ceramic samples (performed by Jack Spawton, Materials department, University of Oxford) revealed the presence of cracks not visible with optical microscopy in all the quasi-statically and dynamically indented specimens.

For alumina, the larger and shallower crater generated by the dynamic test, despite the presence of some micro-cracks at the centre of the indentation, appears also to damage less severely the material. Another difference between the two testing conditions is that the dynamic indentation produces fewer – but far longer– radial cracks than the quasi-static test. Finally, both quasi-statically and dynamically indented alumina specimens exhibit mainly inter-granular propagation of cracks.

ZTA targets, instead, display a single circular crack for both dynamic and quasi-static testing conditions. Although the crack generated by the dynamic indentation has a larger

diameter and a small amount of micro-cracking is observed inside the ring, the loading rate appears to have a reduced effect on the appearance of the cracks in ZTA samples. Fig. 3.43 shows the comparison cracks generated by the quasi-static and the dynamic indentation, revealing very little differences in their aspect.

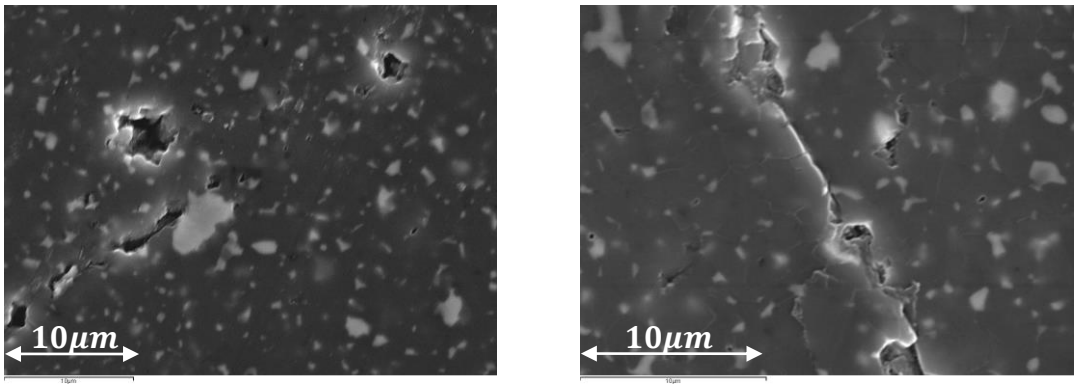



**Fig. 3.43:** Ring crack appereance of quasi-static (left) and dynamic (right) indented ZTA

Finally, the possible presence of crystal transformation in the TZP samples during the dynamic indentation tests prevents the direct comparability of the specimens indented at different load rates. The full understanding of the dynamic behaviour of TZP requires more in-depth analyses, which have been carried out in other works within the framework of the project. However the phenomenon is still far from being fully understood and is a potential topic for future works.

To conclude, the comparison between dynamic and quasi-static indentation tests shows that an higher strain-rate corresponds to a reduced depth of the crater and to a more spread damage with the production of numerous micro-cracks. Similar mechanisms have been observed in the simulations presented in Section 4.4.

### *3.3.4 Impact tests on different grades of silicon carbide*

The preliminary dynamic characterization of two different grades of silicon-carbide (SiC) is performed impacting the targets with tungsten-carbide projectiles. The aim of the tests is to identify the effect of the grain size on the failure mechanism of silicon carbide, by

comparing the damage of two set of specimens with different grades, subjected to the same loading conditions (i.e. impact velocities).

The choice of tungsten-carbide projectiles is motivated by the necessity of making a measurable indent in the target, and to the inability of any other projectile tested (i.e. listed in Section 3.3.2) to generate any mark on the surface of such a hard material like silicon-carbide.

*Description of the test*

Unlike in the tests reported in the previous section, the SiC samples are machined into squares, because of manufacturing constraints. In particular the SiC is sintered in rectangular ($200x200mm$) plates of different thicknesses, and the extreme difficulty in drilling discs out of those plates led to the preliminary choice of cutting $25x25mm$ square targets. The edge length of the target is imposed equal to the diameter of the backing bar, therefore leaving the four corners of the sample "unsupported". The targets are held in place with the same technique adopted for the tests presented in the previous sections (i.e. the sample is glued to the baking bar with silicone grease). However, given the increased dimensions of the sample, the layer of grease required to hold the specimen in place is thicker, possibly affecting the results.

The response of the specimen is both filmed with the high-speed camera and measured using the strain-gauged bar. Finally, the post-mortem analysis are carried out on the targets to verify any possible differences between the two grades of SiC to link with the diversity of the material properties.

*Material properties*

In this section a summary of the characterization of the two grades of silicon carbide, named *SiC-D* and *SiC-E*, (performed by Emilio Lopez Lopez, Materials department, University of Oxford) are reported.

| **Property** | **SiC-D** | **SiC-E** |
|---|---|---|
| $E\ [GPa]$ | $430 \pm 12$ | $433 \pm 13$ |
| $\sigma_f^t\ [MPa]$ | $493 \pm 38$ | $345 \pm 52$ |
| $\sigma_f^c\ [GPa]$ | $3.0 \pm 0.4$ | $1.7 \pm 0.1$ |

**Table 3.11:** Characterization of the two grades of silicon carbide

The Young's modulus ($E$) has been evaluated using the Impulse Excitation Technique (IET), the fracture strength in tension ($\sigma_f^t$) by 4-points-bending tests, and the fracture strength in compression ($\sigma_f^c$) by quasi-static uniaxial compression tests. A sample of the SEM micrograph of the two materials is presented in Fig. 3.44:

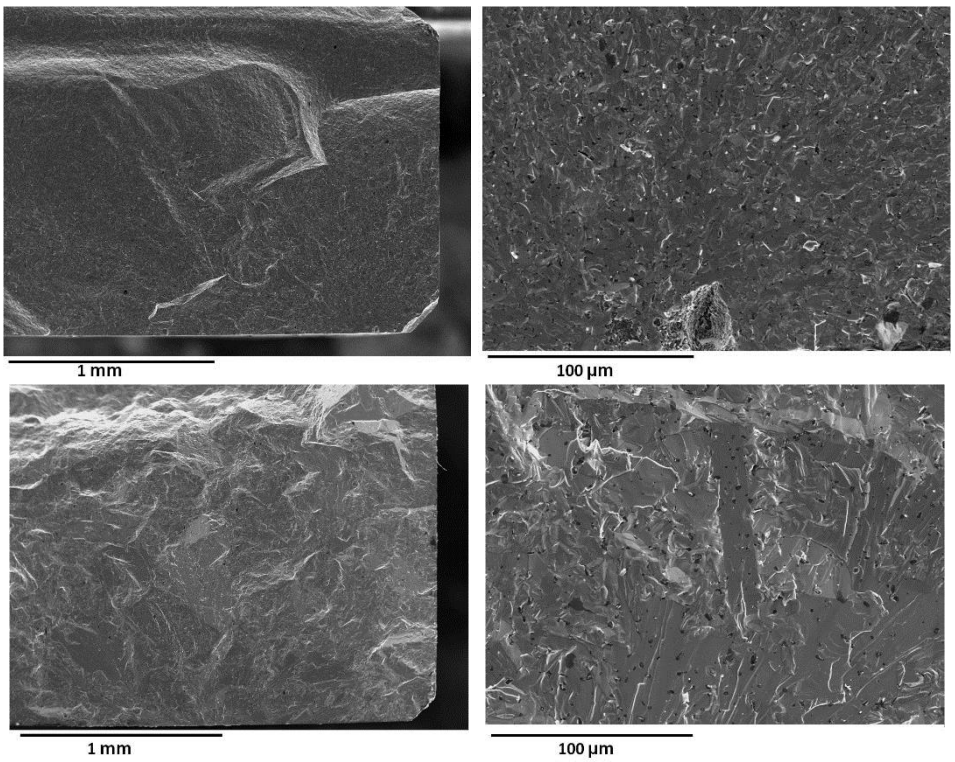



**Fig. 3.44:** SEM micrographs of the fracture surfaces of SiC-D (top) and SiC-E (bottom)

The morphology of the fracture surfaces of the two materials is different. On the fracture surface of the SiC-D specimen can be identified the critical defects ($\sim 20\mu m$) that are not visible on the rougher fracture surface of the SiC-E specimens.

*Results and discussion*

Three tests per each grade of SiC have been carried out, at a consistent impact velocity of $\sim 100\, m/s$ , and the results are summarised in Table 3.12.

| **Target** | **Mass** $[g]$ | **Velocity** $[m/s]$ | **Target status** | **Damage Area** $[mm^2]$ | **Depth** $\mu m$ |
|---|---|---|---|---|---|
| SiC-D1 | 4.5 | 106.26 | Intact | $\sim 3.6$ | $\sim 16$ |
| SiC-D2 | 4.5 | 100.74 | Broken | – | – |
| SiC-D3 | 4.5 | 102.39 | Intact | $\sim 4.3$ | $\sim 16$ |
| SiC-E1 | 4.5 | 99.31 | Broken | – | – |
| SiC-E2 | 4.5 | 98.79 | Intact | $\sim 3.8$ | $\sim 7$ |
| SiC-E3 | 4.5 | 97.42 | Intact | $\sim 3.0$ | $\sim 8$ |

**Table 3.12:** Summary of the impact tests on different grades of silicon-carbide

The projectile, as already shown in Section 3.3.2, consistently shatters in several pieces at the impact. The targets, instead, have a not consistent behaviour, with only one out of three targets breaking for both grades of silicon carbide.

The post-mortem analysis shows that the SiC-E specimens exhibit a shallower crater, accompanied by a damaged area slightly larger, in comparison to the SiC-D targets.

The forces measured by the backing bar (reported in Fig. 3.45 and Fig. 3.46), instead, do not provide a clear pattern on the failure mechanisms in the two set of tests.

There is no feature of the force-time curves to correlate with the failure of either the SiC-D or SiC-E broken targets. In particular, the force-time curves measured during the test of the targets SiC-D2 and SiC-D3 are extremely similar, despite the fact that the first target broke, whilst the latter remained intact. Also the lower compressive force peak measured during the test on SiC-D1 is apparently not connected with a different damage level of the target with respect to SiC-D3 specimen.

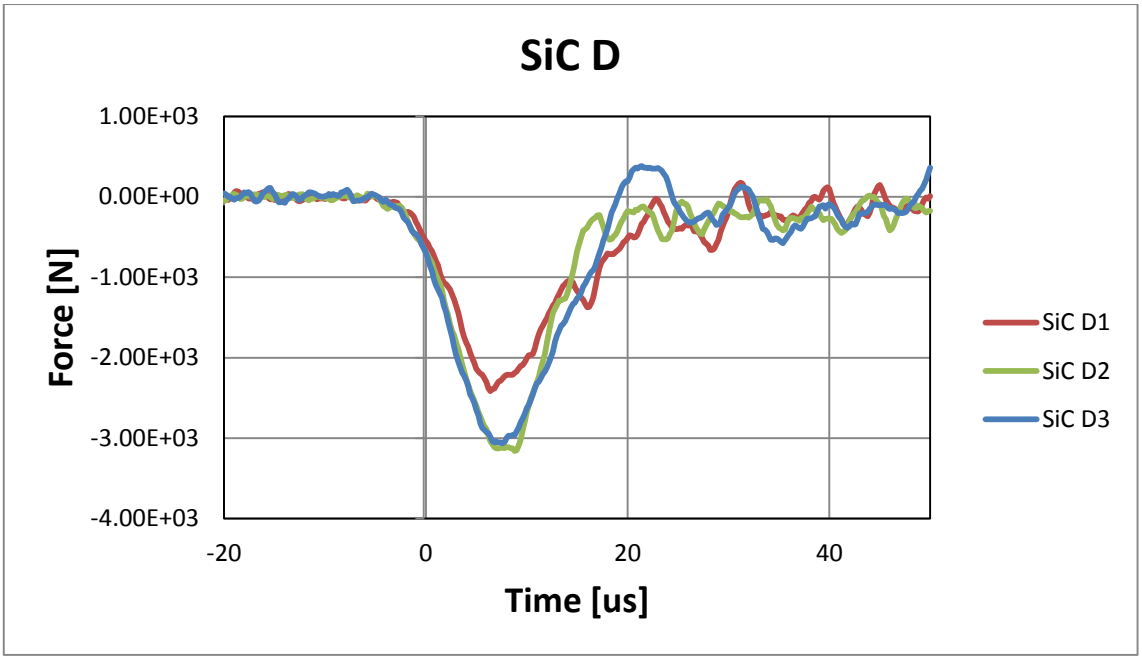



**Fig. 3.45:** Backing bar measurements for the impact tests on SiC D targets

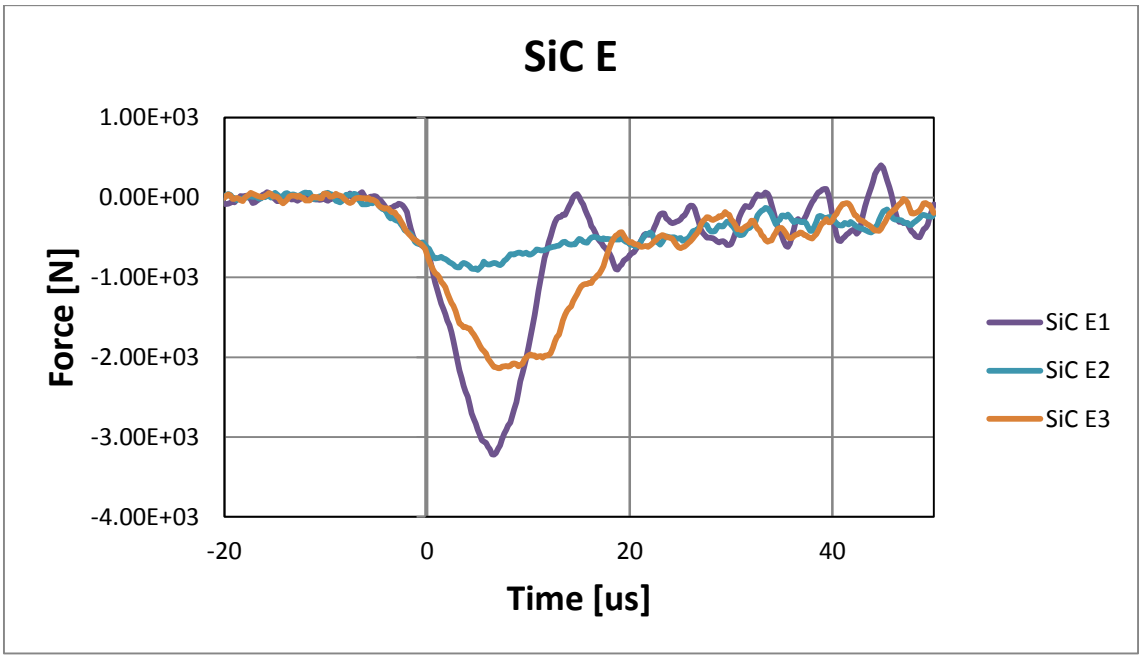



**Fig. 3.46:** Backing bar measurements for the impact tests on SiC E targets

The SiC-E targets have an even more irregular behaviour, with the only broken target (SiC-E1) resulting in a compressive peak larger than the other two specimens that remained intact, and comparable with the ones obtained testing SiC-D2 and SiC-D3 targets.

Different explanations can be provided to justify the irregularity of the backing bar measurements. The similarity of the forces measured by the backing bar during the testing of

broken and intact targets can be explained by considering the failure due to the bending of the unconstrained corners of the specimen, as can be hinted from the camera footage reported in Fig. 3.47.

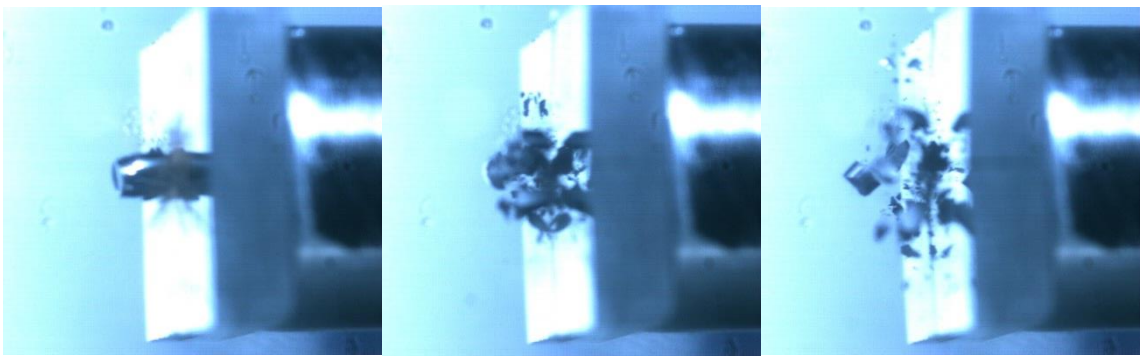


**Fig. 3.47:** Camera footage of the impact on SiC-E1 specimen

The low peak forces measured during some tests, instead, may be due to an excessive thickness of the layer of silicone grease used to hold the target on the backing bar that possibly damped the force transferred from the target to the backing bar.

This set of tests, though not being able to successfully characterise the two grades of silicon-carbide, provide precious pieces of information to better design the tests on SiC targets that are part of the future work planned in the framework of a continuation project.

## 3.4 Conclusions

In this chapter the experimental work performed both at the micro- and at the macro-scales is presented. The aim of the experiments was to characterise the behaviour of the ceramic materials analysed (i.e. alumina, TZP, ZTA, SiC), providing both direct measurements of the physical properties as well as validation for the numerical simulations presented in the next chapters.

### *3.4.1 Micro-scale*

The aim of the experimental tests at the micro-scale presented in this thesis is to observe the deformation and cracking mechanisms at the grain level, measuring the elastic properties, failure strength, and stress intensity factor of the microstructure. In particular, micro-cantilever beams are milled from the surface of polycrystalline alumina samples using FIB, and then deflected with a nano-indenter until their complete failure.

The methodology to calculate the Young's modulus, the failure strength of the beams, and the stress intensity factor at the notch tip, from the measurements of applied force and displacement of the indenter, was developed by modifying the Euler-Bernoulli theory for the deflection of straight beams. The post-mortem analysis of the last set of beams reveals that the "preferred" failure mechanisms are cracks initiating at the grain boundaries and propagating inter-granularly.

The results collected from the experiments are then used in Section 4.3.3, both as input for the numerical models (i.e. elastic properties of the single grain and failure strength of the grain boundary), and as verification of the simulations (i.e. elastic deformation and failure of polycrystalline beams).

### *3.4.2 Macro-scale*

The experimental tests at the macro-scale focus on the characterisation of ceramic materials at different strain-rates.

In Section 3.2 the technique adopted to measure the elastic properties of polycrystalline alumina is illustrated. The macroscopic measurements of the elastic properties of the material are used as a validation of the representativeness of the microstructural models of polycrystalline domains reported in Section 4.3.1.

In Section 3.3 the design of an impact test providing results comparable to quasi-static indentation tests is presented. The dynamic indentation tests are carried out using a single

stage gas gun supported by indirect measurement systems such as a high-speed camera and an instrumented support that records the force transmitted from the target, as described in Section 3.3.1. The design of the gas gun, as well as of the other devices comprising the characterisation system is illustrated in detail.

As part of the design of the dynamic indentation test, two sets of preliminary impact tests have been performed. First the outer velocity of 167 projectiles fired with vessel pressures (expressed in $Pa$) of between $10^5$ to $10^8$ times the mass of the projectile (expressed in $kg$) has been measured, and compared against the analytical prediction presented in Section 3.3.1, showing excellent agreement. Then the behaviour of several types of projectiles have been tested, to explore the best compromise between brittleness and hardness of the material for the desired testing conditions. Two type of projectiles have been selected to perform the tests presented in this work: quenched steel for the comparison of indentation tests at multiple rates, and tungsten carbide for the impact against silicon carbide targets.

Finally four different materials are characterised: alumina, zirconia-alumina composite (ZTA), tetragonal zirconia polycrystals (TZP), and silicon carbide (SiC).

For the first three materials the rate-effect is highlighted by comparing dynamic and quasi-static indentations performed with similar indenters and load paths. To guarantee the comparability of the testing condition across the two rates, ductile (quenched steel) projectiles have been used, thus avoiding the fracture of the projectile at the impact. The dynamic indentation generates a shallower and broader crater in alumina (with respect to the quasi static indentation), but does not create a visible damage in ZTA and TZP (Section 3.3.3).

Alumina tests, in particular, have been used to validate the numerical model developed during this study, as presented in Section 5.2.

The silicon carbide is, instead, only tested at high strain-rates comparing the behaviour of two different grades of SiC. Given high hardness of the ceramic material tested, tungsten carbide projectiles have been used to impact the target. This set of tests, despite not providing

unambiguous indications about the mechanical response of the two materials, provides important pieces of information on the testing technique, identifying two criticalities in the shape of the specimen and in the mechanism to hold it to the backing bar. In particular the bending of unsupported parts of the specimen (e.g. corners of the plate) seems to cause early failure. Additionally, the layer of grease used to hold the target damps the force transmitted to the backing bar, affecting the measurements (Section 3.3.4).

# 4 MICROSTRUCTURAL MODELLING

The development of detailed models of response mechanisms at the micro-scale is key to improve the understating of ceramic materials, providing physically meaningful information on deformation and damaging mechanisms, particularly in the scarcity of detailed experimental data due to the difficulties in the experimental characterization of the material at the grain scale.

The currently available computational power, however, is still too limited to allow for the simulation of the microstructural behaviour of macroscopic specimens. Nevertheless the quantitative information gathered from the simulations at the grain level is an extremely important input for the correct modelling of ceramic material, in a multi-scale approach.

In this chapter a methodology for the modelling of deformation and failure of ceramic materials at the microstructural scale is presented. In particular, the numerical work presented focuses mainly on the simulation of the behaviour of polycrystalline $\alpha$-Alumina, $Al_2O_3$ (alumina). The main motivations for this choice are its extremely wide range of applications, the availability of numerous and consistent measurements of the properties of the single crystal in literature, and the limited anisotropy of the single crystal, that allows for relatively small RVE (Representative Volume Elements).

First a method for the generation of virtual topology statistically representative of real polycrystalline microstructures is presented (Section 4.1), then the procedure to build FE models from the so-generated geometries is illustrated in Section 4.2. Several simulations of quasi-static deformation and failure of the microstructure are presented in Section 4.3, alongside the validation of the results against both analytical solutions and experimental measurements described in Section 3.1. Finally dynamic deformation and failure (due to both inter- and trans-granular crack propagation) of ceramic are presented in Section 4.4 and 4.5.

## 4.1 Generation of virtual microstructures

The ability to produce statistically representative models of real polycrystalline microstructures is crucial for the correct simulation of both the elastic behaviour and the failure mechanisms of real ceramic materials at the grain scale.

In this section, first a methodology for generating arbitrarily shaped polycrystalline microstructures based on Voronoi tessellation is presented, and then the flexibility offered by the methodology developed, both in terms of reproducible morphology and texture properties, of the grains is illustrated.

### *4.1.1 Generation of arbitrarily shaped polycrystalline aggregates*

As presented in Section 2.3.1, Voronoi tessellations are particularly suitable to model polycrystalline materials, giving a good statistical representation of real microstructures with a numerical discretization describable analytically with simple features (i.e. planar faces and linear edges).

In particular the methodology presented in this thesis is based on the so-called "Hardcore-Voronoi" tessellation that can be expressed mathematically as:

$$\{R_P\} = \{\boldsymbol{x} \in R^3 | d(\boldsymbol{P_i}, \boldsymbol{x}) \leq d(\boldsymbol{P_k}, \boldsymbol{x}), k = 1,2, \dots, N : k \neq i\} \tag{30}$$

$$\left|\boldsymbol{P_i} - \boldsymbol{P_j}\right| > \rho_H \; \forall i, j = 1,2, \dots, N : i \neq j \tag{31}$$

Eq. (30) states the classic Voronoi tessellation for which the generic *cell* $\{R_P\}$ consists of all the points closer to the i-th *nucleus* ($P_i$) than to any other nucleus.

Eq. (31), instead, expresses the Hardcore assumption that imposes a minimum distance $\rho_H$ in between the nuclei. The main effects of the Hardcore assumption are to reduce the number of the small cells and to regularise the shape of the grains, hence improving the quality of the FE models of the microstructure.

*Voronoi tessellation statistics*

The geometrical properties of the so-generated cells can be expressed in terms of distributions of "equivalent radius" and of "number of first neighbours" (i.e. number of faces) of the cells.

These two parameters are used to explore the effect of $\rho_H$ in the isotropic Hardcore assumption upon the morphology of the structure (Fig. 4.1). The curves are also compared with other (regular) discretization techniques proposed in literature (i.e. cubes [63], dodecahedra [64], truncated octahedra [65]) and real polycrystalline structures (i.e. Al-Sn [69], and $\beta$-Titanium alloy [131]).

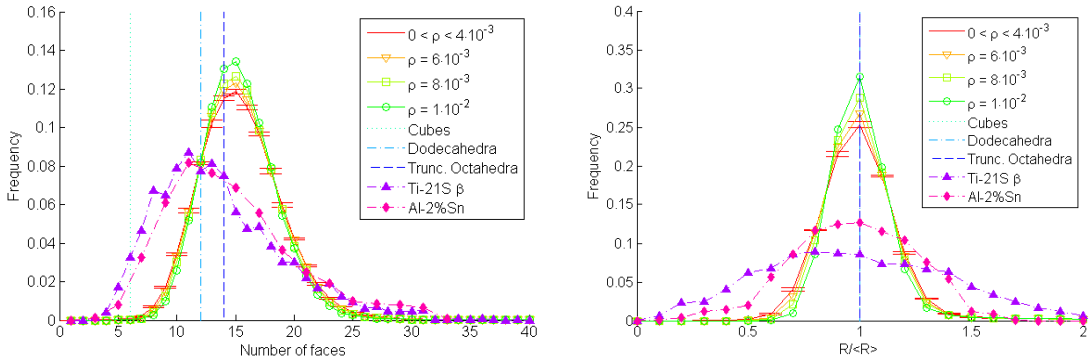



**Fig. 4.1:** Distributions of the number of faces (left) and normalised grain radius (right) of different tessellations and real polycrystalline structures

The solid lines in Fig. 4.1 represent the number of faces and the grain radius distributions of a tessellation with $10^5$ grains of a cubic domain with unit edge length. The isotropic "Hardcore" assumption slightly affects the distribution of the number of first neighbours, whilst the reduction of the small entities (i.e. cells with small radius) with the increasing of $\rho_H$, and the contemporary increasing of the number of average-size cells, is more pronounced. Despite those variations, the Hardcore Voronoi tessellation is still able to qualitatively reproduce the first-order properties of real polycrystalline morphologies.

*Nuclei seeding procedure*

Contrary to most of the techniques developed to generate aggregate microstructures from Voronoi tessellations (e.g. [85], [86], [132]), the method presented in this thesis does not impose the shape of the polycrystalline domain a-priori, allowing the cells to grow unconfined. The final shape of the structure is obtained cutting the cells with planes and surfaces that carve the unconfined cells mimicking the real machining procedure.

Theoretically the seeding volume can consist of the whole three-dimensional space. However reducing the size of the seeding domain (and consequently the number of nuclei) reduces substantially the computational cost of the tessellation procedure.

Since the domain in which the nuclei are seeded does not affect the final shape of the structure, it is defined as a volume big enough to contain the desired structure, thereby avoiding border effects. For sake of simplicity in this thesis it is defined as a boxed volume (Fig. 4.2), even if, theoretically, it can assume any possible shape.

The first $(N-8)$ nuclei are positioned arbitrarily – following the "Hardcore" assumption – inside the seeding domain (crosses in Fig. 4.2), whilst the last 8 nodes are located in correspondence of the vertices of the box (circles in Fig. 4.2).

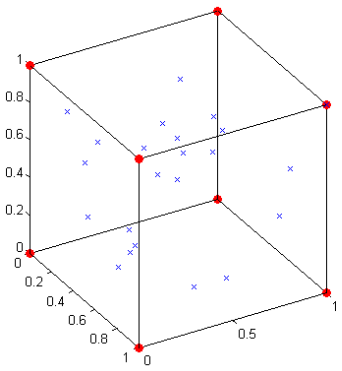



**Fig. 4.2:** Random distribution of nuclei in a cubic seeding volume, and additional nuclei on the vertices

The addition of the nuclei on the vertices of the domain ensures that the cells belonging to the internal nuclei are all bounded (i.e. the volume of the cells is finite). The

cells generated from the external nuclei, instead, are unbounded and need the addition of an extra node to bind them. In particular the extra node is positioned coinciding with the nucleus itself, to ensure the convexity of the cell.

The discretization is performed with the standard Voronoi approach, whilst the connectivity of the nodes to define the polygonal faces is defined with an algorithm inspired by the "minConvexHull" code (part of the "geom3d" library by Legland [133]).

The cells generated grow unconfined – but bounded – hence the tessellation decomposes the whole seeding domain and a portion of the surrounding space. The final shape of the domain is obtained first cropping such aggregate along arbitrarily oriented planes, and then – if required – performing concave cuts on the convex domain.

*Convex cropping*

The cropping method suggested in this thesis mimics the outcome of real cutting along a plane. The procedure developed to crop a cell by intersection with an arbitrarily oriented plane (Fig. 4.3) can be outlined as follows:

1) Detect the nodes "outside" the cropping plane (red circle).
2) Determine the nodes connected to each of the previously detected "external" nodes (red asterisks).
3) Find the intersection of the edges connecting the external and internal nodes (detected in steps 1 and 2) with the cropping plane (blue crosses).
4) Redefine the faces intersecting the cutting plane by erasing the external nodes and adding the nodes created in step 3.
5) Create a new face with the nodes projected on the cropping plane (green face).
6) Erase the potential degenerated faces and grains.

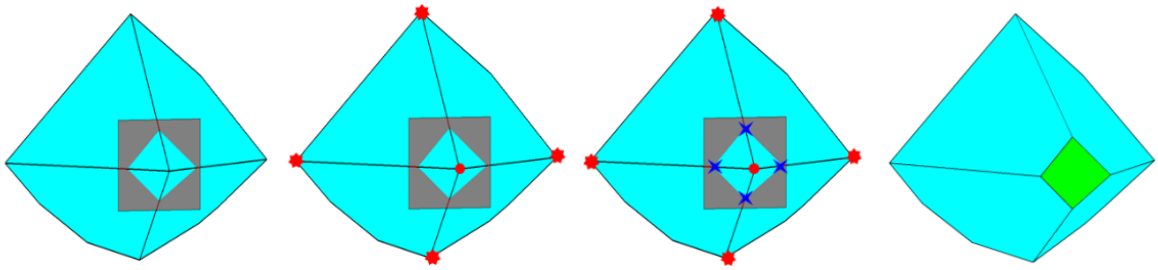


**Fig. 4.3:** Procedure to cut the grain

The repetition of this procedure for all the cells and all the cropping planes results in the complete decomposition of the desired convex solid shape with Voronoi cells, topologically representative of the section of a real polycrystalline microstructure

The cropping operations may generate duplicate entities (both nodes and faces). Their removal is necessary to avoid errors in the further special discretisation procedures. Moreover the cropped structure may exhibit very small edges (i.e. nodes very close to each other), which, if not removed, would lead to either distorted or extremely small elements.

The identification and removal procedures can be highly demanding in terms of computational time, therefore it has to be addressed carefully. In the method presented the detection of the nodes closer than a certain threshold value ($\rho_P$) is performed on an indexed list. If a node is found too close to a previous one it is eliminated and the indices shifted. Finally the eventual duplicated surfaces are eliminated.

Since there is no theoretical limit to the number, the position, and the orientation of the cropping plane, the method presented allows for the generation of any desired convex shape delimited by planar surfaces. Fig. 4.4 shows some examples of the obtainable geometries.

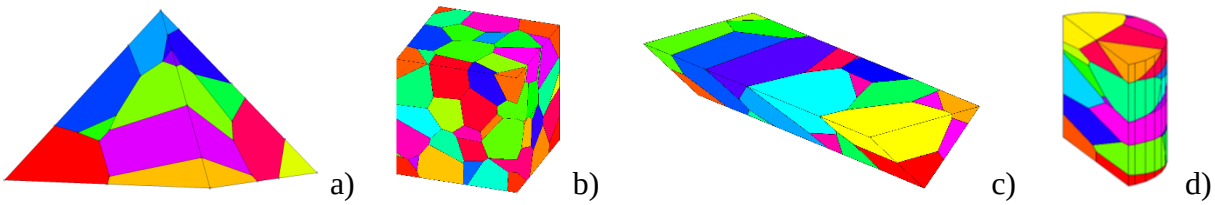



**Fig. 4.4:** Examples of solid shapes: cube (a), pyramid (b), triangular prism (c), and half-cylinder (d)

*Concave cutting*

To extend the capability of the proposed method to generate also concave geometries an additional procedure to perform cuts along planar surfaces is implemented.

The procedure consists of splitting the desired concave shape into multiple convex subdomains, which are successively merged together, thus eliminating the extra nodes and faces on the temporary cutting planes, as illustrated in Fig. 4.5, in which a triangular cut (i.e. orange lines) is made to a rectangular cell aggregate.

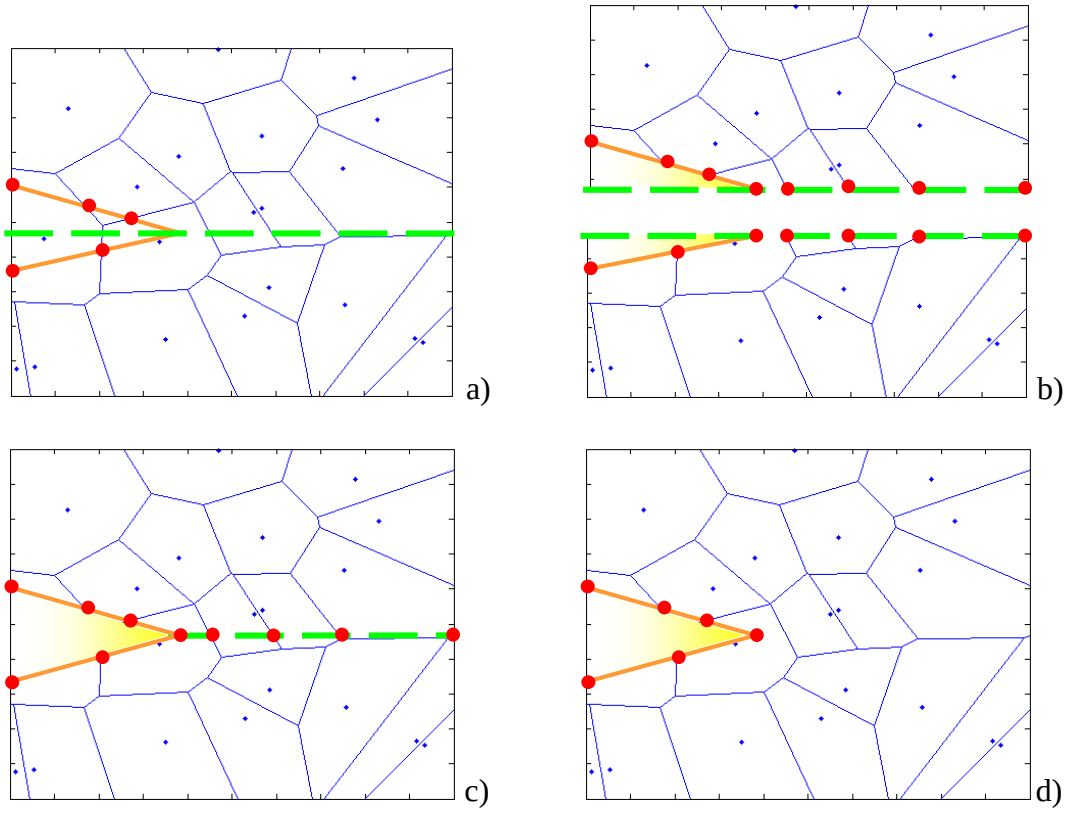



**Fig. 4.5:** Cutting of a concave domain

The (concave) notched plate is split into two convex subdomains delimited by the "permanent" and the "temporary" cutting planes, respectively illustrated by the solid orange and the dashed green lines (Fig. 4.5b). The subdomains are cropped following the procedure illustrated in the previous section, and subsequently merged together (Fig. 4.5c), eliminating the extra nodes and unrequired faces (Fig. 4.5d).

Five different scenarios can be encountered in the process of merging the part of the single cells belonging to two separate subdomains:

- The cell is crossed only by one permanent cutting plane.
- The cell is crossed only by multiple permanent cutting planes.
- The cell is crossed only by one temporary cutting plane.
- The cell is crossed both by temporary and permanent cutting planes.
- Neither temporary nor permanent cutting planes affect the cell.

Whilst in the first case no additional procedure is required after the cropping of the cell, the presence of multiple permanent cutting planes crossing a single cell indicates that the cell is split into multiple volumes. The spatial discretisation of each of those volumes is performed separately, but they are still considered as a single grain in terms of properties in the final FE model.

Conversely, if the cell is crossed by only a temporary cut, the faces split by the cutting plane are merged together, whilst the faces and the nodes lying on the cutting plane are deleted.

Finally, the crossing of both a temporary and a permanent cutting plane makes a cell concave. The faces split by the temporary cutting plane are merged together, whilst the faces and nodes lying on the temporary cutting plane are deleted, excluding the nodes in common with the permanent cutting planes (i.e. the notch tip in Fig. 4.5d).

To create concave geometries with more than two permanent cutting surfaces a temporary cutting plane per each additional face of the concave cut is added (see Fig. 4.6 for three and four faces concave cuts).

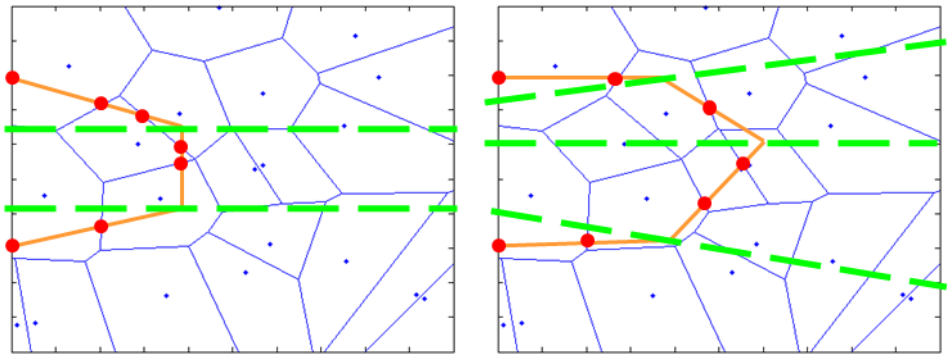


**Fig. 4.6:** Cutting of a concave domain with three (left) and four (right) faces

Repeating the procedure illustrated per each temporary cutting plane (and the two permanent cutting planes related) allows the generation of any desired concave cut. The procedure can be applied as many times as needed, in order to generate a domain with multiple concave cuts.

Combining the convex cropping method presented in the previous section with the concave cutting procedure the unconfined Voronoi tessellation can be "machined" in any possible shape. Some examples of obtainable geometries are shown in Fig. 4.7:

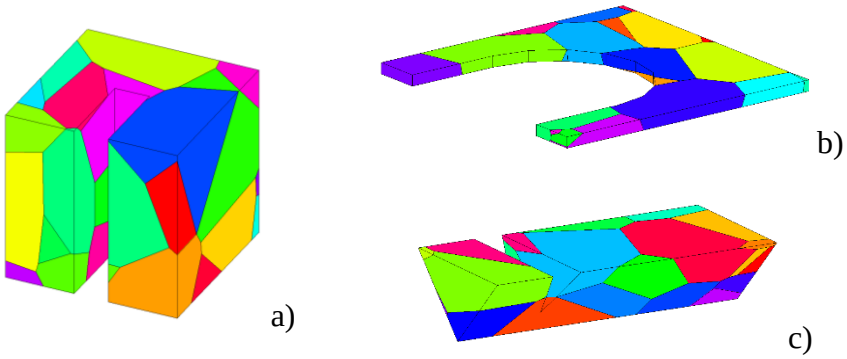



**Fig. 4.7:** Examples of concave shapes: cube with rectangular notch (a), plate with semi-circular slot (b), triangular prism with triangular notch (c)

In the structures represented in Fig. 4.7 each colour represents a single grain, highlighting the capability of the cutting method to split a single grain into two different volumes, still considering them as a single entity.

### *4.1.2 Definition of morphology and texture properties*

Among all the properties of the microstructure, the correct reproduction of morphology (i.e. shape of the grains) and texture (i.e. crystallographic orientation) is particularly important, because they are first order properties, thus strongly influencing the mechanical properties of polycrystalline materials.

The ability to model these properties increases the capability of the method developed to reproduce a wider range of materials, providing the capability to explore the effect of various manufacturing and machining processes (that affect the microstructure) on the mechanical properties of the material.

*Morphology*

The hypotheses of uniform grain growth at the base of the interpretation of Hardcore Voronoi tessellation in terms of polycrystalline ceramic microstructure (as presented by Boots [119]) limits the modelling of real polycrystalline microstructures, since the presence of elongated grains has been experimentally observed in numerous metallurgical and ceramic microstructures [134]. The non-uniformity of the grains can be linked to manufacturing processes such as sintering [135] or rolling [136] (for metals).

For ceramic materials the presence of elongated grains often results in noticeable differences in the mechanical properties. For alumina, for example, has been observed that the presence of elongated grains increases the strength and the fracture toughness of the material, and that the alignment of the grains enhances this effect [137].

In this work two methods are proposed to reproduce the presence of aligned elongated grains. The first consists of an extension of the “Hardcore” assumption affecting the nuclei seeding procedure, whilst the second is a geometrical transformation of the cells.

The extension of the "standard" Hardcore assumption presented in Eq. (32) imposes separate Hardcore radii in three orthogonal directions, hence allowing for the generation of elongated cells. The distance between the nuclei in the standard Hardcore assumption, presented in Eq. (31), can be expressed explicitly as:

$$\left|\boldsymbol{P_i} - \boldsymbol{P_j}\right| > \rho_H \Rightarrow \sqrt{\left(P_{ix} - P_{jx}\right)^2 - \left(P_{iy} - P_{jy}\right)^2 - \left(P_{iz} - P_{jz}\right)^2} > \rho_H \tag{32}$$

Introducing three factors $(H_1, H_2, H_3)$ multiplying the differences between the coordinates, Eq. (32) becomes:

$$\sqrt{H_1 \cdot \left(P_{ix} - P_{jx}\right)^2 - H_2 \cdot \left(P_{iy} - P_{jy}\right)^2 - H_3 \cdot \left(P_{iz} - P_{jz}\right)^2} > \rho_H \tag{33}$$

These three new constants extend the Hardcore assumption defining an ellipsoid around each nucleus in which no other nucleus is allowed, Fig. 4.8.

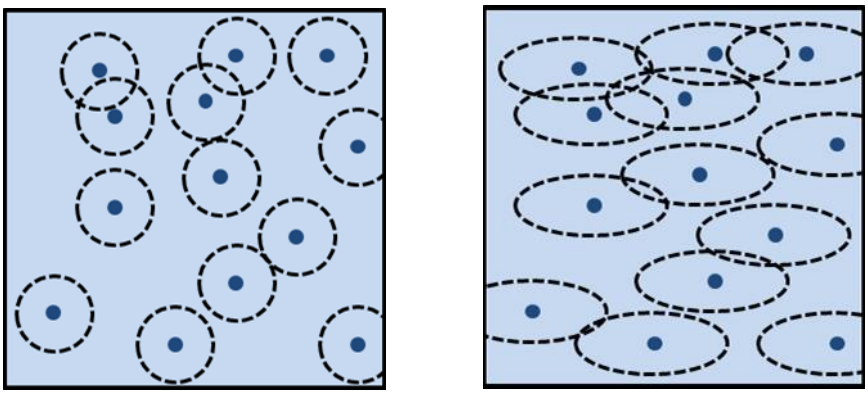


**Fig. 4.8:** Comparison of the "isotropic" (left) and the "extended" (right) Hardcore assumptions

Evidently – as illustrated by Fig. 4.8 – the particular equivalence: $H_1 = H_2 = H_3 = 1$ corresponds to the standard (i.e. isotropic) Hardcore assumption, reducing the ellipsoid into a sphere.

The effect of the extended Hardcore assumption is visually illustrated in the structures presented in Fig. 4.9, in which the top of view of two three-dimensional tessellations of a square plate - one performed with the isotropic Hardcore assumption (Fig. 4.9a) and the other with the extended Hardcore assumption (Fig. 4.9b) imposing $H_1 = 0.25$ – are presented.

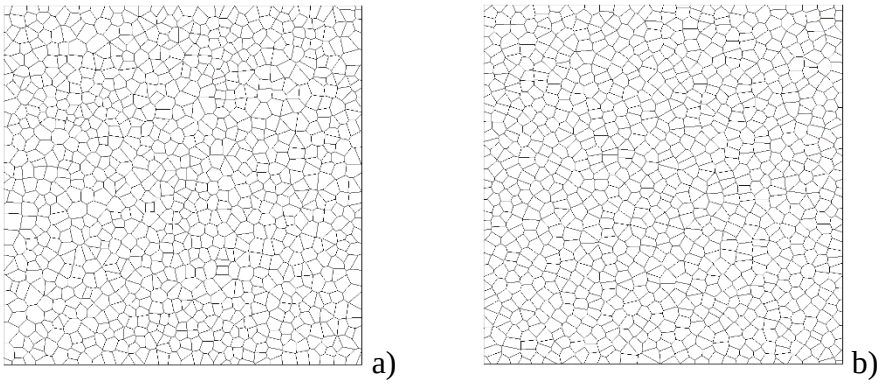



**Fig. 4.9:** Comparison of 1000 grains structures with "isotropic" (left) and extended (right) Hardcore assumptions

The value of $\rho_H$ is the same for both the structures, showing how the approach proposed allows the modification of the tessellation properties, stretching the cells in a specified direction without losing the advantages of the Hardcore assumption (i.e. absence of small and/or highly irregular cells).

The effect of the isotropic and extended Hardcore assumptions are quantified in terms of size, number of faces, and aspect ratio of the grains as shown in Fig. 4.10:

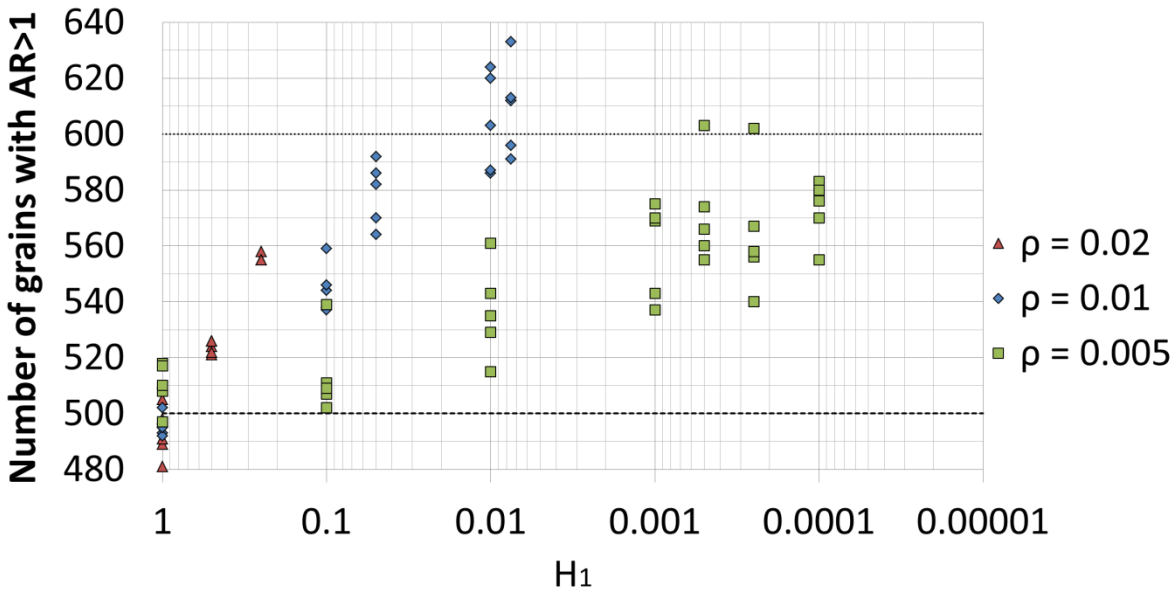



**Fig. 4.10:** Variation of the aspect ratio (AR) distribution with both $\boldsymbol{H_1}$ and $\boldsymbol{\rho}$

A parametrical study of the tessellations of a 1000 grains square plate with unitary side length (and thickness 100 times smaller), varying both the Hardcore radius $\rho_H$ and the parameter $H_1$ defined in Eq. (33) (whilst $H_2 = H_3 = 1$), is performed.

The graph in Fig. 4.10 summarises the results of the parametrical study, reporting on the vertical axis the number of grains with an aspect ratio ($AR$) bigger than 1 (i.e. the maximum distance between nodes along the direction of $H_1$ is bigger than the one along the direction of $H_2$), and on the horizontal axis the relative value of $H_1$. For each combination of Hardcore radius and $H_1$, 5 structures are generated to verify the statistical variability of the results.

For the isotropic Hardcore assumption ($H_1 = 1$) half the grains ($500 \pm 20$) exhibit $AR > 1$ for all the three Hardcore radii analysed. Decreasing $H_1$ the number of grains with $AR > 1$ increases noticeably, with a rate that depends on the Hardcore radius. The minimum possible values of $H_1$ for the different $\rho_H$ are determined by the maximum possible dimension of the Hardcore volumes that can fit in the domain.

Within the combinations analysed, the most effective result stretches on average $\sim 61\%$ of the grains (with a top value of more than 63%) along the direction of $H_1$, showing the ability of the proposed extended Hardcore approach in controlling the statistical properties of the virtual aggregate to fit to the required characteristic of the aggregate to be simulated. The distributions of grain size and number of first neighbours, instead, seem to be only marginally affected by the variation of the value $H_1$.

If a more pronounced elongation of the grain shape is required an additional technique has been implemented to stretch the grains in the desired directions after the tessellation has been performed. The procedure consists of translating the nodes of the tessellation along arbitrary directions, stretching the cells indefinitely.

The effects of this procedure are illustrated in Fig. 4.11:

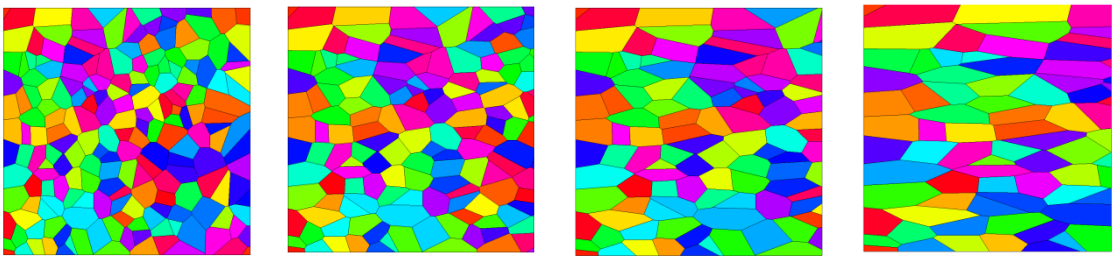


**Fig. 4.11:** Stretching of the tessellation (left) by 50%, 100%, and 200% (left to right) in the horizontal direction

The aggregate in Fig. 4.11 (left) is stretched first by 50%, then by 100%, and finally by 200%. The stretching procedure manipulates the cells after their generation, without modifying the connectivity of the nodes, hence keeping the distribution of first neighbours absolutely identical. The distribution of grain size, instead, is affected by the directionality of this procedure, generally broadening the bell shape curve of the kind presented in Fig. 4.1. However the effect is comparable to the statistical variance of the results, and therefore considered of second order.

*Texture*

Aiming to validate the numerical methodology developed against the experimental results presented in Section 3.1, the numerical work presented in this chapter focuses mainly on the simulation of the behaviour of polycrystalline $\alpha$-Alumina, $Al_2O_3$ (alumina).

The symmetries of alumina crystals – trigonal structure of class $(\bar{3}m)$ – presented in Section 2.1.3 are implemented in the numerical models by defining the stiffness tensor of the single grain, which can be expressed as:

$$\begin{Bmatrix} \sigma_{xx} \\ \sigma_{yy} \\ \sigma_{zz} \\ \sigma_{yz} \\ \sigma_{zx} \\ \sigma_{xy} \end{Bmatrix} = \begin{bmatrix} C_{11} & C_{12} & C_{13} & C_{14} & 0 & 0 \\ C_{12} & C_{11} & C_{13} & -C_{14} & 0 & 0 \\ C_{13} & C_{13} & C_{33} & 0 & 0 & 0 \\ C_{14} & -C_{14} & 0 & C_{44} & 0 & 0 \\ 0 & 0 & 0 & 0 & C_{44} & C_{14} \\ 0 & 0 & 0 & 0 & C_{14} & C_{66} \end{bmatrix} \begin{Bmatrix} \varepsilon_{xx} \\ \varepsilon_{yy} \\ \varepsilon_{zz} \\ \varepsilon_{yz} \\ \varepsilon_{zx} \\ \varepsilon_{xy} \end{Bmatrix} \tag{34}$$

where $C_{66} = 0.5 \cdot (C_{11} - C_{12})$ [8].

The experimental tests on polycrystalline alumina presented in Section 3 are all performed on specimens exhibiting a very weak – if any – texture (i.e. the crystallographic orientations seem to be fairly random). To reproduce this condition in the numerical models, a randomly oriented coordinate system is assigned to each grain, indicating the crystal orientation.

The information on the texture of a polycrystalline specimen can be represented with the *pole figures* like the ones presented in Fig. 4.12.

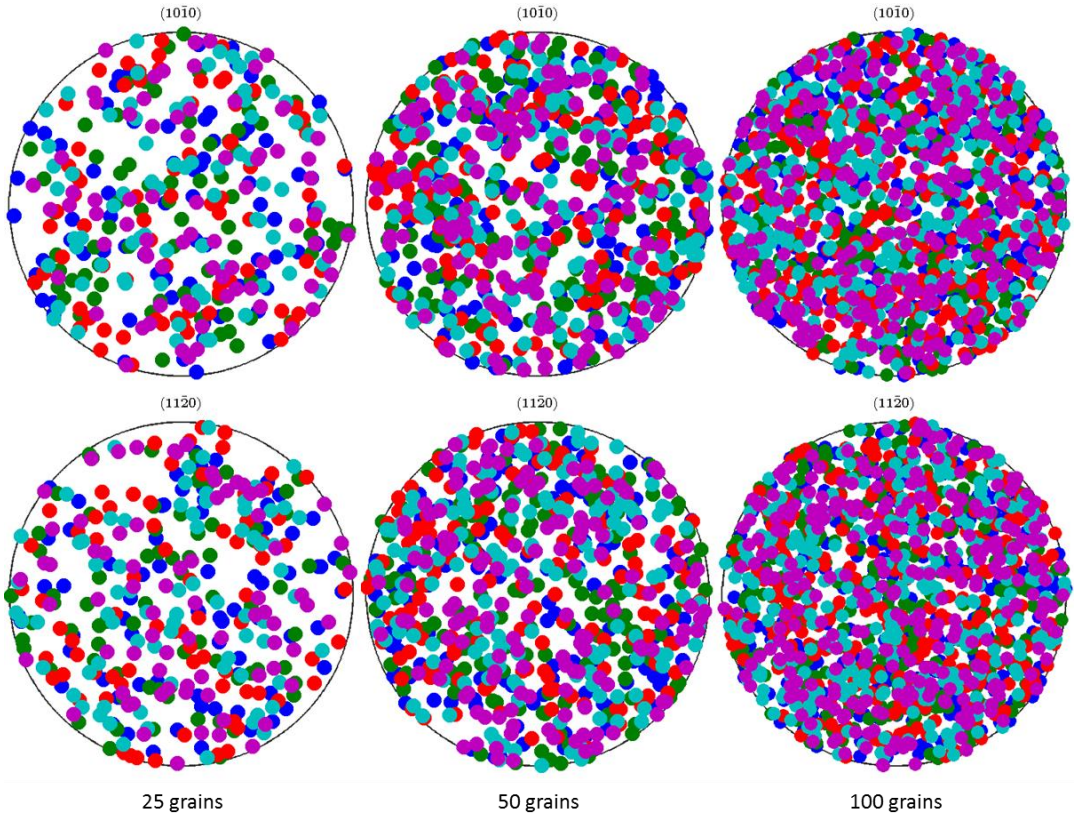



**Fig. 4.12:** Pole figures representing the grain orientation of three sets of specimens

Fig. 4.12, in particular, shows the crystallographic orientation of three sets of models, consisting respectively of 25 (left), 50 (centre), and 100 (right) grains. In each pole figure are reported 5 different textures related to the same grain morphology, showing the consistent randomness of the orientations. The models presented correspond to three of the morphologies analysed in Section 4.3.1.

## 4.2 Finite Elements model

This section describes the procedure adopted to create the Finite Elements (FE) model of the polycrystalline topologies generated with the method presented in the previous section. The grains are meshed singularly, and then they are assembled together allowing for the insertion of interface entities on the grain boundaries.

With this approach the grains are defined as separate domains with individual material properties, to allow for the reproduction of the multiple crystallographic orientations of the type presented in Fig. 4.13. The interface elements on the grain boundaries permit to simulate the initiation and propagation of inter-granular cracks.

Firstly the technique adopted for meshing the grains is illustrated in Section 4.2.1, then in Section 4.2.2 the derivation of the material properties to describe the elastic behaviour of the single crystal of $\alpha$-Alumina is presented, and finally in Section 4.2.3 the procedure to assemble the grains and the definition of the interface entities are reported.

### *4.2.1 Meshing procedure*

The meshing of the single grain is performed adopting the widely utilised "bottom-up procedure". It consists of discretising – in order – vertices, edges, faces, and cells (i.e. 0D, 1D, 2D and 3D entities), with the *n*-D mesh generation constrained by the (*n*-1)-D mesh and the element lengths interpolated from it.

The 0D meshing consists of attributing to each vertex a characteristic length. Such lengths determine the size of the 1D elements that discretise the edges that, in turn, determine the size of the 2D elements that discretise the faces, which, finally, are the base for the three-dimensional meshing of the whole domain.

The randomness at the base of the process developed to generate the grain geometry leads to faces and cells with irregular geometries. Even adopting the Hardcore approach, such

irregularity prevents the use of quadrilateral and hexahedral elements to discretise respectively faces and cells despite them being widely recognised to provide more accurate results compared to other type of elements [138]. The triangular and tetrahedral elements, instead, are able to discretise not-regular geometries without suffering an extreme grade of distortion, but in their linear form may provide largely uncorrected results under some loading conditions (e.g. bending) due to the widely known *locking* mechanism.

To provide accurate results without forcing the elements to undergo an excessive grade of distortion, quadratic triangular and tetrahedral elements (i.e. elements with additional nodes at the middle of the edges) are introduced. Such elements are proven to combine the versatility in meshing complex structures (i.e. limited element distortion) with good results, introducing, in most cases, an increase in the computational cost [138].

Finally, the algorithm implemented retains the possibility of meshing with either linear or quadratic tetrahedral elements, because for some loading conditions (e.g. pure tension) the use of linear tetrahedral elements reduces the computational cost without affecting the accuracy of the simulations.

The meshing libraries from the GMSH package are used to perform all the meshing steps of the bottom-up procedure [139].

### *4.2.2 Bulk properties of the grains*

The material models are assigned separately to every single grain, each of which is modelled as a fully anisotropic linear elastic domain with arbitrary crystallographic orientation. As illustrated in Section 2.1.1, the plastic deformation of the grains has been observed to be a second order effect for alumina, hence justifying the focus of this thesis on the elastic-brittle behaviour of the material.

The constitutive relation of the material is expressed through Hooke's law, written using the compact Voigt notation:

$$\sigma_i = C_{ij}\varepsilon_j \tag{35}$$

Alumina is a hard brittle material with a hexagonal-rhombohedral structure, and – as presented in Section 2.1.3 – its properties depend on the crystallographic orientation [140]. In particular, alumina crystal has a trigonal structure of class ($\bar{3}m$), and its stiffness matrix – using symmetry considerations to reduce the number of independent constants $C_{ij}$ – can be expressed as:

$$\begin{Bmatrix} \sigma_{xx} \\ \sigma_{yy} \\ \sigma_{zz} \\ \sigma_{yz} \\ \sigma_{zx} \\ \sigma_{xy} \end{Bmatrix} = \begin{bmatrix} C_{11} & C_{12} & C_{13} & C_{14} & 0 & 0 \\ C_{12} & C_{11} & C_{13} & -C_{14} & 0 & 0 \\ C_{13} & C_{13} & C_{33} & 0 & 0 & 0 \\ C_{14} & -C_{14} & 0 & C_{44} & 0 & 0 \\ 0 & 0 & 0 & 0 & C_{44} & C_{14} \\ 0 & 0 & 0 & 0 & C_{14} & C_{66} \end{bmatrix} \begin{Bmatrix} \varepsilon_{xx} \\ \varepsilon_{yy} \\ \varepsilon_{zz} \\ \varepsilon_{yz} \\ \varepsilon_{zx} \\ \varepsilon_{xy} \end{Bmatrix} \tag{36}$$

where $C_{66} = 0.5 \cdot (C_{11} - C_{12})$ [8].

The crystal has only six independent elastic constants, and – despite its three-fold symmetry – is not orthotropic. Many authors have experimentally measured the components of the stiffness (and compliance) tensors, and the values are quite consistent in the literature (e.g. [27, 28, 141]).

In Table 4.1 the values used to define the stiffness and the compliance matrices of the models presented in this work (measured by Hovis et al. [28]) are reported, and the maximum difference from the values measured in the other publications cited [27, 141].

The crystallographic orientation of the grain is imposed assigning a randomly oriented local coordinate system to each grain, whose axes coincide with the principal direction of the stiffness matrix defined in Eq. (36).

| | $GPa$ | | $10^{-11}Pa^{-1}$ |
|---|---|---|---|
| $C_{11}$ | 497 ($\pm^{0.6}_{0.0}$) | $S_{11}$ | 2.35 |
| $C_{12}$ | 163 ($\pm^{0.6}_{0.3}$) | $S_{12}$ | -0.70 |
| $C_{13}$ | 116 ($\pm^{1.2}_{0.5}$) | $S_{13}$ | -0.38 |
| $C_{14}$[3] | 22 ($\pm^{0.9}_{0.0}$) | $S_{14}$ | -0.48 |
| $C_{33}$ | 501 ($\pm^{2.3}_{0.0}$) | $S_{33}$ | 2.16 |
| $C_{44}$ | 147 ($\pm^{0.4}_{0.0}$) | $S_{44}$ | 6.93 |

**Table 4.1:** Non-zero terms of the stiffness (**C**) and compliance (**S**) matrices for $\boldsymbol{\alpha}$-$\boldsymbol{Al_2O_3}$

### *4.2.3 Definition of the grain boundaries and assembly of the structure*

Alumina exhibits predominantly inter-granular fracture mode because of the noticeable difference in strength between the grain boundaries and the grains themselves. In particular the experimental work performed by A. Norton (and partially presented in this thesis) suggests that the grain of alumina exhibit a value of toughness about 2.5 times higher than the grain boundaries [126].

Since the possible crack paths are known a-priori (i.e. grain boundaries), the de-bonding approach introduced in Section 2.3.3 can be adopted to accurately simulate the crack propagation mechanisms observed in polycrystalline alumina by inserting interface elements on the grain boundaries. In order to allow for the insertion of such interface entities the grains – that are meshed separately following the procedure illustrated in Section 4.2.1 – are assembled together in the final structure after a procedure of homogenization of the 2D meshes on the coincident faces.

[3] The sign of $C_{14}$ has been long disputed, and only recently accepted as positive, therefore only the magnitude of $C_{14}$ is compared with the other measurements in literature.

The homogenization procedure consists of imposing the same bi-dimensional special discretisation of the coincident faces of two neighbour grains. It is achieved by comparing the position of the nodes on the coupled faces and – if any mismatch is found – adjusting their coordinates to make them coincident. The imposition of the same 0D, 1D, and 2D element length on two geometrically identical surfaces, generally guarantees an initial good level of matching of the meshes. However any excessive displacement of the nodes during the homogenization procedure that may distort the 3D elements is carefully monitored and avoided.

Once the spatial discretisation of the coincident faces are homogenised, the three-dimensional mesh of the grains is performed, the material properties are assigned to each crystal, and the grains are assembled together to construct the FE model of the microstructure.

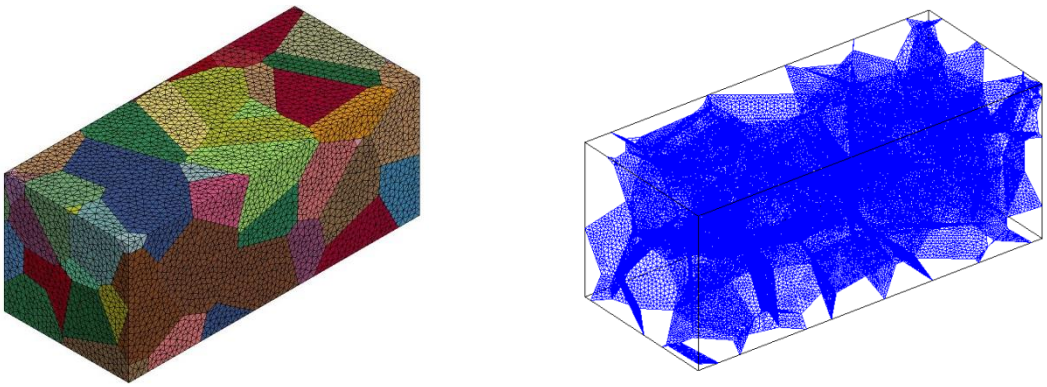


**Fig. 4.14:** FE model (left) and element faces on the grain boundaries (right)

The models built to predict the elastic behaviour of the polycrystalline aggregate (Section 4.3.1 and 4.3.2) are generated merging the nodes on the grain boundaries, therefore eliminating any possibility of simulating the failure of the structure.

The models presented in Sections 4.3.3, 4.4.1, and 4.4.2, instead, are built inserting "tie-break" contacts across all the grain boundaries. The "tie-break" contacts adopted in this work bind together the coincident faces of the generic elements $i$ and $j$ across a grain boundary ($\Gamma_{ij}$), until the normal ($\sigma_N$) and the tangential ($\sigma_T$) stresses satisfy the condition:

$$\left(\frac{\sigma_N}{S_N}\right)^2 + \left(\frac{\sigma_T}{S_T}\right)^2 = 1 \tag{37}$$

The normal and the tangential stresses are normalised respectively with respect to the tensile ($S_N$) and the tangential ($S_T$) failure strengths. After the failure the interface loses the ability to carry any tensile load (i.e. the elements linked to that contact are de-bonded), and a no-interpenetration condition is imposed to the free faces (i.e. the contact becomes a standard surface-to-surface contact).

These conditions can be summarised analytically as:

$$\begin{cases} t_N \leq 0 & \forall x \in \Gamma_{ij} \\ [\![u]\!]^{ij} \geq 0 & \forall x \in \Gamma_{ij} \\ [\![u]\!]^{ij} \cdot t_N = 0 & \forall x \in \Gamma_{ij} \end{cases} \tag{38}$$

The first and second equations impose respectively the loss of ability of carrying tension the absence of interpenetration on the interface. The third relation identifies the two possible cases: *contact*, with null displacement jump ($[\![u]\!]^{ij}$) and negative reaction force ($t_N$), or *detached*, with positive jump displacement and no reaction force.

The values of $S_N$ and $S_T$ are evaluated from measurements of the grain boundary toughness performed with micro-cantilever beam tests (carried out by Andrew Norton, Materials Department, University of Oxford) as described in Section 3.1. The tensile failure stress is imposed to be $S_N = 5GPa$, whilst the effect of the shear stress is considered to be negligible (i.e. $S_T \gg S_N$).

Finally – despite the marked inclination of alumina to fail along the grain boundaries – the simulations presented in Section 4.5 explore the combination of trans- and inter-granular failure mechanisms of the polycrystalline structure. The inter-granular crack propagation is modelled with the insertion of the tie-break contact on the grain boundaries, whilst the trans-granular cracks are generated with the element deletion technique with a local stress-based erosion (LSE) criterion. This criterion imposes the instant deletion of the element that reaches

a certain effective stress $\sigma_C = 12GPa$. As for the values of $S_N$ and $S_T$, $\sigma_C$ is evaluated from micro-cantilever tests.

## 4.3 Simulation and validation of quasi-static deformation and failure

The methodology developed is then used to generate numerical models of several polycrystalline microstructures, aiming to reproduce the elastic deformation and the failure of alumina microstructures.

First (Section 4.3.1) cubic models consisting of different number of grains are generated to explore the definition of representative volume elements (RVE) for the prediction of the elastic properties of the structure. The results are then compared against macroscopic experimental measurements, showing a very good agreement.

Secondly (Section 4.3.2) the effect of the grain texture on the stress localisation at the crack tip is analysed by creating polycrystalline plates with a sharp triangular notch. The stress intensity factor predicted with the model with anisotropic grains is compared against the analytical results (for isotropic grains) showing the noticeable influence of the grain texture on the magnitude of the stress and of the opening displacement of the crack.

Finally (Section 4.3.3) the micro-cantilever test presented in Section 3.1 is modelled and the numerical results are validated against experimental measurements.

### *4.3.1 Evaluation of the Young's modulus of a polycrystalline aggregate*

Given a polycrystalline structure subjected to uniaxial traction – under the assumption of purely elastic deformation of the grains and total absence of cracks – simplified relations to calculate the isotropic elastic moduli (i.e. Young's Modulus and Poisson's Ratio) of the aggregate can be obtained from the uniaxial formulation of Hooke's law, as follows:

$$E = \frac{\bar{\sigma}_1}{\bar{\varepsilon}_1}; \qquad \nu = -\frac{\bar{\varepsilon}_2}{\bar{\varepsilon}_1} = -\frac{\bar{\varepsilon}_3}{\bar{\varepsilon}_1}; \tag{39}$$

The Young's modulus $E$ is calculated as the ratio of the average stress to the average strain in the direction of the external load (respectively $\bar{\sigma}_1$ and $\bar{\varepsilon}_1$). The Poisson Ratio $\nu$, instead, is calculated as the ratio between the strain in the directions perpendicular to the load ($\bar{\varepsilon}_2$ or $\bar{\varepsilon}_3$) and the average strain in the direction of the load.

Since the considered volumes of material consist of a finite number of grains, apparent and effective properties – that theoretically coincide only when the number of grains approaches infinity [142] – have to be distinguished. However, it is possible to define a RVE as a structure with a finite number of grains, whose apparent properties can be considered to be equal to the effective properties of the material, within a certain tolerance.

Numerous authors have investigated the determination of RVE for polycrystalline materials, and it has been shown that the number of grains that define an RVE is proportional to the anisotropy of the material [143, 144]. Specifically Nygards [145] found a roughly linear dependence between the anisotropy of the single crystal (expressed as the Zener ratio [146]) and the size of the RVE for polycrystalline materials with cubic symmetry. For materials exhibiting such symmetry combined with a reduced anisotropy – as for example gold, nickel, or copper – 20 grains are enough to define a RVE that predicts the elastic properties with an error of less than 10% [73, 143].

Since alumina crystals also have limited anisotropy, but with a trigonal structure, the RVEs defined to predict the elastic properties of polycrystalline alumina are imposed to consist of at least 25 grains. In particular, to explore the influence of the number of grains on the predicted results three sets of cubic aggregates are generated, consisting of 25, 50, and 100 grains ($n_{gr}$), with constant average grain size $\overline{d_{gr}}$ (i.e. increasing domain volume V proportionally to the number of grains) and constant $\rho_H$, as reported in Table 4.2.

In all the models, the maximum length of the 1D elements is defined equal to the minimum edge length allowed ($\rho_P$), hence producing a very refined mesh that minimises the number of distorted elements.

| $n_{gr}$ | $n_{top}$ | $L$ $[\mu m]$ | $Vol$ $[\mu m^3]$ | $\overline{d_{gr}}$ $[\mu m]$ | $\rho_H$ $[\mu m]$ | $\rho_P$ $[\mu m]$ |
|---|---|---|---|---|---|---|
| 25 | 10 | 2.52 | 16.00 | 1.07 | 0.5 | 0.05 |
| 50 | 10 | 3.17 | 31.86 | | | |
| 100 | 10 | 4.00 | 64.00 | | | |

**Table 4.2:** Dimensions of the three sets of topologies

The grains are discretised with linear tetrahedral elements – since such elements provide a good accuracy for the type of load applied to the structure – and are modelled as continuum elastic bodies, as shown in Section 4.2.2. The nodes on the grain boundaries are merged together to eliminate any possible inelastic behaviour.

To have a statistically significant number of results, 10 different topologies were generated ($n_{top}$) per set (i.e. number of grains), and 5 random distributions of crystal orientations were assigned to each topology. Hence 50 models are produced per number of grains, for a total of 150 models analysed (Fig. 4.15).

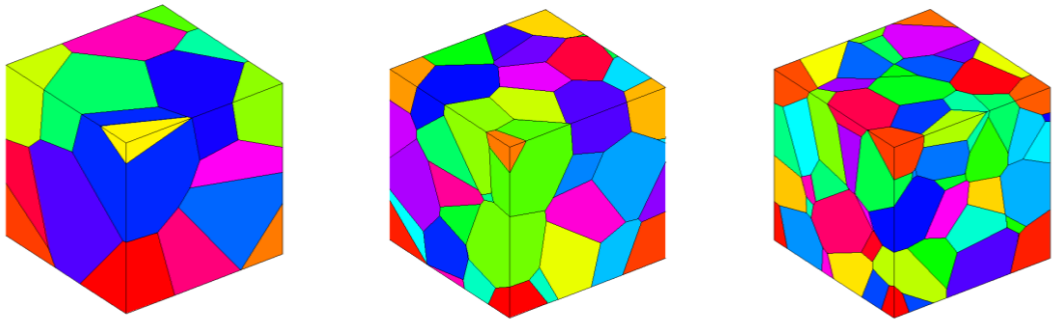


**Fig. 4.15:** Examples of topologies consisting of 25, 50, and 100 grains

The simulation consists of applying a quasi-static tensile load to two opposite faces of the cubic domain with the other two pairs of faces free from constraint, and the elastic response is calculated from the average stresses and strains in the model, following Eq. (39).

The results of the simulations are summarised in Fig. 4.16, which shows the Young's moduli predicted against the number of grains in the model alongside with macroscopic experimental measurements.

The triangles represent the result of a single simulation, whilst the asterisks represent the average Young's modulus of a single topology over the 5 different distributions of grain orientation. The results referring to the same topology share the same marker colour.

The three horizontal lines with error bars represent the experimental values obtained with acoustic measurements on macroscopic samples of polycrystalline alumina with different grain sizes presented in Section 3.2. The numerical results are in excellent agreement with the measurements performed on the coarsest grains. The possible texture induced by the high sintering pressure applied during the sintering of the samples with smaller grain size is suspected to be responsible for the apparent increase of the Young's modulus measured.

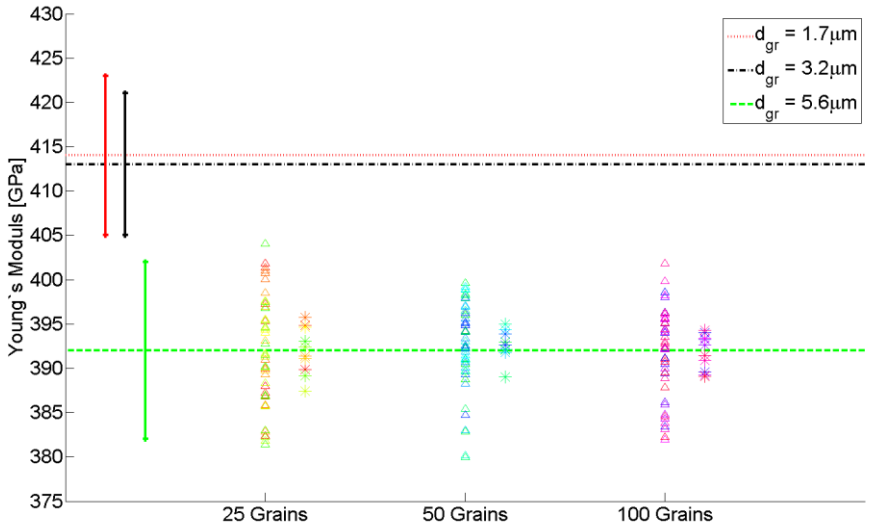



**Fig. 4.16:** Young's moduli of the single simulations (triangles), the single topology (asterisks), and measured experimentally (lines)

All the numerical results fall in a quite narrow range of values: $[380 \div 404]GPa$ for the single simulation and $[387 \div 396]GPa$ for the average value of the single topology, and the range of predicted values seems to be scarcely affected by the number of grains.

The numerical simulations exhibit quite a good agreement with the macroscopic experimental measurements, reported in Section 3.2.

Plotting the results as histograms (Fig. 4.17), instead, shows some differences emerging with the increase of the number of grains.

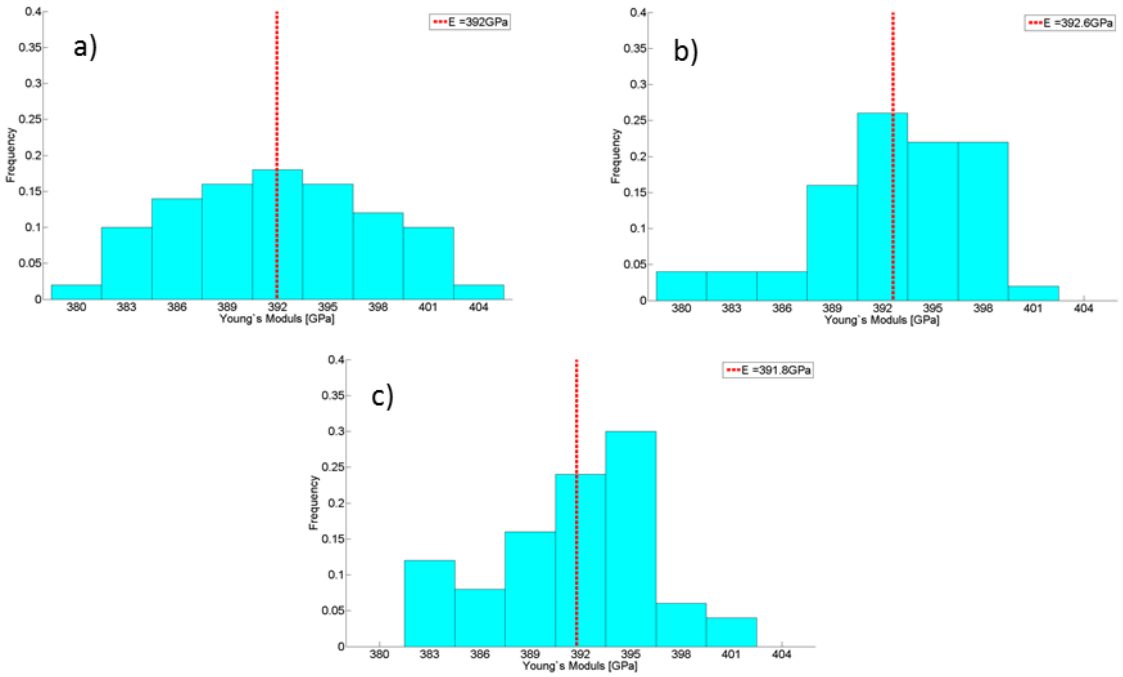



**Fig. 4.17:** Distribution of Young's modulus values for models with 25 (a), 50 (b), and 100 (c) grains

The models with 25 grains give a quite scattered set of results, whilst by increasing the number of grains the values of the predicted Young's moduli focus in around the average value (i.e. about 70% of the Young's moduli calculated from models consisting of 100 grains are within 1% difference from the average value).

Finally the average Young's moduli for the three sets of simulations (vertical dashed lines in Fig. 4.17) are extremely close to each other and slightly lower than the values measured experimentally for aggregates with comparable grain size (~5.3%). This confirms

that an improvement in the accuracy of the single RVE can be obtained averaging the results of uncorrelated samples [147].

### *4.3.2 Evaluation of the stress-intensity-factor at the tip of a notched plate*

After having validated the capability of the virtual polycrystalline topologies to correctly predict the macroscopic elastic properties of the material, more models are generated to verify the ability to simulate localised phenomena. In particular the possibility of producing concave domains is exploited generating polycrystalline notched plates to evaluate the pure mode I stress intensity factor ($K_I$) at the notch tip.

The evaluation of the stress intensity factor at the crack tip has been largely explored and the well-known analytical definition of the stress intensity factor for an isolated crack (of length $a$) in an infinite medium – subject to uniform tensile load $\sigma$ – has been calculated in several ways:

$$K_{I\infty} = \sigma\sqrt{\pi a} \tag{40}$$

Several corrections of this generic equation have been proposed over the last decades, to describe different configuration of plate and cracks. In particular, for the single edge crack plate loaded in tension (Fig. 4.18) different corrections are available in the literature that take into account the finite dimensions of the plate and the position of the crack.

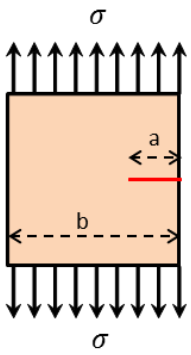



**Fig. 4.18:** Single edge crack plate with finite width (b) subject to pure tension load

The numerical results presented in this thesis are compared with the analytical solution reported by Lemaitre and Chaboche in their book [148] for the plate with finite width:

$$K_I \approx K_{I\infty} \cdot H_I \cdot H_{II} \tag{41}$$

$$H_I = \sqrt{\frac{2b}{\pi a}\tan\left(\frac{\pi a}{2b}\right)} \tag{42}$$

$$H_{II} = \frac{0.752 + 2.02\frac{a}{b} + 0.37\left[1 - \sin\left(\frac{\pi a}{2b}\right)\right]^3}{\cos\left(\frac{\pi a}{2b}\right)} \tag{43}$$

Where $H_I$ corrects Eq. (40) including the effect of the finite width of the plate ($b$), and $H_{II}$ takes into account of the position of the notch on the edge of the plate.

The numerical models of the notched plate are based on the topology presented in Fig. 4.19, which consists of a polycrystalline plate with a single V-shaped notch (~10° opening angle) at the middle of one side, with a depth of 2.5 $\mu m$.

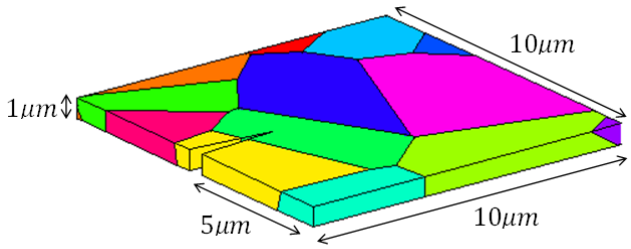



**Fig. 4.19:** Polycrystalline notched plate

The shape of the notch has been chosen to exploit the capability of the cutting method presented in Section 4.1 to generate concave polycrystalline shapes. The angle at the notch tip, however, has been proved to have a negligible effect on $K_I$ (i.e. less than 1%) for values of the angle between 0° and 30° [149].

Firstly – to evaluate the possibility of a mesh size effect – three different models (Fig. 4.20), with different maximum element length ($l^{el}_{max}$), have been generated from the same

topology (Fig. 4.19). The grains are modelled as isotropic elastic domains to allow the comparison of the numerical and analytical results.

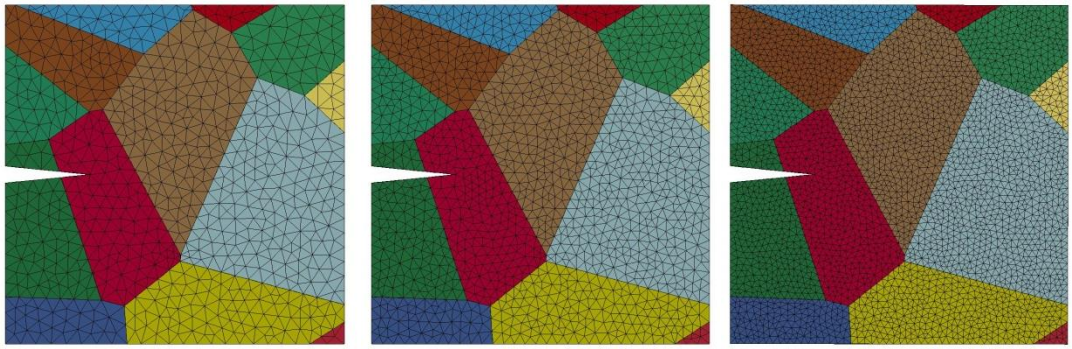


**Fig. 4.20:** Models of the notched plate with different mesh sizes: 0. 4$\boldsymbol{\mu m}$ (a), 0.3$\boldsymbol{\mu m}$ (b), and 0.2$\boldsymbol{\mu m}$ (c)

A remote tensile load is applied to the plate boundaries, perpendicularly to the crack, and the stress intensity factor is calculated from the position of the node at the crack tip and of the closest nodes at each side of the notch (i.e. tail nodes), with the relationship:

$$K_I = \frac{E}{4(1+\nu)(1-\nu)}\sqrt{\frac{\pi}{2r}}(u_U - u_D) \tag{44}$$

Where $E$ is the Young's modulus of the material, $\nu$ is the Poisson ratio, $r$ is the average distance of the two tail nodes to the tip node, and $u_U$ and $u_D$ are the displacement of the tail nodes (respectively on the top and bottom face of the crack) in the direction of the remote load [150]. Finally $\kappa$ is the Kolosov constant, defined as:

$$\kappa = \begin{cases} 3-4\nu & plane\ strain \\ \dfrac{3-\nu}{1+\nu} & plane\ stress \end{cases} \tag{45}$$

The plain stress assumption is employed herein, since the structure can be geometrically considered a thin plate.

The stress intensity factors obtained from the three different numerical models (i.e. $l_{max}^{el}$ equal to 0.4μm, 0.3μm, and 0.2μm) are compared with analytical evaluation of $K_I$, showing excellent agreement (Table 4.3).

| $l_{max}^{el}$ $[\mu m]$ | $\sigma$ $[GPa]$ | $\mathrm{K_I}^{num}$ $\left[GPa\sqrt{mm}\right]$ | $\mathrm{K_I}^{an}$ $\left[GPa\sqrt{mm}\right]$ | Error |
|---|---|---|---|---|
| 0.4 | 1.0 | 0.1334 | 0.1325 | 0.67% |
| 0.3 | 1.0 | 0.1340 | | 1.08% |
| 0.2 | 1.0 | 0.1419 | | 1.88% |

**Table 4.3:** Comparison of $\boldsymbol{K_I}$ evaluated numerically, with different mesh refinements, and analytically

The small error in the prediction of $K_I$ is mainly due to the use of the average $r$ that varies over the three models. However the magnitude of the error is considered acceptable in this context.

Having verified the accuracy of the predictions, independently from the mesh size, for the isotropic grains, the effect of the anisotropy in the elastic behaviour of the grains is explored. Five distributions of random grain orientations are assigned to the aggregate with the coarser mesh (i.e. $l_{max}^{el} = 0.4\mu m$). Since the hypothesis of isotropic deformation at the base of Eq. (44) is not verified, the stress intensity factor cannot be evaluated for these models.

| Model | $\sigma$ $[GPa]$ | $\sigma_{11}^{max}$ $[GPa]$ | $(u_U - u_D)$ $[\mu m]$ |
|---|---|---|---|
| Iso (a) | 1.0 | 7.87 | 0.0226 |
| Anis1 (b) | 1.0 | 6.31 | 0.0170 |
| Anis2 (c) | 1.0 | 6.51 | 0.0174 |
| Anis3 (d) | 1.0 | 6.29 | 0.0164 |
| Anis4 (e) | 1.0 | 6.31 | 0.0165 |
| Anis5 (f) | 1.0 | 6.63 | 0.0176 |

**Table 4.4:** Comparison of the maximum principal stress at the notch tip ($\boldsymbol{\sigma_{11}^{max}}$) and the crack opening displacement ($\boldsymbol{u_U - u_D}$) for the isotropic and anisotropic models

As alternative measures of the elastic deformation Table 4.4 reports the opening displacement of the tail nodes ($u_U - u_D$), and the maximum principal stress ($\sigma_{11}^{max}$) in the element at the crack tip (i.e. the maximum in the model).

Within the anisotropic models examined different grain orientations cause a variation in the crack opening of up to 8%, and of more than 5% in the maximum principal stress at the crack tip. The differences between the isotropic and the anisotropic models are even more marked: up to almost 40% difference in the opening displacement against 25% difference in the stress.

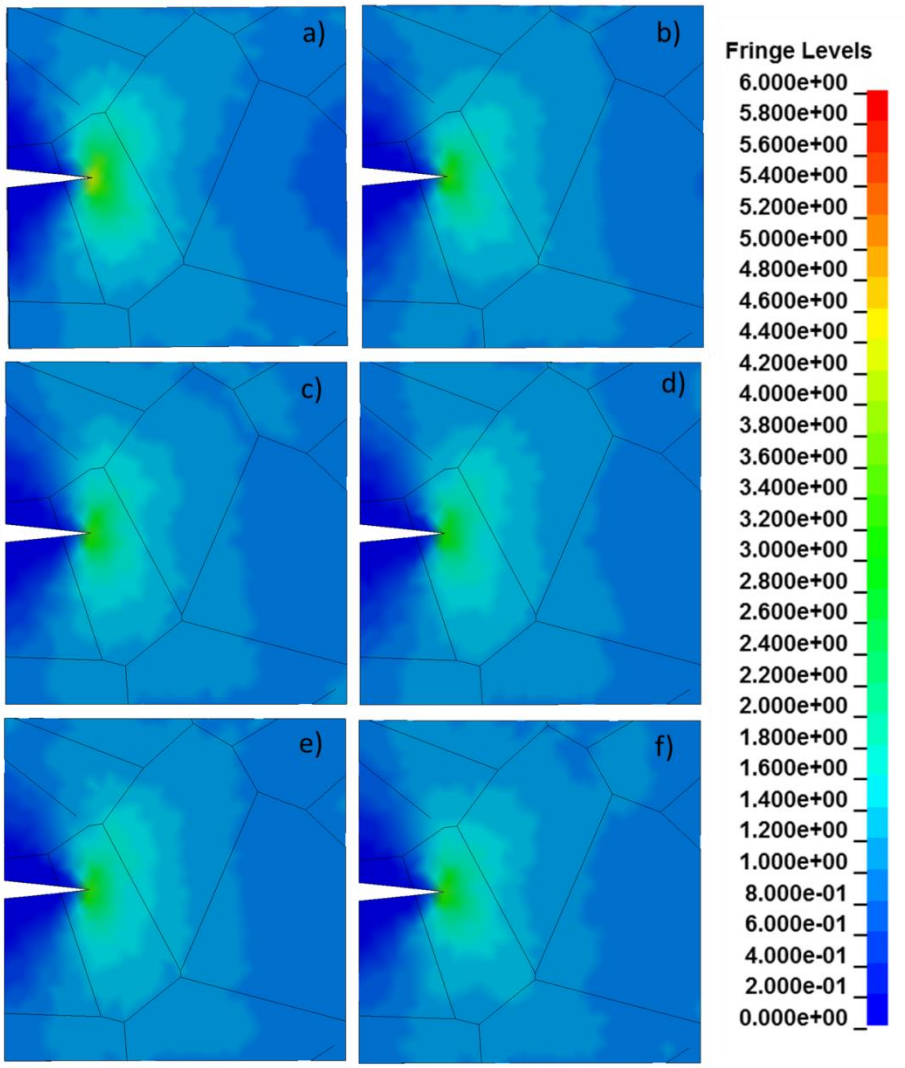


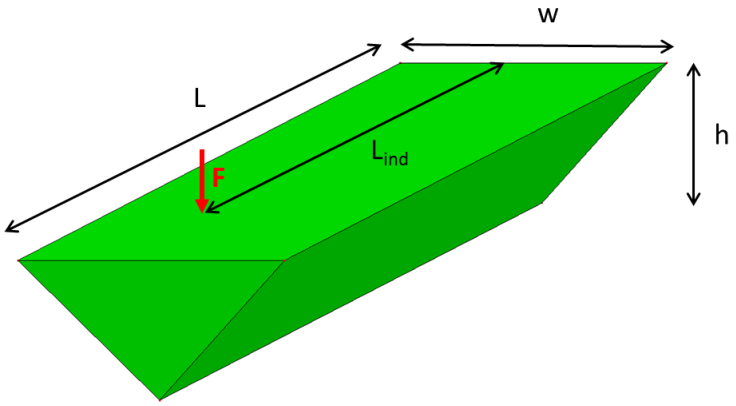

**Fig. 4.21:** Contour of the maximum principal stress ($\boldsymbol{\sigma_{11}^{max}}[\boldsymbol{GPa}]$) in the isotropic (a) and anisotropic (b-f) plates

These differences are also reflected in the stress distribution in the structure, as shown by the contours of the maximum principal stress presented in Fig. 4.21.

The results highlight the capability of the model in capturing the localised phenomena, which is crucial to understand the mechanisms of crack initiation and propagation in the material. The behaviour of the plates consisting of randomly oriented anisotropic grains confirms that, whilst the elastic properties can be predicted also with regular (non-representative) microstructures (e.g. cubes, hexahedra, truncated octahedra) by increasing the RVE, the localised phenomena in a polycrystalline medium strongly depend upon the topology of the grain aggregate. Hence, generating statistically valuable models of polycrystalline structures, able to correctly predict localised phenomena, is extremely important to simulate and better understand the micro-mechanics of polycrystalline materials.

### *4.3.3 Modelling and simulation of the micro-cantilever beam test*

To simulate the micro-cantilever beam tests a model of the geometry of the specimen has been created. It consists of an extruded isosceles triangle, fully constrained at one end, and subject to a linearly increasing load at a distance of $L_{ind}$ from the fixed end. The dimensions of the model and of the loading point reproduce the average geometry of the experimental tests, as reported in Fig. 4.22:




| | |
|---|---|
| $L\ [\mu m]$ | 20 |
| $w\ [\mu m]$ | 4.2 |
| $h\ [\mu m]$ | 2.47 |
| $L_{ind}\ [\mu m]$ | 17.23 |

**Fig. 4.22:** Dimensions of the model of the micro-cantilever beam and position of the loading point

Following the method illustrated in Section 4.1, three different models are cut from unconfined aggregates with the same average grain size and meshed with quadratic tetrahedral elements.

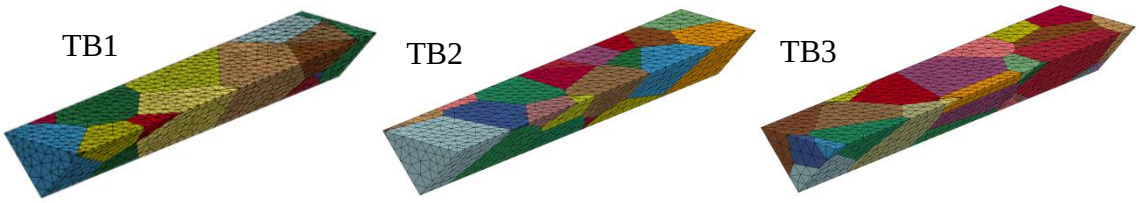



**Fig. 4.23:** Virtual micro-cantilever beams

Despite the constant average gain size of the unconfined aggregate, the three beams consist of different number of grains, 15, 20, and 24 respectively. This scatter can be related to the reduced dimension of the specimen with respect to the size of the single grain, and has been noticed also in the experimental samples.

Besides the similarity of the number and average size of the grains, the models are able to reproduce also the approximate shape of the crystals, as can be noticed by the visual comparison presented in Fig. 4.24.

Four FE models are generated per each topology: one with isotropic grains and three with crystals modelled as fully anisotropic bodies – following the symmetry presented in Section 4.2.2 – with random texture.

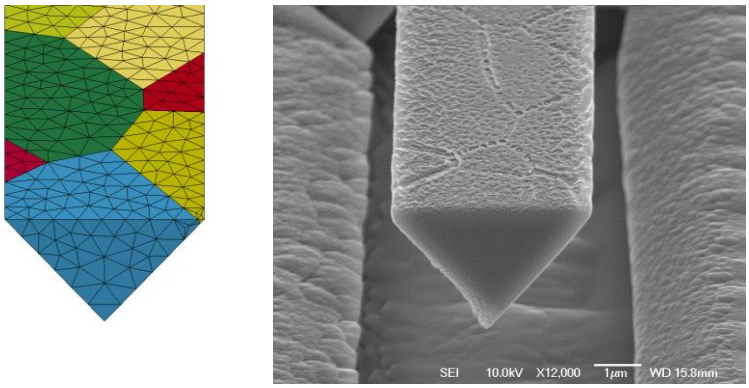



**Fig. 4.24:** Visual comparison of a virtual and an experimental beam

The models with isotropic grains are created to isolate the effect of the geometry over the grain orientation, whilst the models with anisotropic grains show the influence of the grain orientation – for a given geometry – on the elastic deformation and the failure mechanisms of the beam.

The values of the elastic properties of both the isotropic and the anisotropic grains are reported in Table 4.5:

| Anisotropic | | Isotropic | |
|---|---|---|---|
| $C_{11}$ | 497 $GPa$ | $E$ | 398 $GPa$ |
| $C_{12}$ | 163 $GPa$ | | |
| $C_{13}$ | 116 $GPa$ | | |
| $C_{14}$ | 22 $GPa$ | $\nu$ | 0.22 |
| $C_{33}$ | 501 $GPa$ | | |
| $C_{44}$ | 147 $GPa$ | | |

**Table 4.5:** Single grain properties for the anisotropic and the isotropic models

The properties of the anisotropic grains are the same as those reported in Section 2.1.3 and 4.2.2, whilst the isotropic elastic constants are estimated from the direct experimental measurements presented in Section 3.2. The load is modelled as a linearly increasing force, applied – perpendicularly to the top face of the beam – to all the nodes within a certain distance from the indentation point, equal to the dimension of the actual indenter tip. The validation of the numerical simulations against the experimental tests is performed comparing both the elastic behaviour and the failure mechanisms.

The elastic behaviour is expressed in terms of Young's modulus of the polycrystalline material, calculated using the Euler-Bernoulli equation.

The results are summarised in Fig. 4.25. To highlight the small differences between the data sets, the origin of the vertical axis is set at $300\ GPa$.

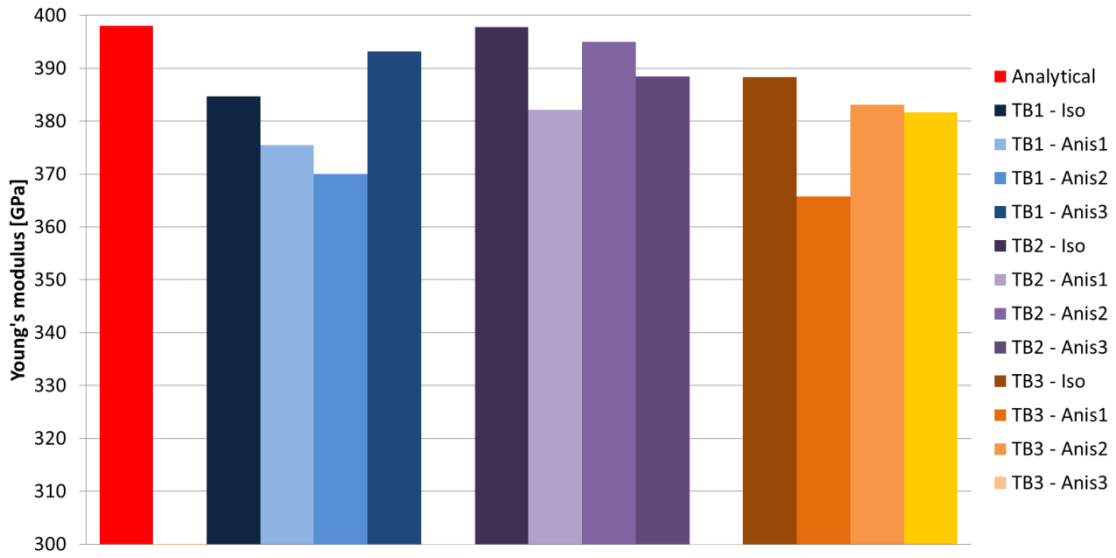



**Fig. 4.25:** Apparent Young's modulus of the micro-cantilever beams

The first bar (i.e. analytical) represents the perfect elastic behaviour of a fully isotropic beam, and is defined as the value of the Young's modulus of the single grain in the isotropic models reported in Table 4.5 (i.e. $E = 398\ GPa$).

The second bar represents the behaviour of the beam $TB1$ with isotopic grains, whilst the three following bars represent the behaviour of the same beam with anisotropic grains and three different crystal orientation distributions. Analogously the last two groups of bars are respectively the results of the beams $TB2$ and $TB3$, first for the simulation with isotropic, then with anisotropic grains.

The results summarised in Fig. 4.25 show that the beams consisting of isotropic grains are slightly more flexible than the analytical prediction, whilst theoretically there should not be any difference. Such mismatch can be related to the failure of few grain boundaries during the elastic deformation of the structure (e.g. failure of the contact across small element faces

can be triggered by numerical noise). However, the difference is constantly below 4%, therefore considered negligible.

Also the grain orientation seems to have a limited effect the elastic behaviour of the beams. In particular the maximum difference in the Young's modulus between the isotropic beams and the correspondent (i.e. sharing the same topology) anisotropic beams is within 6%.

The comparison of the numerically evaluated values against the measurements presented in Section 3.1 and the numerical predictions illustrated in Section 4.3.1 is reported in Fig. 4.26:

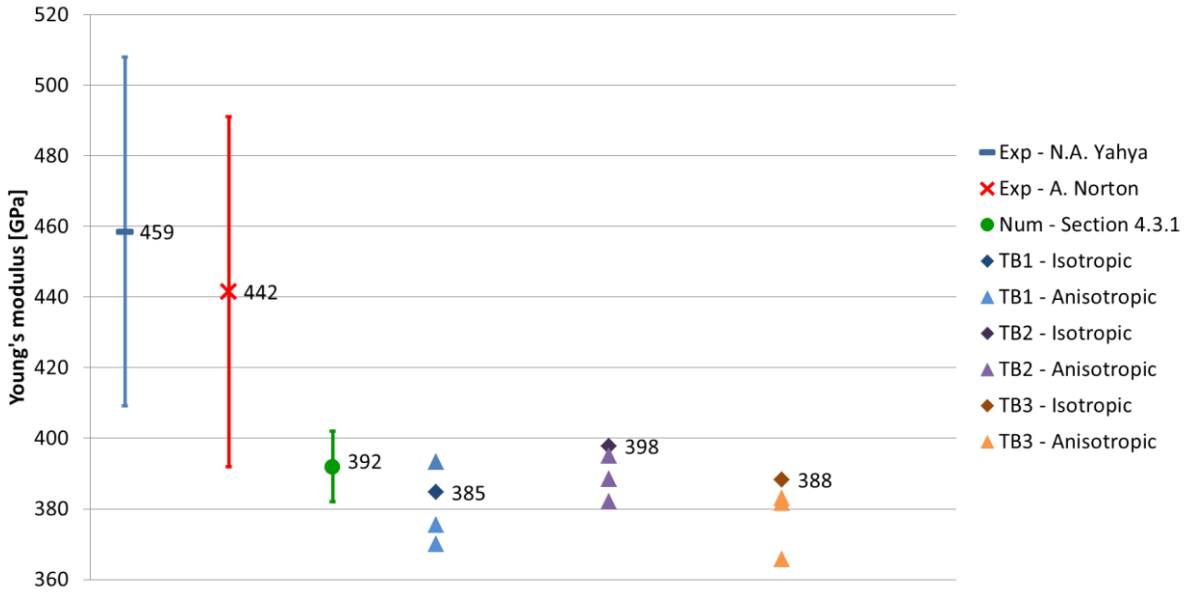



**Fig. 4.26:** Comparison of the numerical and experimental values for the Young's modulus

As for the comparison presented in Fig. 4.16, the values of the Young's modulus measured experimentally (i.e. blue dash and red cross) are slightly higher than the numerical predictions. The high values of the Young's modulus measured with experimental cantilever beams is suspected to derive from the error in the measurement of the dimensions of the beams, due to the presence of deposited material, as described in Section 3.1.3.

Finally, it is interesting to note the extremely good agreement of the elastic properties of the beams presented in this section with the cubic specimens presented in Section 4.3.1 (i.e.

green circle), therefore giving an additional validation to the ability of the adopted approach to correctly simulate the elastic behaviour of ceramic materials.

The inelastic behaviour, instead, is compared in terms of failure strength. In particular the numerical results are validated against beams failing because of the propagation of an inter-granular crack that initiates on a grain boundary, since the FE models are constrained to simulate this particular fracture behaviour. A visual comparison of the numerical and experimental inter-granular fracture surface is shown in Fig. 4.27:

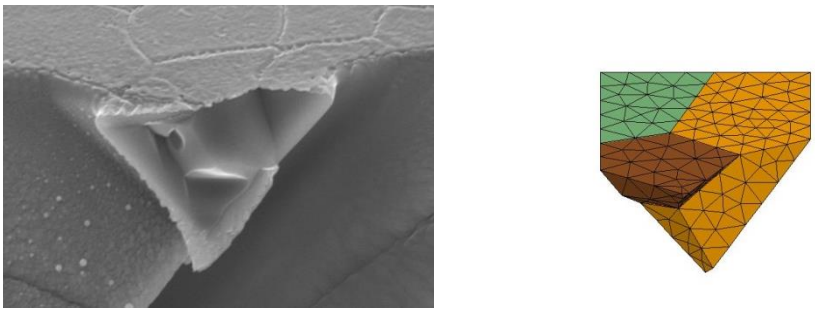


**Fig. 4.27:** Visual comparison of the experimental and numerical fractured surfaces

The graph in Fig. 4.28 compares the fracture strength measured experimentally against the values calculated from the numerical simulations of the micro-cantilever beam tests.

The experimental values reported by the red bar in Fig. 4.28 refer to beams failed propagation of inter-granular cracks initiated on a grain boundary (presented in Section 3.1.3).

The three subsequent sets of bars (analogously to Fig. 4.25) represent, respectively, the behaviour of the beams $TB1$, $TB2$ and $TB3$, first with isotropic grains, then with anisotropic grains with different crystal orientation distributions.

The scatter in the numerical prediction is due to the variation of $L_f$ along the broken surface, whilst the asterisks under some bars indicate the initiation of the crack, which in some cases is not immediately followed by the complete failure of the beam.

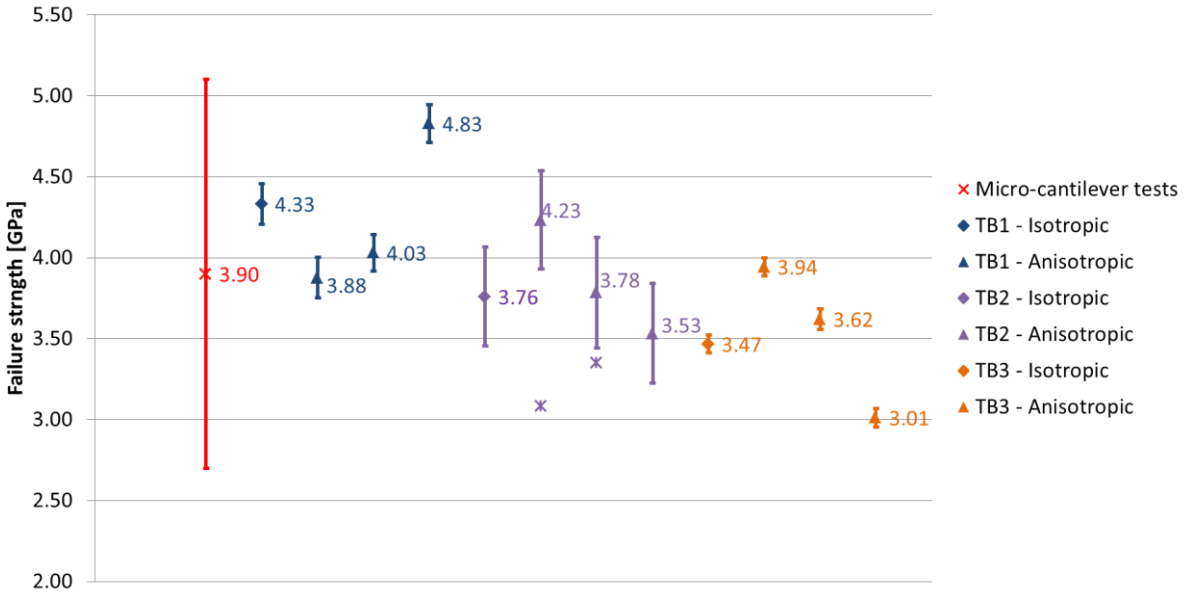



**Fig. 4.28:** Failure strength of the micro-cantilever beams

The scatter in the results – both experimental and numerical – is due to the combination of the inclination of the grain boundaries and the orientation of the neighbouring grains (for the non-isotropic simulations), and underlines the highly stochastic nature of the cracking phenomenon, even without taking into account the variability of the grain boundary strength and the possible presence of defects in the material. It also highlights the importance of numerical simulations to explore the effect of microstructure parameters (e.g. size, shape, and orientation of the grains, strength of the grain boundary) on the macroscopic properties of the material to develop novel materials with improved performance.

To conclude, in this framework, the agreement of numerical and experimental results (both on the elastic deformation and on the failure load) demonstrates that the methodology presented in this thesis is able to generate representative models of the polycrystalline microstructure of ceramic materials, and to reproduce the elastic behaviour and the inter-granular cracking initiation and propagation of ceramic materials, using exclusively fundamental and – most important – directly (and consistently) measurable properties of the material.

## 4.4 Simulation of dynamic failure

After having demonstrated the capability of the model to correctly predict both the elastic deformation and the initiation and propagation of inter-granular cracks in ceramic materials under quasi-static loading conditions, in this section the propagation of cracks under dynamic behaviour is analysed.

The virtual tests presented in this section show the ability of the generated numerical microstructures to reproduce the rate dependence of the crack propagation observed in the failure of real polycrystalline materials, without introducing any rate-dependency in the definition of the interfaces.

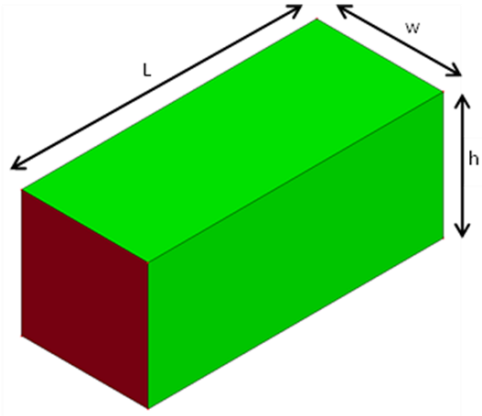
Given the characteristics of the test proposed, a direct validation against experimental results would be extremely challenging – if not impossible – to obtain, and therefore is not presented in this thesis. However the numerical results are compared qualitatively with experimental evidence, showing the ability of the adopted physical-based approach to capture some important features in the failure of polycrystalline materials at high strain rate.

In Section 4.4.1 a wide parametrical study is presented, to explore the effect of the geometry of the specimen and of the load on the propagation of inter-granular cracks within polycrystalline domains subjected to pulse loads. In Section 4.4.2, the variation of the crack pattern in a polycrystalline plate hit by a rigid ball at different impact velocities is illustrated.

### *4.4.1 Propagation of cracks induced by a compressive pulse load*

In this section, different compression loads are applied to polycrystalline aggregates to observe the influence of geometrical and loading parameters on the crack propagation within the microstructure.

The virtual test designed consists of applying a compressive pulse load perpendicularly to one face of a brick-shaped polycrystalline structure, whilst the opposite face (red in Fig. 4.29) is constrained in the direction of the load.




| | |
|---|---|
| $L\ [\mu m]$ | 5.6 |
| $w\ [\mu m]$ | 2.4 |
| $h\ [\mu m]$ | 2.4 |

**Fig. 4.29:** Dimensions of the compression specimen

The grains are meshed with quadratic tetrahedral elements (Fig. 4.30a), and the interfaces are added on the grain boundaries (Fig. 4.30b), as reported in Section 4.2.

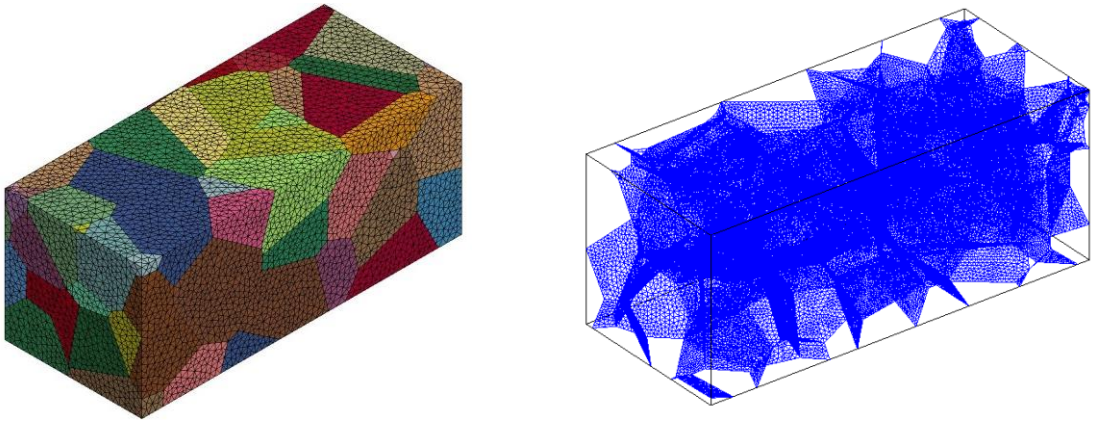


**Fig. 4.30:** FE model (a) and contact segments on the grain boundaries (b)

The grains are still modelled as continuum elastic bodies. Both the isotropic and the anisotropic constitutive models are used, with the parameters introduced in the previous sections, and reported in Table 4.6.

| Anisotropic | | Isotropic | |
|---|---|---|---|
| $C_{11}$ | 497 $GPa$ | $E$ | 398 $GPa$ |
| $C_{12}$ | 163 $GPa$ | | |
| $C_{13}$ | 116 $GPa$ | | |
| $C_{14}$ | 22 $GPa$ | $\nu$ | 0.22 |
| $C_{33}$ | 501 $GPa$ | | |
| $C_{44}$ | 147 $GPa$ | | |

**Table 4.6:** Single grain properties for the anisotropic and the isotropic models

It has been shown that for dynamic simulations the grains of alumina may have an inelastic behaviour – either deforming plastically or breaking. However those phenomena are quite limited, and therefore in this work such second order effects are neglected.

Finally, the load consists of a square pulse pressure – defined by its magnitude (Π) and duration ($\Delta t$), as described in Fig. 4.31 – applied uniformly on the face of the structure.

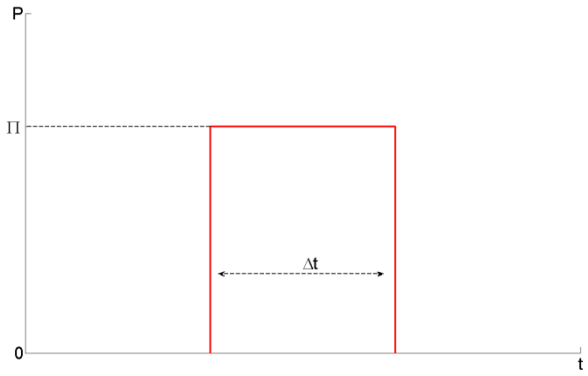



**Fig. 4.31:** Square pulse load applied to the specimen

The parametrical study presented in this section consists of the investigation of the effects of grain topology, texture, load magnitude, and pulse duration on the failure of the microstructure.

First the effect of the grain topology is studied. To exclude the effect of the crystal orientation, in the FE models the grains are defined as isotropic domains. A load of magnitude

5.0 $GPa$, and duration $2 \cdot 10^{-4} \mu s$ is applied to 5 different specimens, whose properties are summarised in Table 4.7.

| Name | Number of grains | Number of interfaces | $\Pi$ $[GPa]$ | $\Delta t$ $[\mu s]$ |
|---|---|---|---|---|
| CP1 | 72 | 76020 | 5.0 | $2 \cdot 10^{-4}$ |
| CP2 | 75 | 73648 | | |
| CP3 | 61 | 76820 | | |
| CP4 | 73 | 73600 | | |
| CP5 | 67 | 76708 | | |

**Table 4.7:** Summary of the models

The damage (i.e. inter-granular crack propagation) caused by the stress wave travelling in the specimen is quantified plotting the percentage of failed contacts against the duration of the test and (equivalently) the position of the stress wave front.

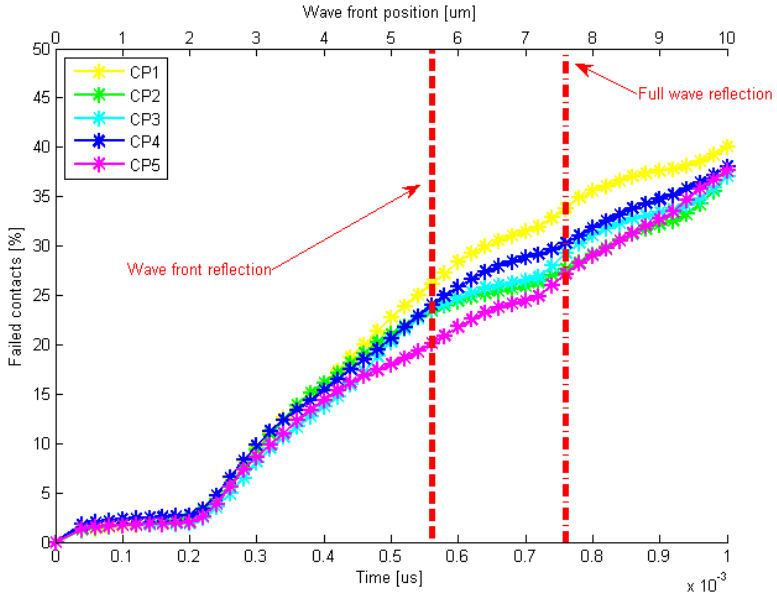



**Fig. 4.32:** Percentage of interfaces failed for different topologies with isotropic grains

The two dashed vertical lines in Fig. 4.32 indicate respectively the instant the stress wave front reaches the free end of the specimen ($\tau_1$), and the moment the stress wave is fully reflected ($\tau_2$).

The first quantity is evaluated from the macroscopic density and Young's modulus of the material using the relationship:

$$\tau_1 = \frac{L}{c} = L\sqrt{\frac{\rho}{E}} \tag{46}$$

Where $c$ is the sound speed in the material ($\sim 10^4 ms^{-1}$ using the isotropic definition of alumina grains presented in in Fig. 4.32).

The time for the full reflection of the wave ($\tau_2$), is evaluated as the sum of $\tau_1$ and the pulse duration $\Delta t$:

$$\tau_2 = \tau_1 + \Delta t \tag{47}$$

All the curves in Fig. 4.32 show a slight increase in the percentage of failed interfaces at the beginning of the simulation. The failed interface curves have a roughly constant slope until the entire pulse has been transmitted to the specimen (i.e. $2 \cdot 10^{-4} \mu s$), then the number of opening interfaces starts growing considerably. The initial sudden growth of the cracks can be identified as numerical error, due to the failure of a small percentage of interfaces ($0.9 \div 1.3\%$) whose area is small enough for the numerical noise in the prediction of the normal stress $\sigma_N$ to trigger the failing condition of the contact (defined in Section 4.2.3). Given the negligible number of contacts involved, the numerical error generated is considered acceptable.

Once the whole pulse is transmitted to the specimen, the cracks start to initiate and propagate along the favourably oriented grain boundaries. The process of breaking the contacts dissipates energy, and this may explain the decreasing slope of all the curves in this section. The scatter in the behaviour of the curves before $\tau_1$ is minimal.

To visualise the cracking mechanism in the virtual tests presented, the view of crack pattern evolution of the most severely damaged structure (i.e. CP1) is plotted in Fig. 4.33.

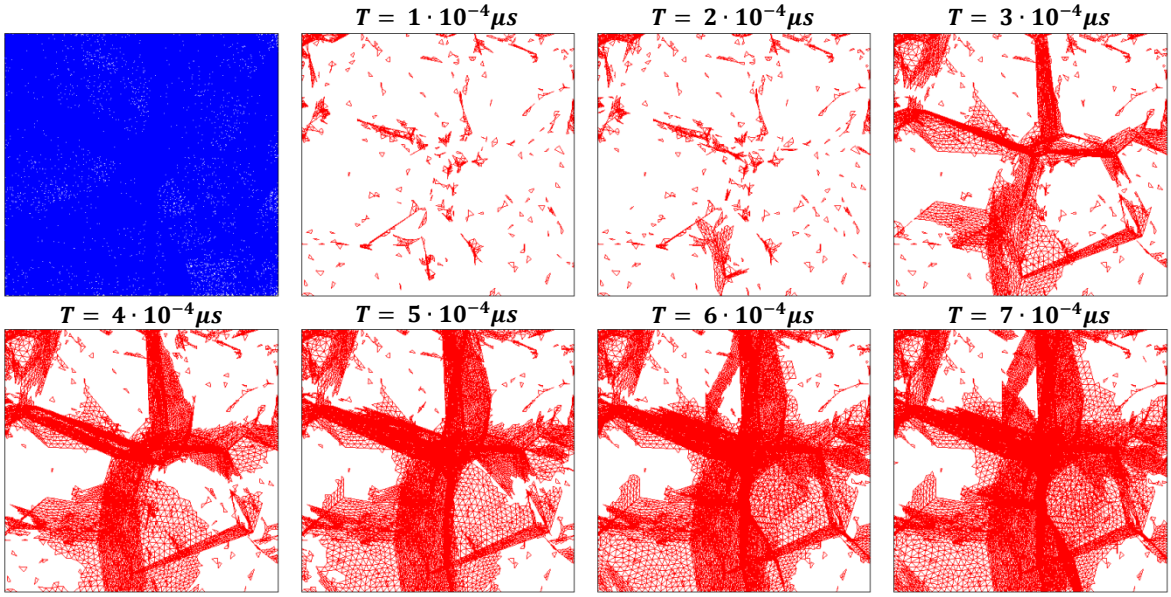



**Fig. 4.33:** Crack propagation in the structure CP1

The top left image shows all the existent contacts in the intact structure, then – from left to right and top to bottom – the evolution of the failed interfaces (red triangles) is reported, with an image every $10^{-4} \mu s$.

Since, in this set of tests, the shear stress is neglected in the determination of the failing condition, the compression pulse can only initiate cracks because of lateral deformation of the structure. This mechanism was observed in all the simulations, and is quite evident in Fig. 4.33, where the cracks initiated mainly on the grain faces that are close to be tangent to the direction of the load. Also a limited number of interfaces inclined with respect to the load direction have been observed to fail. Their failure seems to be mainly driven by the propagation of cracks initiated at other grain boundaries.

The simulations show a minimal effect of the topology upon the crack propagation in the microstructure. Therefore the models presented can be considered – within a certain

approximation – representative volume elements (RVE) of the inelastic behaviour of polycrystalline alumina under compressive loading conditions.

The topology that expresses the most severe damage within the ones presented in Table 4.7 (i.e. CP1-iso-A1) is used as the base model for the parametrical study that explores the effect of texture, load magnitude, and load duration on the crack propagation. In particular – including the models with different topologies – the four sets of models consist of the model CP1-iso-A1 with the addition of:

- 4 topologies of the structure with isotropic grains (CPx-iso-A1)
- 3 random distributions of orientations of the anisotropic crystals (CP1-xxx-A1)
- 2 magnitudes and durations of the load, with constant momentum (CP1-iso-x1)
- 3 durations and magnitudes of the load, with constant magnitude (CP1-iso-Ax)

In Table 4.8 the configuration "*CP1-iso-A1*" (common to all the four sets) is highlighted in bold, whilst the parameters varying are framed by thick red borders.

The momentum ($q$) is defined as the product of the force applied on the specimen and the duration of the pulse:

$$q = \Pi \cdot \Delta t \cdot (w \cdot h) \tag{48}$$

Assuming the constancy of the cross sectional area, the momentum is proportional to the area underneath the load curve presented in Fig. 4.31.

The influence of the anisotropy of the grains is illustrated in Fig. 4.34, where the behaviour of the model with isotropic grains (i.e. CP1-iso-A1) is compared with three models consisting of the same topology with randomly oriented anisotropic grains.

| Name | Topology | Grain orientation | $\Pi$ $[GPa]$ | $\Delta t$ $[\mu s]$ | $q$ $[\mu N \cdot \mu s]$ |
|---|---|---|---|---|---|
| **CP1-iso-A1** | **CP1** | **Isotropic** | **5.0** | $\mathbf{2 \cdot 10^{-4}}$ | **5.76** |
| CP2-iso-A1 | CP2 | Isotropic | 5.0 | $2 \cdot 10^{-4}$ | 5.76 |
| CP3-iso-A1 | CP3 | Isotropic | 5.0 | $2 \cdot 10^{-4}$ | 5.76 |
| CP4-iso-A1 | CP4 | Isotropic | 5.0 | $2 \cdot 10^{-4}$ | 5.76 |
| CP5-iso-A1 | CP5 | Isotropic | 5.0 | $2 \cdot 10^{-4}$ | 5.76 |
| | | | | | |
| **CP1-iso-A1** | **CP1** | **Isotropic** | **5.0** | $\mathbf{2 \cdot 10^{-4}}$ | **5.76** |
| CP1-anis1-A1 | CP1 | Anis1 | 5.0 | $2 \cdot 10^{-4}$ | 5.76 |
| CP1-anis2-A1 | CP1 | Anis2 | 5.0 | $2 \cdot 10^{-4}$ | 5.76 |
| CP1-anis3-A1 | CP1 | Anis3 | 5.0 | $2 \cdot 10^{-4}$ | 5.76 |
| | | | | | |
| CP1-iso-B1 | CP1 | Isotropic | 2.5 | $4 \cdot 10^{-4}$ | 5.76 |
| **CP1-iso-A1** | **CP1** | **Isotropic** | **5.0** | $\mathbf{2 \cdot 10^{-4}}$ | **5.76** |
| CP1-iso-C1 | CP1 | Isotropic | 10.0 | $1 \cdot 10^{-4}$ | 5.76 |
| | | | | | |
| CP1-iso-A2 | CP1 | Isotropic | 5.0 | $5 \cdot 10^{-5}$ | 1.44 |
| CP1-iso-A3 | CP1 | Isotropic | 5.0 | $1 \cdot 10^{-4}$ | 2.88 |
| **CP1-iso-A1** | **CP1** | **Isotropic** | **5.0** | $\mathbf{2 \cdot 10^{-4}}$ | **5.76** |
| CP1-iso-A4 | CP1 | Isotropic | 5.0 | $3 \cdot 10^{-4}$ | 8.64 |

**Table 4.8:** Summary of the set of models, with the varying parameters highlights with thick borders

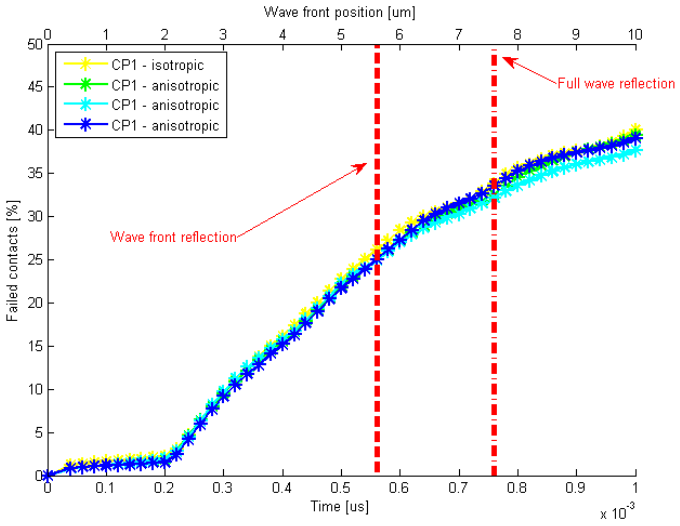



**Fig. 4.34:** Percentage of interfaces failed for the same topology with different crystal orientations

Fig. 4.34 shows the almost total independence of the crack propagation mechanism over the grain orientation for the loading conditions examined, thus confirming that the models presented are RVE of the inelastic behaviour of polycrystalline alumina under compression.

Having verified that the influence of the geometric parameters (i.e. topology and texture) is exiguous, the effect of the loading condition on the crack propagation is explored, firstly varying the magnitude of the pulse (keeping the momentum constant) and then varying the duration of the pulse (for a fixed magnitude).

The influence of the magnitude is explored by applying to the same structure (i.e. the topology "CP1" with isotropic grains) three different loads – respectively with a magnitude of 2.5 (CP1-iso-B1), 5.0 (CP1-iso-A1), and 10.0 $GPa$ (CP1-iso-C1) – varying the pulse duration to keep the momentum constant.

Only the reflection of the stress wave front ($\tau_1$) is reported in Fig. 4.35, because $\tau_2$ is no longer common to all the simulations (due to the variation of the pulse duration).

As observed previously, about 1% of the interfaces fail instantaneously in all the simulations (due to the numerical error already described) and the curves of failed contacts

remain constant until the entire pulse has been transmitted to the specimen. Then the curve slope rises showing the differences between the three simulations.

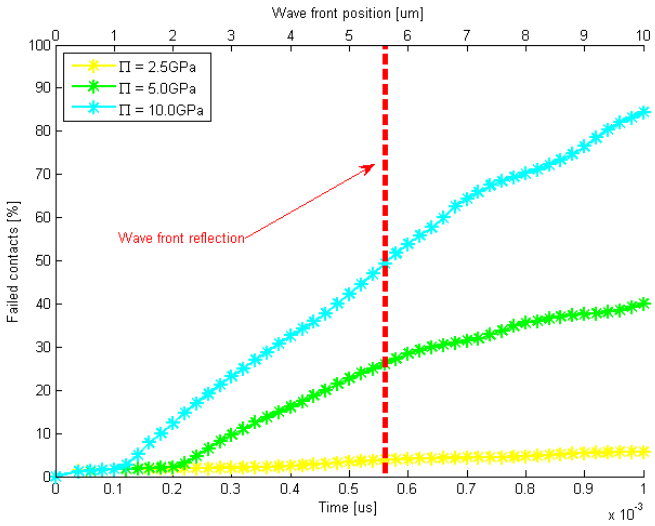



**Fig. 4.35:** Percentage of interfaces failed for different load magnitude, with constant momentum

The load with the lower magnitude (i.e. 2.5 $GPa$) is not able to generate significant damage in the specimen, breaking less than 5% of the total interfaces by the time the stress wave travels through the whole specimen (i.e. $\tau_2$). Increasing the load, the number of failed contacts grows: 31% for the load of magnitude 5.0 $GPa$, and 64% for the load of magnitude 10.0 $GPa$.

More detailed information can be by obtained studying the crack patterns, captured in Fig. 4.36:

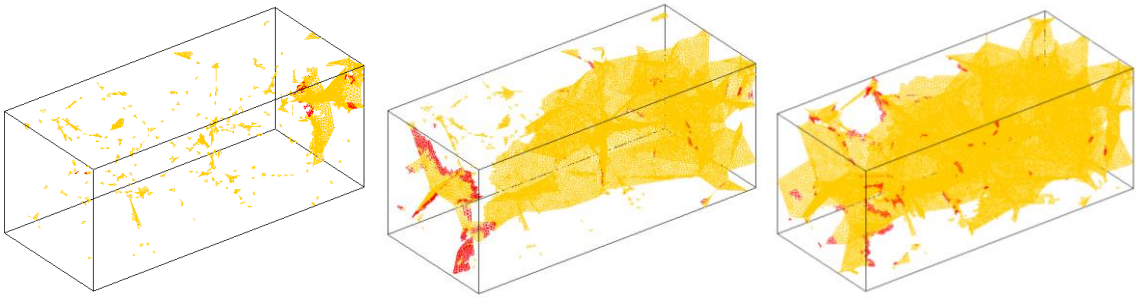


**Fig. 4.36:** Interfaces failed when the wave front reflects, for the models CP1-iso-B1, CP1-iso-A1, CP1-iso-C1

In the model CP1-iso-B1 (i.e. magnitude $2.5\,GPa$) the stress wave initiates some cracks in proximity to the loaded face, and then propagates through the whole specimen almost without causing any additional damage Fig. 4.36a. The sparse cracks are partially initiated by the wave, and partially due to the initial numerical error observed in all the graphs presented in this section.

Doubling the magnitude (i.e. model CP1-iso-A1), the number of failed interfaces increases drastically (Fig. 4.36b). The cracks initiate and propagate along the most favourably oriented planes, as already presented in Fig. 4.33.

Doubling again the magnitude of the load (i.e. model CP1-iso-C1) the majority of the interfaces breaks before the wave front reaches the end of the specimen. The crack pattern is extremely branched and the specimen is fragmented in several volumes (Fig. 4.36c).

Finally, the effect of the pulse length with constant magnitude is analysed. Four loads with the same magnitude and different durations: 0.05 $ns$ (CP1-iso-A2), 0.1 $ns$ (CP1-iso-A3), 0.2 $ns$ (CP1-iso-A1), and 0.3 $ns$ (CP1-iso-A4) are applied to the topology CP1 with isotropic grains. The influence of $\Delta t$ on the number of failed interfaces is appreciable, even if not comparable with the effect of the magnitude, as shown in Fig. 4.37.

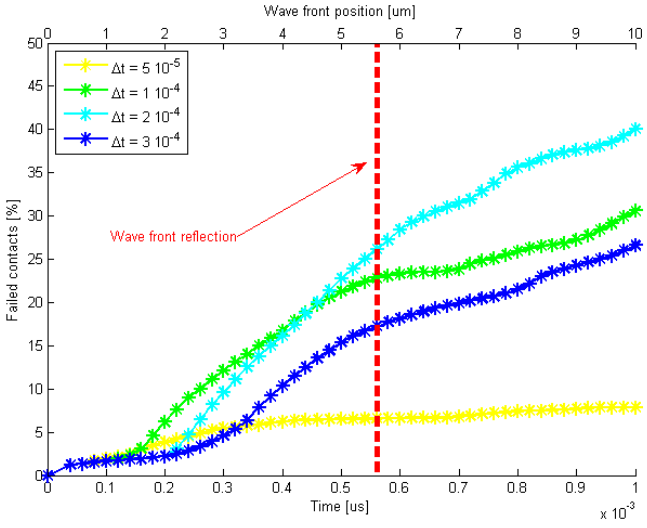



**Fig. 4.37:** Percentage of interfaces failing for different load durations with constant magnitude

As observed in all the previous simulations, the number of contacts rises instantaneously to about 1% due to the small interfaces, remaining practically constant until the entire load is transmitted to the specimen.

In the model subjected to the shortest pulse (i.e. $5 \cdot 10^{-5}\ \mu s$) the load is able to initiate a small number of cracks (less than 7% of the total) in the proximity of the loaded surface, and then travels in the specimen almost without affecting the grain boundaries.

Doubling the pulse duration (i.e. $1 \cdot 10^{-4}\ \mu s$), the number of failed interfaces increases drastically, reaching almost 24% of the total when the wave front reaches the end of the specimen (i.e. $\tau_2$).

Doubling $\Delta t$ again (i.e. $2 \cdot 10^{-4}\ \mu s$), the number of failed interfaces when the stress wave has travelled through all the structure is about 31%. It is interesting to notice that initially the percentage of broken contacts is lower in the model with longer pulse, to then increase during the simulation. The initial lack of failed interfaces is due to the late start of the crack initiation, but then the cracks propagate further because of the bigger momentum.

Increasing the pulse duration again (i.e. $3 \cdot 10^{-4}\ \mu s$), the number of failed interfaces when the wave front reflects decreases to about 19%. This apparently low value can be explained with the late start of the crack initiation, so cracks are not able to propagate much further before the wave reflects at the end of the specimen.

To conclude – for the given dimensions of the specimen and grain size – the geometrical parameters (both grain topology and orientation) do not seem to greatly affect the mechanisms of initiation and propagation of the cracks within the microstructure, thus showing that the models analysed are RVE for the given loading conditions.

Oppositely, the load parameters (i.e. magnitude and duration of the pulse load) have a significant effect on the inelastic behaviour of the polycrystalline domain. In particular, the

percentage of interfaces failed when the wave front reaches the end of the specimen increases with the magnitude and, up to a threshold, with the pulse duration.

The models presented, despite not having a direct validation with either analytical or experimental results, demonstrate the ability of the approach presented in capturing (at least qualitatively) some key features of the failure mechanism of polycrystalline ceramics, showing many common aspects with experimental (macroscopic) observations both in the fracture patterns and the dependencies on the load parameters.

### *4.4.2 Impact of a rigid sphere on a polycrystalline plate*

In this section the impact of a rigid sphere against a polycrystalline plate at different velocities is presented.

The target is a square plate ($L = 20\ \mu m$ and $h = 1\ \mu m$) fully constrained on the side faces. The plate consists of 51 grains modelled as isotropic bodies, spatially discretised into quadratic tetrahedral elements ($l_{max}^{el} = 0.5\ \mu m$), and then assembled together inserting contacts on the grain boundaries to allow for inter-granular crack propagation The structure and the interfaces are graphically presented in Fig. 4.38.

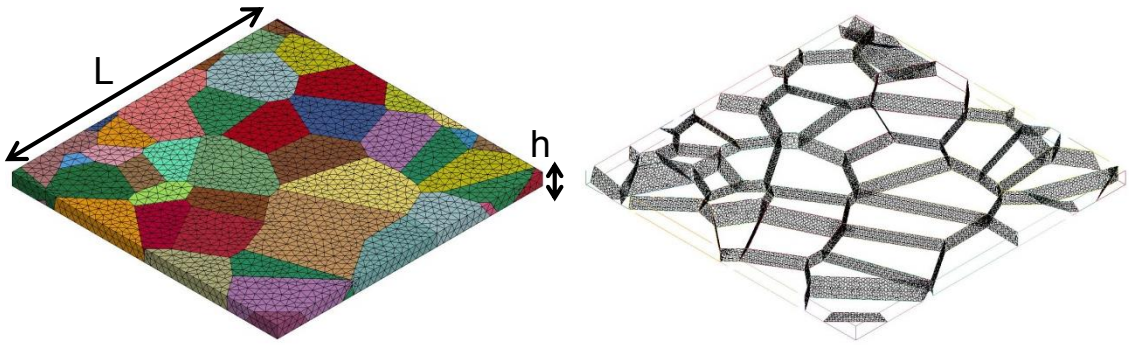
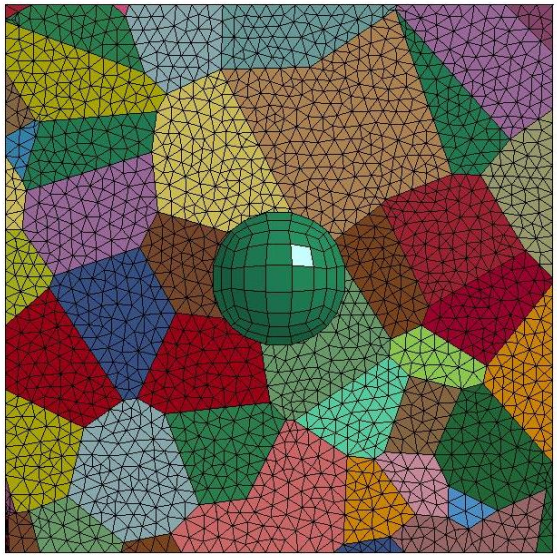
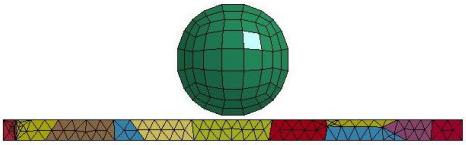



**Fig. 4.38:** Grains and interfaces of the FE model of the target

The impactor, instead, consists of a rigid sphere (2.5 $\mu m$ radius) with an assigned initial velocity $V$ (perpendicular to the main surface of the plate), impacting the target in the centre of the top face.





| Model | Impact velocity $[^m/_s]$ |
|---|---|
| P1-A | 200 |
| P1-B | 400 |
| P1-C | 600 |
| P1-D | 800 |
| P1-E | 1000 |

**Fig. 4.39:** Model of the test and table of the impact velocities

The complete model and the impact velocities are reported in Fig. 4.39.

As for the tests presented in the previous section, the effect of the different loading conditions (i.e. impact velocities) is analysed by plotting the percentage of contacts failing in time (Fig. 4.40).

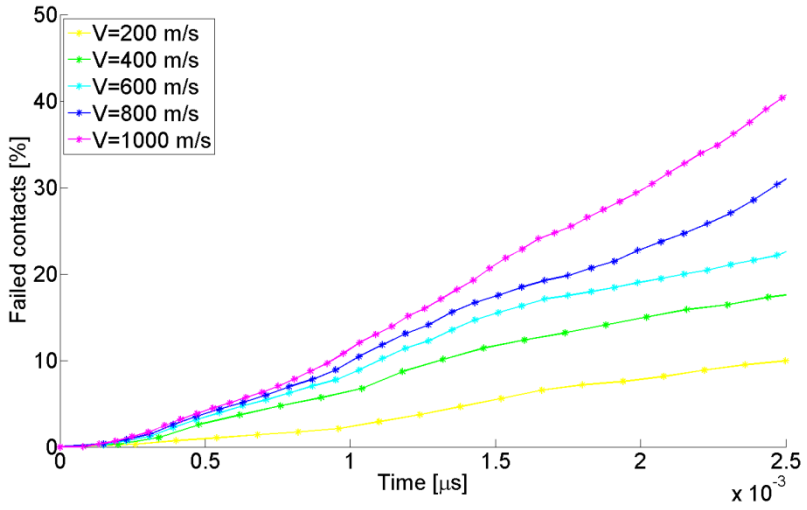



**Fig. 4.40:** Percentage of interfaces failed for different impact velocities

The time-zero is the instant of the impact.

As expected, an increase of the impact velocity corresponds to an increase in the number of the failed contacts.

The behaviour of the curves cannot be described with simple considerations on the stress wave propagation, given the complexity of the loading conditions, which are a combination of the non-constant input load (i.e. the impactor slows whilst penetrating the target) and of the non-uniform reflection of the stress waves on the plate boundaries. This complexity reflects in a highly irregular shape of the curves that exhibit kinks and change of slope not ascribable to a single mechanism.

More information about the failure mechanisms of the target at different impact velocities are obtainable by analysing the evolution in time of the crack propagation for the different loading conditions.

In Fig. 4.41 the evolution of the crack pattern for the different impact velocities is reported, showing the failed interfaces at the same four instants in time (columns) for all the five impact velocities tested (rows).

At low velocities the crack propagation seems to be driven mainly by the branching of the crack that initiates in the impact region. Increasing the velocity, the stress wave that propagates from the impact point initiates multiple cracks in areas that have not been reached yet by the branching of the main crack. Eventually most of the cracks initiated by the stress wave coalesce to generate a net of cracks, thus breaking the specimen in several small domains.

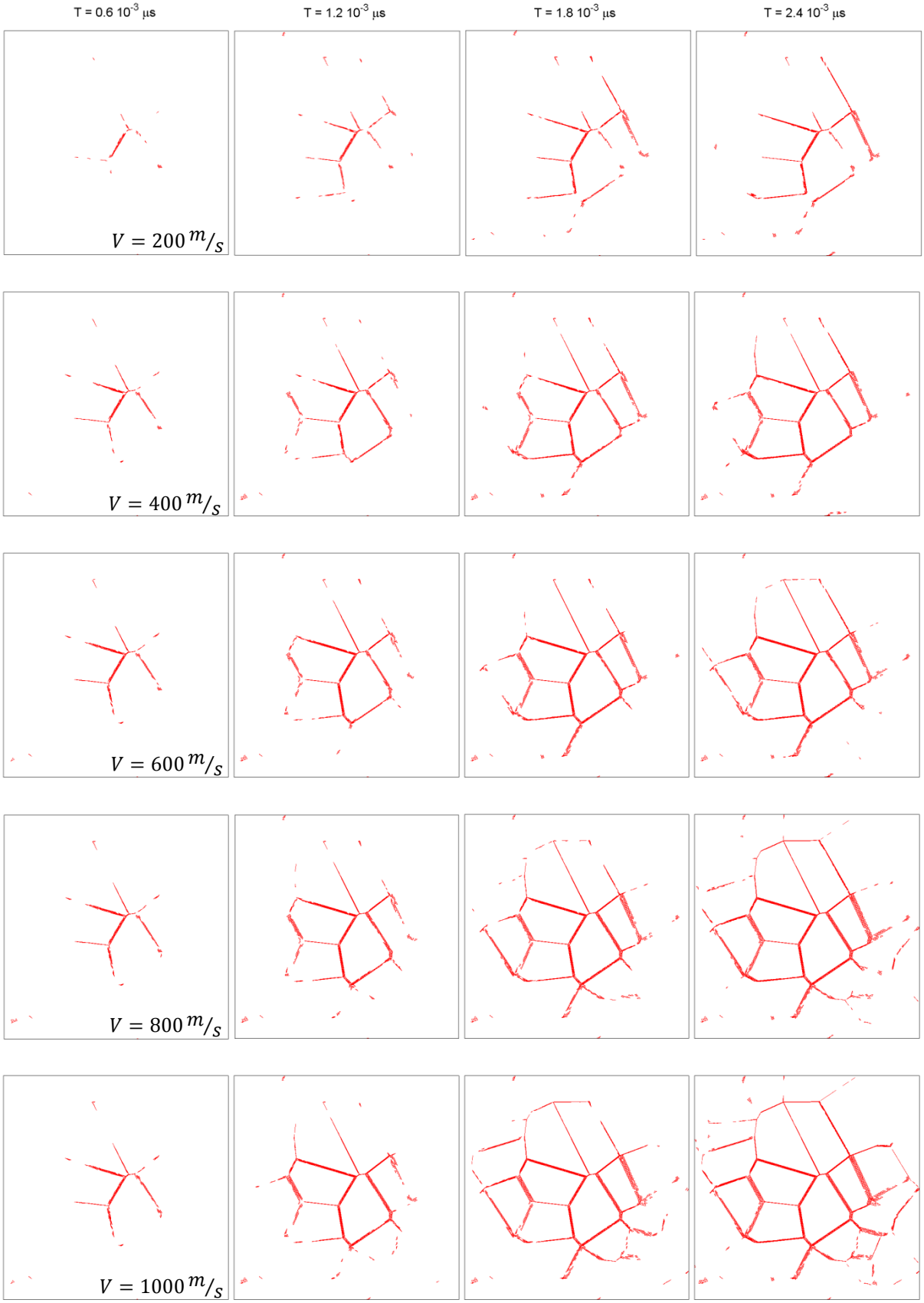



**Fig. 4.41:** Crack pattern at different times (columns) after the impact for the analysed velocities (rows)

To visualise those mechanisms, the effect of the impact velocity on the maximum principal stress pattern in the back of the target is reported in Fig. 4.42.

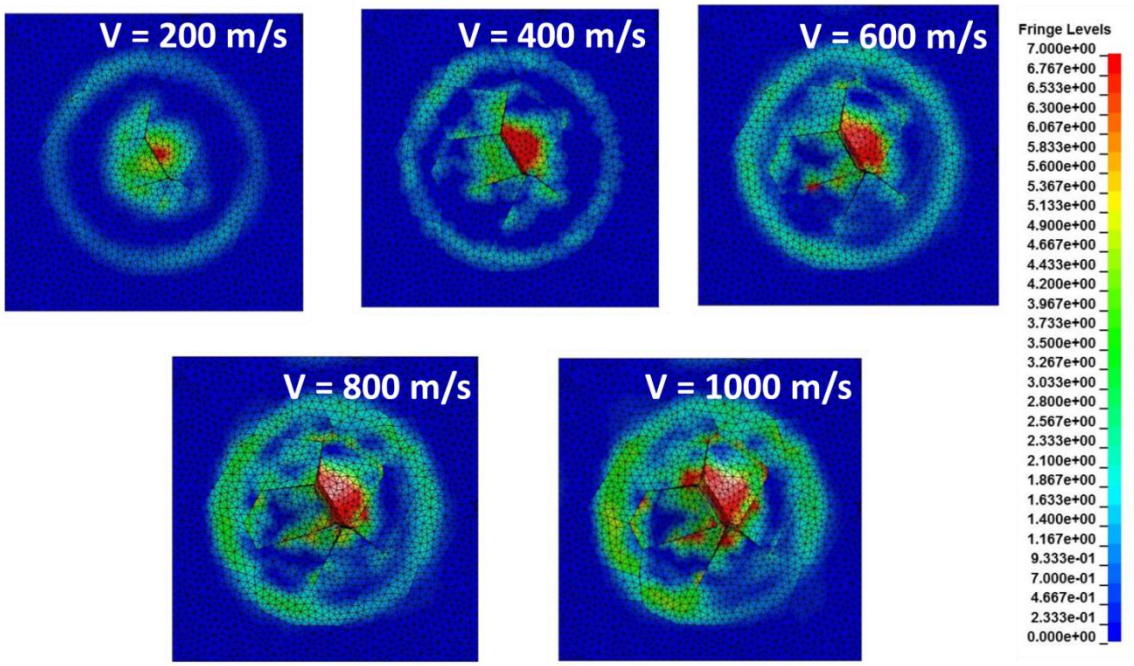



**Fig. 4.42:** Maximum principal stress in the target after $\mathbf{1.2 \cdot 10^{-3}}$ $\boldsymbol{\mu s}$ from the impact

From Fig. 4.42 is evident how, at low velocities, the magnitude of the stress propagating from the impact point is too small to trigger the failure of the interfaces at the grain boundaries (i.e. initiate cracks). Therefore, the only mechanism that leads to the increasing of the damage is the propagation of the crack initiated at the impact point, due to the penetration of the projectile.

At higher velocities, instead, the magnitude of the stress wave is high enough to induce the failure of the most favourably oriented interfaces, generating a multitude of growing cracks, eventually coalescing with each other and with the principal branching crack propagating from the impact point.

Similar behaviour in the damage propagation in brittle materials at different strain rates has been observed in many experimental tests and also described theoretically [151]. Hence, despite the lack of direct experimental verification of such virtual tests, the behaviour

of the models can be considered qualitatively accurate, and the approach presented is able to capture the changing of failure mechanisms in ceramic materials on impact.

## 4.5 Simulation of trans-granular crack propagation

Finally, a preliminary attempt to simulate the combination of trans- and inter-granular crack propagation mechanisms is made, adding the possibility of deleting elements to simulate the growth of a crack within a grain.

There are many criticalities concerning the simulation of crack propagation with the element deletion technique with a local stress-based erosion (LSE) criterion. Among all, the most critical ones are the loss of mass given by the erosion of the element and the mesh dependence of the results, as explained in Section 2.3.3.

The grains are modelled as continuum isotropic elastic bodies, discretised into quadratic tetrahedral elements, and assembled inserting contacts on the grain boundaries. The crack propagation within the single grain is simulated with the erosion of the elements that reach the critical equivalent stress. The value of the critical stress for the element deletion (i.e. $\sigma_C = 12.5\ GPa$) is obtained from the experimental results presented by Norton [126].

Given the remarkable difference between the strength of the grain boundaries and of the grains themselves within polycrystalline alumina, the initiation of trans-granular cracks needs to be forced, creating a stress concentration inside a grain at least 2.5 times higher than the highest tension across any grain boundary. To focus the stress a geometrical configuration similar to the one presented in Section 4.3.2 is defined: a square plate with a single V notch on one edge. The design of the grains imposes that the notch tip falls inside a grain, far enough from any grain boundaries. Such a precaution avoids the failure of any inter-granular interfaces before the conditions for the trans-granular crack initiation are fulfilled.

The results presented in this section refer to the two topologies reported in Fig. 4.43:

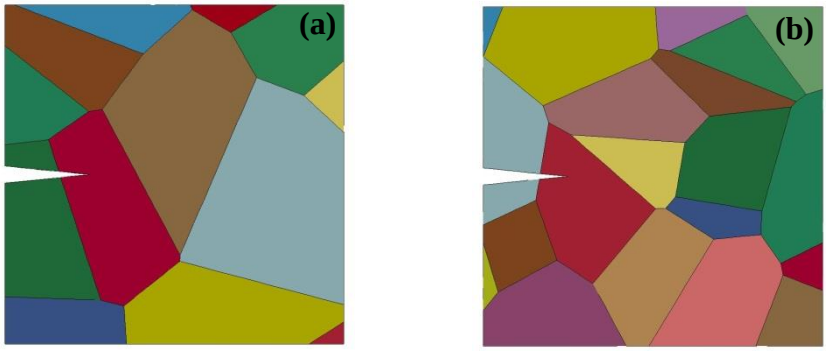



**Fig. 4.43:** Topologies of the notched plate

First the influence of the mesh size – that is notoriously important when the element removal technique is used – is explored. The model shown in Fig. 4.43a is discretised with three different maximum element sizes ($l_{max}^{el}$), respectively equal to $0.4\mu m$, $0.3\mu m$, and $0.2\mu m$. The models used are identical to the ones presented in Section 4.3.2, where the mesh-independence of the stress intensity factor ($K_I$) at the notch tip is demonstrated.

Subsequently the topology shown in Fig. 4.43b is used to illustrate the influence of the different crystalline topologies on the trans-granular crack propagation.

The three FE models generated from the first geometry are reported in Fig. 4.44:

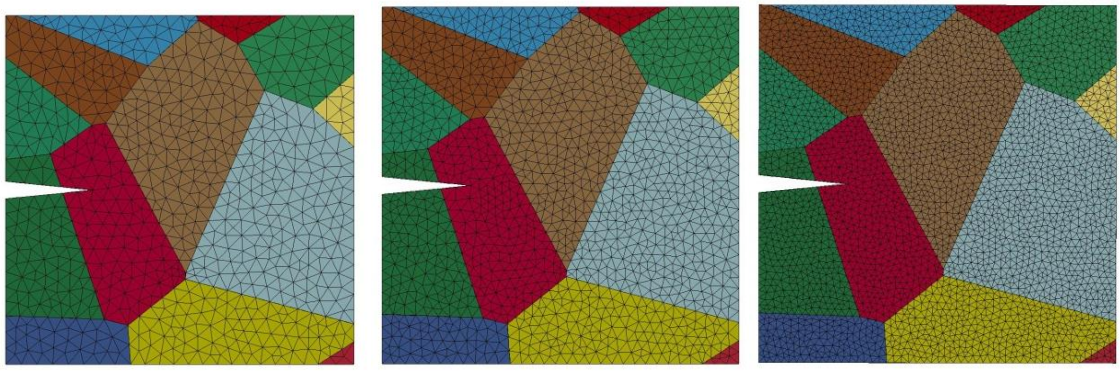


**Fig. 4.44:** Models of the notched plate with different mesh sizes: $0.4\boldsymbol{\mu m}$ (a), $0.3\boldsymbol{\mu m}$ (b), and $0.2\boldsymbol{\mu m}$ (c)

A linearly increasing tensile load $\sigma$ is applied normally to the top surface (in Fig. 4.44) whilst the bottom face is fully constrained in the direction of the load.

With the increasing of the load the V notch opens and the stress concentrates at the notch tip until the stress in the element at the notch tip reaches the critical value for the single crystal, triggering the deletion of the element. This event starts the propagation of the trans-granular crack, as illustrated in Fig. 4.45.

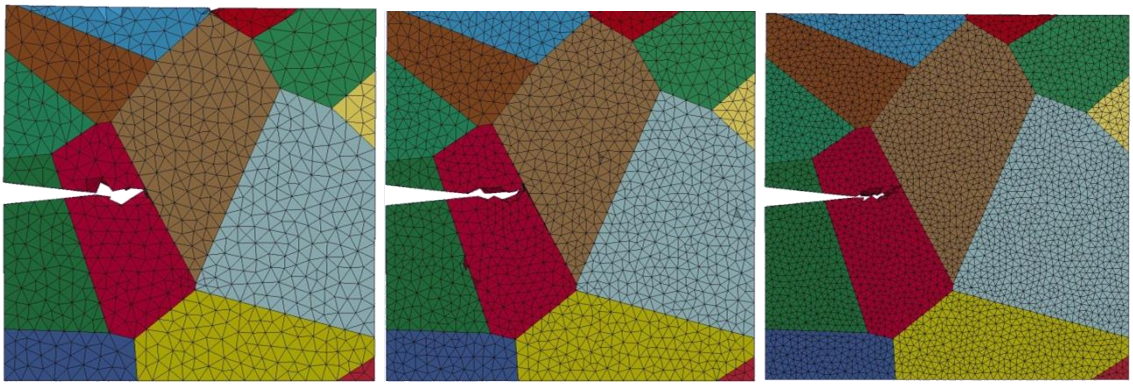


**Fig. 4.45:** Propagation of the trans-granular crack from the notch tip to the closest grain boundary

The crack propagates from the notch tip to the closest grain boundary, where it stops and initiates an inter-granular crack that propagates until the complete failure of the structure, as shown in Fig. 4.46.

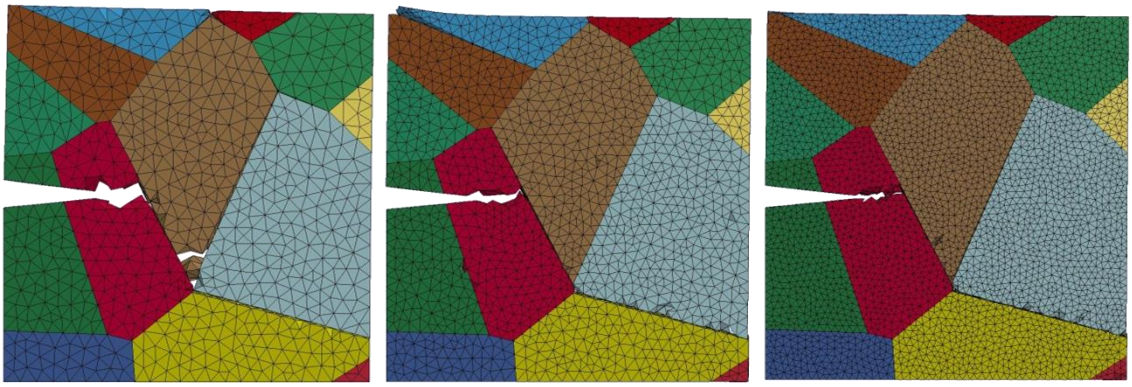


**Fig. 4.46:** Failure of the structure due to the combination of trans- and inter-granular crack propagation

The path of the crack seems quite consistent across the three models, with the width of the crack decreasing with the refining of the mesh because of the reduction of the element size. It is also worth noticing that in the model with the coarser mesh the inter-granular crack

initiates a trans-granular crack in proximity to a sharp corner of the brown grain in Fig. 4.46. This behaviour, however, disappears in the simulations with finer meshes.

The mesh sensitivity of the test can be quantified by comparing the failure loads ($\bar{\sigma}_F$) of the three different models, as reported in Table 4.9.

| $l_{max}^{el}$ $[\mu m]$ | $\bar{\sigma}_F$ $[GPa]$ | Mesh sensitivity [%] |
|---|---|---|
| 0.2 | 1.001 | - |
| 0.3 | 1.146 | 14.49 |
| 0.4 | 1.241 | 23.98 |

**Table 4.9:** Summary of the failure load of the structure and the mesh sensitivity

The mesh sensitivity is measured as the percentage difference of the failure load from that of the model with the finest mesh. As expected, the mesh size significantly affects the results in terms of crack initiation load. This effect is due to the high gradient of stress around the crack tip that discourages the use of the effective stress to trigger the initiation of the cracks.

However, the simulations reported provide relatively accurate description of some qualitative behaviours of the material. In particular all the simulations presented predict a slight upward curvature of the trans-granular crack, which eventually hits the closest interface roughly perpendicularly to the grain boundary. This behaviour has been frequently observed experimentally and can be justified by the tendency of the crack to find the shortest path to the weak entity (i.e. the grain boundary in this particular case). To verify that the curvature of the crack is due to the ability of the model to capture this mechanism – and is not linked to other causes, as for example the asymmetry of the loading conditions – another FE model is created with a different topology.

The geometry presented in Fig. 4.43b is designed to have the grain boundary closest to the notch tip (i.e. the interface on which the trans-granular crack is expected to end) appreciably inclined with respect to the vertical direction, to induce a more pronounced curvature in the trans-granular crack.

To enhance the opening of the notch a tensile load is applied symmetrically with respect to the symmetry plane of the notch, on the top and bottom surface only in correspondence of the first half of the notch (i.e. for the one eighth of the surface closest to the left corners of plate). In a homogeneous, isotropic plate this load should initiate a crack that propagates horizontally, but, as shown in Fig. 4.47, the presence of grain boundaries induces the crack to deviate from the horizontal direction towards the direction perpendicular to the weak interface.

The notable curvature of the trans-granular crack, despite the symmetric loading conditions and the isotropy of the grains, proves that the approach adopted is able to reproduce the deflection of the crack towards the defect (in this case a relatively weak grain boundary), thus giving qualitative insights into the behaviour of polycrystalline microstructures of brittle materials.

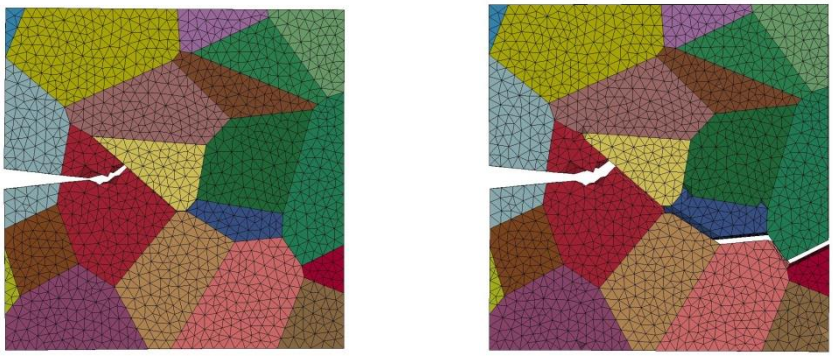


**Fig. 4.47:** Propagation of the trans-granular crack (left) and complete failure of the structure (right)

The crudity of the element removal technique, however, makes the results quantitatively inaccurate, also because of the adoption of the LSE criterion (instead of a

criterion based on, for example, the stress intensity factor) that enhances the mesh sensitivity of the simulations. However they are considered to be a good preliminary application for the prediction of the qualitative behaviour of polycrystalline materials that exhibit grain boundaries noticeably weaker than the grains themselves (e.g. alumina).

## 4.6 Conclusions

In this chapter the approach developed to model the failure of ceramic microstructures under different loading conditions is presented.

### *4.6.1 Generation of microstructural models*

First, in Section 4.1, a new method for the generation of FE models which are statistically representative of polycrystalline microstructures is illustrated in detail. The approach presented consists of generating the topology by cutting the unconfined Voronoi cells along planar faces, to shape the domain into any desired (convex or concave) form.

The main novelties presented by the method illustrated are:

- The ability to model non-uniform grain growth, by either extending the Hardcore assumption to consider non-spherical initial nuclei domain, or by manipulating the geometry of the grains generated.
- The absence of the a-priori definition of the domain (contrary to other common similar algorithms, e.g. [85], [86]), thus avoiding any border effect on the grain morphology both in convex and concave bodies.

The so-generated grains are singularly discretised in (either linear or quadratic) tetrahedral elements, and assembled into the final structure (Section 4.2). The possibility to insert cohesive interfaces on the grain boundaries and to assign the material properties

separately to each grain provide the ability to simulate the initiation and propagation of cracks within materials with arbitrary texture.

The models generated are exportable – at present – both in the commercial software *Abaqus FEA* and *LS-DYNA*, as well as in the in-house simulation software *DEST*, to perform numerical analyses.

### *4.6.2 Simulations of deformation and failure of the microstructure*

The method illustrated is used to generate several different models of polycrystalline microstructures, in order to simulate the deformation and the failure of ceramic materials at the grain level.

First the global (Section 4.3.1) and local (Section 4.3.2) elastic behaviour of ceramic aggregates are simulated and validated against both analytical calculations and experimental measurements, demonstrating the ability of the methodology presented to predict the macroscopic elastic moduli of polycrystalline aggregates as well as the localisation of stress at the crack tip.

Then, in Section 4.3.3, the micro-cantilever beam tests presented in Section 3.1 are modelled, and the failure of the specimens due to the inter-granular propagation of the cracks is simulated. The direct validation of the numerical results against the experimental measurements confirms the accuracy of the prediction of the elastic behaviour of polycrystalline ceramic microstructures, and demonstrates the ability of the model to reproduce the inter-granular failure of the specimens.

In Section 4.4, instead, the numerical models are used to explore the behaviour of the microstructure of polycrystalline ceramics under dynamic loading conditions. First a parametrical study of the influence of the morphology and the loading conditions on the crack propagation within a polycrystalline domain subjected to pulse compressive loads is

presented. Then the effect of the impact velocity on the failure of a polycrystalline plate is illustrated. The lack of direct experimental validation due to the extreme complexity of performing measures at the grain scale with the required time resolution allows only qualitative considerations on the failure mechanisms simulated. However, the comparison of the results with post-mortem experimental observations shows the ability of the models to capture the effect of the loading properties on the crack propagation (Section 4.4.1) as well as the transition of the crack propagation mechanism from a single branching crack at relatively low rates, to multiple coalescing micro-cracks at relatively high rates (Section 4.4.2).

Finally, in Section 4.5, the combination of trans- and inter-granular crack propagation mechanisms have been explored. Despite all the limitations presented in Section 2.3.3, the LSE criterion has been adopted as an initial step of the developing of the trans-granular crack propagation method. Ideas for further work to improve the accuracy of the technique presented is presented in Section 7.2.

### *4.6.3 Summary of the outcomes*

The simulations performed are all based exclusively on directly measured intrinsic material properties of the individual features of ceramic materials at the microscale (i.e. the elastic anisotropic behaviour of grains and cohesive behaviour of grain boundaries). The methodology developed has generated models capable of reproducing the increasingly complex deformation and failure behaviour exhibited by polycrystalline microstructures. This enables the extremely important validation of the direct measurements performed (e.g. compliance matrix of the grain, strength of the grain boundary) and provides insights into the deformation and failure mechanisms within a ceramic microstructure at different strain rates.

In particular, the correct prediction of the elastic moduli of the ceramic material guarantees the statistically representativeness of the models generated, given the high reliability of the x-ray measurements of the single crystal compliance.

The accurate reproduction of the failure of polycrystalline micro-cantilever beams, instead, provides both a verification of the directly measured mechanical properties of the single grain boundary, as well as an indication of the effect of the anisotropy and orientation of the grains on the strength of polycrystalline structures.

Finally, the qualitative agreement of the results of the simulations of the loading rate effect on the failure pattern with experimental observations suggests a minor rate-sensitivity of the mechanical properties of grains and grain boundaries. In particular the numerical results indicate that different failure patterns (i.e. few major cracks propagating at low rates, and several micro-cracks coalescing at high rates) are linked with the propagation of stress waves within the material, as described in Section 4.4. A quantitative validation of the results is hindered by the lack of direct measurements at the desired length-scale. This limitation could be circumvented adopting a multi-scale modelling approach, which allows to simulate microscopical features of macroscopic domains, as suggested in the future work chapter (Section 7.2.3).

# 5 MACROSCOPIC CONSTITUTIVE MODEL

The simulation of ceramic microstructures presented in the previous chapter, provides extremely important pieces of information about the influence of the fundamental properties of the material on the overall behaviour of the ceramic under different loading conditions. Its role is, therefore, particularly important to understand the deformation and failure mechanisms in view of the development of novel materials with improved performance. However, the computational cost required to explicitly model the whole grain structure of a macroscopic device is far beyond the capability of the modern computers, which implies the necessity of macroscopic continuum models to simulate the behaviour of macroscopic structures.

Within the continuum models developed in the past decades, the constitutive models developed by Johnson and Holmquist (commonly known as JH1 [88], JH2 [89], and JHB [90]) are arguably the most used material models for simulation of the response of ceramic materials to impact loading. The modified Johnson-Holmquist material model (also known as JH2), in particular, has also been implemented in several pieces of commercial software, including Autodyn, Epic, and LS-Dyna [91], and is widely used for armour design and simulation [92, 93]. Given the availability of the material parameters of numerous ceramic materials in literature, this constitutive model was considered to be the appropriate starting point for the development of an innovative material model for the simulation of the failure of ceramic materials.

Because it is not possible to modify the constitutive model already implemented in LS-Dyna, a “user defined material model” [152] was developed and included in an ad hoc modified LS-Dyna solver, as presented in Section 5.1.

Once the user defined material model had been coded, the approach proposed for the development of the innovative constitutive model consists of a systematic improvement of the

JH2 model (i.e. an isotropic, phenomenological, continuum model) including first the anisotropic nature of the damage (presented in Section 5.2), and then a more "physical" definition of the damage (presented in Section 5.3).

## 5.1 "Modified Johnson-Holmquist" (JH2) constitutive model

The JH2 formulation imposes the elastic behaviour of the material until a certain threshold is reached. Then the material softens gradually as the damage increases, until its complete failure, when the value of the damage reaches its maximum (i.e. $D = 1$) [89, 93, 153]. The damage is defined analogously to the Johnson-Cook model for metals [154], and it consists of a scalar value equal to the sum of the ratios of the plastic strain increment ($\Delta\varepsilon_p$) over the plastic strain to fracture under constant pressure ($\varepsilon_p^f$) for each time-step:

$$D = \sum \frac{\Delta\varepsilon_p}{\varepsilon_p^f} \tag{49}$$

The plastic strain to fracture under constant pressure ($\varepsilon_p^f$) is function of the pressure ($P^*$) and the maximum tensile strength ($T^*$) normalised to the pressure at the Hugoniot Elastic Limit ($P_{HEL}$), and two material constants ($D_1$ and $D_2$):

$$\begin{cases} P^* = P/P_{HEL} \\ T^* = T/P_{HEL} \end{cases} \tag{50}$$

$$\varepsilon_p^f = D_1(P^* + T^*)^{D_2} \tag{51}$$

As the damage increases, the critical stress surface shrinks from the intact ($D = 0$) to the failed ($D = 1$) condition, as shown in Fig. 5.1. In particular, the critical stress ($\sigma^*$) decreases from the intact material condition ($\sigma_i$) to the strength of the completely failed material ($\sigma_f$), following the relationship:

$$\sigma^* = \sigma_i - D(\sigma_i - \sigma_f) \tag{52}$$

The strength of the intact and failed material are defined as:

$$\begin{cases} \sigma_i = A(P^* + T^*)^N \cdot \sigma_{HEL} \\ \sigma_f = B(P^*)^M \cdot \sigma_{HEL} \end{cases} \tag{53}$$

The two strengths are a function of the stress at the Hugoniot Elastic Limit[4] ($\sigma_{HEL}$), the normalised pressure ($P^*$) and maximum tensile strength ($T^*$), and four material constants ($A$, $B$, $M$, and $N$).

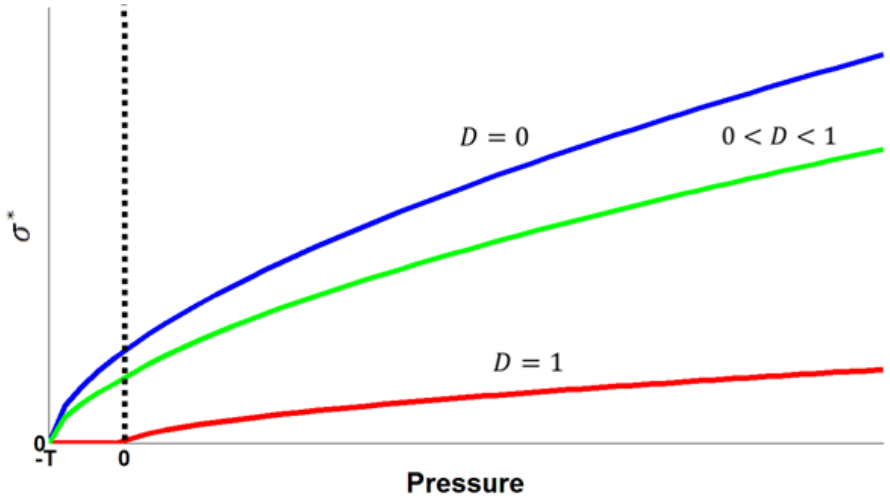



**Fig. 5.1:** Definition of the material strength in JH2 model

To determine if the element has reached the critical stress the trial deviatoric stresses ($S_{ij}^{tr}$) and the trial effective stress ($\bar{\sigma}^{tr}$) are evaluated as:

$$\begin{cases} S_{ij}^{tr} = S_{ij}^{(n-1)} + 2G\dot{e}_{ij}\Delta t \\ \bar{\sigma}^{tr} = \sqrt{\frac{3}{2} S_{ij}^{tr} : S_{ij}^{tr}} \end{cases} \tag{54}$$

Where $S_{ij}^{(n-1)}$ is the deviatoric stress at the previous time step, $G$ is the shear modulus, $\dot{e}_{ij}$ is the deviatoric strain rate, and $\Delta t$ is the time increment.

The type of behaviour of the material is evaluated from the volumetric strain ($\mu$) and the comparison of the trial effective stress ($\bar{\sigma}^{tr}$) with the critical stress ($\sigma^*$), as follows:

[4] The definitions of $P_{HEL}$ and $\sigma_{HEL}$, alongside their derivation from the Hugoniot Elastic Limit are reported in Appendix C

- **elastic** ($\bar{\sigma}^{tr} \leq \sigma^*$)
- **tensile inelastic** ($\bar{\sigma}^{tr} > \sigma^*$ and $\mu < 0$)
- **compressive inelastic** ($\bar{\sigma}^{tr} > \sigma^*$ and $\mu > 0$)

Where $\mu = Tr(\varepsilon) = (\rho - \rho_0)/\rho_0$.

In the first case the material follows the classic linear elastic laws, hence the effective stresses are just the trial stresses and the hydrostatic pressure is calculated from the volumetric stress and the bulk modulus ($K_1$):

$$\begin{cases} \bar{\sigma} = \bar{\sigma}^{tr} \\ P = K_1 \mu \end{cases} \tag{55}$$

In the second case the damage instantaneously increases to 1, which corresponds to complete brittle failure of the domain:

$$\begin{cases} \bar{\sigma} = \sigma^* = \sigma_f \\ P = K_1 \mu \end{cases} \tag{56}$$

In the compressive elastic case, instead, the stresses are returned to the critical stress surface, and the hydrostatic pressure is a third degree polynomial function of the volumetric strain:

$$\begin{cases} \bar{\sigma} = \sigma^* \\ P = K_1 \mu + K_2 \mu^2 + K_3 \mu^3 \end{cases} \tag{57}$$

The plastic strains increment deriving from the radial return of the deviatoric stress is then used to calculate the increment of damage, as reported in Eq. (49):

$$D = \sum \frac{\Delta \varepsilon_p}{\varepsilon_p^f} \tag{49}$$

The described constitutive law was implemented as a user defined material model in LS-Dyna and compared with the JH2 model already implemented in the software.

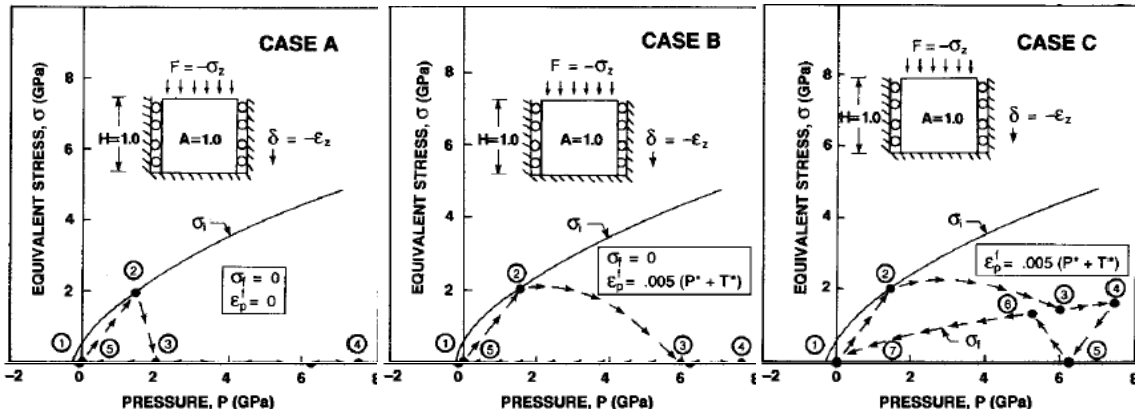



**Fig. 5.2:** JH2 test cases [89]

To verify the correctness of the implemented algorithm, three test cases (Fig. 5.2) are simulated with both the constitutive models, and the results are compared in Fig. 5.3. The three test cases are introduced by Johnson and Holmquist in the work that first defines the JH2 model [89], and consist of the same FE model subject to the same load with three different sets of material parameters.

The model of the test cases consists of a single cubic element subject to a uniform compressive load perpendicularly to one face (top). The opposite face (bottom) is fully constrained and the side faces are constrained only in the direction perpendicular to the load (i.e. the domain is fully confined without sliding friction). The load increases linearly until a certain deformation is reached, and then decreases symmetrically back to zero.

The differences between the results reported in Fig. 5.3 are due to the different values assigned to $B$ and $D_1$, which influence respectively the failed material strength defined in Eq. (52), and the plastic strain under constant pressure defined in Eq. (50), as reported in Fig. 5.2.

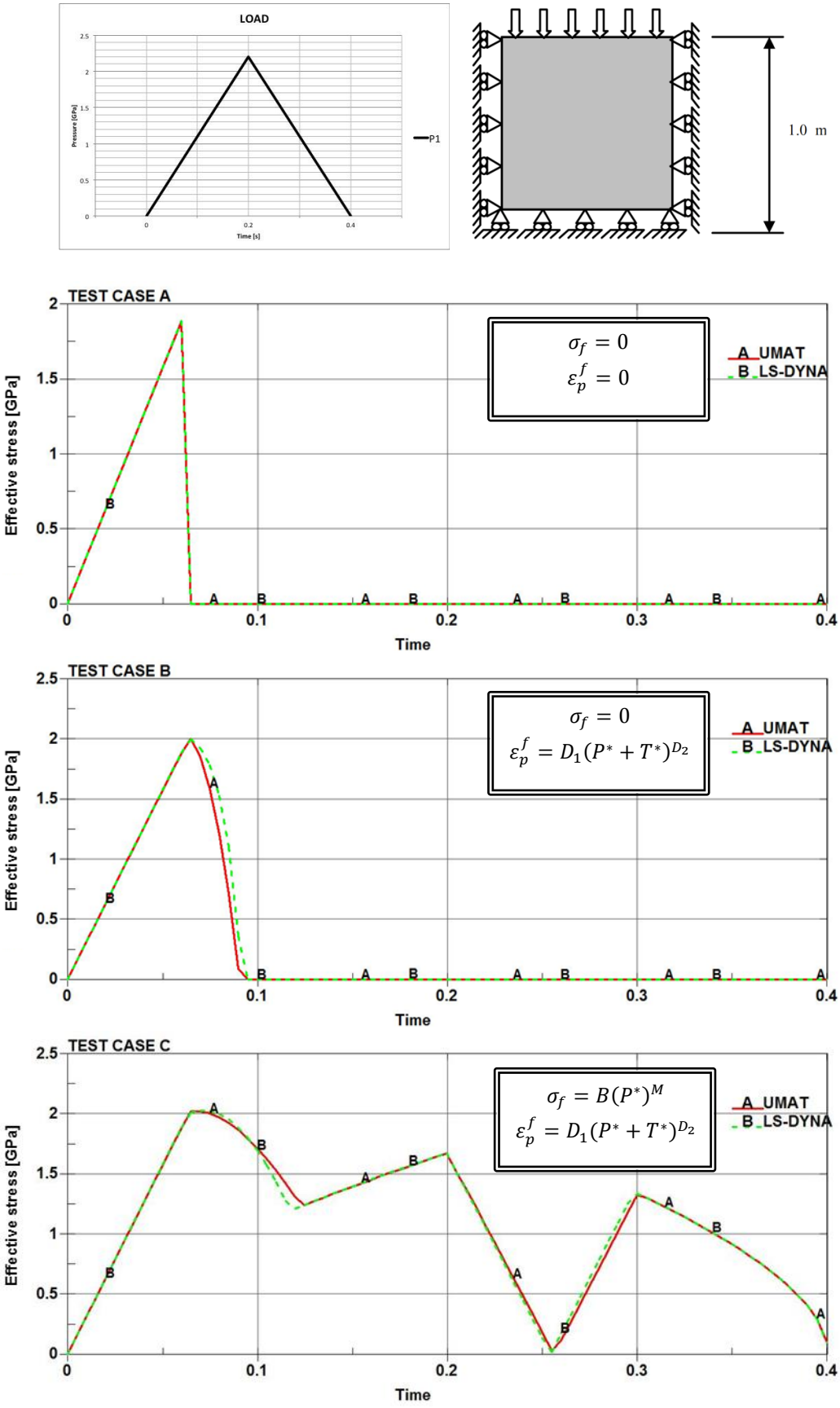



**Fig. 5.3:** Comparison of test case results using user defined material and LS-Dyna JH2

In *Case A* ($D_1 = B = 0$), $\varepsilon_p^f$ is zero, so as soon as the trial stress ($\bar{\sigma}^{tr}$) overshoots the critical stress ($\sigma^*$) the damage increases instantaneously from 0 to 1. The strength of the failed material ($\sigma_f$) is zero as well, therefore the structure is not able to carry any load after the failure.

In *Case B* ($D_1 \neq 0$ and $B = 0$), $\varepsilon_p^f$ has a non-zero value, thus, when $\bar{\sigma}^{tr} > \sigma^*$, the damage increases gradually from 0 to 1. On the other hand, $\sigma_f$ is still zero, so the material does not have any strength after the complete failure.

In *Case C* ($D_1 \neq 0$ and $B \neq 0$), $\varepsilon_p^f$ has a non-zero value, so, when $\bar{\sigma}^{tr} > \sigma^*$, the damage increases gradually from 0 to 1, and $\sigma_f$ being non-zero as well, the material retains reduced strength in compression after its complete failure.

The comparison shows an excellent agreement between the user defined material model and the JH2 implemented in LS-Dyna, therefore the first has been used as a base to improve the JH2 model, overcoming some of the simplifying assumptions contained in the original formulation, which limit the understanding of the real behaviour of the ceramic material at the impact.

One of the principal assumptions of the JH2 model is that the material is modelled as continuum isotropic medium, whilst, in reality the damage of ceramics is mainly due to crack propagation inside the material, which is an intrinsically anisotropic and discontinuous phenomenon. Moreover, the phenomenological nature of the method – which needs up to 20 constitutive constants inferred from 12 different experimental tests – hides the effect of the physical properties on the material behaviour, hindering possible ways to improve the material performance.

In this work two main modifications are proposed. First in Section 5.2 a possible method to take into account the anisotropy of the failure process by modifying the definition

of the damage variable is illustrated. In Section 5.3, then, the phenomenological approach to crack initiation is modified considering crack growth mechanisms, thus linking the damage evolution in the material to its physical properties.

## 5.2 Implementation of the anisotropy

Probably the most limiting fundamental assumption of the JH2 method is the postulate of isotropic evolution of the damage within the single element, since the failure of ceramic materials under impact is mainly due to the propagation and branching of cracks [99], which are intrinsically anisotropic phenomena.

The anisotropic evolution of the damage is implemented by defining $D$ as a diagonal matrix (instead of a scalar value like in JH2 model). The projection of the damage along three orthogonal directions localises the damage on planes, instead of spreading it within the whole volume.

A diagonal damage tensor derives from the choice of the principal orthotropic frame as the direction of the problem. The choice of developing this approach – even if theoretically the model could support a fully populated damage tensor – is preparatory for the further improvement presented in Section 5.3.

The definition of the damage at the generic time step $(n+1)$ presented in (49) can be reformulated as the sum of the pre-existent damage and the damage increment at the time-step $(n)$:

$$D^{(n+1)} = \sum_{1}^{n+1} \frac{\dot{\varepsilon}_p \Delta t}{\varepsilon_f^p} = D^{(n)} + \frac{\dot{\varepsilon}_p \Delta t}{\varepsilon_f^p} \tag{58}$$

Using the incompressibility condition (i.e. the sum of the plastic strain rate components is zero), the equivalent plastic strain rate ($\dot{\varepsilon}_p$) can be factored:

$$\dot{\varepsilon}_p^2 = \dot{\varepsilon}_{p11}^2 + \dot{\varepsilon}_{p22}^2 + \dot{\varepsilon}_{p33}^2 + 2\left(\dot{\varepsilon}_{p23}^2 + \dot{\varepsilon}_{p13}^2 + \dot{\varepsilon}_{p12}^2\right) \tag{59}$$

The components of the plastic strain rate in the principal stress coordinates ($\dot{\varepsilon}_{p1}^2$, $\dot{\varepsilon}_{p2}^2$, and $\dot{\varepsilon}_{p3}^2$) can be defined as[5]:

$$\begin{aligned} \dot{\varepsilon}_p^2 = \left(\dot{\varepsilon}_{p11}^2 + \dot{\varepsilon}_{p13}^2 + \dot{\varepsilon}_{p12}^2\right) + \left(\dot{\varepsilon}_{p22}^2 + \dot{\varepsilon}_{p23}^2 + \dot{\varepsilon}_{p12}^2\right) + \\ \left(\dot{\varepsilon}_{p3}^2 + \dot{\varepsilon}_{p23}^2 + \dot{\varepsilon}_{p13}^2\right) = \dot{\varepsilon}_{p1}^2 + \dot{\varepsilon}_{p2}^2 + \dot{\varepsilon}_{p3}^2 \end{aligned} \tag{60}$$

This allows for the definition of the damage increment along a generic principal direction $j$ as:

$$dD_j = \frac{\dot{\varepsilon}_{pi} \cdot \Delta t}{\varepsilon_f^p} \tag{61}$$

The damage increments along the separate principal directions can be combined into a diagonal matrix ($dD_{j,k}$):

$$dD_{j,k} = \begin{bmatrix} dD_1 & 0 & 0 \\ & dD_2 & 0 \\ symm & & dD_3 \end{bmatrix} \tag{62}$$

The partial damage increments are linked to the total damage increment by the relationship:

$$dD = \sqrt{dD_1^2 + dD_2^2 + dD_3^2} \;\Rightarrow\; D^{(n+1)} = D^{(n)} + dD \tag{63}$$

The damage increments in the three principal directions are used to determine the critical stress in those directions, as:

$$\sigma_j^* = \sigma_{i_j}^{(anis)} \cdot \sqrt{1 - D} \cdot \sqrt{1 - \sum_1^{n+1} \frac{dD_j^2}{dD}} \tag{64}$$

[5] The shear terms ($\dot{\varepsilon}_{p12}^2$, $\dot{\varepsilon}_{p13}^2$, and $\dot{\varepsilon}_{p23}^2$) are included in the formulation because, for materials with a fully populated compliance/stiffness matrix (e.g. single crystal alumina), a principal stress state can induce a non-principal strain state.

The critical stress in the generic principal direction $j$ is function of the intact material strength in the same direction ($\sigma_{i_j}^{(anis)}$), the total damage ($D$) and the sum of all the damage increments at the previous time step in the same direction.

If the effective stress is higher than the critical stress in one direction, the deviatoric stresses are returned radially to the critical surface. This procedure is performed separately along the three principal directions – in contrast with the isotropic approach that is based exclusively on effective quantities.

### *5.2.1 Single element verification*

The approach presented is tested on three test cases, the first consisting of a single element cube fully confined on all the faces but one (top), on which is applied a linearly increasing compressive load ($P_1$) (Fig. 5.4). The second and the third test the same single cubic element with an additional compressive load on the right face ($P_2$) first with half the magnitude (Fig. 5.5) and then identical to $P_1$ (Fig. 5.6). All the results of the anisotropic models are compared against the isotropic response of the material.

The newly defined quantity $\sigma_i^{(anis)}$ is a diagonal 3x3 matrix that represents the strength of the intact material along the principal directions. This variable takes into account the possible initial anisotropy of the material (e.g. due to not uniform pressure during the sintering process) that is neglected in the original JH2 formulation. For sake of simplicity and clarity of representation of the results, the three $\sigma_{i_j}^{(anis)}$ are imposed to be equal to each other and proportional to the isotropic intact strength of the material by a calibration parameter $\beta$:

$$\sigma_i^{(iso)} = \sqrt{\beta} \cdot \sigma_i^{(anis)} \tag{65}$$

The effect of $\beta$ on the damage evolution is also explored in the test cases presented in Fig. 5.4, Fig. 5.5, and Fig. 5.6.

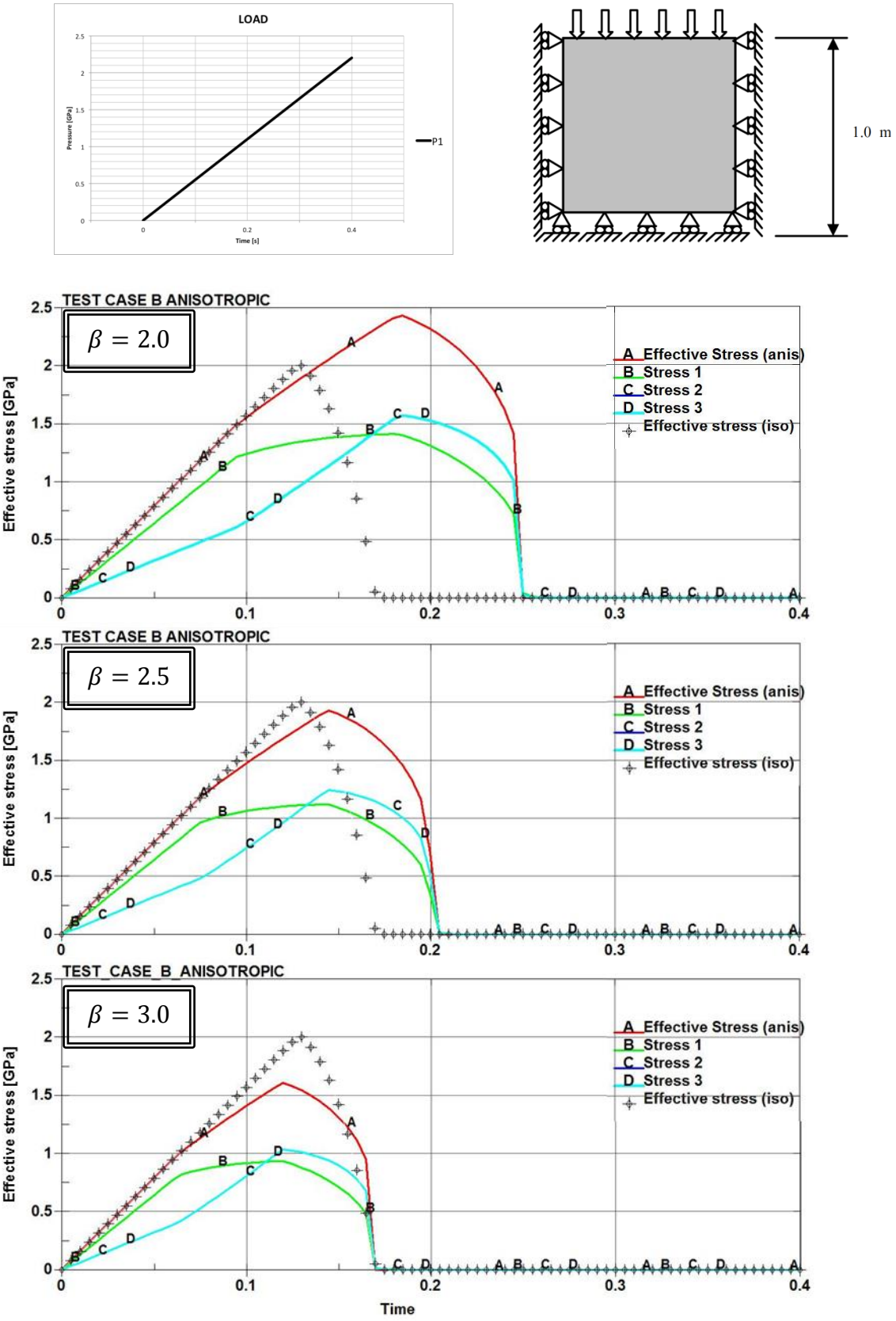



**Fig. 5.4:** Comparison of stresses between the isotropic and anisotropic models subject to uniaxial load

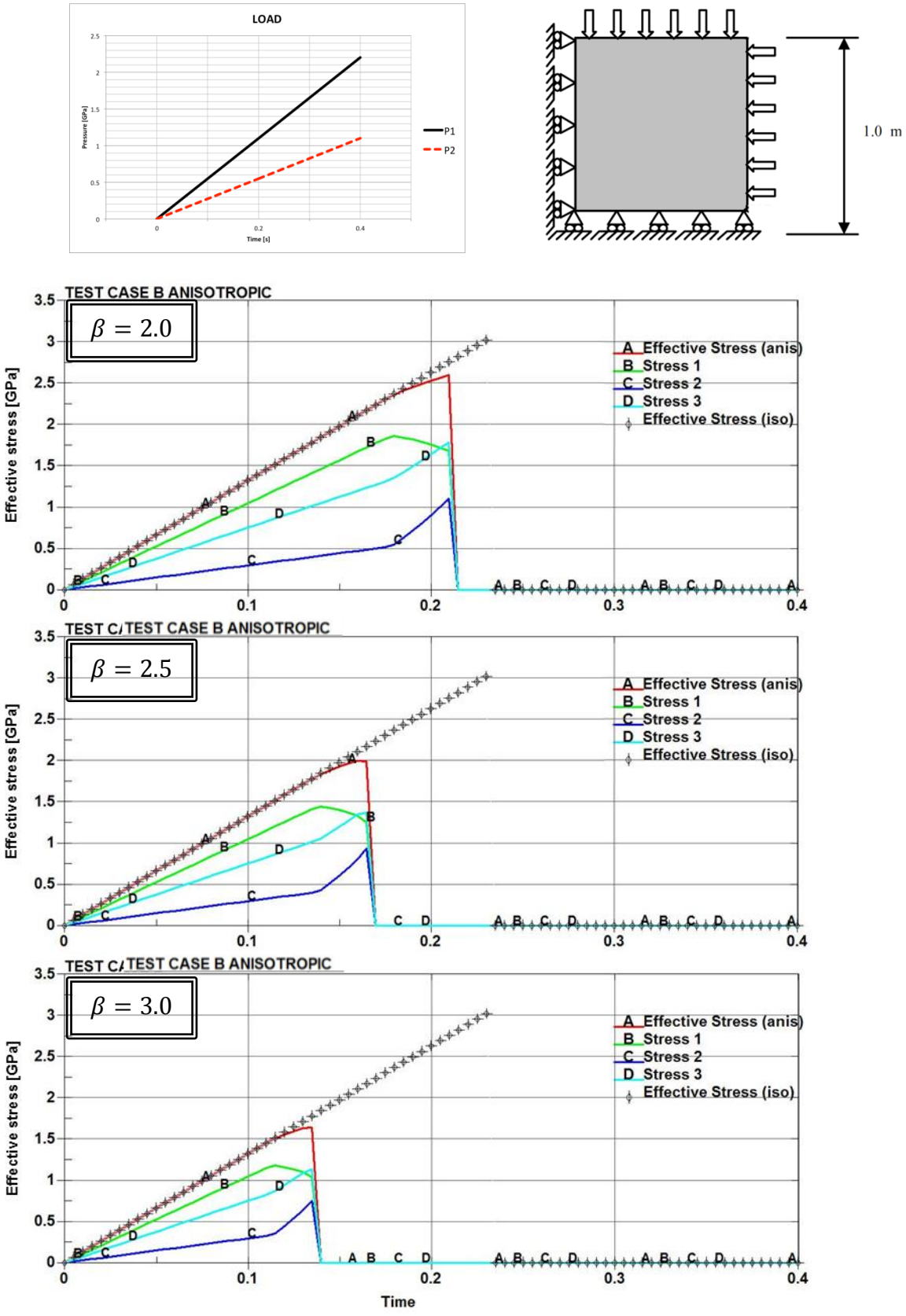



**Fig. 5.5:** Comparison of stresses between the isotropic and anisotropic models subject to asymmetric biaxial load

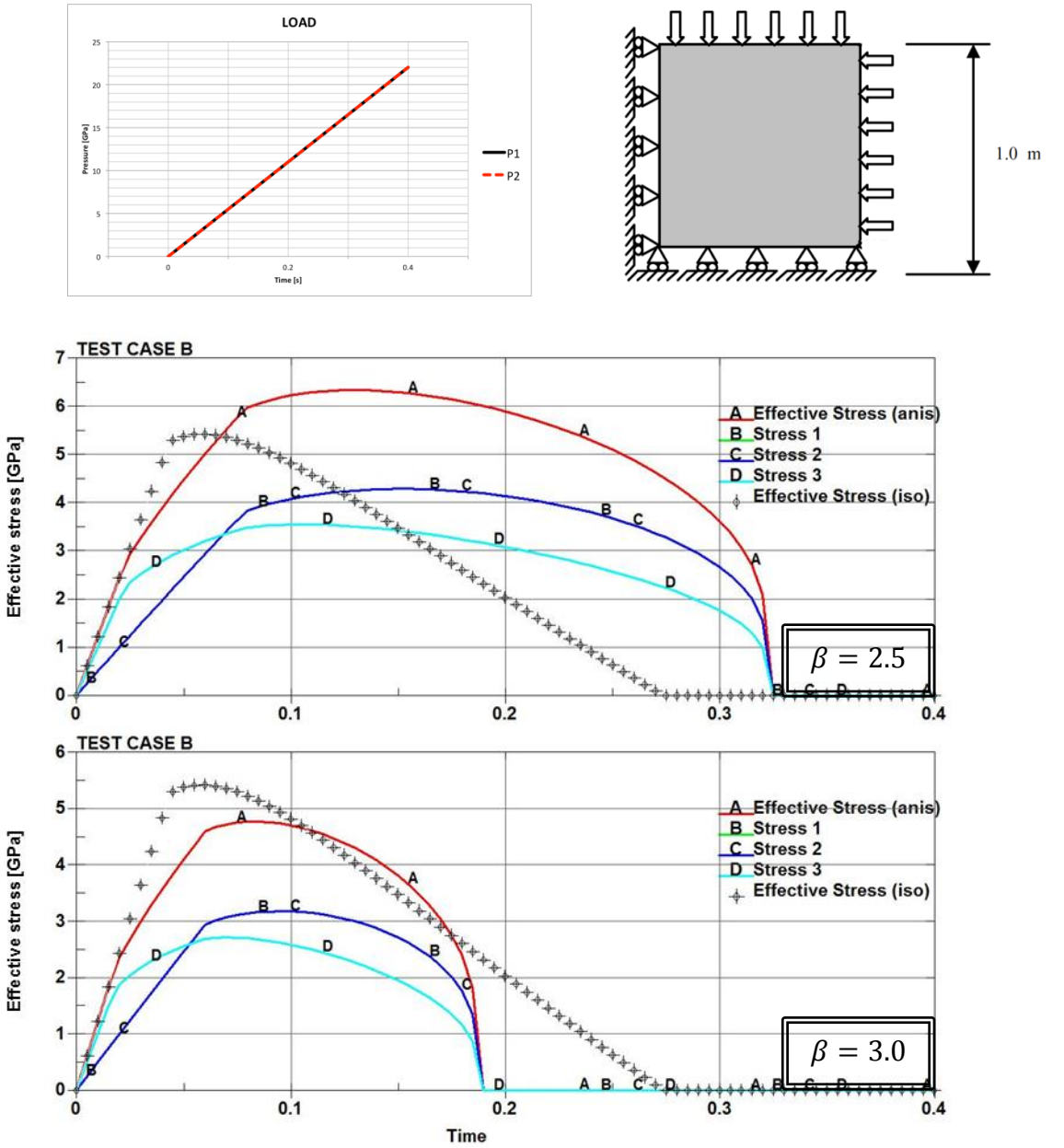



**Fig. 5.6:** Comparison of stresses between the isotropic and anisotropic models subject to symmetric biaxial load

The red curve (marked A) represents the effective stress evaluated with the anisotropic material model, whilst the stress components in the principal directions are described by the green (B, Stress 1), blue (C, Stress 2) and cyan (D, Stress 3) curves. Finally the crosses represent the effective stress evaluated with the JH2 model presented in Section 5.1.

The loading conditions defined in the three test cases imply that, in all the models, the principal directions are perpendicular to the cube faces.

Fig. 5.4 shows how the higher stress in the direction of the load (i.e. direction 1) triggers the increment of the damage in that direction. The softening of the material in the load direction increases the rate of growth of the stress in the perpendicular directions (identical because of the symmetry) until the material starts softening in those directions too, to then fail completely.

In Fig. 5.5 the stress in the direction of the bigger load ($P_1$) is again the first to reach the critical value. Then the damage starts growing in the unloaded direction (i.e. direction 3) due to the effect of the confinement, which leads to a sudden failure of the material, in accordance with the behaviour observed in the isotropic simulation.

Lastly, in Fig. 5.6 the stress in the unloaded direction grows faster than the in the two other directions because of the confinement effect, thus reaching the critical stress value first. Subsequently the stresses in the loaded directions reach the critical threshold too, leading to the complete failure of the material.

In all the three test cases illustrated, the combination of the separately evolving stresses in the principal directions reflects in the presence of a "hardening-type" behaviour of the effective stress (i.e. additional stress is required to propagate the damage once started), before the material softens and fails completely. This "hardening" effect is absent in the isotropic approach.

The effect of the calibration parameter $\beta$, or more generally, the effect of the initial strength of the material $\sigma_i^{(anis)}$ on the damage initiation is quite relevant for the accuracy of the final results, and therefore the appropriate values must be determined per each analysed material. Also the formulation of the damage evolution law is not supported by any experimental or numerical evidence, and needs to be calibrated to better simulate the real behaviour of ceramic materials.

### *5.2.2 Impact test validation*

The model is validated comparing the numerical simulation of with both isotropic and anisotropic JH2 models against the experimental results presented in this thesis.

The FE model adopted, illustrated in Fig. 5.7 consists of a quenched steel projectile impacting perpendicularly a cylindrical alumina target, backed by an aluminium bar, reproducing the impact tests presented in Section 3.3.3.

The constitutive models adopted for the projectile and the backing bar are respectively elastic-plastic and purely elastic, whilst the target is modelled with the two JH2 models presented in the previous sections (i.e. “classic” and “anisotropic”).

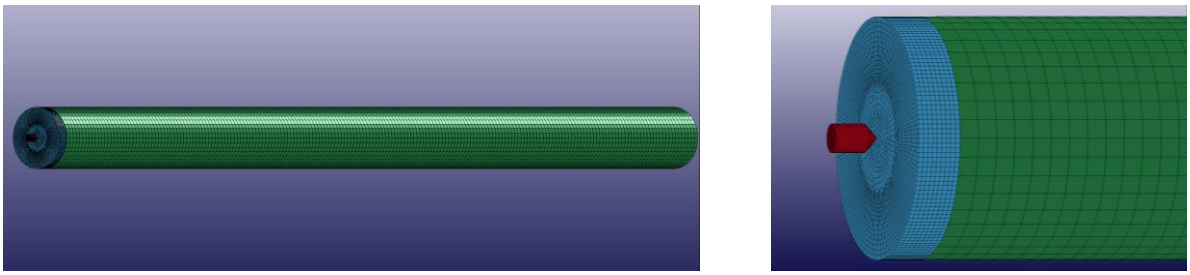


**Fig. 5.7:** FE model of the impact test

The results reported in Fig. 5.8 compare the experimental measurement of the force transmitted from alumina targets to the backing bar at the impact (already described in Fig. 3.35) against both the isotropic (classic) JH2 model and the anisotropic variation suggested in the previous section. Multiple values of $\beta$ are used to illustrate the influence of this parameter on the overall behaviour of the system.

All the simulations seem to be in reasonable good agreement with the experimental results, with the force peak lowering and broadening as $\beta$ increases. In particular the adoption of $\beta = 2$ seems to provide the best fitting results.

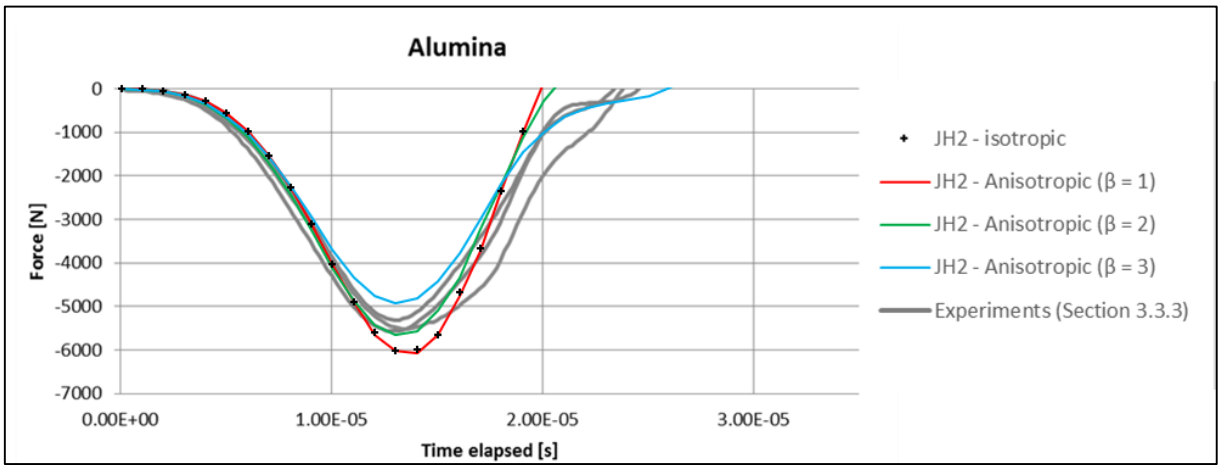



**Fig. 5.8:** Backing bar measurement for impact test on alumina targets

Despite measuring similar stress wave profiles in the backing bar, differences can be observed in the evolution of the damage in the impacted area. Specifically, the introduction of the anisotropic evolution of the damage induces a spreading of the "damaged area", without however changing the damage pattern (i.e. damaged zone confined to the surface of contact between projectile and target). Within the anisotropic models, the damaged area increases with the parameter $\beta$, as it has the effect to lower the critical stress – see Eq. (65) – thus "weakening" the material.

A comparison of the damaged area predicted by the isotropic and the anisotropic models is reported in Fig. 5.9, alongside the diameter of the ring crack measured experimetally and reported in Table 3.10 (white circle).

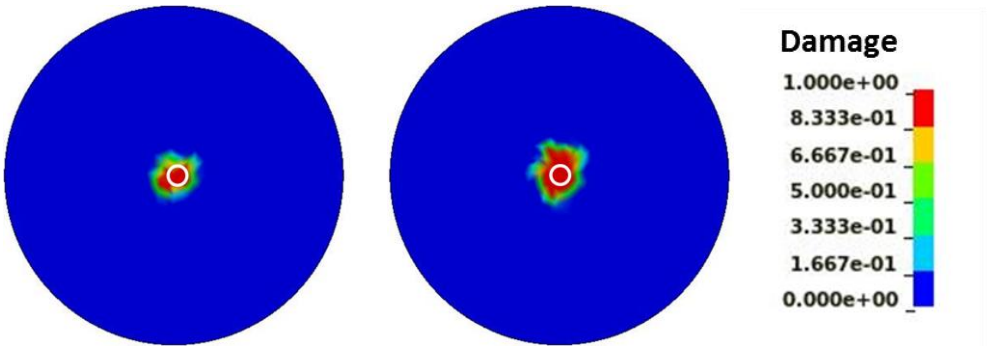



**Fig. 5.9:** Damage distribution on the target using the isotropic (left) and anisotropic (right) JH2 material model

Due to the smeared definition of the damage parameter the numerical models are not able to reproduce the correct shape of the crack. However, the comparison against the ring crack observed experimentally provides a further confirmation of the validity of the model. The slightly bigger area predicted numerically is also in accordance with the experimental observations that highlight the presence of short radial cracks propagating from the impact area, as can be observed in Fig. 3.41a.

The tests performed confirm the validity of the JH2 model for the specific loading conditions analysed, for which the anisotropic evolution of the damage seems to have a limited influence on the overall behaviour of the system. Nevertheless the introduction of the damage matrix – in place of the single scalar value defined in the classic JH2 – is functional to the development of more "physically based" constitutive model, presented in the next section. In particular, to create a link between the constitutive model and the real mechanisms governing the failure of ceramic materials, the model presented in the next section embeds considerations on the crack growth mechanisms in place of the phenomenological relations used to define the damage in the JH2 models, which might help in the comparison of the numerical results with the experimental observation of the damaged zones.

## 5.3 Introduction of a new "crack-based" damage evolution

In this section a new definition of the damage is introduced to embed some considerations about the mechanisms governing the failure of brittle materials.

Ceramic materials contain defects (e.g. micro-cracks, small holes, poorly bonded particles) that can act as the nuclei of macroscopic cracks under certain loading conditions. Despite several topologically different features have been observed to act as nuclei [155],

their mechanical behaviour in compression has been proven to be accurately described by isolated sharp inclined cracks [98, 99].

Therefore, the starting of the damage growth in a ceramic medium, with a reasonably low number of initial defects, can be assumed to depend on the behaviour of a single sharp crack – isolated from the array of randomly oriented penny-shaped cracks – within an elastic continuum medium (Fig. 5.10).

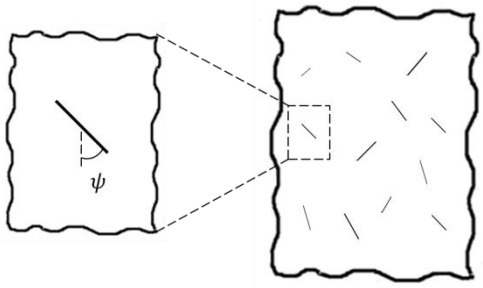



**Fig. 5.10:** Pattern of isolated inclined cracks and sample volume with a single inclined penny-shaped crack

Considering the sample volume subject to a purely compressive load (i.e. all the principal stresses are compressive), with $\sigma_1$ the most compressive principal stress and $\sigma_3$ the least compressive principal stress (i.e. $|\sigma_1| > |\sigma_2| > |\sigma_3|$), the stress state on the crack can be decomposed in shear ($\tau$) and normal ($\sigma$) components (Fig. 5.11a), defined respectively as:

$$\tau = (\sigma_3 - \sigma_1) \sin\psi \cos\psi \tag{66}$$

$$\sigma = \sigma_1 \sin^2\psi + \sigma_3 \cos^2\psi \tag{67}$$

The stress state results in an opening force $F_W$ acting in direction of $\sigma_3$ (Fig. 5.11b), that depends on the friction coefficient $\mu$, the crack radius $a$, and the inclination of the crack $\psi$ (defined in Fig. 5.10):

$$F_W = (\tau + \mu\sigma)\pi a^2 \sin\psi \tag{68}$$

The opening force $F_W$ creates a mode I stress state, inducing the crack to grow in the direction of $\sigma_1$, as illustrated in Fig. 5.11c.

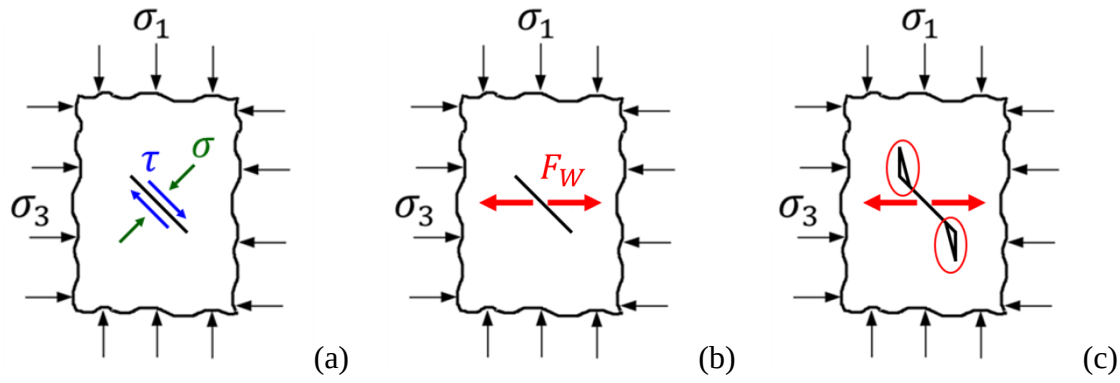



**Fig. 5.11:** Stress state on the crack (a), opening force created by the stress state (b) and crack growing direction induced by the opening force (c)

The analytical model presented is validated by numerous experimental observations, such as for example the one presented by Vekinis et al. [156].

To embed these considerations in the anisotropic model presented in the previous section, the damage definition is modified to consider only the damage increment in the direction of the maximum principal stress. Since the principal directions can rotate during a simulation – because of either the change of the remote load or the damage evolution affecting the stress state in the volume – the approach proposed follows the rotation of the principal stress directions.

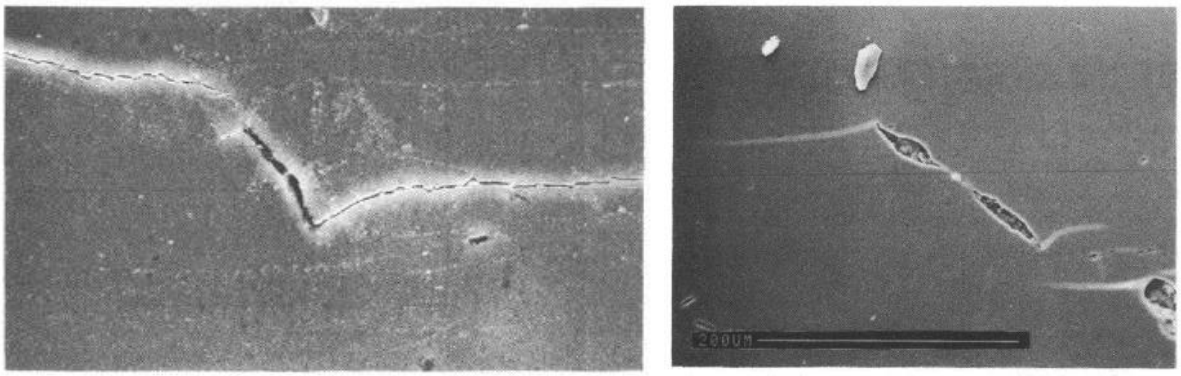


**Fig. 5.12:** Propagation of micro-cracks under horizontal compression load [156]

The two main difficulties of evaluating the damage along the principal directions are related to the tensor rotations involved to follow the variation of the principal coordinates

system. Some commercial software (e.g. Abaqus) have already implemented procedure for the efficient rotation along the principal directions, however this thesis an alternative approach has been developed to allow for the implementation of the material model in a wide range of FE analyser, as for example the already mentioned in-house software DEST. In particular the two main issues addressed are related to the high computational cost of the tensor rotation and the accumulation of the error deriving from the iterative rotation of the same tensor from global to principal direction and back at each time step.

### *5.3.1 Non-iterative rotation*

The first issue is approached implementing a non-iterative method for the rotation of 3x3 symmetric matrices [157], which is less computationally expensive than the classic iterative matrix rotation method. The proposed methodology solves the characteristic equation with a change of variables, instead of calculating iteratively the solution.

The characteristic equation of a generic 3x3 symmetric matrix is:

$$0 = -\det(A - \lambda I) = -det\begin{bmatrix} a_{00} - \lambda & a_{01} & a_{02} \\ a_{01} & a_{22} - \lambda & a_{12} \\ a_{02} & a_{12} & a_{22} - \lambda \end{bmatrix} = \lambda^3 - c_2\lambda^2 + c_1\lambda - c_0 \quad (69)$$

The terms $c_0$, $c_1$, and $c_2$ of the characteristic equation are defined as:

$$\begin{cases} c_0 = a_{00}a_{11}a_{22} + 2a_{01}a_{02}a_{12} - a_{00}a_{12}^2 - a_{11}a_{02}^2 - a_{22}a_{01}^2 \\ c_1 = a_{00}a_{11} + a_{00}a_{22} + a_{11}a_{22} - a_{01}^2 - a_{02}^2 - a_{12}^2 \\ c_2 = a_{00} + a_{11} + a_{22} \end{cases} \quad (70)$$

To eliminate the square term, the variable $\lambda$ is substituted with:

$$\lambda = \xi + \frac{c_2}{3} \quad (71)$$

The characteristic equation can, then, be rewritten in terms of $\xi$ as:

$$\xi^3 - \frac{3c_1 - c_2^2}{3}\xi + \frac{-2c_2^3 + 9c_1c_2 - 27c_0}{27} = 0 \quad (72)$$

For a more compact formulation of the solutions the following parameters are defined:

$$\begin{cases} a = -\dfrac{3c_1 - c_2^2}{3} \\ b = \dfrac{-2c_2^3 + 9c_1c_2 - 27c_0}{27} \\ \vartheta = \dfrac{1}{3}atan2\left(\sqrt{\dfrac{a^3}{27} - \dfrac{b^2}{4}}, \dfrac{b}{2}\right) \end{cases} \tag{73}$$

Finally the generic roots of the so-written characteristic equation are calculable analytically as:

$$\begin{aligned} \lambda_0 &= \frac{c_2}{3} + 2\sqrt{-\frac{a}{3}}\cos(\vartheta) \\ \lambda_1 &= \frac{c_2}{3} - \sqrt{-\frac{a}{3}}\left(\cos(\vartheta) + \sqrt{3}\sin(\vartheta)\right) \\ \lambda_2 &= \frac{c_2}{3} - \sqrt{-\frac{a}{3}}\left(\cos(\vartheta) - \sqrt{3}\sin(\vartheta)\right) \end{aligned} \tag{74}$$

To further reduce the computational cost of the operation, the model provides simplified equations to evaluate the roots for the condition: $\frac{a^3}{27} = \frac{b^2}{4}$ are introduced.

The calculation of the rotation matrix $[M]$ is performed by solving the equation $[M]\boldsymbol{v} = 0$ for each eigenvalue $\lambda$ and the corresponding eigenvector $\boldsymbol{v}$, as illustrated in [157].

The non-iterative approach performs the rotation of a 3x3 symmetric matrix about 4.5 times faster than the classic iterative method, maintaining a comparable accuracy, thus saving a valuable amount of computational time.

### *5.3.2 Minimization of the cumulative error*

The second issue in the evaluation of the damage along the maximum principal direction is to avoid the accumulation of the error incidental to the single rotation. Usually the errors are negligible – with respect to the magnitude of the terms in the matrix – for the single rotation but may significantly affect the accuracy of the simulation if accumulate for a high number of time step. The growth of the error to values that would affect the validity of the

simulation is avoided by rotating only the incremental values. All the operations are performed in the principal coordinate system, and only the radially returning stress and the damage increment are rotated from principal to local coordinates. The magnitude of those two quantities is sensibly smaller than the values of the stresses; hence the error in the rotation of such matrices is much smaller than what would be obtained rotating back and forth the stress tensor.

Given the solutions presented the method is described in the flowchart in Fig. 5.13.

In the first block, the trial stress tensor in local coordinates ($\sigma_{ij}^{tr}$) is evaluated from the strains at the previous time step, the maximum principal stress ($\sigma_1$) is the first eigenvalue of the rotation matrix ($[M] = [\lambda_0\ \lambda_1\ \lambda_2]$) evaluated as in equation (74), and the critical stress in global coordinates ($\sigma_{ij}^{*}$) is calculated as combination of the initial strength of the material ($\sigma_{i_j}$) and the damage in global coordinates ($D_{ij}$):

$$\sigma_{ij}^{*} = \sigma_{i_j}\left(1 - D_{ij}\right) \tag{75}$$

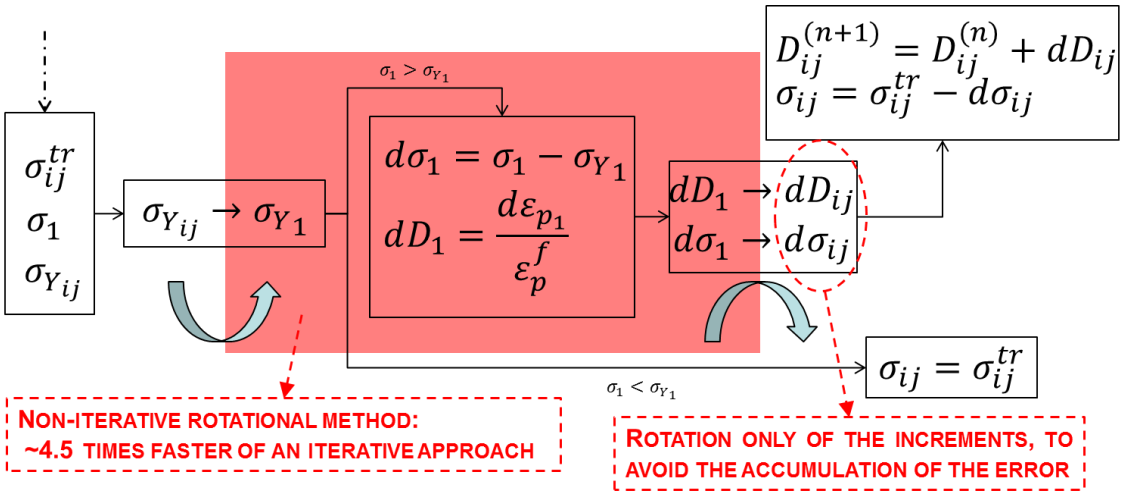



**Fig. 5.13:** Chart of the rotation method proposed

In the first block, the trial stress tensor in local coordinates ($\sigma_{ij}^{tr}$) is evaluated from the strains at the previous time step, the maximum principal stress ($\sigma_1$) is the first eigenvalue of

the rotation matrix ($[M] = [\lambda_0\ \lambda_1\ \lambda_2]$) evaluated as in equation (74), and the critical stress in global coordinates ($\sigma_{ij}^*$) is calculated as combination of the initial strength of the material ($\sigma_{i_j}$) and the damage in global coordinates ($D_{ij}$):

$$\sigma_{ij}^* = \sigma_{i_j}\left(1 - D_{ij}\right) \tag{76}$$

In the second block, then, the critical stress tensor is rotated in the principal direction using the rotation matrix $[M]$:

$$\left[\sigma_{ij}^*\right] = [M]^{-1}[\sigma_{123}^*][M] \tag{77}$$

The maximum principal stress ($\sigma_1$) is then compared with the critical stress in the same direction ($\sigma_1^*$). If $\sigma_1 < \sigma_1^*$ the material behaves elastically and the stress tensor is just the trial one. If, instead, $\sigma_1 > \sigma_1^*$, the radial return ($d\sigma_1$) and the damage increment ($dD_1$) in the direction of the maximum principal stress are calculated and then rotated in global coordinates:

$$d\sigma_1 = \sigma_1 - \sigma_1^* \Rightarrow d\sigma_{ij} = [M]\begin{bmatrix} d\sigma_1 & 0 & 0 \\ 0 & 0 & 0 \\ 0 & 0 & 0 \end{bmatrix}[M]^{-1} \tag{78}$$

$$dD_{ij} = [M]\begin{bmatrix} dD_1 & 0 & 0 \\ 0 & 0 & 0 \\ 0 & 0 & 0 \end{bmatrix}[M]^{-1} \tag{79}$$

Finally those two quantities are used to update the stress and damage tensors.

The methodology presented to rotate the damage tensor leads to the formulation of a fully populated tensor (capturing the anisotropic nature of the damage in ceramic materials), avoiding any accumulation of the numerical error that derives from the single rotation.

The implementation of the suggested method, although providing a more physical based evaluation of the damage, based on considerations on the growth mechanism of a single crack, still requires the determination of some parameters to describe the initiation and evolution of the damage. The experimental characterisation of these parameters, besides requiring complex techniques that have still to be developed to full extent, would present

similar limitations to the ones illustrated for the JH2 material model (as discussed at the end of Section 5.1).

A promising alternative to the experimental evaluation, instead, would be the use of the micro-mechanical models presented in Chapter 4, within a multi-scale approach, to evaluate the required macroscopic parameters, based exclusively on directly measured properties at the microscale.

## 5.4 Conclusions

In this chapter the most widely used constitutive model to simulate the behaviour of ceramic materials (i.e. JH2) is first described and then analysed in all its limitations. In particular, two main simplistic assumptions adopted in that model have been identified to severely limit its validity: the isotropic definition of the damage and the completely phenomenological definition of the isotropic damage evolution.

Two possible improvements to extend the capability of the model, overtaking those two simplistic assumptions that limit its validity are presented in Section 5.2 and Section 5.3.

In particular in Section 5.2 an approach to simulate the anisotropy of the damage evolution is proposed by defining a damage tensor instead of a scalar value, thus imposing the damage to propagate separately along the three principal directions. The anisotropic approach is compared with the isotropic (i.e. JH2) model, showing similar global predictions, but highlighting the different failure mechanisms in the orthogonal directions. Furthermore the anisotropic approach increases the number of parameters to define, transforming the initial strength of the material from a scalar value to a 3x3 matrix.

In Section 5.3, then the completely phenomenological definition of the damage evolution defined in the original JH2 model is (partially) substituted by physically based laws,

linking the damage evolution to mechanisms of propagation of a single isolated crack in a volume subjected to a purely compressive load. This innovative approach involves the calculation of the principal stress directions and the rotation of the damage and stress tensors in the principal coordinate system at every time-step. Two procedures to reduce the computational cost and limit the accumulation of the error deriving from the subsequent rotations are also presented respectively in Section 5.3.1 and Section 5.3.2.

The developed "crack based" material model is fully anisotropic and introduces important considerations about the mechanisms behind the damage evolution in ceramic materials. However, as the model is still partially phenomenological (i.e. some parameters have to be calibrated, not being directly related to any specific property of the material), it requires to be accompanied by either experimental or numerical characterisation of the material to be simulated.

The formulation of the constitutive model presented in this chapter lays the foundations for the development of a multi-scale approach to link the results obtained at the micro-scale (presented in Chapter 4) to the effective behaviour of the material observable at macroscopic length scale. The development of the actual multi-scale approach is not within the aim of the present thesis, but the work presented provides fundamental "building blocks" needed to achieve such a goal. Suggestions on the possible implementation of the multi-scale approach are outlined in Chapter 7.

# 6 CONCLUSIONS

The work presented in this thesis aims to increase the understanding of the behaviour of ceramic materials, thus providing a deeper comprehension of their deformation and the failure mechanisms, which are of extreme importance when defining a methodology to improve the performance of ceramics for disparate applications.

The work addresses the study of ceramic materials – with a methodology that combines both experimental characterisation and numerical modelling – at two distinct scales: the *micro-scale,* which refers to the microstructure (i.e. grain and grain boundaries) of the material, and the *macro-scale*, which treats the material as a smeared homogeneous medium.

From the numerical point of view, the methods developed at the two scales constitute the building blocks of a multi-scale approach to simulate deformation and failure of ceramic materials. Within this framework, the experimental work presented has the double function of validating the numerical simulations as well as increasing the understanding of the mechanisms involved in the failure of the material at different scales.

## 6.1 Micro-scale

At the grain scale an innovative method to generate statistically representative models of polycrystalline microstructures has been implemented. The method developed differs significantly from the ones already present in literature, offering flexibility in terms of both properties and shape of the microstructure generated.

The method consists of the generation of an unconfined aggregate with Voronoi tessellation, which is subsequently cropped along planes and planar surfaces, thus producing any desired – convex or concave – shape. Additional features to impose anisotropy in the shape of the grains (i.e. preferred growth directions) are added, further increasing the

versatility of the method. The spatial discretisation procedure implemented consists of meshing each grain separately and then assembling the whole structure together adding interface entities at the grain boundaries, this allowing for the propagation of inter-granular cracks in the structure.

Directly measured material properties are used to create FE models of several geometries to simulate a variety of deformation and failure mechanisms.

In the quasi-static regime (Section 4.3) the numerical models are used to predict both global (i.e. Young's modulus) and local (i.e. stress intensity factor) elastic properties of polycrystalline aggregates, as well as the failure strength linked to the inter-granular crack propagation. The elastic prediction are validated against both experimental measurements and analytical calculations. The failure of the polycrystalline aggregate, instead, is validated by comparing experimental results and numerical simulation of the same micro-cantilever test. All the validations presented showed excellent agreement between the numerical results and the experimental measurements, demonstrating the capability of the methodology developed to generate representative models of polycrystalline ceramic microstructures.

In the dynamic regime, the rate dependence of the inter-granular crack propagation mechanisms has been explored. First, a wide parametrical study on the effect of both geometrical and loading parameters on the propagation of cracks within a domain subjected to a pulse load is presented. Then, the effect of the projectile velocity on the crack propagation within a polycrystalline plate impacted by a rigid sphere is analysed. Given the extreme difficulties in observing the crack propagation at the desired scale and velocity, the dynamic simulations cannot be directly verified against experimental evidence. However, behaviours in the damage propagation similar to the ones reproduced by the simulations have been observed in many experimental tests, hence confirming the qualitative accuracy of the simulations.

## 6.2 Macro-scale

The experimental characterisation of the material at the macro-scale presented in this thesis focuses on the effect of the strain-rate on the crack propagation mechanisms. The design of the testing equipment (i.e. single-stage gas gun) and of the impact test technique presented in Section 3.3 are functional to the development of a novel procedure that highlights the rate effect by comparing dynamic and static indentation tests with similar indenters and loading paths. This procedure enabled an increase in understanding of the mechanisms involved in the failure of ceramic materials at impact.

On the numerical side, a novel constitutive model for ceramic materials is presented. The model introduces original approaches to overtake the limitations made apparent in the critical review of the state-of-the-art material models.

The introduction of a damage tensor, in place of a scalar value, takes into account the intrinsic anisotropic nature of the crack propagation mechanisms, which are the principal cause of failure of ceramic materials. Additionally, a new definition of damage is introduced to embed mechanisms at the base of the single crack propagation, thus enhancing the "physical bases" of the constitutive model. This innovative approach requires the calculation of the principal stress directions and the rotation of the damage and stress tensors into the principal coordinate system at every time step. Two procedures to reduce computational cost of the calculation of the principal directions and to limit the accumulation of the numerical error deriving from the rotation procedures are developed and implemented in the constitutive model.

The introduction of the mechanical considerations on the growth of isolated cracks in the formulation of the damage evolution algorithm reduces the phenomenological nature of the macroscopic constitutive model developed, with respect to the "classic" JH2 model.

However, it still requires the characterisation of some parameters, which could be obtained from micro-mechanical modelling within a multi-scale approach. This topic, which is not within the scope of the present thesis, is presented in the next chapter within the suggestions for future work.

# 7 FUTURE WORK

The work presented in this thesis provides important insights into the mechanisms involved in the deformation and failure of ceramic materials, both at micro- and macro-scales. However it is far from being fully exhaustive of the topic, in fact it opens multiple research opportunities that would further increase both the understanding of the behaviour of ceramic materials at multiple scales and rates, as well as the capability to model the phenomena involved.

A partial list of the possible future works related to the research presented in this thesis is reported in the following sections.

## 7.1 Experimental work

### *7.1.1 In-situ observation of 3D crack propagation*

The experimental work presented in this thesis, despite providing extremely important insights in the failure of ceramic materials both at the micro- and the macro-scales, is still based either on post-mortem direct characterisation or on indirect measurements.

The use of in-situ tomography techniques to observe the propagation of cracks within the domain during the test would increase significantly the understanding of the mechanisms governing the crack propagation at all the length scales.

### *7.1.2 Continuing the development of methodology for dynamic indentation*

The dynamic indentation technique developed in this thesis is of extreme importance to explore the rate effect on the failure mechanisms of ceramic materials. However some improvements can be introduced to the methodology to improve its validity as well as to explore the rate-dependency of the crack propagation at smaller length scales.

The main criticality of the dynamic indentation tests reported in this thesis is the permanent deformation (and possibly fracture) of the indenter, which limits the comparability with the corresponding quasi-static tests. Possible designs involve the use of harder (non-disposable) indenters attached to a support with limited freedom of movement. The momentum can be transmitted to the indenter support by an impacting rod, thus regulating the duration and transmitted force by adjusting the length and the velocity of the impactor.

To explore the effect of the strain-rate at small length scales, instead, techniques to accelerate small projectiles can be designed, based for example on laser excitation.

## 7.2 Numerical work

On the numerical side there are numerous challenges in developing additional features to the models presented in this thesis. Solving these challenges would increase the range of phenomena that is possible to reproduce. Of particular interest for the modelling of the micro-mechanic of ceramic materials are: trans-granular crack propagation and grain plasticity, whilst for the macroscopic model the implementation of a multi-scale approach to use the results of lower scales simulations is of high importance.

### *7.2.1 Trans-granular crack propagation*

The limitation of the FEM to accurately simulate trans-granular crack propagation is evident from the simulations presented in Section 4.5.

Multiple methods have been proposed to propagate cracks independently from the space discretisation of the structure, either based on adaptive re-meshing of the domain or on alternative computational methods (e.g. XFEM, RKPM).

The adoption of a meshless method (e.g. RKPM) in particular seems to be an extremely promising approach to overtake the limitations expressed by the FEM in terms of crack propagation.

### *7.2.2 Grain plasticity*

In this thesis the grains are modelled as perfectly elastic bodies. However, as stated in Section 2.1, the plasticity expressed by ceramic materials is limited but not absent. Furthermore there are particular loading conditions that are believed to enhance the presence of plastic deformation. Plastic deformation has been observed in specimens subjected to high strain rate deformations as well as in the area around an indentation [3].

There are numerous constitutive models of grain plasticity, and the addition of this feature into the micro-structural models would provide further detail to the simulations.

### *7.2.3 Multi-scale model*

The limits of the currently available computational power hinder the possibility of model the microstructural features of macroscopic domains. However the importance of embedding the micro-mechanic into models with a relatively coarse spatial discretisation emerges clearly from the work presented in this thesis. In particular, the determination of the parameters in the macroscopic "crack based" constitutive model developed could be obtained from simulations of the microstructural behaviour of the material.

A possible way of "bridging" the different scales is to adopt a multi-scale approach that combines the information gathered at the smaller scale (i.e. control scale) into the larger scale (i.e. target scale).

Depending on the approach adopted to link the control and the target scales, the multi-scale methods can be classified in 4 main categories: serial, simultaneous, hierarchical and parallel. Exploring the different methods and possibly developing one tailored to the

simulation of failure of ceramic materials at different scales is highly challenging and of extreme interest in the framework of modelling ceramic materials.

# APPENDIX

## A. Effect of the shear deformation on the micro-cantilever beam

In this appendix the effect of the shear deformation in the evaluation of the Young's modulus presented in Section 3.1.2 is evaluated.

The Euler-Bernoulli beam theory is based on the assumption that the cross sections of a cantilever beam loaded at the free end remain perpendicular to the neutral axis, therefore exhibiting a purely bending deformation. This hypothesis is true only for long thin beams. For short beams Timoshenko suggested a correction to take into account the effect of the shear deformation [128], which can be expressed as:

$$E = \frac{F}{\delta}\frac{L_{ind}^3}{3I} + \frac{2(1+\nu)F}{\kappa^2 \delta A} L_{ind} \tag{80}$$

The first term is the same of the Euler-Bernoulli formulation, whilst the second term represents the effect of the shear.

To isolate the influence of the shear term, the equation can be rewritten as:

$$E = \frac{F}{\delta}\frac{L_{ind}^3}{3I} \cdot \left(1 + \frac{6I(1+\nu)}{\kappa^2 L_{ind}^2 A}\right) \tag{81}$$

Substituting the values of the Poisson's ratio ($\nu$), moment of inertia ($I$), distance between the loading point and the fixed end ($L_{ind}$), and cross sectional area ($A$) relative to the beam geometry and material considered in this work, the equation becomes:

$$E \cong \frac{F}{\delta}\frac{L_{ind}^3}{3I} \cdot \left(1 + \frac{8.357 \cdot 10^{-3}}{\kappa^2}\right) \tag{82}$$

Several definition of the shear coefficient ($\kappa$) have been proposed in the past century, as reported by Kaneko in his review [158]. Without getting involved in a the complex evaluation of the correct $\kappa$ for a triangular cross section, it suffices to notice that for all the

formulations proposed in literature its value is of the order of 1, therefore making the effect of the shear of the order of 1%. In this context this value of approximation is considered acceptable, and therefore the shear effect is neglected.

## B. Stress intensity factor in the notched micro-cantilever beam

The stress intensity factor at the crack tip of notched beams is evaluated performing a parametrical study on the effect of the position and depth of the notch.

The graph reported in Fig. B.1 shows the variation of the compliance of the beam with the notch depth for different positions of the notch along the beam.

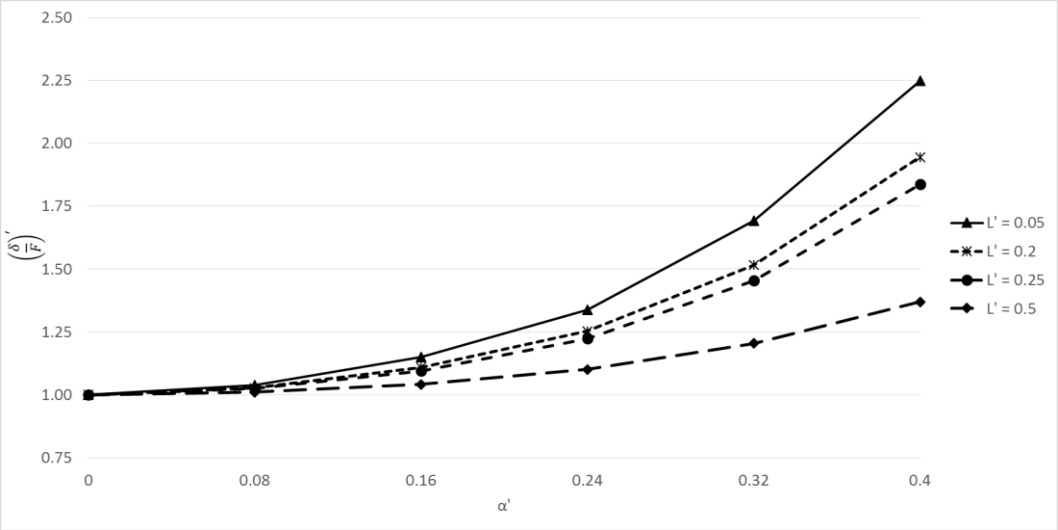



**Fig. B.1:** Normalised compliance vs. normalised notch depth for different positions of the notch

The compliance of the beam is normalised against the analytical solution of the un-notched beam, whilst the notch depth $(\alpha')$ and position $(L')$ are normalised against the height and the length of the beam, respectively.

The numerical simulations performed suggest that for small straight through notches (i.e. $\alpha' < 0.4$) the stress intensity factor can be interpolated with a $4^{th}$ order polynomial

equation. In particular, for notches positioned at $0.2 \cdot L_f$ from the built end (i.e. $L' = 0.2$), which is typical for the experiments reported in this thesis, $K_{Ic}$ can be evaluated as:

$$K_{Ic} = \frac{12F_f L_f}{wh^2} 1.12\sqrt{\pi\alpha}\left[1 + 0.123\frac{\alpha}{h} + 5.456\left(\frac{\alpha}{h}\right)^2 + 0.073\left(\frac{\alpha}{h}\right)^3 - 0.023\left(\frac{\alpha}{h}\right)^4\right] \quad (83)$$

## C. Definition of the properties at the Hugoniot Elastic Limit

The implementation of the JH2 model presented in Section 5.1 requires the definition of the volumetric strain ($\mu_{HEL}$), the pressure ($P_{HEL}$), and the stress ($\sigma_{HEL}$) at the Hugoniot elastic limit ($HEL$).

The volumetric elastic strain can be calculated iteratively from $HEL$ and the shear modulus $G$ from the relation:

$$HEL = K_1\mu_{HEL} + K_2\mu_{HEL}^2 + K_3\mu_{HEL}^3 + \frac{4}{3}G\frac{\mu_{HEL}}{1+\mu_{HEL}} \quad (84)$$

Subsequently the normalisation terms reported used in Eq. (50) and (53) can be calculated as:

$$P_{HEL} = K_1\mu_{HEL} + K_2\mu_{HEL}^2 + K_3\mu_{HEL}^3 \quad (85)$$

$$\sigma_{HEL} = \frac{3}{2}(HEL - P_{HEL}) \quad (86)$$

# REFERENCES


1. Bengisu, M., *Engineering ceramics*. 2001: Springer.
2. Bhargava, A., *Engineering Materials: Polymers Ceramics and Composites*. 2005: PHI Learning Pvt. Ltd.
3. Evans, A., *Fracture toughness: the role of indentation techniques.* Fracture Mechanics Applied to Brittle Materials, 1979. **678**: p. 112.
4. Ashby, M., et al., *The mechanical properties of natural materials. I. Material property charts.* Proceedings of the Royal Society of London. Series A: Mathematical and Physical Sciences, 1995. **450**(1938): p. 123-140.
5. Chen, W.W., et al., *Dynamic fracture of ceramics in armor applications.* Journal of the American Ceramic Society, 2007. **90**(4): p. 1005-1018.
6. Lundberg, P., R. Renström, and B. Lundberg, *Impact of metallic projectiles on ceramic targets: transition between interface defeat and penetration.* International journal of impact engineering, 2000. **24**(3): p. 259-275.
7. Walley, S., *Historical review of high strain rate and shock properties of ceramics relevant to their application in armour.* Advances in Applied Ceramics, 2010. **109**(8): p. 446-466.
8. Nye, J.F., *Physical properties of crystals: their representation by tensor and matrices*. 1957, Oxford: Clarendon Press
9. Phillips, F.C., *An introduction to crystallography*. 1971: Oliver and Boyd Edinburgh.
10. Hahn, T. and H. Klapper, *International Tables for Crystallography*. 2006. p. 794.
11. Lovett, D., *Tensor properties of crystals*. 1999: CRC Press.
12. Petrovic, J., et al., *Tensile mechanical properties of SiC whiskers.* Journal of Materials Science, 1985. **20**(4): p. 1167-1177.
13. Bažant, Z.P. and M.T. Kazemi, *Size effect in fracture of ceramics and its use to determine fracture energy and effective process zone length.* Journal of the American Ceramic Society, 1990. **73**(7): p. 1841-1853.
14. Wachtman, J.B., W.R. Cannon, and M.J. Matthewson, *Mechanical properties of ceramics*. 2009: John Wiley & Sons.
15. Marquis, E.A., et al., *Probing the improbable: imaging C atoms in alumina.* Materials Today, 2010. **13**(10): p. 34-36.
16. Wiederhorn, S., *Fracture of sapphire.* Journal of the American Ceramic Society, 1969. **52**(9): p. 485-491.
17. Cuccureddu, F., et al., *Surface morphology of c-plane sapphire (α-alumina) produced by high temperature anneal.* Surface Science, 2010. **604**(15): p. 1294-1299.
18. Burke, S.K., S.M. Cousland, and C.M. Scala, *Nondestructive characterization of advanced composite materials.* Metals Forum, 1994. **18**: p. 85-109.
19. King, R.G. and P.M. Delaney, *Confocal microscopy.* Metals Forum, 1994. **18**: p. 21-29.
20. Marrow, T.J., G.A.D. Briggs, and S.G. Roberts, *In-situ scanning acoustic microscopy of crack bridging in alumina.* Journal of the European Ceramic Society, 1994. **14**: p. 111-116.
21. Wilkinson, A.J. and P.B. Hirsch, *Electron diffraction based techniques in scanning electron microscopy of bulk materials.* Micron, 1997. **28**(4): p. 279-308.
22. Bhandari, Y., et al., *3D polycrystalline microstructure reconstruction from FIB generated serial sections for FE analysis.* Computational Materials Science, 2007. **41**(2): p. 222-235.

23. Groeber, M., *A framework for automated analysis and simulation of 3D polycrystalline microstructures.Part 1: Statistical characterization.* Acta Materialia, 2008. **56**(6): p. 1257-1273.
24. Groeber, M., *A framework for automated analysis and simulation of 3D polycrystalline microstructures. Part 2: Synthetic structure generation☆.* Acta Materialia, 2008. **56**(6): p. 1274-1287.
25. Groeber, M.A., et al., *3D reconstruction and characterization of polycrystalline microstructures using a FIB–SEM system.* Materials Characterization, 2006. **57**(4-5): p. 259-273.
26. Spoor, P., et al., *Elastic constants and crystal anisotropy of titanium diboride.* Applied Physics Letters, 1997. **70**(15): p. 1959-1961.
27. Gladden, J.R., et al., *Reconciliation of ab initio theory and experimental elastic properties of Al[sub 2]O[sub 3]*. Applied Physics Letters, 2004. **85**(3): p. 392.
28. Hovis, D.B., A. Reddy, and A.H. Heuer, *X-ray elastic constants for α-Al[sub 2]O[sub 3]*. Applied Physics Letters, 2006. **88**(13): p. 131910.
29. Evenschor, P., W. Frohlich, and V. Hauk, *Calculation of the X-ray elastic constants of polycrystalline hexagonal metals from single-crystal data.* Z Metallkunde, 1971. **62**(1): p. 38-42.
30. Brinksmeier, E. and H. Siemer. *Calculation of X-Ray Elastic Constants of Aluminum Oxide Ceramics*. in *International Conference on Residual Stresses*. 1989. Springer.
31. Ye, J., et al., *Extraction of bulk metallic-glass yield strengths using tapered micropillars in micro-compression experiments.* Intermetallics, 2010. **18**(3): p. 385-393.
32. Johansson, S., et al., *Fracture testing of silicon microelements insitu in a scanning electron microscope.* Journal of Applied Physics, 1988. **63**(10): p. 4799-4803.
33. Di Maio, D. and S. Roberts, *Measuring fracture toughness of coatings using focused-ion-beam-machined microbeams.* Journal of materials research, 2005. **20**(02): p. 299-302.
34. Motz, C., T. Schöberl, and R. Pippan, *Mechanical properties of micro-sized copper bending beams machined by the focused ion beam technique.* Acta Materialia, 2005. **53**(15): p. 4269-4279.
35. Armstrong, D.E., A.J. Wilkinson, and S.G. Roberts, *Measuring anisotropy in Young's modulus of copper using microcantilever testing.* Journal of materials research, 2009. **24**(11): p. 3268-3276.
36. Chan, Y., A. Ngan, and N. King, *Use of focused ion beam milling for investigating the mechanical properties of biological tissues: a study of human primary molars.* Journal of the mechanical behavior of biomedical materials, 2009. **2**(4): p. 375-383.
37. Armstrong, D., M. Rogers, and S. Roberts, *Micromechanical testing of stress corrosion cracking of individual grain boundaries.* Scripta Materialia, 2009. **61**(7): p. 741-743.
38. Norton, A., et al., *Microcantilever investigation of fracture toughness and subcritical crack growth on the scale of the microstructure in Al2O3.* Journal of the European Ceramic Society, 2015.
39. Armstrong, D., A. Wilkinson, and S. Roberts, *Micro-mechanical measurements of fracture toughness of bismuth embrittled copper grain boundaries.* Philosophical Magazine Letters, 2011. **91**(6): p. 394-400.
40. Kuhn, H. and D. Medlin, *ASM Handbook. Volume 8: Mechanical Testing and Evaluation.* ASM International, Member/Customer Service Center, Materials Park, OH 44073-0002, USA, 2000. 998, 2000.

41. Sharpe Jr, W.N. and W.N. Sharpe, *Springer handbook of experimental solid mechanics*. 2008: Springer.
42. Field, J., et al., *Review of experimental techniques for high rate deformation and shock studies.* International journal of impact engineering, 2004. **30**(7): p. 725-775.
43. Winkel, J. and D. Adams, *Instrumented drop weight impact testing of cross-ply and fabric composites.* Composites, 1985. **16**(4): p. 268-278.
44. Davies, R., *A critical study of the Hopkinson pressure bar.* Philosophical Transactions of the Royal Society of London. Series A. Mathematical and Physical Sciences, 1948: p. 375-457.
45. Kolsky, H., *An investigation of the mechanical properties of materials at very high rates of loading.* Proceedings of the Physical Society. Section B, 1949. **62**(11): p. 676.
46. Staab, G. and A. Gilat, *A direct-tension split Hopkinson bar for high strain-rate testing.* Experimental Mechanics, 1991. **31**(3): p. 232-235.
47. Duffy, J., J. Campbell, and R. Hawley, *On the use of a torsional split Hopkinson bar to study rate effects in 1100-0 aluminum.* Journal of Applied Mechanics, 1971. **38**(1): p. 83-91.
48. Lewis, J.L. and W. Goldsmith, *A biaxial split Hopkinson bar for simultaneous torsion and compression.* Review of scientific instruments, 1973. **44**(7): p. 811-813.
49. Erlich, D., D. Shockey, and L. Seaman. *Symmetric rod impact technique for dynamic yield determination*. in *Shock Waves in Condensed Matter-1981*. 1982. AIP Publishing.
50. Taylor, G., *The use of flat-ended projectiles for determining dynamic yield stress. I. Theoretical considerations.* Proceedings of the Royal Society of London. Series A. Mathematical and Physical Sciences, 1948. **194**(1038): p. 289-299.
51. VanLandingham, M.R., *Review of instrumented indentation*. 2003, DTIC Document.
52. Thunborg Jr, S., G. Ingram, and R. Graham, *Compressed Gas Gun for Controlled Planar Impacts Over a Wide Velocity Range.* Review of scientific instruments, 1964. **35**(1): p. 11-14.
53. Bourne, N., *A 50 mm bore gas gun for dynamic loading of materials and structures.* Measurement science and technology, 2003. **14**(3): p. 273.
54. Seigel, A., *Unsteady one-dimensional flows(One-dimensional unsteady flow in hydrodynamic shock tube, and in light gas gun).* 1966. 29 P, 1966.
55. Baczmański, A., et al., *Examination of the residual stress field in plastically deformed polycrystalline material.* Philosophical Magazine A, 1994. **69**(3): p. 437-449.
56. Ortiz, M. and S. Suresh, *Statistical properties of residual stresses and intergranular fracture in ceramic materials.* Journal of Applied Mechanics, 1993. **60**: p. 77-84.
57. Sukumar, N., et al., *Brittle fracture in polycrystalline microstructures with the extended finite element method.* International Journal for Numerical Methods in Engineering, 2003. **56**(14): p. 2015-2037.
58. Ghosh, S., K. Lee, and S. Moorthy, *Multiple scale analysis of heterogeneous elastic structures using homogenization theory and Voronoi cell Finite Element Method.* International Journal of Solids and Structures, 1994. **32**(1): p. 27-62.
59. Kumar, S. and S.K. Kurtz, *Simulation of material microstructure using a 3D Voronoi tessellation: Calculation of effective thermal expansion coefficient of polycrystalline materials.* Acta Metallica materialia, 1994. **42**(12): p. 3917-3927.
60. Kumar, S., S.K. Kurtz, and V.K. Agarwala, *Micro-stress distribution within polycrystalline aggregate.* Acta Mechanica, 1996. **114**: p. 203-216.

61. Wu, M.S. and M.D. He, *Prediction of crack statistics in a random polycrystal damaged by the pile-ups of extrinsic grain-boundary dislocations.* Philosophical Magazine A, 1999. **79**(2): p. 271-292.
62. Wu, M.S. and J. Niu, *A theoretical analysis of crack nucleation due to grain boundary dislocation pile-ups in a random ice microstructure.* Philosophical Magazine A, 1995. **71**(4): p. 831-854.
63. Raabe, D., Z. Zhao, and W. Mao, *On the dependence of in-grain subdivision and deformation texture of aluminium on grain interaction.* Acta Materialia, 2002. **50**: p. 4379-4394.
64. Zhao, Z., et al., *Influence of in-grain mesh resolution on the prediction of deformation textures in fcc polycrystals by crystal plasticity FEM.* Acta Materialia, 2007. **55**(7): p. 2361-2373.
65. Jivkov, A.P. and T.J. Marrow, *Rates of intergranular environment assisted cracking in three-dimensional model microstructures.* Theoretical and Applied Fracture Mechanics, 2007. **48**(3): p. 187-202.
66. Anderson, M., G. Grest, and D. Srolovitz, *Computer simulation of normal grain growth in three dimensions.* Philosophical Magazine B, 1989. **59**(3): p. 293-329.
67. Krill Iii, C. and L.-Q. Chen, *Computer simulation of 3-D grain growth using a phase-field model.* Acta Materialia, 2002. **50**(12): p. 3059-3075.
68. Wakai, F., N. Enomoto, and H. Ogawa, *Three dimensional microstructural evolution in ideal grain growth - general statistics.* Acta Materialia, 2000. **48**: p. 1297-1311.
69. Döbrich, K., M. Rau, and C.E. Krill III, *Quantitative characterization of the three-dimensional microstructure of polycrystalline al-sn using X-ray microtomography. , 35 A(7),* . Metallurgical and Materials Transactions A: Physical Metallurgy and Materials Science, 2004. **35 A**(7): p. 1953-1961.
70. Aurenhammer, F., *Voronoi diagrams - A survey of fundamental geometric data structure.* ACM Computer Surveys, 1991. **23**(3).
71. Barbe, F., et al., *Intergranular and intragranular behaviour of polycrystalline aggregates. Part 1: FE model.* International Journal of Plasticity, 2001. **17**: p. 513-536.
72. Barbe, F., et al., *Intergranular and intragranular behaviour of polycrystalline aggregates. Part 2: Results.* International Journal of Plasticity, 2001. **17**: p. 537-563.
73. Fritzen, F. and T. Böhlke, *Periodic three-dimensional mesh generation for particle reinforced composites with application to metal matrix composites.* International Journal of Solids and Structures, 2011. **48**(5): p. 706-718.
74. Fritzen, F., T. Böhlke, and E. Schnack, *Periodic three-dimensional mesh generation for crystalline aggregates based on Voronoi tessellations.* Computational Mechanics, 2008. **43**(5): p. 701-713.
75. Ramella, M., et al., *Finding galaxy clusters using Voronoi tessellations.* Astronomy and Astrophysics, 2001. **368**(3): p. 776-786.
76. Poupon, A., *Voronoi and Voronoi-related tessellations in studies of protein structure and interaction.* Current Opinion in Structural Biology, 2004. **14**(2): p. 233-241.
77. Tanemura, M. and M. Hasegawa, *Geometrical models of territory I. Models for synchronous and asynchronous settlement of territories.* Journal of Theoretical Biology, 1980. **82**(3): p. 477-496.
78. Du, Q., V. Faber, and M. Gunzburger, *Centroidal Voronoi tessellations: applications and algorithms.* SIAM review, 1999. **41**(4): p. 637-676.

79. Baccelli, F. and B. Błaszczyszyn, *On a coverage process ranging from the Boolean model to the Poisson-Voronoi tessellation with applications to wireless communications.* Advances in Applied Probability, 2001: p. 293-323.
80. Ohser, J. and K. Schladitz, *3D images of materials structures: processing and analysis*. 2009: John Wiley & Sons.
81. Lautensack, C. and S. Zuyev, *Random laguerre tessellations.* Advances in Applied Probability, 2008: p. 630-650.
82. Mecke, J. and L. Muche, *The Poisson Voronoi tessellation I. A basic identity.* Mathematische Nachrichten, 1995. **176**(1): p. 199-208.
83. Muche, L., *The Poisson Voronoi tessellation II. Edge length distribution functions.* Mathematische Nachrichten, 1996. **178**(1): p. 271-283.
84. Boots, B.N., *The arrangment of Cells in Random Network.* Metallography, 1982. **15**: p. 53-62.
85. Rycroft, C., *Voro++: A three-dimensional Voronoi cell library in C++*. Lawrence Berkeley National Laboratory, 2009.
86. Quey, R., P. Dawson, and F. Barbe, *Large-scale 3D random polycrystals for the finite element method: Generation, meshing and remeshing.* Computer Methods in Applied Mechanics and Engineering, 2011. **200**(17): p. 1729-1745.
87. Addessio, F.L. and J.N. Johnson, *A constitutive model for the dynamic response of brittle materials.* Journal of Applied Physics, 1990. **67**(7): p. 3275-3286.
88. Johnson, G. and T. Holmquist, *A computational constitutive model for brittle materials subjected to large strains, high strain rates and high pressures.* Shock Wave and High-Strain-Rate Phenomena in Materials, 1992: p. 1075-1081.
89. Johnson, G.R. and T.J. Holmquist, *An improved computational constitutive model for brittle materials*. High Pressure Science and Technology. Vol. 2. 1994, New York: AIP Press.
90. Johnson, G.R., T.J. Holmquist, and S.R. Beissel, *Response of aluminum nitride (including a phase change) to large strains, high strain rates, and high pressures*. Journal of Applied Physics, 2003. **94**(3): p. 1639-1646.
91. Ma, Z.-D., H. Wang, and B. Raju, *Function-Oriented Material Design of Joints for Advance Armors Under Ballistic Impact*. 2004, DTIC Document.
92. Holmquist, T.J. and G.R. Johnson, *Response of silicon carbide to high velocity impact.* Journal of Applied Physics, 2002. **91**(9): p. 5858-5866.
93. Cronin, D.S., et al. *Implementation and validation of the Johnson–Holmquist ceramic material model in LS-DYNA*. in *4th European LS-dyna users conference*. 2003.
94. Simha, C., S. Bless, and A. Bedford, *Computational modeling of the penetration response of a high-purity ceramic.* International journal of impact engineering, 2002. **27**(1): p. 65-86.
95. Rajendran, A., *High Strain Rate Behavior of Metals Ceramics, and Concrete*. 1992, DTIC Document.
96. Rajendran, A., *Modeling the impact behavior of AD85 ceramic under multiaxial loading.* International journal of impact engineering, 1994. **15**(6): p. 749-768.
97. Griffith, A.A., *The phenomena of rupture and flow in solids.* Philosophical transactions of the royal society of london. Series A, containing papers of a mathematical or physical character, 1921: p. 163-198.
98. Deshpande, V. and A. Evans, *Inelastic deformation and energy dissipation in ceramics: A mechanism-based constitutive model.* Journal of the Mechanics and Physics of Solids, 2008. **56**(10): p. 3077-3100.

99. Ashby, M.F. and C.G. Sammis, *The damage mechanics of brittle solids in compression.* PAGEOPH, 1990. **133**(3).
100. Denoual, C. and F. Hild, *A damage model for the dynamic fragmentation of brittle solids.* Computer Methods in Applied Mechanics and Engineering, 2000. **183**(3): p. 247-258.
101. Espinosa, H., *On the dynamic shear resistance of ceramic composites and its dependence on applied multiaxial deformation.* International Journal of Solids and Structures, 1995. **32**(21): p. 3105-3128.
102. Espinosa, H.D., P.D. Zavattieri, and S.K. Dwivedi, *A finite deformation continuum\ discrete model for the description of fragmentation and damage in brittle materials.* Journal of the Mechanics and Physics of Solids, 1998. **46**(10): p. 1909-1942.
103. Riou, P., C.E. Cottenot, and M. Boussuge, *Anisotropic damage model for impacted ceramic material: Application to silicon carbide.* International journal of impact engineering, 1998. **21**(8): p. 683-693.
104. Wen, P.H., M.H. Aliabadi, and D.P. Rooke, *Cracks in three dimensions: A dynamic dual boundary element analysis.* Computer Methods in Applied Mechanics and Engineering, 1998. **167**(1): p. 139-151.
105. Benedetti, I. and M.H. Aliabadi, *A three-dimensional cohesive-frictional grain-boundary micromechanical model for intergranular degradation and failure in polycrystalline materials.* Computer Methods in Applied Mechanics and Engineering, 2013. **265**: p. 36-62.
106. Moes, N. and T. Belytschko, *Extended finite element method for cohesive crack growth.* Engineering Fracture Mechanics, 2002. **69**: p. 813-833.
107. Moes, N., J. Dolbow, and T. Belytschko, *A finite element method for crack growth without remeshing.* International Journal for Numerical Methods in Engineering, 1999. **46**(1): p. 131-150.
108. Radovitzky, R., et al., *A scalable 3D fracture and fragmentation algorithm based on a hybrid, discontinuous Galerkin, cohesive element method.* Computer Methods in Applied Mechanics and Engineering, 2011. **200**(1): p. 326-344.
109. Belytschko, T., Y.Y. Lu, and L. Gu, *Element-free Galerkin methods.* International Journal for Numerical Methods in Engineering, 1994. **37**: p. 229-256.
110. Courant, R., *Variational methods for the solution of problems of equilibrium and vibrations.* Bull. Amer. Math. Soc, 1943. **49**(1): p. 1-23.
111. Turner, M., et al., *Stiffness and deflection analysis of complex structures, J. of Aeronaut.* Science, 1956. **23**: p. 805-823.
112. Song, J.-H., H. Wang, and T. Belytschko, *A comparative study on finite element methods for dynamic fracture.* Computational Mechanics, 2007. **42**(2): p. 239-250.
113. Pandolfi, A. and M. Ortiz, *An eigenerosion approach to brittle fracture.* International Journal for Numerical Methods in Engineering, 2012. **92**(8): p. 694-714.
114. Schmidt, B., F. Fraternali, and M. Ortiz, *Eigenfracture: An Eigendeformation Approach to Variational Fracture.* Multiscale Modeling & Simulation, 2009. **7**(3): p. 1237-1266.
115. Espinosa, H.D. and P.D. Zavattieri, *A grain level model for the study of failure initiation and evolution in polycrystalline brittle materials. Part I: Theory and numerical implementation.* Mechanics of Materials, 2003. **35**: p. 333-364.
116. Espinosa, H.D. and P.D. Zavattieri, *A grain level model for the study of failure initiation and evolution in polycrystalline brittle materials. Part II: Numerical examples.* Mechanics of Materials, 2003. **35**: p. 365-394.

117. Zhou, T., et al., *Crack propagation simulation in microstructure of ceramic tool materials.* Computational Materials Science, 2012. **54**: p. 150-156.
118. Simonovski, I. and L. Cizelj, *Computational multiscale modeling of intergranular cracking.* Journal of Nuclear Materials, 2011. **414**(2): p. 243-250.
119. Simonovski, I. and L. Cizelj, *Towards modeling intergranular stress corrosion cracks on grain size scales.* Nuclear Engineering and Design, 2012. **246**: p. 107-114.
120. Xu, X.P. and A. Needleman, *Numerical simulations of fast crack growth in brittle solids.* Journal of the Mechanics and Physics of Solids, 1994. **42**(9): p. 1397-1434.
121. Xu, X.P. and A. Needleman, *Numerical simulations of dynamic interfacial crack growth allowing for crack growth away from the bond line.* International Journal of Fracture, 1995. **74**: p. 253-275.
122. Camacho, G.T. and M. Ortiz, *Computational modelling of impact damage in brittle materials.* International Journal of Solids and Structures, 1996. **33**: p. 2899-2938.
123. Ortiz, M. and A. Pandolfi, *Finite-defiormation irreversible cohesive elements for three-dimensional crack-propagation analysis.* International Journal for Numerical Methods in Engineering, 1999. **44**(1267-1282).
124. Rabczuk, T., *Computational Methods for Fracture in Brittle and Quasi-Brittle Solids: State-of-the-Art Review and Future Perspectives.* ISRN Applied Mathematics, 2013. **2013**: p. 1-38.
125. Falco, S., et al., *Explicit Modeling of Crack Initiation and Propagation in the Microstructure of a Ceramic Material Generated with Voronoi Tessellation.* Developments in Strategic Materials and Computational Design IV, 2013: p. 185-196.
126. Norton, A., *Measuring and Understanding Grain Boundary Properties of Engineering Ceramics*, in *Department of Materials*. 2013, University of Oxford: Oxford.
127. Timoshenko, S., *History of strength of materials: with a brief account of the history of theory of elasticity and theory of structures*. 1983: Courier Dover Publications.
128. Timoshenko, S.P., *LXVI. On the correction for shear of the differential equation for transverse vibrations of prismatic bars.* The London, Edinburgh, and Dublin Philosophical Magazine and Journal of Science, 1921. **41**(245): p. 744-746.
129. Green, D.J., *An introduction to the mechanical properties of ceramics*. 1998: Cambridge University Press.
130. Garvie, R., *Stabilization of the tetragonal structure in zirconia microcrystals.* The Journal of Physical Chemistry, 1978. **82**(2): p. 218-224.
131. Rowenhorst, D.J., A.C. Lewis, and G. Spanos, *Three-dimensional analysis of grain topology and interface curvature in a β-titanium alloy.* Acta Materialia, 2010. **58**(16): p. 5511-5519.
132. Yan, D.-M., et al., *Efficient computation of 3d clipped voronoi diagram*, in *Advances in Geometric Modeling and Processing*. 2010, Springer. p. 269-282.
133. Legland, D. *Graphics Library geom3d*. 2009; Available from: https://www.mathworks.com/matlabcentral/fileexchange/24484-geom3d.
134. Fritzen, F. and T. Böhlke, *Nonuniform transformation field analysis of materials with morphological anisotropy.* Composites Science and Technology, 2011. **71**(4): p. 433-442.
135. Yoon, S., T. Akatsu, and E. Yasuda, *Anisotropy of creep deformation rate in hot-pressed Si3N4 with preferred orientation of the elongated grains.* Journal of Materials Science, 1997. **32**(14): p. 3813-3819.
136. Liu, Q., D. Juul Jensen, and N. Hansen, *Effect of grain orientation on deformation structure in cold-rolled polycrystalline aluminium.* Acta Materialia, 1998. **46**(16): p. 5819-5838.

137. Guazzato, M., et al., *Strength, fracture toughness and microstructure of a selection of all-ceramic materials. Part I. Pressable and alumina glass-infiltrated ceramics.* Dental Materials, 2004. **20**(5): p. 441-448.
138. Cifuentes, A. and A. Kalbag, *A performance study of tetrahedral and hexahedral elements in 3-D finite element structural analysis.* Finite Elements in Analysis and Design, 1992. **12**(3): p. 313-318.
139. Geuzaine, C. and J.-F. Remacle, *Gmsh: A 3-D finite element mesh generator with built-in pre- and post-processing facilities.* International Journal for Numerical Methods in Engineering, 2009. **79**(11): p. 1309-1331.
140. Vodenitcharova, T., et al., *The effect of anisotropy on the deformation and fracture of sapphire wafers subjected to thermal shocks.* Journal of Materials Processing Technology, 2007. **194**(1-3): p. 52-62.
141. Winey, J.M., Y.M. Gupta, and D.E. Hare, *r-axis sound speed and elastic properties of sapphire single crystals.* Journal of Applied Physics, 2001. **90**(6): p. 3109.
142. Ostoja-Starzewski, M., *Material spatial randomness: From statistical to representative volume element.* Probabilistic Engineering Mechanics, 2006. **21**(2): p. 112-132.
143. Benedetti, I. and M.H. Aliabadi, *A three-dimensional grain boundary formulation for microstructural modeling of polycrystalline materials.* Computational Materials Science, 2013. **67**: p. 249-260.
144. Ren, Z.Y. and Q.S. Zheng, *Effects of grain sizes, shapes, and distribution on minimum sizes of representative volume elements of cubic polycrystals.* Mechanics of Materials, 2004. **36**(12): p. 1217-1229.
145. Nygårds, M., *Number of grains necessary to homogenize elastic materials with cubic symmetry*. Mechanics of Materials, 2003. **35**(11): p. 1049-1057.
146. Zener, C., *Elasticity and anelasticity of metals*. 1948: University of Chicago Press.
147. Kanit, T., et al., *Determination of the size of the representative volume element for random composites: statistical and numerical approach.* International Journal of Solids and Structures, 2003. **40**(13-14): p. 3647-3679.
148. Lemaitre, J. and J.L. Chaboche, *Mechanics of soilid materials*. 1990: Cambridge university press.
149. Gross, B. and A. Mendelson, *Plane elastostatic analysis of V-notched plates.* International Journal of Fracture Mechanics, 1972. **8**(3): p. 267 - 276.
150. Tabiei, A. and J. Wu, *Development od the DYNA3D simulation code with automated fracture procedure for brick elements*, in *7th international LS-DYNA users conference*. 2002: Dearborn, Michigan.
151. Ortiz, M., *Microcrack coalescence and macroscopic crack growth initiation in brittle solids.* International Journal of Solids and Structures, 1988. **24**(3): p. 231-250.
152. Halloquist, J.O., *LS-Dyna Theory manual*. 2006, Livermore, California: Livermore Software Thechnology Corporation.
153. Gazonas, G.A., *Implementation of the Johnson-Holmquist II (JH-2) constitutive model into DYNA3D*. 2002, DTIC Document.
154. Johnson, G.R. and W.H. Cook, *Fracture characteristics of three metals subjected to various strains, strain rates, temperatures and pressures.* Engineering Fracture Mechanics, 1985. **21**(1): p. 31-48.
155. Evans, A., et al., *Probabilistic models for defect initiated fracture in ceramics.* Journal of Nondestructive Evaluation, 1980. **1**(2): p. 111-122.

156. Vekinis, G., M. Ashby, and P. Beaumont, *The compressive failure of alumina containing controlled distributions of flaws.* Acta metallurgica et materialia, 1991. **39**(11): p. 2583-2588.
157. Eberly, D.H., *Eigensystems for 3× 3 symmetric matrices (revisited)*.
158. Kaneko, T., *On Timoshenko's correction for shear in vibrating beams.* Journal of Physics D: Applied Physics, 1975. **8**(16): p. 1927.